



Carbon dioxide-Argon-Steam Oxyfuel (CARSOXY) Gas turbines

By

**Odi Fawwaz Awad Alrebei
B.Sc. Aeronautical Eng. & M.Sc. Aerospace Eng.**

A thesis submitted in partial fulfilment of the requirements for the degree of:

Doctor of

Philosophy in

Mechanical and Aerospace Engineering

**CARDIFF UNIVERSITY
SCHOOL OF ENGINEERING**

Cardiff, United Kingdom

December 2019

SIGNED STATEMENTS

DECLARATION

This work has not been submitted in substance for any other degree or award at this or any other university or place of learning, nor is being submitted concurrently in candidature for any degree or other award.

Signed(candidate) Date

STATEMENT 1

This thesis is being submitted in partial fulfillment of the requirements for the degree of PhD in Mechanical and Aerospace Engineering

Signed(candidate) Date

STATEMENT 2

This thesis is the result of my own independent work/investigation, except where otherwise stated, and the thesis has not been edited by a third party beyond what is permitted by Cardiff University's Policy on the Use of Third Party Editors by Research Degree Students. Other sources are acknowledged by explicit references. The views expressed are my own.

Signed(candidate) Date

STATEMENT 3

I hereby give consent for my thesis, if accepted, to be available online in the University's Open Access repository and for inter-library loan after expiry of a bar on access previously approved by the Academic Standards & Quality Committee.

Signed(candidate) Date

IN THE NAME OF ALLAH, THE BENEFICENT, THE MERCIFUL

“Read: In the name of thy Lord Who createth, (1) Createth man from a clot. (2) Read: And thy Lord is the Most Bounteous, (3) Who teacheth by the pen, (4) Teacheth man that which he knew not. (5)”

– SURAH AL-ALAQ, THE HOLY QURAN.

“Whoever takes a path upon which to obtain knowledge, Allah makes the path to Paradise easy for him.”

-THE PROPHET MUHAMMAD (PEACE BE UPON HIM).

TABLE OF CONTENTS

FIGURES INDEX	IX
TABLES INDEX	XIII
NOMENCLATURE	XV
ACKNOWLEDGEMENTS	XVII
PUBLICATIONS	1
SUMMERY	2
CHAPTER ONE-INTRODUCTION.	4
1.1 Motivation	4
1.2 Energy policy	4
1.2.1 Energy dependence	5
1.2.2 Natural gas dependence	6
1.3 Gas turbines emissions	8
1.4 CARSOXY gas turbines	9
1.5 Thesis aims and objectives	10
1.6 Thesis structure	11
CHAPTER 2–Literature Review	14
2.1 Energy demands and challenges	14
2.2 Alternative Working Fluids	14
2.3 Oxyfuel combustion	16
2.4 CARSOXY combustion	17
2.5 Complex and combined gas turbine cycles	18
2.5.1 Recuperative and humidified cycles (complex cycles)	18
2.5.2 Combined cycle /cogeneration (bottoming)	21
2.6 Carbon capture and storage (CCS)	22
2.6.1 CCS main categories	22
2.6.2 Carbon dioxide separation methods	24
2.7 Air separation unit (ASU)	25
2.7.1 Air separation main methods	25
2.7.2 Cryogenic distillation types	26
2.7.2.1 Thermally linked distillation column, with a side rectifier [92]	25
2.7.2.2 Thermally linked distillation column, with a side stripper [92]	27
2.7.2.3 Side rectifier vs side stripper	27
2.7.3 Low pressure (LP) distillation column vs elevated pressure (EP) distillation column.	28
2.7.4 Single distillation column vs. double-distillation column.	28
2.7.5 Integrating Heat pump techniques with ASU to enhance argon production.	28
2.7.5.1 Conventional Argon production [88]	28
2.7.5.2 EP Argon production [88]	29
2.8 Steam methane reforming (SMR)	29
2.8.1 SMR limitations	30
2.9 Water-gas shifting (WGS)	31
2.9.1 WGS applications	31
2.9.2 WGS Catalyst	32
2.9.3 WGS reactors	32
2.10 Classical combustion	33
2.11 A comprehensive review of the current state-of-the-art of combustion alternative working fluids.	35
2.11.1 The current state-of-the-art of oxygen-carbon dioxide-fuel combustion.	35
2.11.2 The current state-of-the-art of oxygen-steam-fuel combustion.	37
2.11.3 The current state-of-the-art of oxygen-inert gases-fuel combustion.	40

2.12 Chapter summary	43
CHAPTER 3 – METHODOLOGY	46
3.1 Methodology Sequence	46
3.2 The methodology of the parametric study of various thermodynamic cycles for the use of various CARSOXY blends	48
3.2.1 MATLAB Code Development	49
3.2.2 MATLAB Code Validation	51
3.3 The methodology of modelling CARSOXY Production	52
3.3.1 Initial and Final values	52
3.3.2 Steam-Methane Reforming (SMR) modelling	55
3.3.3 Water Gas Shifting (WGS) Modelling	56
3.3.4 Water Pressure Swing Adsorption (PSA) Modelling	56
3.3.5 Air Separation Unit (ASU) Modelling	57
3.3.6 Carbon Capture and Storage (CCS) Modeling	58
3.3.7 Heat Exchanged Gas Turbine (HXGT) Cycle Modeling	58
3.3.8 Model Validation	59
3.4 The methodology of assessing CARSOXY techno-economic	60
3.4.1 Techno-economic Setup of the CARSOXY model	61
3.4.2 Techno-economic Setup of an Air-driven HXGT model	61
3.4.3 Electricity generation and consumption modelling for the Air-driven gas turbine	62
3.4.4 Electricity generation and consumption modelling for the CARSOXY cycle	63
3.4.5 Techno-economic Assumptions	63
3.4.6 Raw material and products pricing	64
3.4.7 Equipment Pricing	67
3.5 The methodology for assessing flame chemiluminescence and emissions.	74
3.5.1 Chemiluminescence imaging systems	74
3.5.2 Emission analyses system	75
3.5.3 Burner specifications	76
3.5.4 Working fluid calibration	77
3.5.5 Acoustic properties	77
3.5.6 Experiment procedure and matrix	78
3.5.7 Certainty	80
3.5.8 Intensifier gate signal pulse width /gain selection	80
3.5.9 Number of images justification	82
3.5.10 Background correction and temporal averaging	83
3.5.11 Chemiluminescence and heat release fluctuations	84
3.5.12 Specially resolved images	85
3.5.13 Identifying the location of the highest heat intensity centre	86
3.5.14 Identifying the area of the highest heat intensity centre	86
3.6 Methodology for assessing flame induced fluorescence.	87
3.6.1 PLIF components and setup	88
3.6.2 Experiment procedure and matrix	90
3.6.3 PLIF image processing and data analyses	91
3.6.3.1 Laser energy shot-to-shot variation	92
3.6.3.2 Background and laser sheet image corrections	92
3.6.3.3 Flame properties detection	94
3.6.3.4 Damköhler number (Da) estimation for nonpremixed flames	95
CHAPTER 4 – A PARAMETRIC STUDY OF VARIOUS THERMODYNAMIC CYCLES FOR THE USE OF VARIOUS CARSOXY BLENDS	99
4.1 Analyses intervals	99
4.2 Efficiency results with respect to variable compressor inlet temperatures and compressor pressure ratio.	101
4.2.1 Simple cycle	101

4.2.2 Heat exchanged cycle	102
4.2.3 Free turbine & simple cycle	103
4.2.4 Evaporative cycle	105
4.2.5 Humidified cycle	106
4.2.6 Section summary	107
4.3 Efficiency results with respect to variable molar fractions of Ar, CO ₂ , and H ₂ O.	109
4.4 Efficiency results with respect to the turbine inlet temperature	111
4.5 Discussion	112
4.6 Conclusion	113
CHAPTER 5 – A NOVEL APPROACH OF PRODUCING CARSOXY	115
5.1 Sensitivity analyses	115
5.1.1 SMR sub-model sensitivity analysis	116
5.1.1.1 SMR molar fractions vs H ₂ O feed	116
5.1.1.2 SMR molar fractions vs CH ₄ feed	117
5.1.1.3 SMR molar fractions vs CH ₄ split ratio	118
5.1.1.4 SMR molar fractions vs Furnace Air mass flow rate	118
5.1.2 WGS sub-model sensitivity analysis	119
5.1.3 ASU sub-model sensitivity analysis	120
5.1.3.1 ARO2RECT molar fractions vs BOOSTER discharge pressure	120
5.1.3.2 ARO2RECT molar fractions vs ATMIR mole flow rate	121
5.1.3.3 ARO2RECT molar fractions vs AIRLP mole flow rate	122
5.1.3.4 ARO2RECT molar fractions vs LPDC number of stages	122
5.1.3.5 ARO2RECT molar fractions vs LPDC Distillate rate	123
5.1.3.6 ARO2RECT molar fractions vs LPDC Boil-up rate	123
5.1.3.7 ARO2RECT molar fractions vs O2ARHOT Feed stage location in the LPDC	124
5.1.3.8 ARO2RECT molar fractions vs ARO2RECT and O2LPDC Feed stage location in the LPDC product stage location in the LPDC	124
5.1.3.9 Oxygen-Argon-Carbon dioxide compression vs Oxygen-Argon compression	125
5.2 Calibration and final results	125
5.2.1 SMR-WGS-PSA Calibration	128
5.2.2 ASU Calibration	132
5.3 Discussion	134
5.4 Conclusion	135
5.5 Future work	136
CHAPTER 6 –CARSOXY Techno-economics	138
6.1 Capital costs and operation costs	138
6.2 Raw material costs and product sales	142
6.3 Payout period and Engineering, procurement and construction (EPC) period	144
6.4 Operation cost and product sales breakdowns throughout the project's life	145
6.5 Revenue Breakdown	147
6.7 Net present value	150
6.8 Rates of return and profitability index Results	151
6.9 Conclusion	153
CHAPTER 7 – CARSOXY chemiluminescence imaging and emission analyses.	156
7.1 NO, NO ₂ and NO _x emissions	157
7.2 CO emissions	157
7.3 $\sigma_{OH^*/\overline{OH}}$ at \dot{V}_{WF} of 80 L/min and \dot{V}_{CH_4} of 1L/min.	158
7.4 $\sigma_{OH^*/\overline{OH}}$ at \dot{V}_{WF} of 60 L/min and \dot{V}_{CH_4} of 1L/min.	159
7.5 $\sigma_{OH^*/\overline{OH}}$ at \dot{V}_{WF} of 40 L/min and \dot{V}_{CH_4} of 1L/min.	160
7.6 $\sigma_{OH^*/\overline{OH}}$ functions of frequency ($\sigma_{OH^*/\overline{OH}}(f)$)	161

7.7 Area of highest heat intensity ($A_{\overline{OH}_{Max}}$) at \dot{V}_{WF} of 80 L/min and \dot{V}_{CH_4} of 1L/min.	162
7.8 Area of highest heat intensity ($A_{\overline{OH}_{Max}}$) at \dot{V}_{WF} of 60 L/min and \dot{V}_{CH_4} of 1L/min.	164
7.7 Area of highest heat intensity ($A_{\overline{OH}_{Max}}$) at \dot{V}_{WF} of 40 L/min and \dot{V}_{CH_4} of 1L/min.	166
7.8 Centre of highest heat intensity ($C_{\overline{OH}_{Max}}$) at \dot{V}_{WF} of 80 L/min and \dot{V}_{CH_4} of 1L/min.	169
7.9 Centre of highest heat intensity ($C_{\overline{OH}_{Max}}$) at \dot{V}_{WF} of 60 L/min and \dot{V}_{CH_4} of 1L/min.	169
7.10 Center of highest heat intensity ($C_{\overline{OH}_{Max}}$) at \dot{V}_{WF} of 40 L/min and \dot{V}_{CH_4} of 1L/min.	170
7.11 Discussion	171
7.12 Conclusion	173
CHAPTER 8 – PLANER LASER-INDUCED FLUORESCENCE AND CHEMILUMINESCENCE ANALYSES OF CARSOXY COMBUSTION.	175
8.1 $\sigma_{OH^*/\overline{OH}}$ of CARSOXY and CH ₄ /air flames at constant Reynolds numbers/ chemiluminescence	175
8.2 $\sigma_{OH^*/\overline{OH}}$ of CARSOXY and CH ₄ /air flames at constant λ_{oxy} / chemiluminescence	176
8.3 $\sigma_{OH^*/\overline{OH}}$ functions of Re and λ_{oxy} ($\sigma_{OH^*/\overline{OH}}(Re)$ and $\sigma_{OH^*/\overline{OH}}(\lambda_{oxy})$)/ chemiluminescence	178
8.4 Area of the highest heat intensity ($A_{\overline{OH}_{Max}}$) of CARSOXY and CH ₄ /air flames at constant Reynolds numbers/ PLIF	179
8.5 Area of the highest heat intensity ($A_{\overline{OH}_{Max}}$) at constant λ_{oxy} / PLIF	181
8.6 Centre of the highest heat intensity ($C_{\overline{OH}_{Max}}$) at constant Re and \dot{V}_{CH_4} of 1L/min/ PLIF	182
8.7 Centre of the highest heat intensity ($C_{\overline{OH}_{Max}}$) at constant λ_{oxy} / PLIF	183
8.8 Damkohler number (Da) and combustion diagrams/ PLIF	184
8.8.1 Damkohler number (Da)	185
8.8.2 Borghi regime diagram	186
8.9 Modified Damkohler number (Da) and Borghi regime diagram	188
8.10 Discussion and conclusion	190
8.11 limitations	192
CHAPTER 9 – DISCUSSION AND FUTURE WORK	194
9.1 Outcomes of the parametric study	194
9.2 Outcomes of analyzing the novel approach of producing CARSOXY	194
9.3 Outcomes of the Techno-economic assessment of the ASU-SMR-WGS-PSA-CCS-HXGT cycle	195
9.4 Outcomes of the chemiluminescence imaging and emission analyses over a range of instability conditions (excitation frequencies [50Hz-700Hz]) and variable volumetric flowrates	194
9.5 Outcomes of PLIF and Chemiluminescence analyses over a range of λ_{oxy} and fluid Reynold's numbers	196
9.6 Future work	197
REFERENCES	199
APPENDIX 3	212
Appendix 3.1 Cycle analyses MATLAB code	212
Appendix 3.1.2 Heat exchanged gas turbine cycle	213
Appendix 3.1.3 Simple cycle and free turbine arrangement code	214
Appendix 3.1.4 Evaporation cycle code	215
Appendix 3.1.5 humidified gas turbine cycle code	216
Appendix 3.2.1 Image procession (background correction, averaging and fluctuation)	217
Appendix 3.2.2 Abel deconvolution code	218
Appendix 3.3 PLIF image processing and analyses codes	219
Appendix 3.3.2 PLIF Laser energy shot-to-shot correction	219
Appendix 3.3.3 PLIF Laser sheet profile correction [150]	220
Appendix 3.3.4 PLIF flame properties [150]	221

APPENDIX 4	222
Appendix 4.1 Efficiency results with respect to variable compressor inlet temperatures and compressor pressure ratio.	222
Appendix 4.2 Efficiency results with respect to variable molar fractions of Argon, CO ₂ , and H ₂ O.	223
Appendix 4.3 Efficiency results for blend 58 and the new suggested blend	224
Appendix 4.4 Efficiency results with respect to the turbine inlet temperature	225

FIGURES INDEX

Figure 1.1 Typical chemical composition of natural gas	7
Figure 1.2 UK annual liquefied natural gas imports by exporting country in 2015.	7
Figure 1.3 Nature of Different emission constituents against equivalence ratios	9
Figure 2.1 The original CARSOXY cycle	18
Figure 2.2 cooling techniques coupled with recuperation	19
Figure 2.3 Steam injections	20
Figure 2.4 Evaporative gas turbine cycle	20
Figure 2.5 SMR integrated with heat exchanged cycle	21
Figure 2.6 Gas turbine-steam turbine cogeneration	22
Figure 2.7 Simplified diagram of a post-combustion capture process using reactive solvents	23
Figure 2.8 pre-combustion CCS	23
Figure 2.9 Oxyfuel combustion CCS	24
Figure 2.10 thermally linked distillation column	27
Figure 2.11 Argon productions	29
Table 2.12 SMR process	40
Figure 2.13 Conventional WGS reactors	32
Figure 2.14 shell and tube WGS reactor	33
Figure 2.15 Can combustors	33
Figure 2.16 Annular combustor	34
Figure 2.17 Premixed vs diffusive combustion	35
Figure 2.18 flammability upper and lower limits of CO ₂ -O ₂ - CH ₄ combustion at three oxygen fractions (namely 29%, 32% and 36%) in comparison to air- CH ₄ combustion	36
Figure 2.19 Visual length of CO ₂ - O ₂ - CH ₄ flames at three oxygen fractions (namely 29%, 32% and 36%) in comparison to air- CH ₄ flame	36
Figure 2.20 Trend lines (black) for literature data for humidified gas turbine cycles	38
Figure 2.21 laminar flame speed of O ₂ - H ₂ O- CH ₄ and O ₂ - CO ₂ - CH ₄ combustions	39
Figure 2.22 Comparison of cost distributions for oxy-steam (O ₂ - H ₂ O- CH ₄) combustion and oxy- CO ₂ (O ₂ - CO ₂ - CH ₄) combustion	39
Figure 2.23 Temperature contours of hydrogen injection into nitrogen, argon, and xenon	41
Figure 2.24 Maximum temperature and maximum OH concentration	42
Figure 2.25 Spatial variation vs. scalar dissipation between 3 ms and 6 ms after injection	42
Figure 3.1 Schematic diagrams of the cycles.	46
Figure 3.2 ASU-SMR-WGS-PSA-CCS-HXGT model.	54
Figure 3.3 Air-driven HX-GT sub-models.	62
Figure 3.4 ASU-SMR-WGS-PSA-CCS-HXGT model, updated with electricity generation.	65
Figure 3.5 Chemiluminescence Experiment setup	75
Figure 3.6 The 20-kW generic burner system	76
Figure 3.7 Intensifier gate signal pulse width and camera exposure time.	84
Figure 3.8 image intensifier gain transfer curves.	85
Figure 3.9 Regional pixel intensities of the horizontal edge-to-edge line at a vertical coordinate of 23 mm (or 260 pixels).	86
Figure 3.10 A sample of the temporally averaged and background-corrected images.	86
Figure 3.11 Data Sample of the Standard deviation (σ) of the heat release fluctuations ($\overline{OH^* / \overline{OH}}$) (40L/min of (Air or [CO ₂ , Ar, O ₂]) at 200Hz at 8db at 10V).	87
Figure 3.12 A sample of temporally and specially resolved images using Abel deconvolution.	86

Figure 3.13 Sample of the right-hand side ($C_{\overline{\theta H}_{Max}}$) with respect to the burner centerline	86
Figure 3.14 sample of the calculated areas	87
Figure 3.15 PLIF top view	89
Figure 3.15 Absolute gradient of the Laser sheet Gaussian fit	93
Figure 3.16 PLIF laser sheet intensity (A) and Gaussian fit to intensity distribution (B) for image correction.	94
Figure 3.16 Schematic representation of the flame	96
Figure 3.17 S_L for a CH ₄ /air flame and a CH ₄ / CO ₂ - Ar NO _x - O ₂ flame at a range of equivalence ratios.	97
Figure 4.1 Efficiency results for the simple cycle (Wet compression of CARSOXY vs Air).	101
Figure 4.2 Efficiency results for the simple cycle (dry compression of CARSOXY vs Air).	102
Figure 4.3 Efficiency of the heat exchanged cycle (Wet compression of CARSOXY vs Air).	102
Figure 4.4 Efficiency of the heat exchanged cycle (dry compression of CARSOXY vs Air).	103
Figure 4.5 Efficiency results for the free turbine-simple cycle arrangement (Wet compression of CARSOXY vs Air)	104
Figure 4.6 Efficiency results for the free turbine-simple cycle arrangement (Dry compression of CARSOXY vs Air)	104
Figure 4.7 Efficiency results for the evaporative cycle (Wet compression of CARSOXY vs Air)	105
Figure 4.8 Efficiency results for the evaporative cycle (dry compression of CARSOXY vs Air)	106
Figure 4.9 Efficiency results for the humidified cycle (Wet compression of CARSOXY vs Air)	106
Figure 4.10 Efficiency results for the humidified cycle (Dry compression of CARSOXY vs Air)	107
Figure 4.11. Efficiency results for all cycles with dry compression. (Refer to Appendix 4-Figure AP 4.1 for transparent surfaces)	109
Figure 4.12. Efficiency results with respect to variable molar fractions of Argon, CO ₂ , and H ₂ O (Refer to Appendix 4-Figure AP 4.2 for transparent surfaces).	110
Figure 4.13. Efficiency results for blend 58 and the new suggested blend (Refer to Appendix 4-Figure AP 4.3 for transparent surfaces)	111
Figure 4.14. Efficiency results for all cycles with respect to turbine inlet temperature variation. (Refer to Appendix 4-Figure AP 4.4 for transparent surfaces)	112
Figure 5.1: Initial SMR-WGS-PSA model	116
Figure 5.2: SMR sensitivity results (SMR molar fractions vs H ₂ O feed). Lines A, B and C correspond to the H ₂ O flow rates of 175, 225 and 350 kg/h, respectively.	117
Figure 5.3: SMR sensitivity results (SMR molar fractions vs CH ₄ feed). Line D corresponds to the CH ₄ flow rate of 200 [kg/h].	117
Figure 5.4: SMR sensitivity results (SMR molar fractions vs CH ₄ split ratio)	118
Figure 5.5: SMR sensitivity results (SMR molar fractions vs Furnace Air mass flow rate). Line E corresponds to the Airflow rate of 650 kg/h.	119
Figure 5.6: WGS sensitivity results (WGS product molar fractions vs WGS H ₂ O mass flow rate)	120
Figure 5.7: ASU initial Model	120
Figure 5.8: ARO2RECT molar fractions vs BOOSTER discharge pressure	121
Figure 5.9: ARO2RECT molar fractions vs ATMIR mole flow rate	121
Figure 5.10: ARO2RECT molar fractions vs AIRLP mole flow rate	122

Figure 5.11: ARO2RECT molar fractions vs LPDC number of stages	122
Figure 5.12: ARO2RECT molar fractions vs LPDC Distillate rate	123
Figure 5.13: ARO2RECT molar fractions vs. LPDC Boil-up rate	123
Figure 5.14: ARO2RECT molar fractions vs O2ARHOT Feed stage location in the LPDC	124
Figure 5.15: ARO2RECT molar fractions vs ARO2RECT product stage location in the LPDC	124
Figure 5.16: Oxygen-Argon-Carbon dioxide compression vs Oxygen-Argon compression	125
Figure 5.17: Ammonia production (Second mode).	135
Figure 6.1 Total project cost and operational costs.	139
Figure 6.2. The breakdown of the total project capital cost of the CARSOXY cycle	140
Figure 6.3. The breakdown of the total project capital cost of the Air-driven gas turbine cycle	140
Figure 6.4 G&A and Plant overhead costs.	141
Figure 6.5 Total raw material cost and product sales.	142
Figure 6.6 Raw material cost breakdown	143
Figure 6.7 Sales breakdown	143
Figure 6.8 Payout period and Engineering, procurement and construction (EPC) period	144
Figure 6.9 CARSOXY operation cost breakdown	145
Figure 6.10 Air-driven operation cost breakdown	146
Figure 6.11 CARSOXY product sales breakdown	148
Figure 6.12 Air-driven product sales breakdown	147
Figure 6.13 CARSOXY Revenue Breakdown (Note: Depreciation is negligible)	149
Figure 6.14 Air-driven Revenue Breakdown (note: Depreciation is negligible)	150
Figure 6.15 CARSOXY NPV	150
Figure 6.16 Air-driven NPV.	151
Figure 6.17 IRR and MIRR results.	152
Figure 6.18 NRR and IP results.	153
Figure 7.1 NO, NO ₂ and NO _x flue gases at 140 L/min of \dot{V}_{WF} .	157
Figure 7.2 CO emissions at 140 L/min of \dot{V}_{WF} .	158
Figure 7.3 $\sigma_{OH^*/OH}$ at \dot{V}_{WF} of 80 L/min.	159
Figure 7.4 $\sigma_{OH^*/OH}$ at \dot{V}_{WF} of 60 L/min.	160
Figure 7.5 $\sigma_{OH^*/OH}$ at \dot{V}_{WF} of 40 L/min.	160
Figures 7.6 temporally and specially resolved images (at \dot{V}_{WF} of 80 L/min and \dot{V}_{CH_4} of 1L/min, 700-350) Hz.	162
Figures 7.7 temporally and specially resolved images (at \dot{V}_{WF} of 80 L/min and \dot{V}_{CH_4} of 1L/min, 300-50) Hz.	163
Figure 7.8 Area of highest heat intensity ($A_{\overline{OH}_{Max}}$) at \dot{V}_{WF} of 80 L/min.	164
Figure 7.9 Area of highest heat intensity ($A_{\overline{OH}_{Max}}$) at \dot{V}_{WF} of 60 L/min.	164
Figure 7.10 temporally and specially resolved images (at \dot{V}_{WF} of 60 L/min and \dot{V}_{CH_4} of 1L/min, 700-350) Hz.	165
Figure 7.11 temporally and specially resolved images (at \dot{V}_{WF} of 60 L/min and \dot{V}_{CH_4} of 1L/min, 300-50) Hz.	166
Figure 7.12 temporally and specially resolved images (at \dot{V}_{WF} of 40 L/min and \dot{V}_{CH_4} of 1L/min, 700-350) Hz.	167
Figure 7.13 temporally and specially resolved images (at \dot{V}_{WF} of 40 L/min, 300-50Hz).	168
Figure 7.14 Area of highest heat intensity ($A_{\overline{OH}_{Max}}$) at \dot{V}_{WF} of 40 L/min.	168
Figure 7.15 Centre of highest heat intensity ($A_{\overline{OH}_{Max}}$) at \dot{V}_{WF} of 80 L/min.	169

Figure 7.16 Centre of highest heat intensity ($A_{\overline{OH}_{Max}}$) at \dot{V}_{WF} of 60 L/min.	170
Figure 7.11 Centre of highest heat intensity ($A_{\overline{OH}_{Max}}$) at \dot{V}_{WF} of 40 L/min.	170
Figure 8.1.A $\sigma_{OH^*/\overline{OH}}$ at constant working fluid Reynold's numbers at \dot{V}_{CH_4} of 1L/min	176
Figure 8.1.B Sample cases of the chemiluminescence images at constant Re	176
Figure 8.2A $\sigma_{OH^*/\overline{OH}}$ at λ_{oxy} of [35-70].	177
Figure 8.2.B Sample cases of the chemiluminescence images at constant λ_{oxy}	178
Figure 8.3 $A_{\overline{OH}_{Max}}$ at Re of [2000-3750] and \dot{V}_{CH_4} of 1L/min	180
Figure 8.4 Temporally averaged and energy shot-to-shot and laser-sheet corrected PLIF images at Re of [2000-2250] and \dot{V}_{CH_4} of 1L/min	180
Figures 8.5 $A_{\overline{OH}_{Max}}$ at λ_{oxy} of [35-70]	181
Figure 8.6 Temporally averaged and energy shot-to-shot and laser-sheet corrected PLIF images at λ_{oxy} of [35-70].	182
Figure 8.7 ($C_{\overline{OH}_{Max}}$) distribution at constant working fluid Reynold's numbers [2000-3750] and \dot{V}_{CH_4} of 1 L/min	183
Figure 8.8 ($C_{\overline{OH}_{Max}}$) distribution at constant λ_{oxy} [35-70].	184
Figure 8.9 Da at constant working fluid Reynold's numbers [2000-3750] and \dot{V}_{CH_4} of 1 L/min	185
Figure 8.10 Da at constant λ_{oxy} [35-70].	186
Figure 8.11 Borghi regime at constant working fluid Reynold's numbers [2000-3750] and \dot{V}_{CH_4} of 1 L/min	187
Figure 8.12 Borghi regime at constant λ_{oxy} [35-70].	187
Figure 8.13 Da, mod at constant working fluid Reynold's numbers [2000-3750] and \dot{V}_{CH_4} of 1 L/min	188
Figure 8.14 Modified Borghi regime at constant working fluid Reynold's numbers [2000-3750] and \dot{V}_{CH_4} of 1 L/min	189
Figure 8.15 Da, mod at constant λ_{oxy} [35-70].	189
Figure 8.16 Modified Borghi regime at constant λ_{oxy} [35-70].	190

TABLES INDEX

Table 1.1 Global electricity demand by sector	6
Table 1.2 World net electricity generation by resource, shares is in trillion kilowatt-hours	6
Table 1.3 Gas turbine emission categories	8
Table 2.1 CCS technologies states	24
Table 2.2 CO ₂ advantages and disadvantages	25
Table 2.3 air components relative volatility	27
Table 2.4 SMR catalyst	31
Table 2.5. WGS catalysts	32
Table 2.6. Annular combustor vs can combustor	34
Table 2.7. CO ₂ - O ₂ - CH ₄ vs air- CH ₄ combustion.	37
Table 2.8. O ₂ - H ₂ O- CH ₄ vs O ₂ - CO ₂ - CH ₄ combustion.	40
Table 2.9. Comparison of design parameters between air compressors and helium compressors [22-24]	41
Table 3.1. Compositions of the blends. Blend number as in [25].	51
Table 3.2: Initial and final input values.	52
Table 3.3 HXGT Parameters.	58
Table 3.4 Convergence results.	58
Table 3.5 Economic evaluators	60
Table 3.6: ASU-SMR-WGS-PSA-CCS-HXGT mole flow rates for 1 kmol/h of Methane	61
Table 3.7: description of the components of the Air-driven-heat-exchanged cycle.	63
Table 3.8 techno-economic assumptions	64
Table 3.9 Raw martial pricing.	64
Table 3.10 Products pricing.	66
Table 3.11 Quoted pieces of equipment	66
Table 3.12 Heat exchangers material Cost factor vs. Maximum metal temperature	67
Table 3.13. HX, HX2, B1, HXHX and AIRX operation conditions and Ξ	67
Table 3.14 DeCicco's and Ward's cost factors	68
Table 3.15. SMR the HTWGS, LTWGS and the Furnace operation conditions and \hat{C}_{DW}	69
Table 3.16. Klumpar's, Brown's and Fromme's cost factors and constants	70
Table 3.17. B4, H2MIX, N2MIX, CH4SPLIT, ASUSP, S5, and S4A operation conditions and \hat{C}_{KBF}	70
Table 3.18. C, CC, B11, HPCOMPCH4, HPCOMPH2O, CH4AIR, CAIR, CCAIR and TAIR operation conditions and \hat{C}_{2016}	72
Table 3.19 ASPEN-PLUS database pricing	73
Table 3.20 $V, R_e, \dot{m}_{oxygen}, \lambda_{oxy}$ and ϕ_{oxy} of the three \dot{V}_{WF} (40,60,80 L/min).	79
Table 3.21 The actual filled molar fraction values of carbon dioxide, oxygen and argon.	80
Table 3.22 Methane impurities of methane CP grade [198]	80
Table 3.23 Average relative error for the partially averaged images	83
Table 3.24 $V, \dot{V}_{WF}, \dot{m}_{oxygen}, \lambda_{oxy}$ and ϕ_{oxy} of the eight R_e (2000-3750).	90
Table 3.25 $V, \dot{V}_{WF}, \dot{m}_{oxygen}$, and R_e of the nine λ_{oxy} (35-70)	91
Table 4.1 Blend 58 molar fractions	100
Table 4.2 Analyses intervals	100
Table 4.3 CARSOXY ultimate operation conditions (compressor inlet temperatures and pressure ratio)	108
Table 4.4 a sample results of increasing turbine temperatures from 800K to 1200K.	111

Table 5.1: CARSOXY final molar fraction.	128
Table 5.2: ASU-SMR-WGS-PSA-CCS-HXGT mole flow rates for 1 kmol/h of Methane	128
Table 5.3 CARSOXY molar fraction, blend 58	127
Table 5.4 SMR-WGS-PSA calibration methods	127
Table 5.5 uncalibrated molar fractions of the SMR-WGS-PSA	128
Tables 5.6.A and 5.6.B: Attempts 1 and 2: Calibrating the SMR-WGS-PSA sub-models	128
Table 5.6.C: Attempt 3: Calibrating the SMR-WGS-PSA sub-models	129
Table 5.7: Attempt 4: Calibrating the SMR-WGS-PSA sub-models	129
Table 5.8: Attempt 5: Calibrating the SMR-WGS-PSA sub-models	129
Table 5.9: Attempt 6: Calibrating the SMR-WGS-PSA sub-models	130
Table 5.10: Attempt 7: Calibrating the SMR-WGS-PSA sub-models	130
Table 5.11: Attempt 8: Calibrating the SMR-WGS-PSA sub-models	130
Table 5.12: Attempt 9: Calibrating the SMR-WGS-PSA sub-models	131
Table 5.13: Attempt 10: Calibrating the SMR-WGS-PSA sub-models	131
Table 5.14: Attempt 11: Calibrating the SMR-WGS-PSA sub-models	131
Table 5.15: Attempt 12: Calibrating the SMR-WGS-PSA sub-models	131
Table 5.16: Uncalibrated molar fractions of the ASU (initial model)	132
Table 5.17 Calibrating the ASU unit	133
Table 5.18 Calibrating the ASU unit	133
Table 5.19 Calibrating the ASU unit	134
Table 5.20 Calibrating the ASU unit	134
Table 6.1 Economic terms	147
Table 7.1 $\sigma_{OH^*/OH}$ (f) at ([50 Hz -700 Hz]	161
Table 7.3 Average $\sigma_{OH^*/OH}^{CARSOXY}$ and $\sigma_{OH^*/OH}^{Air}$ over the excitation interval [50Hz-700Hz] for $\dot{V}_{WF}=80L/min$, 60L/min and 40L/min.	172
Table 8.1 $\sigma_{OH^*/OH}$ (Re) at Re of [2000 -3750], \dot{V}_{CH_4} of 1L/min.	178
Table 8.2 $\sigma_{OH^*/OH}$ (λ_{oxy}) at λ_{oxy} of [35-70].	179

NOMENCLATURE

A	Cross-sectional area [m ²]
$A_{\overline{OH}}_{Max}$	Area of the highest heat intensity [mm]
A'	The molar fraction of fuel in CARSOXY mixture
a	Actual pixel intensity
B	The molar fraction of the oxygen in CARSOXY mixture
b	Background pixel intensity
C_xH_y	Hydrocarbon fuel, methane (x: 1 and y: 4)
$C_{p_{mix}}$	Specific heat at a constant pressure of a mixture [J/mol.K]
$C_p(i)$	Specific heat at a constant pressure of an ith component in a mixture [J/mol.K]
$C_{v_{mix}}$	Specific heat of a mixture at constant volume [J/mol.K]
CEPCI	Chemical Engineering Plant Cost Index
CEPCI _{updated}	Updated Chemical Engineering Plant Cost Index
CEPCI _{Archived}	Archived Chemical Engineering Plant Cost Index
$C_{updated}$	Updated Price (currency depends on the used reference)
$C_{Archived}$	Archived Price (currency depends on the used reference)
\dot{C}	Raw material and product price (currency depends on the used reference)
\dot{C}_{DW}	Capital costs, Equation 3.18 [€ ₂₀₀₂]
\dot{C}_{KBF}	Capital costs, Equation 3.20 [\$ ₁₉₈₁]
\dot{C}_{2016}	\dot{C}_{DW} and \dot{C}_{KBF} averaged cost [£, 2016]
C_{ASPEN}	ASPEN PLUS-based price [£, 2016]
c	Background corrected pixel intensity
\bar{c}	Temporally averaged and background corrected pixel intensity
$C_{\overline{OH}}_{Max}$	Location of the highest heat intensity [mm]
$\Delta\bar{C}_p$	Change in heat capacity at constant pressure [J/mol.K]
$\langle c \rangle$	Reaction progress variable
D	The density of the gas at the working conditions [kg/m ³]
Da	Damköhler number
Da_{mod}	The modified Damköhler number
f	Fuel to air ratio
f'	material cost factor
$F_T, F_P, F_m,$	Temperature, pressure and material cost factors, respectively. Equation (3.18)
\dot{F}	Cost factor, Equation (3.21)
FSD	Full-Scale deflection
\dot{G}	Mass flow rate, Equation(3.21) (lbs/h)
$HHV_{T'_{0.1}}$	Higher heating Value at the combustion inlet temperature [kJ/Kg]
$HHV_{T'_{0.2}}$	Higher heating Value at the combustion outlet temperature [kJ/Kg]
$H_{wf, T'_{0.2}}$	Enthalpy of the working fluid at the combustion outlet temperature [kJ/mol]
$H_{wf, T'_{0.1}}$	Enthalpy of the working fluid at the combustion inlet temperature [kJ/mol]
$\Delta H_{Reaction, 25^{\circ}C}$	Standard enthalpy change of the combustion reaction
$\Delta H_{products}$	Enthalpy of products [kJ/mol]
$\Delta H_{reactant}$	Enthalpy of reactants [kJ/mol]
$\Delta H_{Reaction, T'_{0.1}}$	Enthalpy of the combustion reaction at the combustion inlet temperature [kJ/mol]
$H_{H_2O, T'_{0.1}}$	Enthalpy of H ₂ O at the combustion inlet temperature [kJ/Kg]

i	Horizontal pixel
I	Intensity [count]
I_{GF}	the Gaussian fitted intensity of the normalized intensity [count]
j	Vertical pixel
K_{KBF}	Cost Constant, Equation (3.20)
k_{DW}	Cost constant, Equation (3.18)
$LHV_{T'_{0,1}}$	Lower heating value at the combustion inlet temperature [kJ/Kg]
LHV	Lower Heating Value [kJ/kg]
L_H	Hydraulic Diameter [m]
L_0	The outer diameter of the swirler nozzle [m]
L_i	The inner diameter of the diffusive injector [m]
L_f	The flame base location where the maximum OH intensity is found [mm]
$M_{C_xH_y}$	Molecular weight of Methane (x: 1 and y: 4) [g/mol]
M_{H_2O}	The molecular weight of H ₂ O [g/mol]
$\dot{m}_{in,REC}^{cold}$	The mass flow rates of heat exchangers cold side [kg/s]
\dot{m}_p	Mass flow rate [kg/], Equation (3.19)
m	m th image
\dot{m}_f	Mass flow rate of fuel [kg/sec]
$\dot{m}_{oxygen,Act}$	Actual Oxygen Mass Flow Rate [g/s]
$\dot{m}_{fuel,Act}$	Actual Fuel Mass Flow Rate [g/s]
n_{H_2O}	Number of moles of H ₂ O produced due to combustion
$n_{C_xH_y}$	Number of moles of Hydrocarbon fuel in CARSOXY mixture
$n_{oxygen,stoic}$	Number of oxygen molecules in stoichiometric combustion of CH ₄ (=2)
$n_{fuel,stoic}$	Number of CH ₄ molecules in stoichiometric combustion (=1)
n	Number of images
n_H	Number of hours
n_D	Number of days
\dot{N}	Number of pieces of equipment
OFR_{Act}	Actual oxygen to fuel ratio
OFR_{stoic}	Stoichiometric oxygen to fuel (CH ₄) ratio (=2)
OH^*/\overline{OH}	Heat release fluctuation
$poco/poci$	Compressor pressure ratio
$p_{in,REC}^{cold}$	Inlet pressure of Heat exchangers cold side [bar]
ΔP	Heat exchangers pressure losses percentage
\acute{P}	Pressure factor, Equation (3.21)
P_{th}	Thermal power [kW]
\dot{Q}	Equipment annual capacity [tons/year], Equations (3.18) and (3.19)
q_v	volume flowrate [m ³ /sec]
r_1	Cost coefficient of Equation (3.17) [€ ₂₀₀₂]
r_i	The volume fraction of i th in CARSOXY mixture
R_{mix}	A gas constant of a gaseous mixture [J/mol·K]
Re	Working fluid average Reynold's numbers
R	Horizontal position [mm] of the Abel-deconvoluted image
SFC	specific fuel consumption
S_L	Laminar flame speed [mm/s]
To, ci	Compressor inlet temperature [K]
To, ti	Turbine inlet temperature [K]
T_{max}	Maximum allowable temperature (°C) for Equation (3.17) and (K) for Tables (3.13-3.17)
\acute{T}	Temperature factor, Equation (3.21)

u_F	Fuel injection velocity [mm/s]
\dot{V}_{CH_4}	The volumetric flow rate of fuel [L/min]
\dot{V}_{WF}	The volumetric flow rate of working fluid [L/min]
V	Velocity [m/s]
\dot{V}	Volume flow rate [m ³ /s]
W_t	Turbine specific work [kJ/Kg]
W_C	Specific work required from the turbine to run the compressor [kJ/Kg]
X'	The molar fraction of the Argon in CARSOXY mixture
x_i	The molar fraction of the <i>i</i> th component in a mixture
X	Horizontal position [mm]
Y	Vertical position [mm]
Y'	The molar fraction of H ₂ O in CARSOXY mixture
γ_{mix}	Heat capacity ratio of a mixture
η	Cycle efficiency
μ_{mix}	The average molecular weight of a mixture [g/mol]
μ_i	The molecular weight of an <i>i</i> th component in a mixture [g/mol]
μ	Dynamic Viscosity [kg/ms]
ν	Kinematic Viscosity [m ² /s]
$\bar{\epsilon}_{REC}$	The purchased capital cost of heat exchangers, Equation (3.17) [€ ₂₀₀₂]
$\bar{\epsilon}_{\text{€},2016}$	The purchased capital cost of heat exchangers escalated to 2016, Equation (3.17) [£, 2016]
$\bar{\epsilon}_{\text{£},2016}$	The purchased capital cost of heat exchangers escalated to 2016 and converted to 2016 sterling pound, Equation (3.17) [£, 2016]
ρ	Density [kg/m ³]
ϕ_{oxy}	Fuel to oxygen equivalence ratio
σ	A molar fraction in products
$\sigma_{OH^*/\bar{O}H}$	The standard deviation of heat release fluctuation
λ_{oxy}	Oxygen to fuel equivalence ratio

ACKNOWLEDGEMENTS

{In the name of God, the infinitely Compassionate and Merciful. Praise be to God, Lord of all the worlds. The Compassionate, the Merciful. Ruler on the Day of Reckoning.}

AL-FATIHA, THE HOLY QURAN.

My sincere appreciations begin with my PhD supervisors, Prof. AGUSTIN VALERA MEDINA and Prof. PHIL BOWEN without whom this work would have never come to life and simply remained unfulfilled Gantt charts. To Prof. AGUSTIN, the best decision I have ever made in my academic journey was joining your research team, you have always opened all the possible opportunities (perhaps, also those which I used to think were impossible) for me to flourish my academic career. I simply cannot thank you enough. To Prof. PHIL, I would like to thank you for your guidance and trust. I have always been honoured by your supervision and always overwhelmed by your valuable knowledge and support. I would like also to thank you for supporting me in publishing conference and journal papers within this thesis.

I would like to express my appreciations to Prof. RICHARD MARSH and Dr DAN PUGH for their efforts on facilitating all resources to conduct our research in the highest possible criteria. I would like also to thank you for your thoughtful input and feedback in all the research meetings. To Dr JON RUNYON, I am grateful for your support on all those long days of experiments, and for being very generous with your valuable knowledge, which has played a major role in completing the experimental stage of the study.

My deepest appreciation for those whom I always remember (GINA GODDARD, Dr TONY GILES, Dr BURAK GOKTEPE and all THE COMBUSTION RESEARCH GROUP) for their assistance and support. I extend my thanks as well to CHRIS LEE, JEANETTE WHYTE AND ADERYN REID for welcoming me to Cardiff University and for their assistance throughout my PhD. I would like to thank Mr MALCOLM SEABORNE with whom we managed to overcome every technical obstacle in my experiments with his experience and wisdom.

To my parents, no words of appreciation and gratitude are enough in front of you. You are the true reason behind every single success in my life and between the lines of every single successful chapter of my life; your names must be written and underlined, IBTISAM MAHMOUD ALZGHOUL and FAWWAZ AWAD ALREBEI. I would like to thank my sisters ASALA, HANEEN, RAHMA, WARD who mean the world to me and my brothers AHED BANI HAMDAN, LAITH HIFAWI and AHMAD ALKHAMISA for their endless support.

Last but not least, I would like to thank my friends MALEK ALI ASHOUR and MAHMOUD ADNAN HAYAJNH for their friendship which is a true treasure.

School of Engineering, Cardiff University

Cardiff, UK.

PUBLICATIONS

Journal papers

1. **Fawwaz Alrebei, Odi**, Ali Al-Doboan, Philip Bowen, and Agustin Valera Medina. " CO₂-Argon- Steam Oxy-Fuel Production for (CARSOXY) Gas Turbines." *Energies* 12, no. 18 (2019): 3580.
2. **Fawwaz Alrebei, Odi**, Ali Al-Doboan, and Agustin Valera Medina. "Parametric study of various thermodynamic cycles for the use of unconventional blends." *Journal of Thermal Science*(2019)

-Under consideration
3. **Fawwaz Alrebei, Odi**, Ali Al-Doboan, Philip Bowen, and Agustin Valera Medina. "Planar Laser- Induced Fluorescence and Chemiluminescence Analyses of CO₂-Argon-Steam Oxy-Fuel (CARSOXY) combustion" *Combustion and Flame*.

-Under consideration

Conference papers

1. **Alrebei O**, Aldoboan A, Bowen P, Valera-Medina A, "CARSOXY combined with Ammonia Production for Efficient, Profitable CCS cycles," International Gas Turbine Congress (IGTC) 2019 Tokyo, Japan.
2. **Alrebei O**, Aldoboan A, Bowen P, Valera-Medina A, "Techno-economics of CO₂-Argon-Steam Oxy-Fuel (CARSOXY) Gas Turbines." International Conference on Energy, Ecology and Environment (ICEEE) 2019 Stavanger, Norway.
3. **Alrebei O**, Aldoboan A, Valera-Medina A, "Parametric Study of Carbon dioxide-Argon-Steam Oxy-fuel (CARSOXY) Gas Turbines." The International Centre for Sustainable Development of Energy, Water and Environment Systems (SDEWES) 2018 Palermo, Italy.

SUMMARY

While Fossil-fuel-fired gas turbines remain the most reliable approach of power production, strict regulations and Acts have been imposed to limit NO_x and carbon emissions. Innovative techniques have become resorts for the power generation industry to overcome such a low level of tolerance. The emerging concept of CO₂-Argon-Steam Oxy-Fuel (CARSOXY) power generation has theoretically proven to increase gas turbine cycle efficiency whilst eliminating NO_x emissions. Nevertheless, facilitating a higher level of technology maturity of CARSOXY gas turbines is essential to promote this technique to the industry within economically feasible scenarios while considering technical aspects of CARSOXY combustion. This thesis covers multidisciplinary aspects to facilitate further studies on CARSOXY, the performance of CARSOXY gas turbines under variable operation conditions and cycle arrangements, the production of CARSOXY, the techno-economic sustainability of CARSOXY and flame characterization. This will aid to bring CARSOXY to more mature status.

A parametric study for several CARSOXY gas turbine cycles has been conducted to identify the ultimate working conditions for each cycle with respect to cycle efficiency. A cycle has been suggested for each range of working conditions. Further increase in CARSOXY cycle efficiency is promised using a newly suggested CARSOXY blend.

CARSOXY gas turbines face the technical and economic challenges of conventional engineering practices for argon and carbon dioxide productions. Therefore, this thesis proposes a novel approach of continuously providing a gas turbine with the required molar fractions of CARSOXY blend. The elegance of this approach appears as an opportunity to use it in sites where ammonia is produced whilst proving its techno-economic sustainability.

Finally, this thesis experimentally assesses CARSOXY in comparison to a CH₄/air flame. OH Chemiluminescence integrated with Planar-Induced Fluorescence imaging techniques have been utilized to study flame stability, and flame geometry over a range of operation conditions. Results from this thesis provide a baseline investigation of CARSOXY gas turbines to be adopted by developers and manufacturers in the future.

CHAPTER ONE

INTRODUCTION.

“We simply must balance our demand for energy with our rapidly shrinking resources. By acting now we can control our future instead of letting the future control us.”

~Jimmy Carter

CHAPTER 1– INTRODUCTION

1.1 Motivation

Gas turbine manufacturers and operators are required to fulfil the increasing demand for power generation within environmental tolerance criterion [1]. Competing against renewable clean sources of energy imposes high expectations on the gas turbine industry to integrate innovative techniques to meet both strict economic and environmental targets [2]. By evaluating the works of literature, reports on fuel variability integrated with CCS techniques have been a motivation for researches to address growing concerns, such as declining conventional fuel sources [3] and global fuel flexibility [4]. However, efficiency decay is always the penalty for such techniques [5]. On the other hand, a vast amount of research [6-24] has been conducted on the use of alternative working fluids, which possess high potential for increasing efficiency and power output in gas turbines. These increases come as a requirement to ensure the integration of other high-energy consuming processes towards the reduction of global carbon footprint. There are several known examples of alternative working fluids, amongst those; this thesis is focused on the CO₂-A_r-steam oxyfuel (CARSOXY) working fluid. A previous study has demonstrated a 13.9% relative efficiency increase using CARSOXY in comparison to an air-driven gas turbine (the 3.9MW Rolls-Royce) [1]. This thesis covers multidisciplinary aspects to facilitate further studies on CARSOXY, the performance of CARSOXY gas turbines under variable operation conditions and cycle arrangements, the production of CARSOXY, the techno-economic sustainability of CARSOXY and flame characterization. This will aid to bring CARSOXY to more mature status. The following sections provide brief introductions to energy policy, energy dependence, NO_x reduction technologies, and CO₂ reduction technologies and the CARSOX concept.

1.2 Energy policy

With 200 independent countries taken part in the United Nations Paris agreement, broad limits have been imposed and accepted to reduce greenhouse gas emissions [26]. As part of fulfilling this global commitment, local and regional regulations have been established. The European Union (EU) on its behalf has to meet an 80% reduction of 1990 emission levels within the upcoming 30 years [27]. Similarly, the Clean Air Act in the United States has issued the New Source Performance Standards (NSPS), which have tightened up the NO_x emission margin of natural gas combustion (i.e. from 75 ppm to 10 ppm), in less than 12 years. Similarly, the Climate Change Act 2008 of the United Kingdom enforces 80% of 1990 carbon emission levels to be reduced within 30 years [28]. It is acknowledged that the UK Climate Change Act is the first national legal framework to regulate gas turbines emissions.

Numerically, the Act aim is to limit the total emissions of 2050 to approximately 1.56 MtCO₂. To have a clear sense of the liability level, this is equal to the same level of emissions of the power sector only in 2010 [29]. This essentially means that the UK is flexible with all emission reduction techniques. To maintain gas turbines amongst these options, carbon and NO_x emissions of gas-fired turbines shall not be underestimated. These are still classified as carbon-intensive techniques. However, operating alongside CCS techniques boosts the chances of gas-fired turbines retain carbon emission compliance. Strategically, the UK carbon plan to meet the Climate Change Act commitment is to reduce 50% of emission levels based on 1990 by 2027 [30] by replacing all coal-fired power stations with new low-carbon power. It is anticipated that at least 2.5 GW/year shall be produced by low-carbon power methods for the next 40 years [30]. This means that for the next 40 years, gas turbine will replace coal-fired gas turbine until the new low-carbon power generation methods are established. Gas-fired power plants will meet the demand peak in 2030 and will be producing 63.3% of the global demand for power [30]. However, the gas-fired role in the energy production industry is uncertain, depending on the future dependence on alternative energy production methods (i.e. nuclear, renewable, etc.).

1.2.1 Energy dependence

Energy consumption has dramatically increased in the last century due to the industrial revolution. Energy demand is mainly influenced by the evolution of technology [31]. The main drivers of the increased energy consumption can be listed as electricity generation for both industrial and residential purposes alongside transportation [31]. This dramatic increase in energy will be further increased in the current century. According to the International Energy Outlook of 2016, energy demand will be increased by 48% of the 2012 levels in 2040 [32]. The largest portion of this energy demand increase will be in the form of electricity generation. Approximately 40% of the generated electricity is consumed by motors. Whilst, 19% is consumed by lighting and 13% is reserved for household application. The remaining consumption is distributed as electronics, resistance heating, trains, electrochemical and miscellaneous. Table 1.1 shows the global electricity consumption by sectors [33].

Table 1.1 Global electricity demand by sector [33].

Sector	Electricity consumption [%]
Lighting	19
Household applications	13
Electronics	8
Resistance heating.	12
Trains	3
Electrochemical	2
Miscellaneous	3
Motors	40

According to the International Energy Outlook of 2016, Electricity is generated mainly by renewables, coal-fired power plants, gas-fired power plants, nuclear and petroleum resources. Approximately 16% is generated by gas-fired power plants, 70% by coal and renewables and 14% is generated by petroleum and nuclear resources based on 2012 electricity world generation. Table 1.2 shows the world net electricity generation by resources in 2012 and the anticipated in 2025 and 2040 [32].

Table 1.2 World net electricity generation by resource, shares in trillion kilowatt-hours s [32].

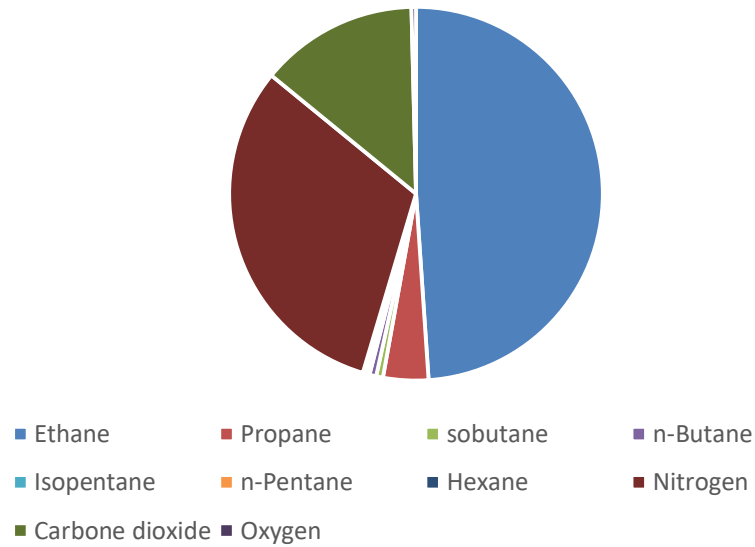
Resource	2012 share	2025 share	2040 share
Renewable	5	8	10
Coal	12	11	11
Natural gas	4	6	10
Nuclear	2	4	4
Petroleum	1	1	1

As shown in Table 1.2 the dependence on natural gas and renewables to generate electricity occupy significant shares. As this thesis targets gas turbine, the focus of the analysis limited to natural gas, section 1.2.1.

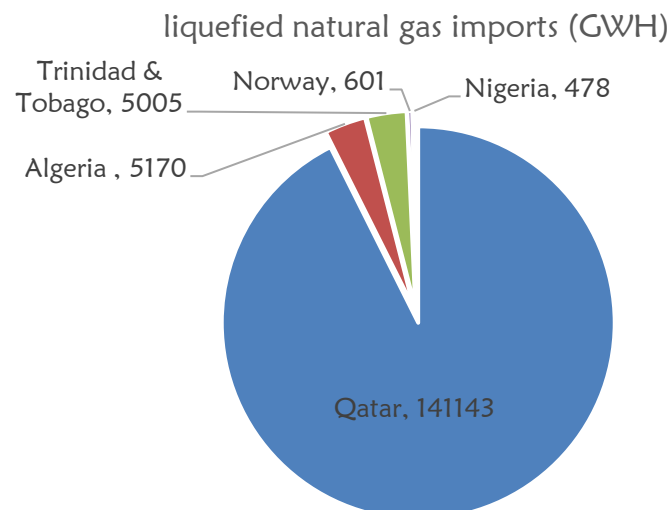
1.2.2 Natural gas dependence

In comparison to diesel and coal, natural gas is considered to be a low-carbon fossil fuel. It is mainly composed of methane (approximately 94. vol%), Figure 1.1 shows the remaining typical chemical composition of natural gas [34].

Remaining composition of Natural gases [vol%]

**Figure 1.1 Typical chemical composition of natural gas [34]**

Natural gas was first discovered in the UK in the 1960s in the Southern North Sea [35]. However, its role became significant in the power generation sector only for the past 27 years, when the first natural gas-fired power station was established in 1992. As reported in 2008, it covered 46% of the UK power demand [35]. In 2010, the UK transferred from domestic gas production to gas imports. In fact, since the discovery of natural gas (the 1960s), 2010 saw the largest annual drop in natural gas production [35]. Moreover, the UK natural gas import dependency is forecasted to be further increased in the long-term future (i.e. 94% in 2050) [36]. The UK depends on imported natural gas either from shipping or pipelines from countries such as Qatar, Algeria, Trinidad & Tobago, Norway, and Nigeria. Figure 1.2 shows the UK annual liquefied natural gas imports by exporting country in 2015 [32].

**Figure 1.2 UK annual liquefied natural gas imports by exporting country in 2015 [32].**

Generating power by natural gas is typically conducted by utilizing natural gas-fired gas turbine stations due to their high capacity. Moreover, these stations provide the feasibility to be integrated to other systems (i.e. fuel gasification facilities, Air separation units, combined and complex cycles) to boost the gross efficiency and become more economically sustainable [37].

1.3 Gas turbines emissions

Gas turbine emissions can be classified into two categories as shown in Table 1.3 [38]. The first category is mainly composed of CO₂. Whilst, the second group is mainly composed of NO_x emissions. The level of the second category emissions (NO_x) is directly affected by the firing temperature. As a result, this sets a challenge between compromising between the NO_x emissions and the high-power demand. The latter essentially requires high levels of firing temperature [38]. Therefore, innovative techniques to compromise between both criteria have been a primary scope of research in the gas turbine industry.

Table 1.3 Gas turbine emission categories [38]

Category 1	Category 2
Carbon dioxide (CO ₂)	Carbon monoxide (CO)
Water vapour (H ₂ O)	Unburned hydrocarbons (UHC)
Oxygen (O ₂)	particulate matter (C)
Nitrogen (N ₂)	Oxides of sulphur (SO _x)
	Oxides of nitrogen (NO and NO ₂) or NO _x

Amongst these techniques which have been investigated is premixed combustion. Essentially, the concept is based on mixing fuel with excess dry air before the combustion chamber [40]. Excess air is utilized as a diluent to control combustion temperature. As a result, NO_x emissions are reduced. Another well-known technique is wet combustion, in this case, the combustion process is diluted with steam instead of dry air. Moreover, steam plays an essential role in increasing the turbine output power by increasing the overall mass flow rate of the working fluid. Therefore, compromising between both requirements (low NO_x and high output power). Wet combustion is typically performed by integrating several humidification techniques (evaporative cycles, steam injection, humidification tower, steam methane reforming, etc.) to the gas turbine unit [41]. However, it must be explicitly mentioned that there is no evidence of deploying wet NO_x control in gas turbines on an industrial scale.

Nevertheless, serious technical issues accompany NO_x reduction techniques. Premixed combustion encounters pressure oscillations and flame instabilities [201-201]. Whilst, humidification techniques penalize the compactness of a power plant and require additional energy to generate steam [41].

Similarly, integrating carbon emissions reduction techniques (pre-combustion, post-combustion and oxyfuel combustion) to gas turbine units imposes efficiency reduction and unsatisfying additional expenses [43]. Therefore, developing efficient and economically satisfying CO₂ capturing techniques has become a necessity rather than a privilege. Especially, since CO₂ emission levels have peaked in the last 10 years [43].

As shown in Figure 1.3, approaching ultra-lean combustion conditions reduces NO_x emissions. However, at this stage, it is crucial to highlight the paradox of reducing NO_x by ultra-lean combustion and the feasibility of deploying CCS units where carbon levels are extremely low. As the concentration of CO₂ in flue gases decreases by approaching ultra-lean combustion conditions, the volume of flue gases directed to the CCS increases [186]. This essentially requires larger CCS units (i.e. higher CCS cost) [186].

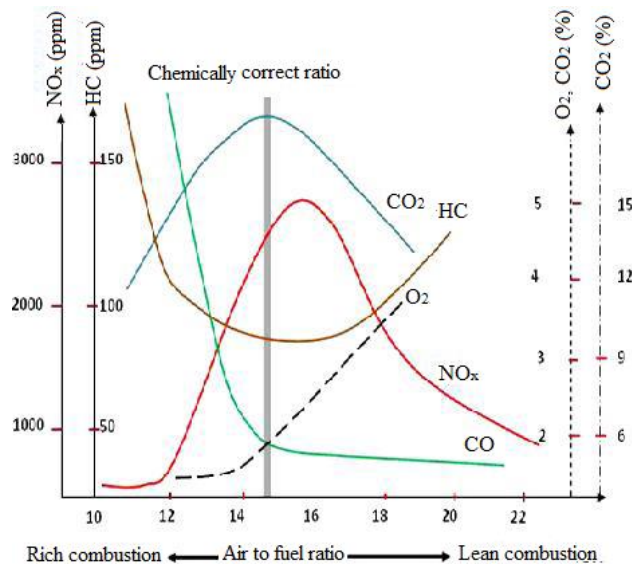


Figure 1.3 Nature of Different emission constituents against equivalence ratios [186].

1.4 CARSOXY gas turbines

The concept of utilizing CARSOXY as an alternative working fluid was first established by Cardiff University [191]. This is the second submitted PhD thesis towards studying multidisciplinary aspects of characterizing CARSOXY gas turbines. The concept of CARSOXY gas turbines is based on taking the advantages of CO₂ recycling together with Oxyfuel combustion to reduce gas turbine emissions. Moreover, injecting steam and Argon is another aspect of this approach to boost the cycle efficiency by enhancing the overall thermodynamic properties of the working fluid. CARSOXY blends can be produced by several techniques. Nevertheless, these should take into account economic sustainability and

minimal energy penalty. Generally, producing the required molar fractions of CO₂ for a CARSOXY blend (i.e. blend 58 [191]) is conducted by the three main techniques of CO₂ sequestration (pre-combustion, post-combustion and oxyfuel combustion CCS). Nevertheless, utilizing a combination of the three techniques can be another novel approach. Similarly, utilizing air separation units (ASU) provides the required CARSOXY levels of argon and oxygen. Humidification cycles and steam injection techniques can be integrated to ensure the essential levels of H₂O. Therefore, CARSOXY gas turbine cycles can be featured by CCS, ASU and humidification facilities. CARSOXY increases cycle efficiency, depending on several parameters (CARSOXY blend compositions, cycle arrangements, operation conditions, etc.). Moreover, since the thermodynamic properties of CARSOXY are similar to Air, it has the potential to replace air-driven power plants to reduce NO_x and CO₂ emissions. Further details are provided in section 2.3.

1.5 Thesis aims and objectives

The first aim of this thesis is to identify the performance of five CARSOXY gas turbine cycles (namely; simple, heat exchanged, free turbine & simple cycle, evaporative and humidified) with respect to cycle efficiency over variable conditions of compressor inlet temperature, turbine inlet temperature and pressure ratios. The second aim is to characterize the impact of CO₂, Ar and H₂O on cycle efficiency in order to select the optimum blend. To meet the first and second aims, the following objective has been taken into consideration:

- A MATLAB code has been developed based on gas turbine theory to perform cycle analysis at the stoichiometric condition. The code has been established to consider the combined effect of two variables on cycle efficiency in order to identify the optimum working condition (i.e. the combined effect of variable compressor inlet temperature alongside variable pressure ratio or variable turbine inlet temperature alongside variable pressure ratio). Similarly, the code has been utilized to consider the combined effect of two components of CARSOXY working fluid on cycle efficiency in order to identify the optimum blend (i.e. the combined effect of the variable molar fraction of CO₂ alongside variable molar fraction of H₂O).

The third aim of this thesis is to theoretically recalibrate the operation conditions of ‘conventional’ industrial models, which feature CARSOXY gas turbines (i.e. CCS, ASU and humidification facilities). The reference [25] has proven the combustibility of CARSOXY using the molar fractions of 23%, 25%, 19%, 11% and 22% of CO₂, Ar, H₂O, CH₄ and O₂, respectively. Therefore, the model shall produce those molar fractions instead of the ‘conventional’ molar fractions (i.e. products with high purity) in an

economically sustainable scenario. To meet the third and fourth aims, the following objectives have been taken into consideration:

- An ASPEN PLUS model has been developed to demonstrate the production of CARSOXY. The model involves the integrations of an air separation unit (ASU), a steam methane reformer (SMR), water gas shift (WGS) reactors, pressure swing adsorption (PSA) units and heat exchanged gas turbines (HXGT) with a CCS unit.
- The independent parameters of the model have been defined and the sensitivities of the model towards those parameters have been characterized. This has qualified the model to be recalibrated by its independent parameters utilizing numerical attempts to produce CARSOXY.
- Comparable techno-economic analyses between CARSOXY and Air-driven gas turbine cycles using the same amount of CH₄ fuel has been conducted to evaluate capital costs, operational costs, payout periods, profitability indexes, net present values and rates of returns.

The fifth aim of this thesis is to experimentally assess CARSOXY in comparison to Air/methane over a variable range of volumetric flow rates, Reynold's numbers and Equivalence ratios to characterize heat release fluctuations and flame geometries. To meet the fifth aim, the following objectives have been taken into consideration:

- OH chemiluminescence imaging integrated with Abel deconvolution techniques have been utilized to flame geometry (i.e. Area of highest heat intensity ($A_{\overline{OH}_{Max}}$), Center of highest heat intensity ($C_{\overline{OH}_{Max}}$)) over a range of instability conditions (excitation frequencies [50Hz-700Hz]) and working fluid volumetric flow rates.
- OH chemiluminescence integrated with PLIF imaging has been used to conduct Damkohler analyses and plot Borghi regime diagrams over a range of Reynold's numbers and Equivalence ratios.

1.6 Thesis structure

This thesis is structured into the following chapters:

- Chapter 1. Introduction: A motivation is provided in this chapter with highlights on global energy policies, including international and national commitments and engagements towards clean energy. This chapter also discusses the increasing trends of energy consumption and spots natural gas dependence in the power generation industry. Emission facts and statistics are provided in this chapter

with projections on potential innovative emission reduction techniques. Finally, a brief introduction to CARSOXY gas turbine is provided in this chapter.

- Chapter 2. Literature review: This chapter provides the reader with brief backgrounds in CARSOXY-related topics. The state of art is evaluated in research areas such as; alternative-working fluids, oxyfuel combustion, CARSOXY combustion, complex cycles, carbon capture and storage (CCS) methods, Air separation methods and classical combustion.
- Chapter 3. Methodology: This chapter describes the methodological approach adopted to generate the results obtained in chapter 4, 5, 6, 7 and 8. Besides, the methodology sequence between the previously mentioned chapters is present in this chapter.
- Chapter 4. A parametric study of various thermodynamic cycles for the use of various CARSOXY blends: This chapter conducts a parametric study for five CARSOXY gas turbine cycles to identify their ultimate working conditions concerning cycle efficiency. This chapter also suggests a new novel blend.
- Chapter 5. A novel approach of producing CARSOXY: This chapter provides a novel approach to produce CARSOXY blend within required molar fractions. It also provides a sensitivity analysis to spot the main features of the suggested approach.
- Chapter 6. CARSOXY Techno-economic: This chapter performs comparable techno-economic analyses between CARSOXY and Air-driven gas turbine cycles under slandered economic evaluators.
- Chapter 7. Chemiluminescence imaging and emission analyses of CARSOXY combustion: This chapter experimentally evaluates CARSOXY combustion in terms of flame stability, flame geometry and emissions over a range of working fluid volumetric flowrates and flame excitation conditions.
- Chapter 8. Planar Laser-Induced Fluorescence and Chemiluminescence Analyses of CARSOXY combustion: This chapter performs Damkohler analyses using of CARSOXY combustion in comparison to CH₄/air over a range of Reynold's numbers and equivalence ratios. In addition, Borghi regime diagrams have been produced for both types of flames.
- Chapter 9. Discussion and Future Work. This chapter provides a summary of the main findings and provides recommendations for future work.

CHAPTER TWO

Literature Review.

“Perhaps, posterity will thank me for having shown that ancients did not know everything.”

~Pierre de Fermat

CHAPTER 2–LITERATURE REVIEW

2.1 Energy demands and challenges

Nowadays, gas turbines are required to meet much stricter emission control regulations. In fact, regulatory authorities have drastically dropped down allowable emission levels in order to overcome the greenhouse effect [44]. Just to name a few, the Clean Air Act in the United States has issued the New Source Performance Standards (NSPS), which have tightened up the NO_x emission margin of natural gas combustion (i.e. from 75 ppm to 10 ppm) in less than 12 years [39]. In addition, with 200 independent countries taken part in the United Nations Paris agreement, broad limits have been imposed and accepted to reduce greenhouse gas emissions [26]. Moreover, the European Union (EU) on its behalf has to meet an 80% reduction of 1990 emission levels within the upcoming 30 years [27].

CO₂ and NO_x emissions can be ratcheted down by increasing the cycle efficiency or by sequestration techniques such as Carbon Capture and Storage (CCS) [45]. High demands for the consumption of energy produced from fossil-fueled gas turbines used in power plants has dramatically led to heightening anthropogenic CO₂ and NO_x emitted from gas combustors [46]. Harmful emissions have directly increased the greenhouse effect with their inherent consequences of climate change leading to the deterioration of the global environment [47]. Most of the systems producing these unwanted emissions are directly linked to power generation, from which gas turbines have a leading role [48]. Thus, stationary gas turbines have been broadly and will continue to be employed in power plants to cover the growing demand for power production [49]. Therefore, novel concepts are required to ensure that emissions are tackled whilst enabling large power production from these systems. Utilizing alternative working fluids is one promising technology that could be used for reducing harmful emissions while recirculating CO₂ in the combustion process [50].

2.2 Alternative Working Fluids

A vast amount of research [6-24] has been conducted on the use of alternative working fluids, which possess high potential for increasing efficiency and power outputs in gas turbines. These increases come as a requirement to ensure the integration of other high-energy consuming processes towards the reduction of global carbon footprint. There are several known examples of alternative working fluids such as helium for the nuclear industry, ammonia/water for organic Rankine cycles and humidified injection techniques.

Out of the potential gases that can be used to increase power and augment efficiency, inert gases present a unique opportunity due to their un-reactive nature coupled with their thermodynamic properties. For

example, helium is known to be the optimal choice in high-temperature gas-cooled nuclear reactors (HTGR) due to its stable radioactive properties [51]. In addition, the use of helium as a working fluid during combustion processes does not require major modifications and follows the existing design practice for combustion gas turbines [42]. However, efficiency losses are the cost of necessary adjustment on the geometry of compressor and turbine blades. This causes end-wall boundary layer growth and secondary flow that impact the final efficiency [53]. Attempts of compromising between the mechanical requirements and high efficiency by introducing inert gases to the working fluid, such as Neon (Ne) and Helium (He) have also been reported in the literature [54]. For instance, an optimum expansion ratio can be reached by optimizing the compositions of both components. Nevertheless, such a composition does not have a significant effect on cycle efficiency. Thus, other gases are needed to improve the overall efficiency, thus reducing maintenance and operating costs. Moreover, the gas blend should also incorporate the utilisation of CO₂ in order to accommodate carbon sequestration at the end of the line.

One method that is under development for the use of carbon dioxide in carbon sequestration systems is known as Oxyfuel combustion. Oxyfuel combustion is a modern technique which uses high oxygen concentrations as the primary oxidant instead of air (i.e. with 21%v. oxygen content) [55]. Oxyfuel combustion produces flue gases (essentially, only steam and CO₂) with approximately 75% lower mass and volume than air/fuel combustion. Therefore, CO₂ is captured and circulated back to the gas turbine working fluid with lower heat losses, thus lowering efficiency losses compared to air/fuel combustion [56].

However, using CO₂ solely in Oxyfuel combustion systems drops the turbine inlet temperature, requiring greater pressure ratios to maintain the same temperature level. Essentially, this entails the use of bigger compressors, which affect the compactness of the gas turbine. Moreover, existing gas turbine arrangements would require major modifications, which as a result postpone the adoption of CO₂ injection [57-58]. As a solution, and introducing the use of another inert gas into the blend, injecting argon (A_r) to the working fluid increases the overall heat capacity. In contrast to He, Ne or other inert gases, A_r is extremely abundant in the atmosphere, making it more affordable. By using argon, turbine inlet temperature can be levelled to its regular value whilst ensuring high specific heat ratios (γ) for greater cycle efficiencies. Therefore, major modifications to existing gas turbine arrangements can be avoided. In addition, the high heat capacity of argon increases power outputs, which paybacks the efficiency penalty due to the implementation of CCS facilities.

However, argon with Oxyfuel combustion costs is much higher if only A_r-O₂- CO₂ blends are employed as working fluids. Advanced humidified systems could be an alternative to raise output power even further, thus increasing efficiencies and reducing costs of extra argon and oxygen. Cycles which integrate

heat recovery (HR) with humidified injection techniques are usually referred to as complex cycles [59]. These cycles increase efficiency and reduce emissions by recovering about 60% of heat losses [60]. Heat recovery methods include heat exchanging and recuperation techniques, such as Gas-to-Gas recuperation. This method is mainly used for low-pressure ratios [61]. For higher pressure ratios; steam injection is a more proper approach [62]. On top of that, thermal efficiencies and output power are increased compared to similar simple gas turbines. However, water is needed and extensive post-treatment is required. This is the major limitation of these humidified cycles [36-64]. A simpler technique is the use of evaporative cycles, which have higher power output, but lower efficiency compared to a similar steam injection cycle. Evaporative cycles allow water to evaporate below its boiling point (i.e. minor water treatment). As shown in Figure 2.4, by placing the evaporator after the compressor, the compressed air counter-contacts the heated water surface. This arrangement stimulates molecules collision and allows water molecules to escape to the surrounding and overcome vapour pressure [78].

Humidification is also used for other purposes, such as cooling and overcoming sizing limitations of the compressor, which is referred to as wet compression [65-66].

The use of all these components, i.e. argon, carbon dioxide, oxygen and steam, generates a new set of blends known as CARSOXY [25]. Previous research clearly shows that the performance of a gas turbine can be increased by using humidification and evaporation means. In addition, heat exchangers are excellent methods of heat recovery. These methods have a higher potential to increase cycle efficiency when a CARSOXY mixture is used as the working fluid. If a suitable cycle configuration is used under the specific operation condition, high techno-economic benefits can be reached. Moreover, a CO₂-Ar - steam mixture has the potential to enhance efficiency while maintaining a relatively low level of CO₂ emissions by further carbon capture and storage techniques, which are considered as one of the imperative requirements for future fossil-fueled gas turbines [67-68]. However, increasing the level of CO₂ in the working fluid of a gas turbine can accumulate carbon deposits and cause blockage in cooling channels in the turbine blades [69], thus special care needs to be taken to set the right amount of carbon dioxide in the working fluid.

2.3 Oxyfuel combustion

In order to limit NO_x and carbon emissions, the Climate Change Act 2008 of the United Kingdom enforces 80% of 1990 carbon emission levels to be reduced within 30 years [70]. An efficient approach to comply with these strict emission margins is Oxy-fuel combustion [71]. NO_x emission is completely eliminated by this technique, while carbon emission is captured by utilizing a simple and cost-effective

condensation process [72]. Nevertheless, using pure oxygen as an oxidizer has several complexities. Most importantly, Oxy-fuel flame temperature far-exceeds that for Air/fuel flames. In fact, it is beyond the material design limits of existing gas turbines [73]. However, the solution lies in the problem, the flame temperature is controlled by recirculating the captured carbon back to the gas turbine in order to dilute the working fluid. The literature is enriched with studies which both theoretically and experimentally characterize O₂/CO₂/fuel combustion, i.e. [74-74]. However, it must be noted that carbon capture and storage (CCS) techniques penalize the cycle efficiency of Oxyfuel gas turbines. As reported by reference [76], the cycle efficiency of a gas-fired plant without CCS drops from approximately 55% to 44% if a CCS unit is integrated. Attempting to attain the same power output level as that without CCS essentially increases the gas turbine size, which penalizes the compactness of the plant [63].

2.4 CARSOXY combustion

Injecting the working fluid with inert gases (i.e. argon) with high heat capacities increases power outputs, which as a result makes up for the CCS efficiency losses. This concept is referred to as CO₂-A_r-steam Oxy-fuel (CARSOXY) gas turbines. If a suitable cycle configuration is used under the specific operation condition, high techno-economic benefits can be reached. Moreover, a CO₂-A_r-steam mixture has the potential to enhance efficiency while maintaining a relatively low level of CO emissions by further carbon capture and storage techniques, which are considered as one of the imperative requirements for future fossil-fueled gas turbines. However, as previously mentioned, special care needs to be taken to set the right amount of carbon dioxide in the working fluid.

The concept of inferring the optimal CARSOXY blend was first established in a 2017 paper [25]. However, choosing the optimal blend was based on testing a random number of blends with random proportions without indicating the effect of each component (i.e. carbon dioxide, argon and steam) on the cycle efficiency. Therefore, this thesis (Chapter 4) studies the combined and individual effect of each component on the cycle efficiency. Based on that, a new optimal blend is re-selected. The choice is based on correlating three intervals of variable molar fractions of carbon dioxide, argon and steam in a three-dimensional efficiency surface. This approach essentially visualizes the highest cycle efficiency as the highest peak on the efficiency surface within the tested intervals of molar fractions. Therefore, the corresponding molar fractions (to the highest peak) can then be chosen as the optimal blend. The new suggested blend in this thesis has the molar fractions of 47% argon, 10% carbon dioxide, 10% H₂O and 33% oxy-fuel (i.e. 11% and 22% for methane stoichiometric combustion). Wet and dry compressions have also been studied and compared in this thesis for both air and CO₂-Argon-Steam mixtures amongst other HR conditions and humidified injection techniques.

Moreover, the original CARSOXY analysis [25] was based only on one cycle arrangement (humidified

gas turbine cycle, Figure 2.1). In this thesis, four other gas turbine arrangements (namely; simple, heat exchanged, free turbine & simple and evaporative) are also examined. Section 2.5 provides a literature review of complex cycle arrangements.

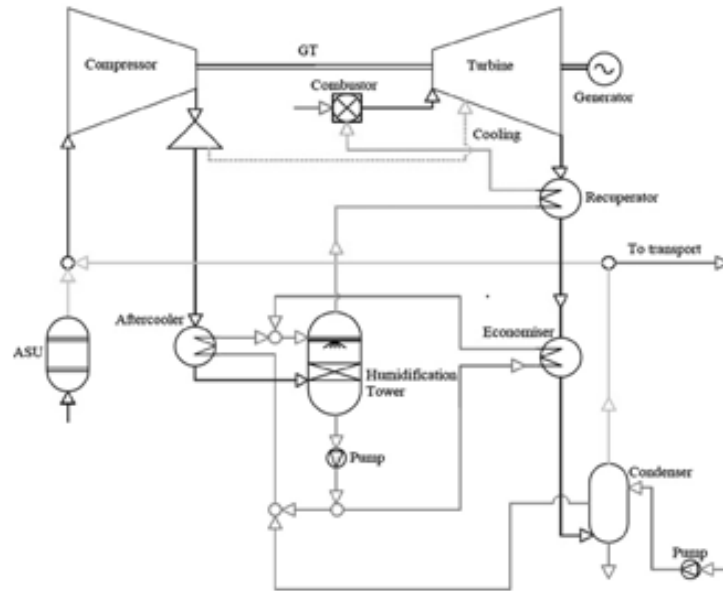


Figure 2.1 The original CARSOXY cycle [49].

By evaluating the literature, several theoretical studies should be conducted on CARSOXY gas turbines to cover multidisciplinary aspects. For example, the feasibility of producing CARSOXY in an economically efficient approach should be addressed (this has been addressed in Chapters 5 and 6). Moreover, experimentally characterize CO₂/Ar/O₂/fuel flame is essential to examine CARSOXY combustion stability. Due to the raised issue of CO₂ injection effect on plant compactness, flame geometrical parameters should also be identified (this has been addressed in Chapters 7).

2.5 Complex and combined gas turbine cycles

Complex or combined gas turbine cycles increase the efficiency and reduce emissions as it is capable of recovering 60% of heat losses [25]. This section discusses the main features which convert a simple gas turbine cycle to a more advanced cycle.

2.5.1 Recuperative and humidified cycles (complex cycles)

Waste energy is discarded as heat to a higher entropy level. As the term implies, heat recovery (HR) methods include heat exchangers to utilize exhaust gas heat. In the case of gas turbines integrated with

heat recovery (HR) facilities (recuperation), discarded heat from the turbine exhaust gases is contained into a heat exchanger to transfer heat from one fluid to another.

Converting heat to useful work can be classified into two categories. These are determined by the number of the required additional cycle. Recuperation cycle recovers heat within the same cycle and no additional cycle required. In contrast, the bottoming cycle recovers heat as an additional cycle. It is wise to initially choose with recuperation technique (same cycle). However, this has to be within the metallurgical limits of the heat exchanger (i.e. overheating is taken into consideration). Beyond these limits, a bottoming cycle becomes essential. Nevertheless, cooling and humidification techniques can be utilized to overcome overheating in recuperative cycles. In fact, recuperative cycles usually involve inter-cooling systems. One industrial example is the WR21 gas turbine developed by Rolls-Royce and Westinghouse which uses an inter-cooling/recuperator technique [61]. Figure 2.2 is a demonstration of the cooling techniques coupled with recuperation within a gas turbine.

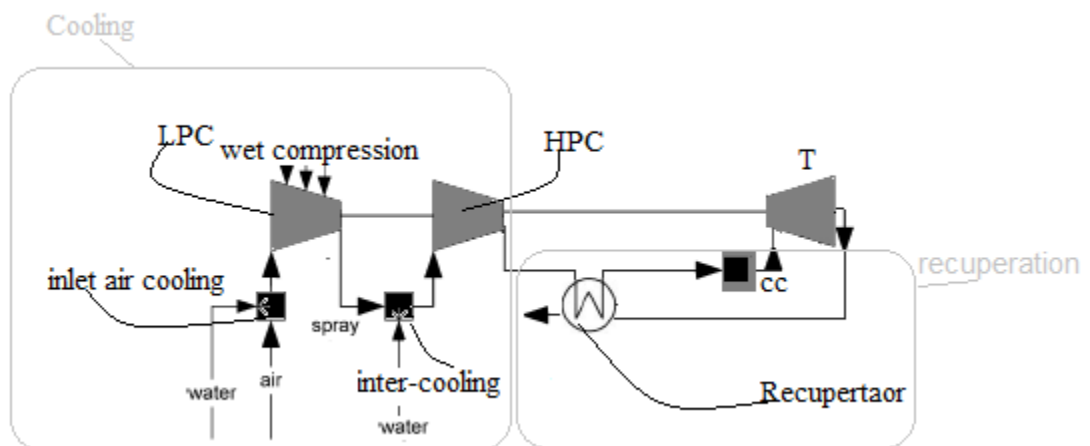


Figure 2.2 Cooling techniques coupled with recuperation, reproduced from the reference [61].

Recuperation can be mainly categorized into gas to gas recuperation, steam injection, evaporation cycles and chemical recuperation. In gas-to-gas recuperation (Figure 2.2), heat exchangers transfer heat between two gas streams (from the compressor outlet and turbine exhaust). This technique utilizes wasted energy at low-pressure ratios (< 5). Further increase in pressure ratios penalizes cycle efficiency [66]. At high-pressure ratios, steam injection overcomes efficiency losses and optimize output power [63]. However, extensive treatment of water (economizers, recuperators, and super-heaters) is required to convert water into steam, Figure 2.3.

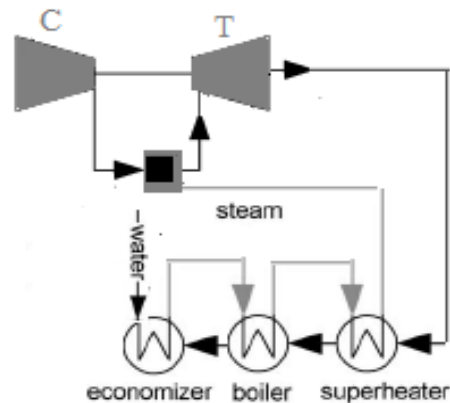


Figure 2.3 Steam injection, reproduced from the reference [66].

In contrast, evaporative cycles allow water to evaporate below its boiling point (i.e. minor water treatment). As shown in Figure 2.4, by placing the evaporator after the compressor, the compressed air counter-contacts the heated water surface. This arrangement stimulates molecules collision and allows water molecules to escape to the surrounding and overcome vapour pressure [78]. The original CARSOXY cycle (Figure 2.1) is one example of the evaporative cycles.

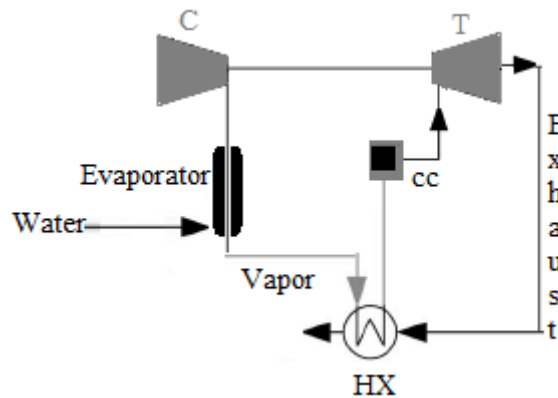


Figure 2.4 Evaporative gas turbine cycle, reproduced from the reference [78].

Chemical recuperation is another recuperation method, which is based on integrating a gas turbine cycle with a steam methane reformer (SMR). The SMR reacts hydrocarbon fuel with steam to produce hydrogen. This reaction is performed at high temperature [79]. This method typically utilizes steam injection techniques to increase hydrogen production. Figure 2.5 is a schematic of an SMR integrated with a heat-exchanged cycle.

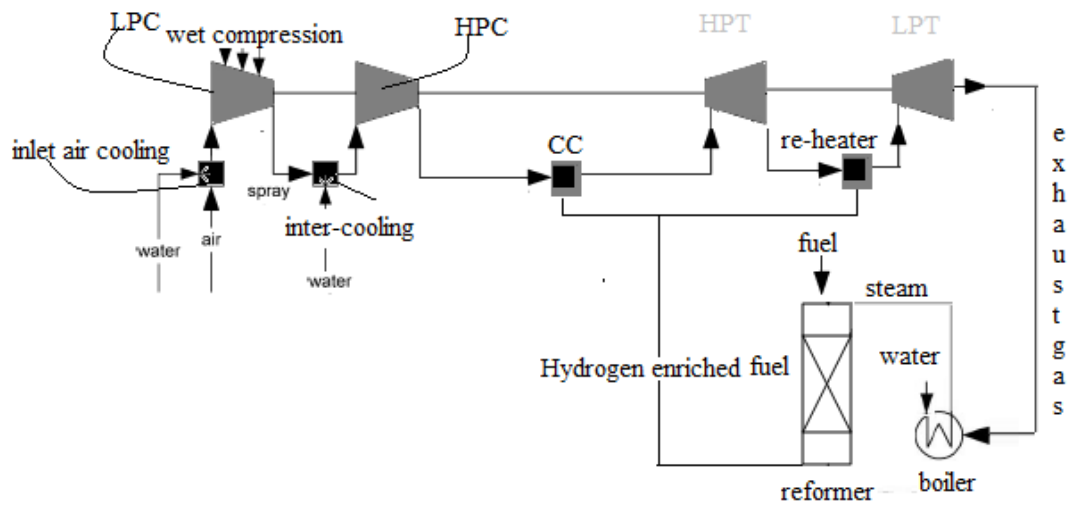


Figure 2.5 A SMR integrated with heat exchanged cycle, reproduced from the reference [79].

2.5.2 Combined cycle /cogeneration (bottoming)

As discussed in section 2.5.1, cogeneration or bottoming cycles are the resort when cooling and humidification techniques fail to maintain a single power generation unit within its metallurgical tolerance. Cogeneration is defined as the simultaneous production of various forms of energy from one power source (normally associated with heat and power-mechanical or electrical) [80]. It is important to consider important design factors such as energy mapping the cascading principle when cogeneration is utilized.

The concept of energy mapping and cascading is utilized between energy sources and users. High-temperature energy source low-temperature energy. The rejected energy could be utilized in another low-temperature process [81]. For example, the rejected heat from a gas turbine (Brayton cycle) in its flue gases can be recuperated to heat steam and drive a Rankine cycle [81].

Those principles must be carefully applied in a process-by-process level (i.e. combustion-pressure expanding) and on a cycle-by-cycle level (i.e. topping cycle-bottoming cycle). Figure 2.6 is a representation of a gas turbine-steam turbine cogeneration. As the names imply, the topping cycle of the gas turbine is in the top cycle in the T-S diagram and the bottoming cycle is the steam turbine cycle.

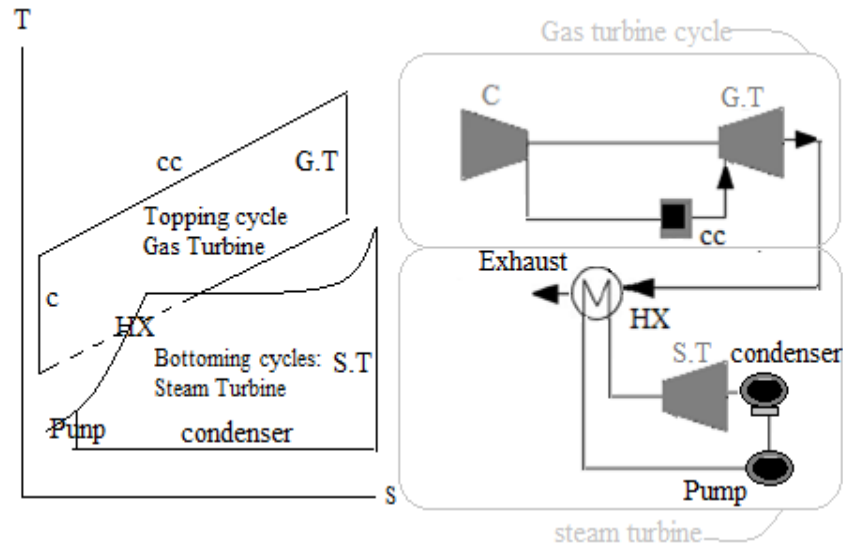


Figure 2.6 Gas turbine-steam turbine cogeneration, reproduced from the reference [80].

2.6 Carbon capture and storage (CCS)

The aim of this section is to review the main technologies of carbon dioxide capture. These can be mainly categorized as pre-combustion, post-combustion and oxyfuel combustion. These techniques have been evaluated from the literature based on multidisciplinary aspects (technology maturity state, economically, advantages and disadvantages).

2.6.1 CCS main categories

Post-combustion CCS captures CO₂ from flue gases. Therefore, no major changes are required and can be easily integrated into the currently used power plants in the market [81]. However, unsatisfying 70% increase in the electricity cost is penalized [82].

One of the main examples of deploying post-combustion CCS in a full commercial scale is the TMC Mongstad in Norway [203]. According to the reference [203], as shown in Figure 2.7, the process starts by separating liquid and solid particulates from combustion flue gases in a separation unit. Flue gases flow from the bottom of the absorber upwards against a counter-current stream of the lean solution. This allows CO₂ to be absorbed and the treated flue gases leave the top of the absorber. Meanwhile, the CO₂-rich solution leaves the bottom of the absorber to the top of the stripper. The CO₂-rich solution flows downward against a counter-current water vapour stream. Most of the remaining CO₂ content is captured by the water vapour stream. Finally, a condensation process is utilized to separate CO₂ from water vapour.

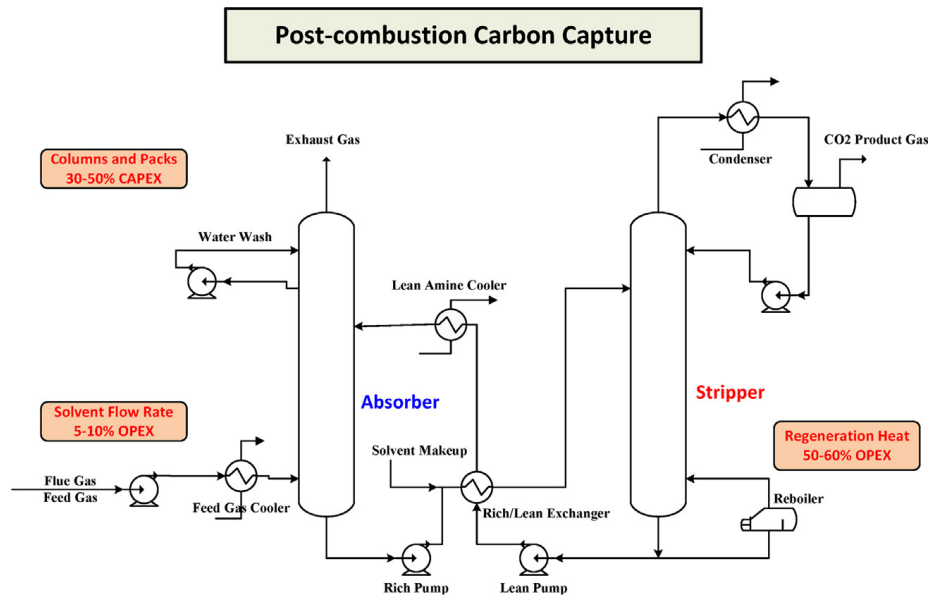


Figure 2.7. Simplified diagram of a post-combustion capture process using reactive solvents [203].

In contrast to post-combustion CCS, pre-combustion CCS is not easy to be integrated into existing power plants. In fact, it requires intensive pre-treatment, especially for coal-fired power plants [83], which penalizes the compactness of the system. However, efficiency losses are significantly less than those for post-combustion [84]. As shown in Figure 2.8, the pre-combustion CCS process starts with a coal gasification process, where coal is transferred into Hydrogen, carbon monoxide and carbon dioxide. This is then followed by a water-gas-shift reaction in order to utilize hydrogen production and converts carbon monoxide to carbon dioxide. At this stage, carbon dioxide can be captured through several separation techniques, absorption, adsorption, membrane separation, hydrate-based separation and cryogenic distillation. The same process is adopted for natural gas fuel. However, the gasification process is replaced by a reforming process. The CO₂ removal efficiency of pre-combustion CCS of natural gas fuel can reach up to ~80% [68].

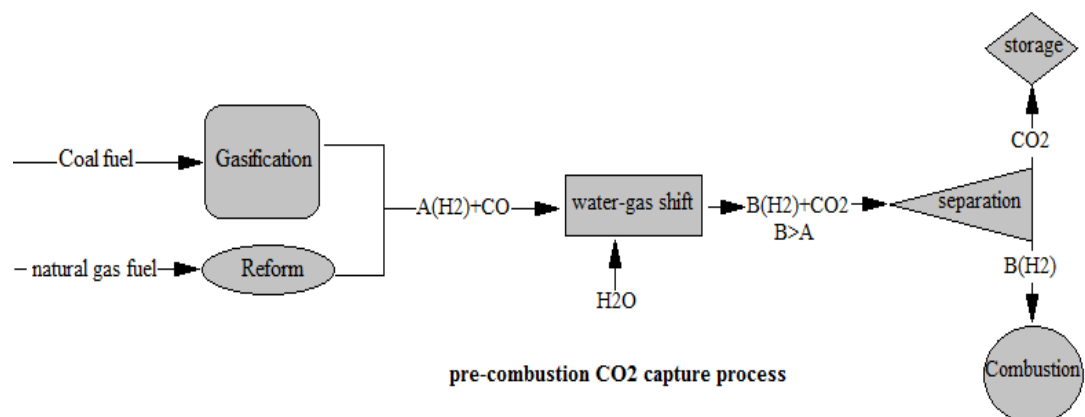


Figure 2.8 pre-combustion CCS, reproduced from the reference [84].

For oxyfuel combustion CCS (Figure 2.8), air is not directly supplied to the combustion chamber. It is first separated in an air separation unit into argon, oxygen, nitrogen and other gases. The extracted oxygen is fed to a combustion chamber. Flue gases of oxyfuel combustion are highly concentrated with carbon dioxide [84]. However, using an air separation unit causes energy losses [84]. For example, the use of the ASU for Oxyfuel lignite-fired power plant has been reported to penalize plant efficiency by as much as 10 % (compared to a conventional pulverized coal plant) [204].

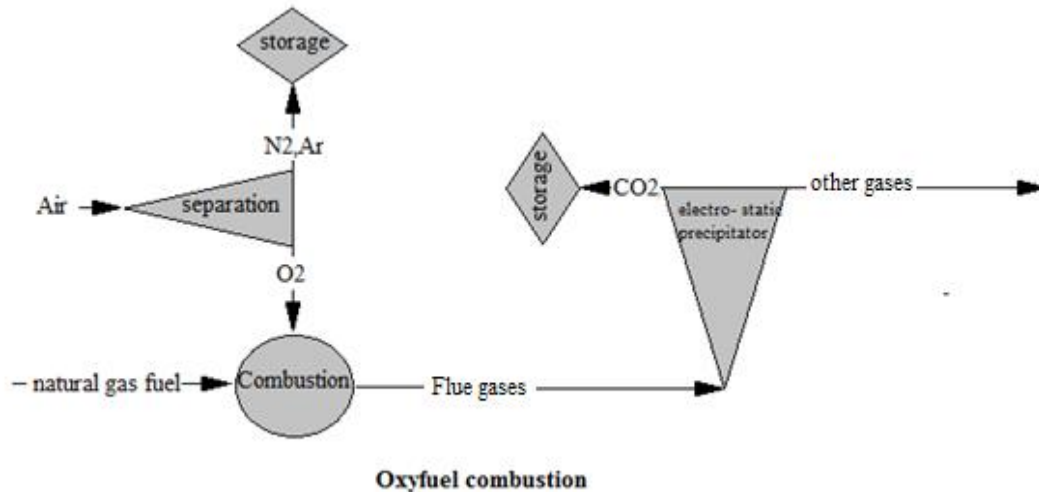


Figure 2.9 Oxyfuel combustion CCS, reproduced from the reference [84].

Table 2.1 summarizes the technology maturity states, economic status, advantages and disadvantages of the three CCS technologies [84].

Table 2.1 CCS technologies states

Capturing technology	Technology status	Capital costs and operation cost	CO ₂ concentration	Thermal efficiency	Advantages	Disadvantages
Post-combustion	Fully Developed	The lowest	The lowest	The highest	Easily integrated into existing plants	Low CO ₂ concentration
Pre-combustion	Fully Developed	Medium	Medium	The lowest	Performance is independent of the power plant scale	Efficiency decay
Oxyfuel combustion	Developed air separation	The Highest	The Highest	Medium	Relatively compact size	Corrosion and efficiency decay

2.6.2 Carbon dioxide separation methods

Absorption is used to separate CO₂ through liquid sorbents. The latter can be extracted through stripping techniques. Ultimately; monoethanolamine (MEA) ensures a 90% of CO₂ absorption efficiency [85]. If the sorbent is in the solid phase (such as; hydrotalcites, molecular sieves, etc.), then the technique is referred to as Adsorption [85]. Membrane separation is another famous technique, which selectively allows CO₂ to pass through a porous composite polymer. Different gases have different molecules size, thus pores are carefully sized to match the CO₂ molecule size [86]. Table 2.2 [68] evaluates the advantages and disadvantages of the most common techniques of CO₂ separation.

Table 2.2 CO₂ advantages and disadvantages

CO ₂ separation method	Advantages	Disadvantages
Absorption	<ul style="list-style-type: none"> • The most developed technology • The Highest CO₂ recovery efficiency (approximately 90%) 	<ul style="list-style-type: none"> • Low efficiency for low CO₂ concentration i.e. Post-combustion • High heat requirements
Adsorption	<ul style="list-style-type: none"> • Recyclable absorbent. • Relatively high CO₂ recovery efficiency (approximately 85%) 	<ul style="list-style-type: none"> • High heat requirements
Membrane separation	<ul style="list-style-type: none"> • Relatively high CO₂ recovery efficiency (approximately 80%) 	<ul style="list-style-type: none"> • Operational issues
Hydrate-bases separation	<ul style="list-style-type: none"> • Negligible energy penalty 	<ul style="list-style-type: none"> • Not fully developed technology
Cryogenic distillation	<ul style="list-style-type: none"> • Fully developed technology 	<ul style="list-style-type: none"> • High energy penalty

2.7 Air separation unit (ASU)

For air-independent gas turbines (i.e. CARSOXY driven gas turbines), it is crucial to study the engineering practice of extracting each individual component of the working fluid. In the case of CARSOXY gas turbines, argon and oxygen are the main constituents, which can be separated from atmospheric air. Since air is composed of 78.12% nitrogen, 20.95% oxygen and 0.93% argon [87], it can provide the necessary amount of argon and oxygen for CARSOXY blends.

2.7.1 Air separation main methods

Air separation methods are classified into three categories (namely; membrane separation, pressure swing absorption and cryogenic distillation) [87-90]. The focus will be on cryogenic distillation because it is a more proper choice for CARSOXY gas turbines since it is capable of separating a ternary mixture into

its individual components (i.e. air can be separated into nitrogen, oxygen and argon). The latter two components of air – also components of CARSOXY- can be obtained within the same cryogenic distillation unit [88]. The other two methods are a less suitable option for mass production [89] (i.e. for CARSOXY production).

2.7.2 Cryogenic distillation types

Cryogenic distillation can be single-column or multi-column. However, the conventional method is the multi-column process [90]. This process mainly consists of a low-pressure column, a high-pressure column and a side rectifier or a stripper. The multi-column distillation remains an economic challenge. However, several economically efficient modifications have been utilized in the process [91]. These modifications are addressed in the following sections.

2.7.2.1 Thermally linked distillation column, with a side rectifier [92]

Figure 2.10 is a representation of generic 3-component distillation separations with side rectifier and stripper which can be used to mimic an ASU [92]. Section 2.7.5 provides a more detailed representation of an ASU, Figure 2.11[88].

As shown in Figure 2.10, a ternary mixture composed of A, B and C components. A is the most volatile component, B and C are the intermediate and the least volatile components, respectively. The mixture is fed to the main distillation column, where component A is extracted from the top of the main column. Component C is extracted from the bottom. The main feed of the ABC mixture is located approximately in the middle of the distillation column. The side feed is located just beneath the main feed and linked to the bottom of the rectifier. The side feed mixture is composed of B and C. The latter component accumulates at the bottom of the side rectifier and B is produced from the top of the side rectifier. Component C from the side rectifier is recycled back to the main column at the same location as the side-feed. This method is adopted when the relative volatility of the two components (B and C) in the side-feed is low.

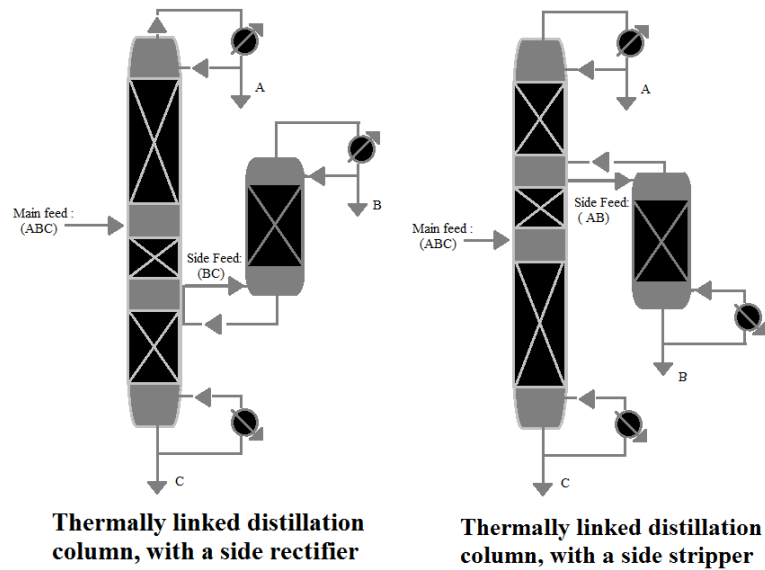


Figure 2.10 thermally linked distillation column, reproduced from the reference [92].

2.7.2.2 Thermally linked distillation column, with a side stripper [92]

If the low relative volatility is between (A and B) instead of (C and B), then a side stripper is a more proper choice. As shown in figure 2.10, the side-feed is located above the main feed and it is linked to the top of the stripper. The side feed mixture is composed of A and B, where B is produced at the bottom of the stripper. A is recycled back to the main column.

2.7.2.3 Side rectifier vs side stripper

Table 2.3 projects the concept of ternary-mixture distillation on air. Since the relative volatility of argon and oxygen (B and C) is lower than that for argon and nitrogen (B and A) [88], then a side rectifier is a better choice for air separation.

Table 2.3 air components relative Volatility [88].

Component	Volatility	In air	Relative Volatility
A	High	Nitrogen	The relative volatility of argon and oxygen (B and C) is lower than that for argon and nitrogen (B and A).
B	Intermediate	Argon	
C	Low	Oxygen	

2.7.3 Low pressure (LP) distillation column vs elevated pressure (EP) distillation column.

Low-pressure distillation columns are used if the by-products of nitrogen production (oxygen and argon) are not stored and dismissed to the surrounding nearly at the atmospheric pressure. However, storing oxygen and argon requires an additional increase in pressure. Therefore, elevated pressure distillation columns are applied. In other words, if the by-products of nitrogen production are compressed to be utilized as main products, then elevated-pressure distillation column becomes necessary [91]. Since the working fluid of CARSOXY gas turbines is required to function at relatively high pressure, the elevated pressure distillation column provides better matching between the ASU and the gas turbine unit.

2.7.4 Single distillation column vs. double-distillation column.

According to the reference [93], a self-heat recuperation of a single distillation column conserves 36% of the energy consumption compared to the conventional double distillation column. Main losses in a double-column air separation process are due to the liquefaction and air compression [94]. However, double-distillation columns remain the most widely used [87].

2.7.5 Integrating Heat pump techniques with ASU to enhance argon production.

Argon recovery can be enhanced using heat pump techniques [89], especially, since the difference between the boiling temperatures of argon and oxygen is approximately 2.8K and the difference in temperature between the top and the bottom of the distillation column is also in this range. There are several arrangements and configurations to apply the heat pump concept in the ASU. However, only the conventional method is discussed. Since the elevated pressure process is expected to best suit the requirements of integrating an ASU with a CARSOXY gas turbine, one more particular configuration suggested by reference [91] is discussed in section 2.7.5.2. This configuration applies the concept of a heat pump at an EP condition.

2.7.5.1 Conventional Argon production [88]

As shown in Figure 2.11, air is fed to the ASU approximately at 5.5-6.5 bar through a heat exchanger to be cooled by its products. A two-stage distillation column separates oxygen and nitrogen, in which the first stage is the high pressure (HP) stage and the second stage is a low pressure (LP) stage. At the HP stage, air feed is separated to N₂ and LOX-(oxygen-enriched liquid). The latter is fed to the LP stage to be separated into N₂ and O₂. Due to the pressure difference between the two stages, there is also a

temperature difference. This allows heat exchange between the two stages (between LP and HP), in which the N₂ vapour -boiling stream- at the top of the HP stage is then condensed by the colder liquid O₂ at the bottom of the LP stage. N₂ is produced from the top of the HP column. As argon has the intermediate boiling temperature, its highest concentration is located at the lower section of the LP column. At this location, a vapour stream is drawn to feed the rectifier. Similar to the Main distillation column, vapour argon -boiling stream- at the top of the rectifier is condensed by the colder LOX liquid. Vaporized LOX is then returned to the LP column.

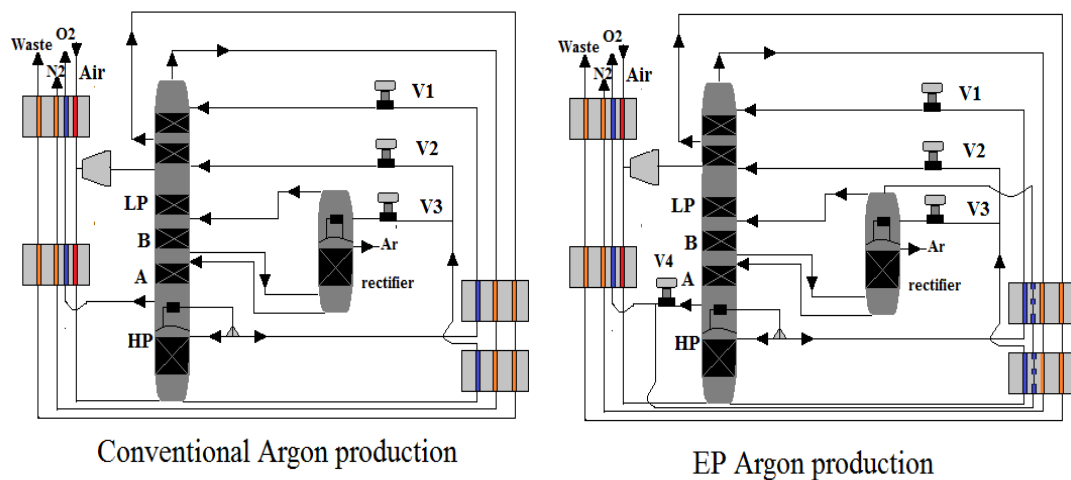


Figure 2.11 Air separation (or argon production), reproduced from the reference [88].

2.7.5.2 EP Argon production [88]

As shown in Figure 2.11, oxygen in the liquid phase is drawn from the bottom of the LP to provide total condensing duty with argon at the top of the rectifier column to enhance argon recovery, as the volatility in the elevated-pressure process is very tight. After providing the total condensing duty, the vaporized oxygen plays another role. It is used as a coolant agent in the system, as the EP process encounters higher levels of temperature. Since the heat pump effect between argon rectifier and oxygen at the bottom of the LP column is utilized, the pressure level at the top of the rectifier remains lower than the pressure level at the bottom of the LP column, thus no compressor is required.

2.8 Steam methane reforming (SMR)

As highlighted in section 2.6.1, SMR is an essential step involved in the carbon capture and storage (CCS) process. In addition, it is one of the fully developed technologies, which is used to produce hydrogen. The real-life results and conditions perfectly match those in theory [89]. Light hydrocarbon fuel (i.e.

methane) reacts with steam to be converted into hydrogen as the main product, carbon monoxide and carbon dioxide as by-products. Some literature includes Water Gas shift (WGS) as a step in SMR since WGS processes accompany SMR in most applications [89]. In the reforming process, two endothermic reactions take place. The first reaction requires 206 kJ to react one mole of methane to one mole of steam. This produces 3 moles of hydrogen and a by-product of one mole of carbon monoxide. WGS utilizes the production of hydrogen of this reaction by converting the by-product carbon-monoxide to hydrogen and carbon dioxide [96]. The second reaction requires no WGS as it directly produces hydrogen and carbon dioxide, where one mole of methane reacts with two moles of steam instead of one. It consumes 165 kJ and produces 4 moles of hydrogen and one mole of carbon dioxide. CCS process is finally followed to capture all the produced carbon dioxide from the entire process. The process is summarized in Figure 2.12.

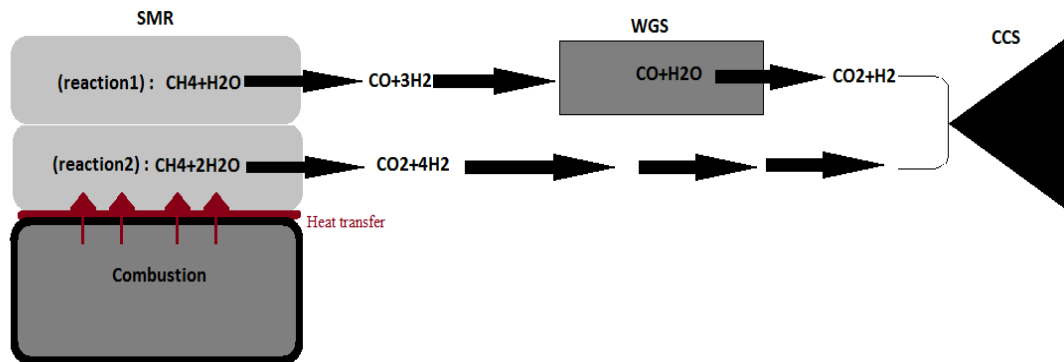


Figure 2.12 SMR process, reproduced from the reference [96].

2.8.1 SMR limitations

SMR is operated in extreme conditions. Since reaction 1 and 2 are endothermic, the temperature approximately reaches 1000K. In fact, it has been described as a "harsh" process [96]. Both reactions are catalytically conducted. This essentially means that catalyst shall be carefully chosen to withstand these extreme conditions, Table 2.4 [97]. Moreover, at high temperature, deposits of carbon dioxide are formed, which causes catalyst deactivation and blockage in the reactor.

Table 2.4 SMR catalyst

Category	Temperature range (°C)
nickel-based	550-850
carbon-based	300-900
zinc-based	300-500
aluminum-based	750-800
cerium-based	300-800
zirconium-based	250-500
nickel-based	550-850

2.9 Water-gas shifting (WGS)

Water-gas shifting is a chemical reaction which converts carbon monoxide and water into carbon dioxide and hydrogen. It is one of the essential reactions involved in carbon capture and storage processes and indeed needed in CARSOXY gas turbines. Water-gas shifting of one mole of carbon monoxide produces approximately 40 KJ. The reaction is typically accelerated by two types of catalysts (namely: iron-based and copper-based) [98].

2.9.1 WGS applications

Whenever carbon monoxide is an unwanted by-product gas, water-gas shifting is a scope of interest. In fact, it is a very reliable way to purify the produced hydrogen from steam-hydrocarbon reforming processes. As discussed in section 2.8, this process is typically integrated with the SMR process, Reactions 2.1 and 2.2 [99].



Ammonia production is another industrial application which highly depends on water-gas shifting to prevent carbon monoxide of reacting with the involved catalyst [100]. Ammonia production is highly expected to be involved in CARSOXY gas turbine cycle arrangement, especially when evaporation injection techniques are used.

2.9.2 WGS Catalyst

Choosing catalysts types depends on two main factors, sulfur tolerance and operation temperature. Iron-based catalysts operate at high temperature (approximately 680 K) and have small sulfur tolerance. At lower operation temperature (approximately 480 K) carbon-based catalysts are used. However, it has negligible tolerance towards sulfur [101]. Table 2.5 demonstrates the main properties of the iron-based and copper-based catalyst [101].

Table 2.5. WGS catalysts

Property	Composition	Stabilizer	Promoter
Iron-based catalyst	74.2% Fe ₂ O ₃ 10% Cr ₂ O ₃ 0.2% MgO Remaining is to balance volatiles	Cr ₂ O ₃	---
Copper-based catalyst	24% ZnO 24% Cr ₂ O ₃ 3% Mn, Al and Mg-oxides Remaining is to balance volatiles	Cr ₂ O ₃	ZnO

2.9.3 WGS reactors

Conventional WGS process is a two-reactor process, Figure 2.13. It involves a high-temperature reactor, which uses Iron-based catalyst. The products of the high-temperature reactor are cooled to be further purified from CO in a low-temperature reactor, which uses a copper-based catalyst. This option is ideal if the inlet boundary condition of the reactor is at high temperature and the desired product (H₂ and CO₂) is required at low temperature with very low residuals of CO [80].

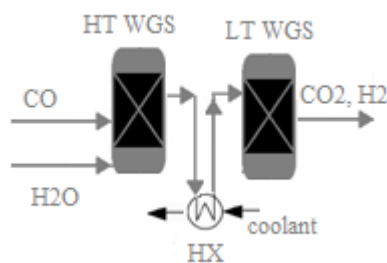


Figure 2.13 Conventional WGS reactors, reproduced from the reference [101].

A shell-tube design is also utilized as a WGS reactor, Figure 2.14 [102]. A tube of the hydrogen-selective membrane is placed inside a shell. The catalytic WGS is conducted around the tube (inside the shell). The membrane plays the separation role by only allowing H₂ to pass through (inside the tube) while the remaining products of the WGS are extracted outside the tube as a CO₂-rich mixture.

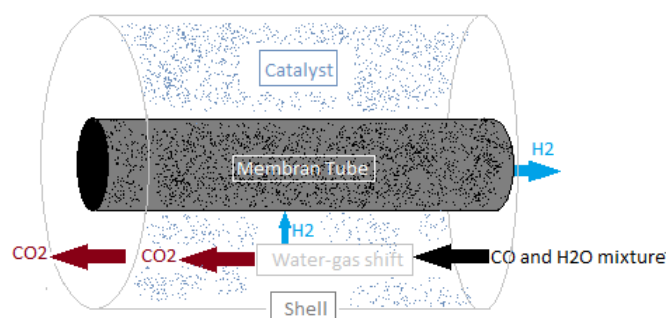


Figure 2.14 shell and tube WGS reactor, reproduced from the reference [102].

2.10 Classical combustion

Combustors can be mainly divided into two categories, can and annular combustors. Can combustors (Figure 2.15) are usually coupled with centrifugal compressors. Airflow is divided into several streams to feed the equally spaced several combustion chambers around the engine shaft. Each combustor has its own fuel supply. Because each combustor has its separate air feed and fuel supply, it is possible to run the gas turbine without using all combustors. This is a crucial advantage, especially in part-load operation conditions. However, this type of combustors is relatively large [103].

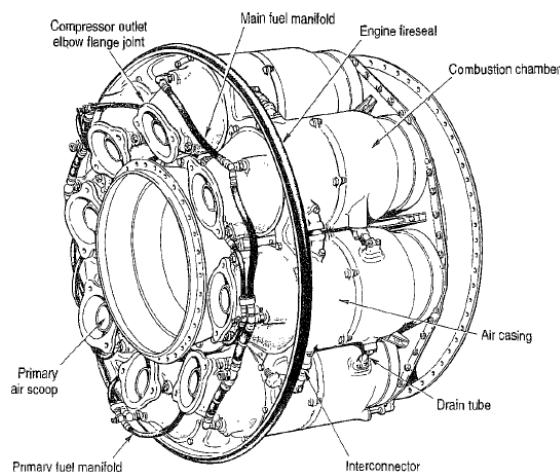


Figure 2.15 Can combustors [103].

The second type (Annular, Figure 2.16) solves the sizing problem of the can combustor. The Annular combustor can fit within a smaller space compared to the can combustors. However, this design comes with a few disadvantages. Unlike the can combustor, it only operates with full fuel and air supplies. In addition, this type of combustors is highly subjected to thermal buckling. Moreover, obtaining even distribution of temperature is more difficult than the can combustor [103]. Table 2.6 compares annular combustors to can combustors.

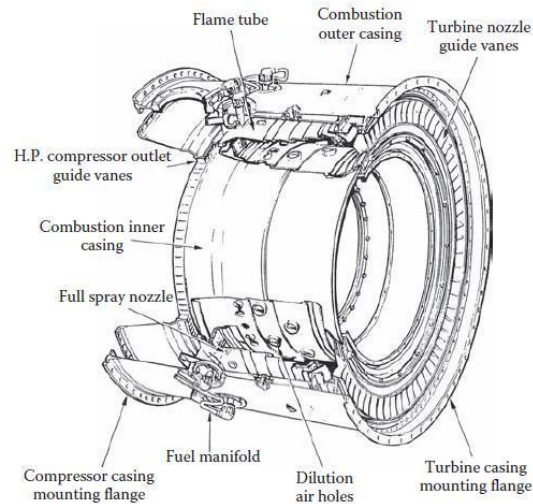


Figure 2.16 Annular combustor [103].

Table 2.6. Annular combustor vs can combustor

Combustor type	Compressor	Advantage	Disadvantage
Can combustor	Centrifugal	Part-load and development process	large
Annular	Axial-flow	Compact size	Low tolerance with part-loading

Combustion methods are classified based on the type of mixing techniques. These are mainly premixed, diffusive and swirl combustion. As the name implies, premixed combustion is based on mixing the oxidizer together with fuel prior to the combustion zone at ambient conditions, Figure 2.17. As the mixture approaches the flame front, the mixture is heated up by conduction and radiation. Flashbacks are the major disadvantage of this method (i.e. combustion occurs in supply streams instead of the burner's exit) [69]. The second method is diffusive combustion; this technique resolves the flashback problem which occurs in premixed combustion. Oxidizer and fuel are supplied to the combustion zone through two different streams to prevent combustion flashback, Figure 2.17. Moreover, this method is considered to be more stable than premixed combustion. In addition, the flame can be maintained within low equivalence ratio [104]. However, this method requires a long mixing distance (hovering flame). Consequently, flue gases have high levels of NO_x and unburned fuel [104]. Swirl combustion is an aerodynamically enhanced combustion. It is based on accelerating heat transfer and circulating active species to the burner's exit by creating a central circulations zone (CRZ) [105]. This method enhances flame stability and reduces NO_x emissions.

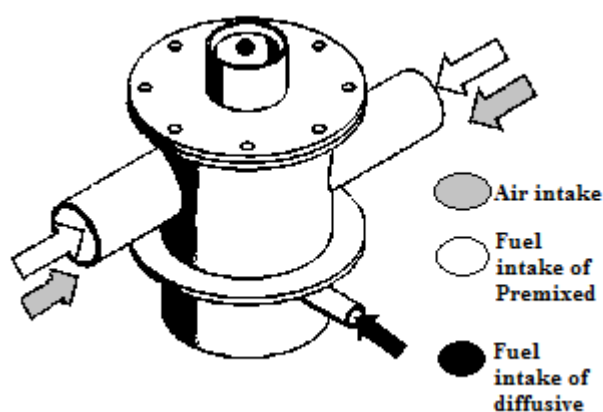


Figure 2.17 Premixed vs diffusive combustion, reproduced from the reference [108].

2.11 A comprehensive review of the current state-of-the-art of combustion alternative working fluids.

The concept of utilizing alternative combustion working fluids is based on replacing air by oxygen with carbon dioxide [6-11], steam[12-16] and inert gases [22-24], individually or collectively. Therefore, this section evaluates the state-of-the-art in utilizing those components as working fluids.

2.11.1 The current state-of-the-art of oxygen-carbon dioxide-fuel combustion.

In comparison to air combustion, oxygen combustion is accompanied by a higher level of temperature. Therefore, oxygen combustion is typically associated with CO₂ dilution and circulation to maintain the temperature within acceptable ranges [6]. However, combustion characteristics and heat release of oxygen- CO₂-fuel combustion varies from those for air-fuel combustion [7]. This is attributed to the differences between N₂ and CO₂ [8]. Replacing N₂ by CO₂ affects several overall physical properties of the working fluid (i.e. heat capacities, density, dynamic viscosity, mass diffusivity and thermal conductivity) [9]. The main advantage of oxy-combustion is the elimination of NO_x emissions. In addition, heat losses and the size of the flue gas treatment unit are reduced because exhaust flue gases are reduced in oxy-combustion compared to air-combustion [10]. However, the high level of CO₂ which typically circulated back to the oxidizer decreases chemical kinetics and causes the reduction in flame laminar speed [11]. As reported by the reference [11], the addition of CO₂ oxy-combustion impacts kinematic viscosity, thermal conductivity and mass diffusivity, thus effecting flammability limits. Figure 2.18 shows the flammability upper and lower limits of CO₂-O₂- CH₄ combustion at three oxygen fractions (namely 29%, 32% and 36%) in comparison to air- CH₄ combustion where the flammability region of CO₂-O₂-CH₄ combustion smaller than that for air-CH₄ combustion. In fact, the CO₂-O₂-CH₄ flammability

region decreases as oxygen fraction decreases. CO₂-O₂-CH₄ mixture with an oxygen fraction of 36% can only achieve 79%-82% of that of air-CH₄ flammability region in the range of Reynolds number considered [11]. Therefore, it can be concluded that high levels of oxygen are required to maintain the same flammability region as that for air-CH₄. Subsequently, air separation units will be required to supply more oxygen, thus additional costs will be penalized to maintain the same flammability region as that for air-CH₄.

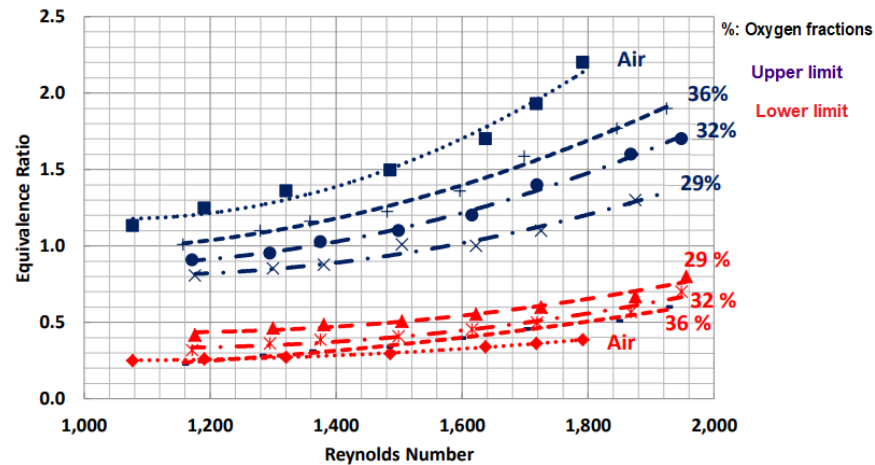


Figure 2.18 flammability upper and lower limits of CO₂-O₂-CH₄ combustion at three oxygen fractions (namely 29%, 32% and 36%) in comparison to air-CH₄ combustion[11].

Nevertheless, CO₂-O₂-CH₄ combustion has slower chemical kinetics in comparison to air-CH₄ combustion [11]. This essentially means that longer CO₂-O₂-CH₄ flames compared to air-CH₄ flames are anticipated. Therefore, the compactness of burners will be negatively affected using CO₂-O₂-CH₄ combustion. In fact, the reference [11] has evaluated the visual length of CO₂-O₂-CH₄ flames at three oxygen fractions (namely 29%, 32% and 36%) in comparison to air-CH₄ flame, Figure 2.19.

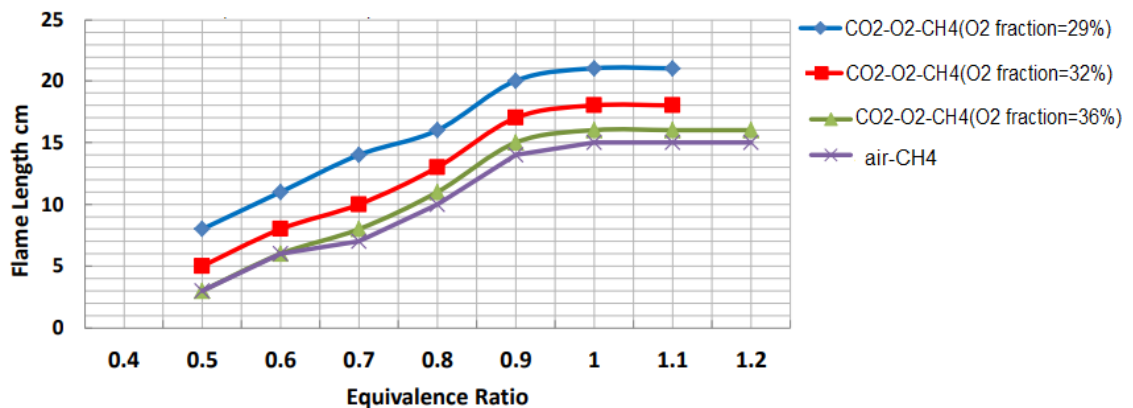


Figure 2.19 Visual length of CO₂-O₂-CH₄ flames at three oxygen fractions (namely 29%, 32% and 36%) in comparison to air-CH₄ flame [11].

The visual flame length of CO₂-O₂-CH₄ at the three oxygen fractions is approximately longer than that for to air-CH₄ flame at all the tested equivalence ratios [0.5-1.2]. Only at an oxygen fraction of 36%, the CO₂-O₂-CH₄ flame lengths were reduced to be approximately equal to those for air-CH₄. This essentially means that additional costs will be penalized in order to supply this high level of oxygen.

Table 2.7. CO₂-O₂-CH₄ vs air-CH₄ combustion.

Property	CO ₂ -O ₂ -CH ₄ (In comparison to air-CH ₄)	air-CH ₄ (In comparison to CO ₂ -O ₂ -CH ₄)
NO _x emission	Eliminated	High NO _x emission
Heat losses	Heat losses are reduced	High heat losses
Flammability region	Limited	Large
Chemical kinetics	Slow	Fast
Compactness	Long flames	Short flame
Cost	Additional costs will be penalized (air separation cost)	Low costs

Table 2.7 provides a summary of CO₂-O₂-CH₄ combustion in comparison to air-CH₄. Although CO₂-O₂-CH₄ combustion eliminates NO_x and reduces heat losses, it negatively affects chemical kinetics, flammability regions and flame compactness. The severity of those negative effects could be reduced by increasing the level of oxygen. However, air separation units will be required to supply more oxygen, thus additional costs will be penalized. Therefore, it can be concluded that using CO₂-O₂ as a working fluid faces serious technical challenges and less likely to be deployed on an industrial scale. The following sections evaluate the probability of utilizing other options as alternative working fluids (i.e. steam-O₂ and inert gases-O₂).

2.11.2 The current state-of-the-art of oxygen-steam-fuel combustion.

The main advantage of injecting steam to gas turbines is the increase of cycle efficiency and specific power outputs in comparison to conventional air-driven simple cycle gas turbines [12]. As shown in Figure 2.20, steam-injected gas turbines have higher efficiency compared to industrial and aero-derivative simple cycle gas turbines. In terms of power outputs, the steam-injected gas turbine has approximately the same power output as an aero-derivative simple cycle gas turbine. However, the power output of the

steam-injected gas turbine is significantly lower than what is available for industrial simple cycle gas turbine. Nevertheless, both aero-derivative and industrial combined cycles demonstrate higher efficiencies and power outputs compared to steam-injected gas turbines. Although Figure 2.19 shows the literature results with respect to efficiency and power output for water-injected, steam-injected and evaporative gas turbines, those are based on a various range of assumptions and not compared to industrial examples.

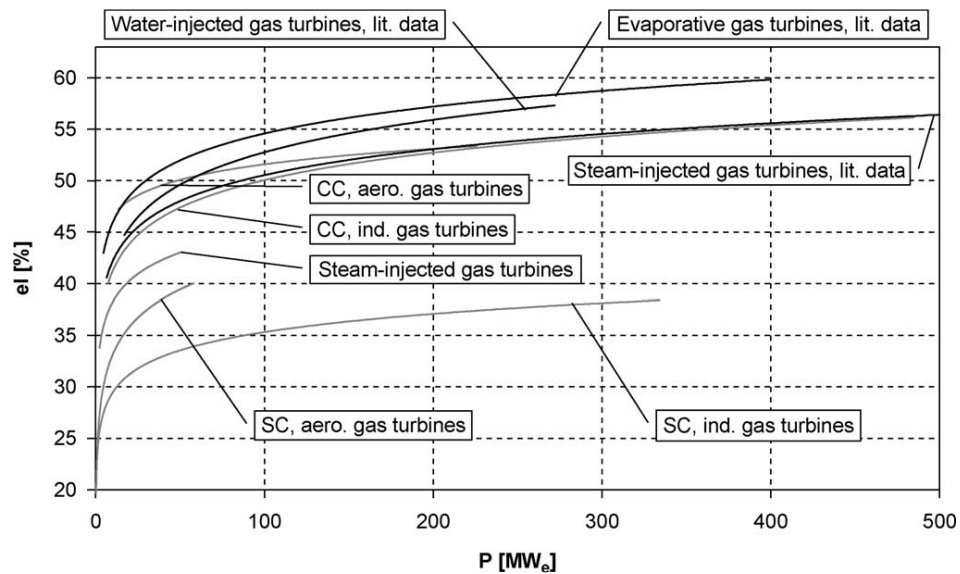


Figure 2.20 Trend lines (black) for literature data for humidified gas turbine cycles compared with trend lines (grey) for existing simple cycle gas turbines, steam-injected gas turbines and combined cycles (ind: industrial, aero: aero-derivative, SC: simple cycle, CC: combined cycle) [13].

As demonstrated in Figure 2.20, steam injection does not always ensure higher efficiency and power output in comparison to air-driven cycles. Therefore, combustion technical aspects are not necessarily compensated by higher efficiencies and those shall be carefully considered. The reference [14] has experimentally and numerically studied O₂-H₂O-CH₄ in comparison O₂-CO₂-CH₄ combustion at stoichiometric condition over a range of diluent (steam or carbon dioxide) molar fractions (i.e. 10%-50%). Both numerical and experimental results have shown that O₂-H₂O-CH₄ has faster laminar flame speed in comparison to O₂-CO₂-CH₄, Figure 2.21.

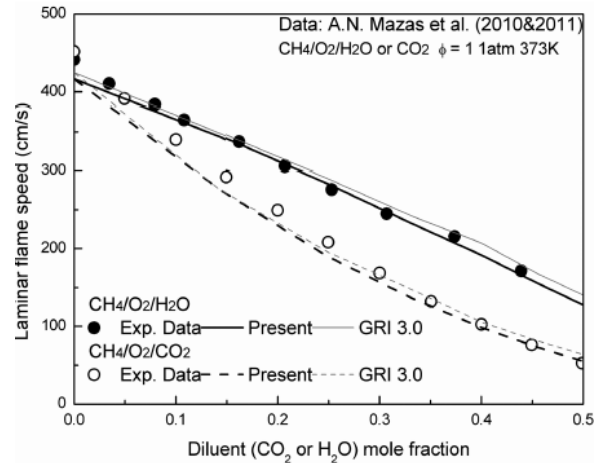


Figure 2.21 laminar flame speed of O₂- H₂O- CH₄ and O₂-CO₂-CH₄ combustions [14].

Regarding CO emissions, the reference [15] numerically and experimentally studied O₂-H₂O-CH₄ in reference to O₂-CO₂-CH₄ combustion and it was found that CO levels were 5-7 times lower for O₂- H₂O-CH₄ in comparison to O₂- CO₂- CH₄ combustion. However, the references [14-15] neither compared O₂-H₂O-CH₄ to air-CH₄ combustion nor provided further conclusions about flame shape or flammability. Finally, the reference [16] has conducted exergy and techno-economic analysis of two conceptual 600 MWe O₂-CO₂-CH₄ and O₂-H₂O-CH₄ combustion power plants (process flow diagram and components details are available by the references [17-20]). O₂-H₂O- CH₄ combustion power plant has 0.90% point of higher net efficiency and 1.01 % points higher exergy efficiency than those in O₂-CO₂-CH₄ combustion power plants. Furthermore, O₂-H₂O-CH₄ power plant has proven to be more economically sustainable in comparison to O₂-CO₂-CH₄ power plant, Figure 2.22. Table 2.8 provides a summary of O₂-H₂O- CH₄ in comparison to O₂- CO₂- CH₄ combustion.

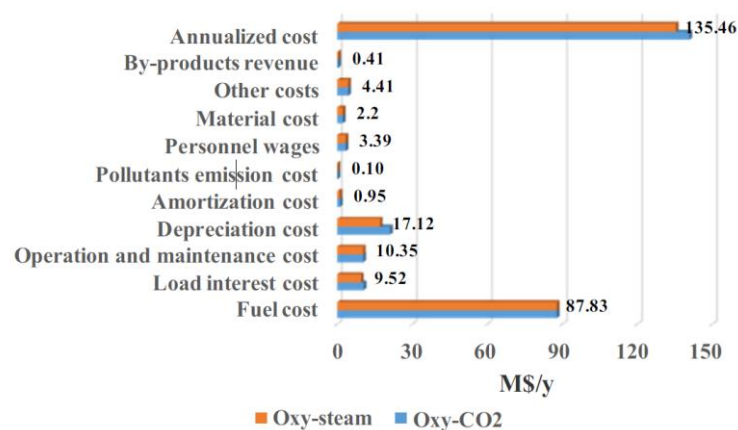


Figure 2.22 Comparison of cost distributions for oxy-steam (O₂-H₂O-CH₄) combustion and oxy-CO₂ (O₂-CO₂-CH₄) combustion (values labelled at strips are for oxy-steam combustion)[16].

Table 2.8. O₂-H₂O-CH₄ vs O₂-CO₂-CH₄ combustion.

Property	O ₂ -H ₂ O-CH ₄ combustion/power plant (In comparison to O ₂ -CO ₂ -CH ₄)	O ₂ -CO ₂ -CH ₄ combustion/power plant (In comparison to O ₂ -H ₂ O-CH ₄)
Laminar flame speed	Fast	Slow
CO emissions	Low	High
Exergy efficiency	High	Low
Net efficiency	High	Low
Cost	Low	High

Within the evaluated studies in the literature on O₂-H₂O-CH₄, it can be concluded that O₂-H₂O-CH₄ power plants do not always ensure higher efficiencies and power outputs in comparison to air-driven cycles (i.e. aero-derivative and industrial combined cycles demonstrate higher efficiencies and power outputs compared to steam-injected or (O₂-H₂O-CH₄) gas turbines, Figure 2.20). Therefore, humidification techniques should be carefully deployed to provide higher efficiency in comparison to air-driven cycles. As summarized in Table 2.8, O₂-H₂-CH₄ combustion/power plants demonstrated more advanced properties. However, within the evaluated studies in the literature, those properties (laminar flame speed, CO emissions, exergy efficiency are only compared to O₂-CO₂- CH₄ combustion/power plant and must be benchmarked against air- CH₄ combustion/power plants in future studies.

2.11.3 The current state-of-the-art of oxygen-inert gases-fuel combustion.

The group of inert gases include helium, neon, argon, krypton, xenon and radon [21]. In the context of combustion and power generation, argon [22], xenon [22] and helium [23-24] have been studied as working fluids due to their higher specific heat ratios and their potential of increasing cycle efficiency in comparison to air [22].

Utilizing helium as a working fluid in closed cycles has the potential of increasing cycle efficiency in comparison to air-driven cycles [23]. However, this techniques has not yet reached an acceptable maturity state to be used on a wide industrial scale (i.e. helium leakage is not easily controlled due to its low molecular weight [23]). Moreover, thermo-fluid properties of helium significantly diverge from those for air. This strongly affects the size and performance of gas turbine compressors, Table 2.9 [24-24]. In comparison to air-driven gas turbines, helium gas turbine operate at low compressor pressure ratios. However, a higher number of stages are required to achieve the required pressure ratio due to its high specific heat. Consequently, end-wall boundary layer growth and secondary flow increase using helium in comparison to air. Further details of helium gas turbines are available in the references [22-24]. The

combustion of hydrocarbon fuel in helium-oxygen environments was reported by the reference [190]. However, experiments were conducted in SPACELAB onboard the Space Shuttle Columbia during the first launch (STS-83) of the Microgravity Science Laboratory mission in April 1997. Although those experiments provided a great deal of information, however, correlating those results to stationary ground combustion is difficult.

Table 2.9. Comparison of design parameters between air compressors and helium compressors
[22-24]

Unit	Air-breathing compressor			Helium compressors		
	C135	C141	NACA	GTHTR300	GT-MHR	
					LP	HP
Number of stages	2	4	8	20	14	19
Design pressure ratio	1.88	2.95	10.26	2	1.7	1.7
Inlet hub-to tip ratio	0.38	0.69	0.48	0.88	0.7	0.9
Exit hub-to-tip ratio	0.57	0.81	0.9	0.91	0.88	0.9
Mass flow/unit annulus area (kg/s.m ²)	207	189	189	447	591	1141

Going back to argon and xenon, the reference [22] has reported the effects of using each individual component of argon, xenon and nitrogen on oxyhydrogen combustion. Results have been produced using computational simulation (CHEMKIN and CFD) and were not experimentally validated. As shown in Figures 2.23 and 2.24, the temperature level of the argon-based flame is lower than that for the xenon-based flame, however, higher than that for the nitrogen-based flame. This is attributed to the higher specific heat ratio of xenon (1.677) compared to argon (1.667) and nitrogen (1.401).

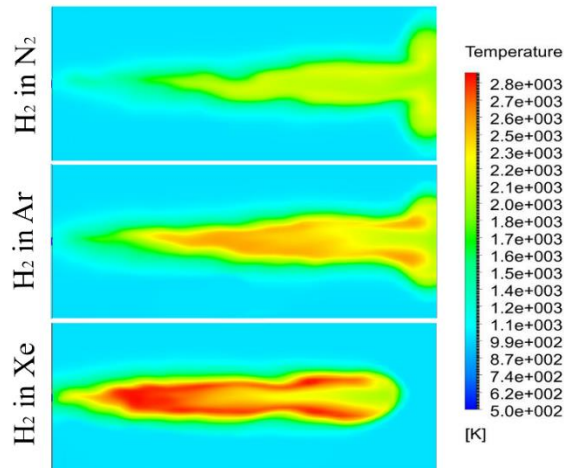


Figure 2.23 Temperature contours of hydrogen injection into nitrogen, argon, and xenon (From top to bottom) [22]

Similarly, the maximum OH mass fraction of argon-based flame is lower than that for the xenon-based flame, however, higher than that for the nitrogen-based flame. Maximum OH mass fraction patterns approximately followed the same patterns as those for maximum temperature, Figure 2.24.

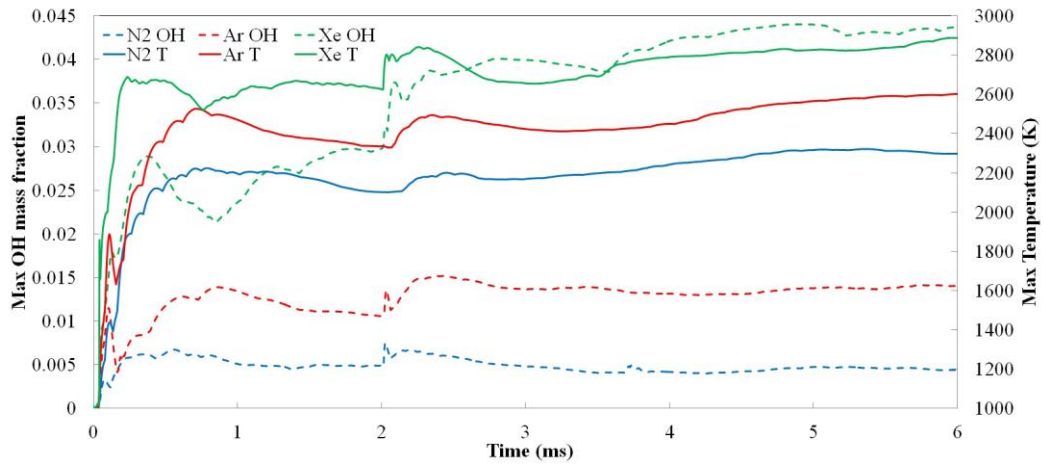


Figure 2.24 Maximum temperature and maximum OH concentration [22].

According to the reference [22], higher mixing rates are related to lower mean spatial variation and mean scalar dissipation. As shown in Figure 2.25, it can be concluded that argon has a higher mean mixing rate since it demonstrates lower partial variation and mean scalar dissipation in comparison to xenon and nitrogen.

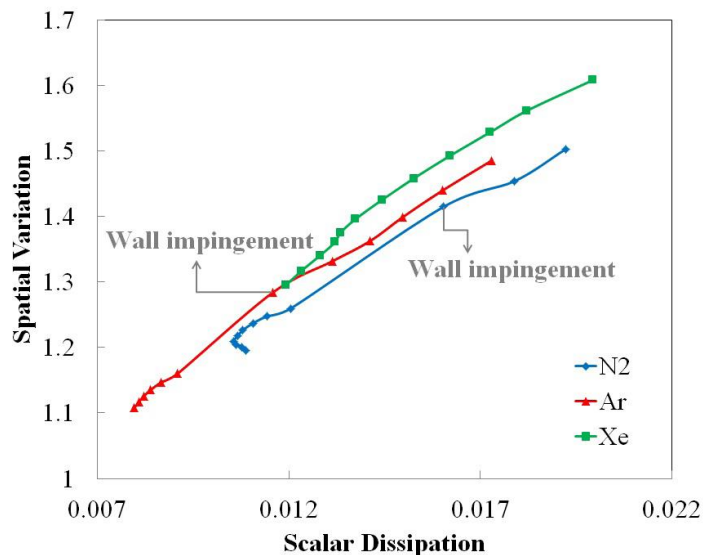


Figure 2.25 Spatial variation vs. scalar dissipation between 3 ms and 6 ms after injection

Therefore, while eliminating NO_x, using oxygen-argon and oxygen-xenon mixtures is expected to increase cycle efficiency due to the high specific heat ratio of xenon (1.677) and argon (1.667) compared

to nitrogen (1.401). However, considering the higher abundance and mixing rate of argon in comparison to xenon, argon is more likely to be adopted to combustion in future.

2.12 Chapter summary

As part of fulfilling this global commitment, local and regional regulations have been established to limit NO_x and CO₂ emissions [39-41]. Most of the systems producing these unwanted emissions are directly linked to power generation, from which gas turbines have a leading role [11]. Thus, stationary gas turbines have been broadly and will continue to be employed in power plants to cover the growing demand for power production [49]. Therefore, novel concepts are required to ensure that emissions are tackled whilst enabling large power production from these systems. Utilizing alternative working fluids is one promising technology that could be used for reducing harmful emissions while recirculating CO₂ in the combustion process [50]. The concept of utilizing alternative combustion working fluids is based on replacing air by oxygen with carbon dioxide [6-11], steam [12-21] and inert gases [22-24], individually or collectively.

Utilizing carbon dioxide as a working fluid in an oxyfuel gas turbine maintains turbine temperature within an acceptable range [6] and reduces heat losses [10] while eliminating NO_x emissions [7]. However, it negatively affects chemical kinetics, flammability regions and flame compactness [11]. The severity of those negative effects could be reduced by increasing the level of oxygen. However, air separation units will be required to supply more oxygen, thus additional costs will be penalized. Therefore, it can be concluded that using CO₂-O₂ as working fluid (without any additional components to enhance the overall thermodynamic properties) faces serious technical challenges and less likely to be deployed on an industrial scale.

The main advantage of injecting steam to gas turbines is the increase of cycle efficiency and specific power outputs in comparison to conventional air-driven simple cycle gas turbines [12]. However, within the evaluated studies in the literature on O₂-H₂O-CH₄, it can be concluded that O₂-H₂O-CH₄ power plants do not always ensure higher efficiencies and power outputs in comparison to air-driven cycles (i.e. aero-derivative and industrial combined cycles demonstrate higher efficiencies and power outputs compared to steam-injected or (O₂-H₂O-CH₄) gas turbines) [13]. Therefore, humidification techniques should be carefully deployed to provide higher efficiency in comparison to air-driven cycles. As summarized in Table 2.8, O₂-H₂-CH₄ combustion/power plants demonstrated more advanced properties. However, within the evaluated studies in the literature [13-16], those properties (laminar flame speed [14], CO emissions [15], exergy efficiency [16] are only compared to O₂-CO₂-CH₄ combustion/power plant and must be benchmarked against air-CH₄ combustion/power plants in future studies.

In the context of using inert gases in combustion and power generation, argon [22], xenon [22] and helium [23-24] have been studied as working fluids due to their higher specific heat ratios and their potential of increasing cycle efficiency in comparison to air [22]. Utilizing helium as a working fluid in closed cycles has the potential of increasing cycle efficiency in comparison to air-driven cycles [23]. However, this technique has not yet reached an acceptable maturity state to be used on a wide industrial scale (i.e. helium leakage is not easily controlled due to its low molecular weight [23]).

While eliminating NO_x, using oxygen-argon and oxygen-xenon mixtures is expected to increase cycle efficiency due to the high specific heat ratio of xenon (1.677) and argon (1.667) compared to nitrogen (1.401) [22]. However, considering the higher abundance and mixing rate of argon in comparison to xenon [22], argon is more likely to be adopted to combustion in future.

The concept of utilizing CARSOXY as a working fluid takes the advantages of using carbon dioxide to maintain turbine temperature within acceptable ranges, argon to increase specific heat ratio, steam to increase the mass flow rate and oxygen to eliminate NO_x emissions. However, inferring the optimal CARSOXY blend shall be considered for a range of working conditions and cycle arrangements. The concept of inferring the optimal CARSOXY blend was first established in a 2017 paper [49]. However, choosing the optimal blend was based on testing a random number of blends with random proportions without indicating the effect of each component (i.e. carbon dioxide, argon and steam) on the cycle efficiency. The original CARSOXY cycle was suggested using a zero-dimensional model [49] and its techno-economic sustainability was not assessed. Finally, CARSOXY shall be further experimentally characterized over a range of various operational conditions to define its flammability limits, flame geometry and its combustion regime.

CHAPTER THREE

METHODOLOGY

“The man of science has learned to believe in justification, not by faith, but by verification”

~ Thomas Huxley

CHAPTER 3 – METHODOLOGY

Initially, a parametric study of various thermodynamic cycles for the use of various CARSOXY blends has been conducted in chapter 4. Secondly, the production of CARSOXY is suggested in chapter 5. Thirdly, the techno-economics of CARSOXY gas turbines is discussed in chapter 6. Finally, the properties of the CARSOXY flame are illustrated in chapter 7 and 8. This chapter describes the methodological approach adopted to generate the results obtained in chapter 4, 5, 6, 7 and 8. Besides, the methodology sequence between the previously mentioned chapters is present in this chapter.

3.1 Methodology Sequence

A parametric study of various thermodynamic cycles for the use of various CARSOXY blends has been conducted. A MATLAB code was developed to examine five different gas turbine arrangements (namely; simple cycle, heat exchanged cycle, free turbine & simple cycle, evaporative cycle and humidified gas turbine cycle, Figure3.1). To obtain comparable results, the code evaluates the cycle performance for both Air/methane and CARSOXY combustions under the same assumptions. Further details of the parametric study methodology are presented in section 3.2.

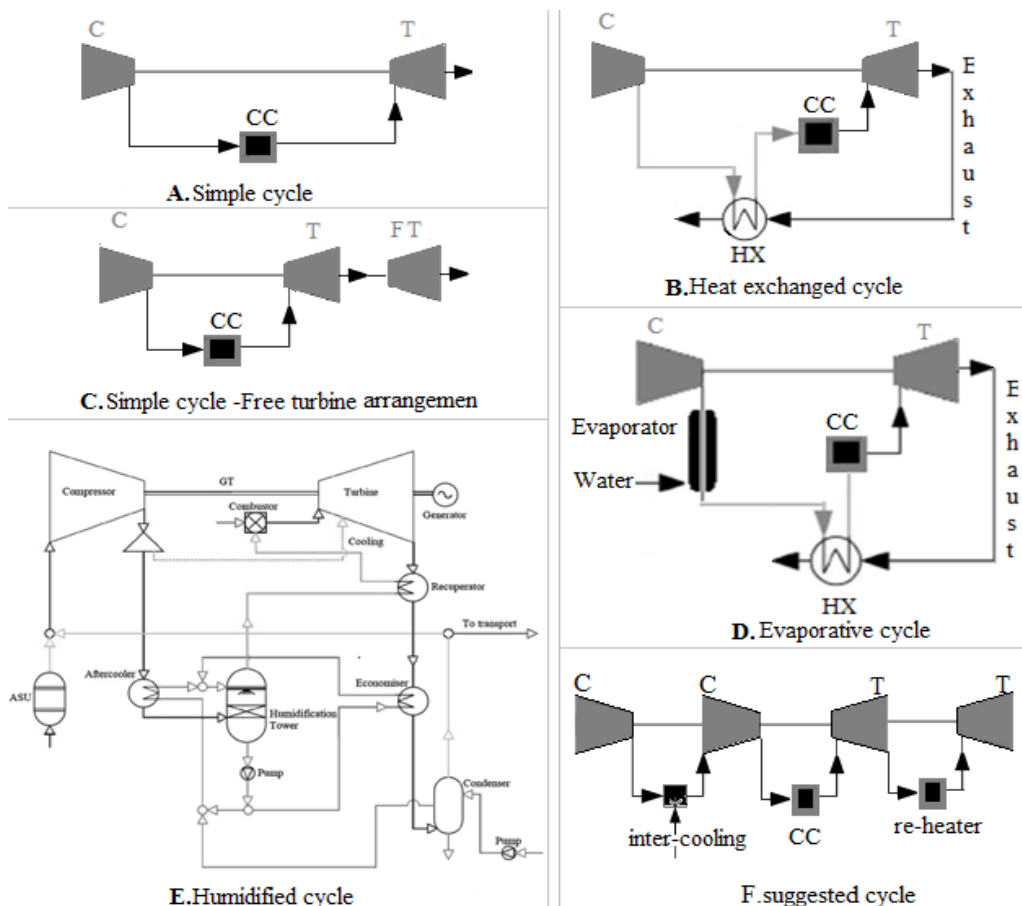


Figure 3.1 Schematic diagrams of the cycles.

Once the ultimate gas turbine cycle- heat exchanged cycle (HXGT) - was determined (discussed in chapter 4), it was adapted to an ASPEN PLUS model, Figure 3.2. The (HXGT) gas turbine cycle was modelled under the same assumptions as those of the MATLAB code, Table 3.3. The cycle was comprised of an air separation unit (ASU), a steam-methane reformer (SMR), water-Gas shift reactors (WGS), Pressure swing adsorption units (PSA) and Heat exchanged gas turbine (HXGT), thus providing a novel industrial approach to produce the CARSOXY blend at the required molar fractions. Obtaining the required CARSOXY molar fractions –model calibration-has been achieved by characterizing the model through an extensive sensitivity analysis, present in chapter 5. Further details of the ASPEN PLUS modelling methodology is presented in section 3.3.

Once the model was calibrated after the sensitivity analyses, its economic parameters were analysed. The analysis was carried out using the default assumptions and pricing methods of ASPEN PLUS V.9 software. The database of the ASPEN PLUS software was used to price some equipment, however, some prices were calculated using cost functions, as those have not been included in the database. Feed material and product streams shall be assigned specific costs. These were obtained from the literature. Further details of the techno-economics methodology are presented in section 3.4.

To experimentally assess CARSOXY in comparison to a CH₄/air flame, OH chemiluminescence imaging integrated with Abel deconvolution techniques have been utilized to study flame stability, and flame geometry (i.e. Area of highest heat intensity ($A_{\overline{OH}_{Max}}$), Center of highest heat intensity ($C_{\overline{OH}_{Max}}$)) over a range of variable volumetric flowrates and instability conditions (excitation frequencies [50Hz-700Hz]). Moreover, NO_x and carbon emissions have also been analyzed. Further details of the chemiluminescence imaging and emission analyses methodology are presented in section 3.5.

Finally, after analysing CARSOXY in comparison to CH₄/air over variable volumetric flowrates, it was essential to perform the analyses over a range of oxygen to fuel equivalence ratios (λ_{oxy}) and fluid Reynold's numbers. OH chemiluminescence integrated with PLIF imaging has been utilized to study several flame properties at Re of [2000-3750] and methane volumetric flow rate (\dot{V}_{CH_4}) of 1L/min and λ_{oxy} of [35-70] (i.e. Area of highest heat intensity ($A_{\overline{OH}_{Max}}$), the centre of highest heat intensity ($C_{\overline{OH}_{Max}}$)). Moreover, Damkohler analyses have been performed and Borghi regime diagrams have been produced for both types of flames

Damkohler analyses suggested by the reference [162] for nonpremixed combustion have been performed to indicate the uniformity of CARSOXY flames in comparison to CH₄/air flames. Moreover, Damköhler number analyses describe the turbulence-chemistry interaction by correlating the characteristic flow time

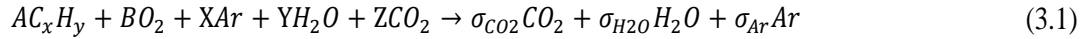
to the characteristic chemical time [162]. To perform the suggested Damkohler analyses, the centre of the highest heat intensity shall be identified, section 3.6.3.4. Once Damkohler analysis is performed, Borghi combustion regime diagrams could be plotted to identify the tendency of CARSOXY flame to approach the connected reaction zone in comparison to Air/methane flame. Since Damkohler analyses and plotting Borghi combustion diagram are typically plotted over ranges of λ_{oxy} and fluid Reynold's numbers [162], this thesis has performed Damkohler analyses and plotted Borghi combustion diagram over ranges of λ_{oxy} [35-70] and fluid Reynold's numbers [2000-3750].

3.2 The methodology of the parametric study of various thermodynamic cycles for the use of various CARSOXY blends

The concept of utilizing CARSOXY as a working fluid takes the advantages of using carbon dioxide to maintain turbine temperature within acceptable ranges, argon to increase specific heat ratio, steam to increase the mass flow rate and oxygen to eliminate NO_x emissions. The concept of choosing the ultimate CARSOXY blend was first established by reference [25]. The reference [25] has suggested the use of 150 different CARSOXY blend and studied their effects on cycle efficiency in comparison to an air-driven simple gas turbine cycle. The reference then defined the blend which insures the highest cycle efficiency and defined it as 'the ultimate' blend (blend 58, Table 3.1). However, the reference's choice of the ultimate blend was only compared to a random number of blends with random compositions without identifying the effect of each individual component. Meanwhile, this thesis studies the combined and individual effect of each component on the cycle efficiency. Based on that, a new ultimate blend is reselected. The choice is based on correlating three intervals of variable molar fractions of carbon dioxide, argon and steam in a three-dimensional efficiency surface. This approach essentially visualizes the highest cycle efficiency as the highest peak on the efficiency surface within the tested intervals of molar fractions. Therefore, the corresponding molar fractions (to the highest peak) can then be chosen as the ultimate blend. Moreover, the original CARSOXY analysis [35] was based only on one cycle arrangement (humidified gas turbine cycle, Figure 3.1). Meanwhile, this thesis analyses four other gas turbine arrangements (namely; simple, heat exchanged, free turbine & simple and evaporative, Figure 3.1). These have been analyzed in reference to the original cycle (humidified gas turbine cycle) under various intervals of working conditions.

3.2.1 MATLAB Code Development

The results in chapter 4 are based on MATLAB codes -Appendix 3.1- which have been developed to conduct the cycle analysis for both CARSOXY and air-driven gas turbines. Assuming the stoichiometric condition of an equivalence ratio of one. Equation (3.1) shows the stoichiometric reaction for carbon dioxide-argon-steam mixture.



The produced results obtained from the code are based on the higher heating values (HHV) of methane combustion which have been driven using Equations (3.2-3.6) [109].

$$\Delta H_{\text{Reaction}, 25^\circ C} = \sum \Delta H_{\text{products}} - \sum \Delta H_{\text{reactant}} \quad (3.2)$$

$$\Delta H_{\text{Reaction}, T'_{0.1}} = \Delta H_{\text{Reaction}, 25^\circ C} + \int_{25^\circ C}^{T'_{0.1}} \Delta \bar{C}_p dT \quad (3.3)$$

$$\text{LHV}_{T'_{0.1}} = -\frac{\Delta H_{\text{Reaction}, T'_{0.1}}}{M_{C_xH_y}} \quad (3.4)$$

$$\text{HHV}_{T'_{0.1}} = \text{LHV}_{T'_{0.1}} + \left[\frac{n_{H_2O} M_{H_2O}}{n_{C_xH_y} M_{C_xH_y}} \times H_{H_2O, T'_{0.1}} \right] \quad (3.5)$$

$$f = \frac{H_{\text{CO}_2, \text{Argon}, \text{Steam}, T'_{0.2}} - H_{\text{CO}_2, \text{Argon}, \text{Steam}, T'_{0.1}}}{\text{HHV}_{T'_{0.2}}} \quad (3.6)$$

Equations (3.7-3.11) show reference equations which are used to drive heat capacities of the Carbon dioxide -Argon-Steam mixture for each stage [110].

$$C_{p_{\text{mix}}} = \sum_i C_{p(i)} x_i \quad (3.7)$$

$$\mu_{\text{mix}} = \sum_i r_i \mu_i \quad (3.8)$$

$$R_{\text{mix}} = \frac{8.314}{\mu_{\text{mix}}} \quad (3.9)$$

$$C_{v_{\text{mix}}} = C_{p_{\text{mix}}} - R_{\text{mix}} \quad (3.10)$$

$$\gamma_{\text{mix}} = \frac{C_{p_{\text{mix}}}}{C_{v_{\text{mix}}}} \quad (3.11)$$

The parametric study has been conducted to produce results in a three-dimensional surface rather than two-dimensional curves, to consider the combined effects of two variables such as the inlet temperature and pressure ratio. Wet and dry compressions have been mathematically modelled by adding the molar fraction of Steam to the Carbon dioxide-Argon mixture before and after the compression stage, respectively. Wet compression refers to a direct Steam feed through the compressor intake.

Neither the effect of Steam temperature nor the implementation methods are addressed. The results in chapter 4 are plotted for the cycle efficiency with respect to both the compressor pressure ratio variation within the range of 2-10 and the compressor inlet temperature variation within the range of 250-600K at constant turbine inlet temperature (1900K). Equations (3.12) and (3.13) show the specific fuel consumption (SFC) and cycle efficiency(η),

$$SFC = \frac{W_t - W_c}{f} \quad (3.12)$$

$$\eta = \frac{3600}{SFC \times HHV_{T'_{0.1}}} \quad (3.13)$$

To obtain the most realistic simulation of the performance, the ratios of pressure losses with respect to the stage inlet pressure in the combustion chamber, heat exchanger cold side, evaporator, heat exchanger hot side and exhaust have been considered as 0.02,0.03,0.02,0.04 and 0.03, respectively [66]. Besides, efficiencies have also been taken into account. The isentropic efficiencies of the compressor and turbine are assumed to be 0.85 and 0.87 respectively, and the mechanical and combustion efficiencies are assumed to be 0.99 and 0.98 respectively [66]. The Evaporator efficiency has been assumed to be 0.87 and heat exchange effectiveness has been assumed to be 0.9 [66]. Average values have been chosen since the aim of this study is to obtain indications for as many cases as possible rather than specific values for a particular case. The remaining parameters involved in the cycle analysis such as W_c , stagnation conditions at the inlets and outlets of each stage have been calculated using conventional cycle analysis [66]. Some of the used equations for gas turbine have been especially derived and implemented in the code such as those used to calculate the inlet temperature of the combustion chamber $T'_{0.1}$ for each cycle shown in Figure 3.1. Heat capacity variation with respect to temperature in the compression and expansion stages of the CARSOXY blends have been studied for three blends which are shown in Table 3.1. As discussed at the beginning of section 3.2, the concept of utilizing CARSOXY as a working fluid takes the advantages of using carbon dioxide to maintain turbine temperature within acceptable ranges, argon to

increase specific heat ratio, steam to increase the mass flow rate and oxygen to eliminate NO_x emissions. The reference [191] has proven the combustibility of blend 58 and thus the performances of CARSOXY cycles in the parametric study were evaluated using this blend. The other two blends (79 and 27) were only used to validate the code as explained in section 3.2.2.

Table 3.1. Compositions of the blends. Blend number as in [25].

Blend	Molar fractions of (Argon, CO ₂ , H ₂ O, fuel, O ₂) [%] [25]
58	(25,23,19, 11, 22)
79	(24,19,19, 12.67, 25, 33)
27	(30, 24, 16, 10, 20)

3.2.2 MATLAB Code Validation

Validation of the code has been performed in two parts. The cycle analysis part of the code has been tested against two particular case studies by Saravanamutto et al [69]. The cases are the air-driven free turbine & simple cycle (Figure 3.1.C) and the air-driven heat exchanged cycle (Figure 3.1.B). The isentropic heat capacity and heat capacity ratio of air at the compression stage has been suggested to be 1.005 kJ/kg.K and 1.4, respectively [69]. At the expansion, these values were set as 1.148 kJ/kg.K and 1.33, respectively. The results of the code exactly matched the results of the case of studies (i.e. the cycle efficiencies results generated by the code –Appendix 3.1-and by Saravanamutto et al [69] were 31.5% and 33.1% for the air-driven free turbine & simple cycle and the air-driven heat exchanged cycle, respectively.

The second part of the validation has been for CARSOXY-driven gas turbines. It was performed via testing the code for a CARSOXY gas turbine cycles to reproduce the heat capacity readings of blends 58, 79 and 27, Table 3.1, against the results from Al-Doboan et al. [25] under the same conditions of analysis, i.e. 10 bar and 900K. The ratios of heat capacities for blends 58, 27 and 79 are 1.22, 1.23 and 1.22, respectively, while those produced via the code are 1.25, 1.26 and 1.25, respectively. Thus, the results from the MATLAB code diverge from those of Al-Doboan et al. [25] by only 2.4%.

3.3 The methodology of modelling CARSOXY Production

The developed approach of producing the required CARSOXY molar fraction involves the integrations of an air separation unit (ASU), a steam methane reformer (SMR), water gas shift (WGS) reactors, a pressure swing adsorption (PSA) unit, a Carbon Capture and Storage (CCS) unit and a Humidified gas turbine (HXGT) cycle. The fully integrated model, Figure 3.2, has been developed using ASPEN PLUS software. The model is based on the Peng-Robinson equation of state. The process for each sub-model is provided in this section. Besides, a brief background for each sub-model is provided as well.

3.3.1 Initial and Final values

As shown in Table 3.2, the parameters of each sub-model are described by their initial and final values. The initial values had been adopted for the SMR, WGS, PSA, ASU, heat exchanged gas turbine and CCS sub-models from the references [119-125], respectively. The initial values have been used to generate the sensitivity results in chapter 5. Besides, the initial values have been used to validate each sub-model against those from the literature (further discussed in section 3.3.8). Meanwhile, the final values are those which are required to calibrate the model to produce the required CARSOXY molar fraction (blend 58, Table 3.1). The final values are also those which have been used to generate the techno-economic results (chapter 6). The initial values of the cycle parameters have been adjusted to the final values throughout multiple numerical attempts, section 5.2.1.

Table 3.2: Initial and final input values.

Parameter	Initial value	Final value
SMR sub-model		
Steam to Carbon mole ratio (S/C)	3.5	0.7
Steam mole flow rate [kmol/h]	60	23.527
Methane mole flow rate [kmol/h]	17.14	33.17
Feed streams Temperature [K]	293.15	293.15
Feed streams pressure [bar]	1	1
LPPUMP and LPCOMP discharge pressure [bar]	1.5*	1.5
HPCOMP _{H2O} and HPCOMP _{PCH4} discharge pressure [bar]	6*	6
SMR to FURNACE Mass split ratio in CH4SPLIT	12.2:1*	4.23:1
SMR reactor temperature [k]	1073	1073
Air to fuel mass ratio of the FURNACE	17.19:1	5.5:1

Table 3.2 continues

Parameter	Initial value	Final value
WGS sub-model		
Water mole flow (WGS _{H2O}) [kmol/h]	17.14	32
WGS _{H2O} pressure [bar]	10	10
WGS _{H2O} temperature [K]	573	573
HTWGS to LTWGS steam mass Split ratio in B4	9:1	9:1
HTWGS temperature [K]	400	400
LTWGS temperature [K]	200	200
S2 temperature [K]	573*	573
PSA sub-model		
B21 and B2 Hydrogen purity [%]	99.99	99.99
B21 and B2 Hydrogen recovery [%]	90	90
ASU sub-model		
BOOSTER discharge pressure [bar]	121.59	76
ATMIR mole flow rate [kmol/h]	5321.4	2642.38
AIRHP1 to AIRHP2 Mass split ratio in ASUSP	1:2.2	1:2.2
AIRLP mole flow rate [kmol/h]	727.5	341.69
N22 to N21 Mass split ratio in ASUSP	1:1	1:1
LPDC		
Number of stages	40	4
Distillate rate [Kmol/h]	4751	2352.7
Boil-up rate [kmol/h]	49392	24458.92
O ₂ N ₂ COLD and N ₂ O ₂ COLD feed stage	2	2
O ₂ ARHOT feed stage	8	2
ARO ₂ RECT product stage1	10	23
N ₂ LPDC product stage	1	1
O ₂ LPDC product stage	40	42
HPDC		
Number of stages	26	26
Reflux ratio	0.5459	0.5459
Boil-up ratio	1.0279	1.0279
AIRTROUT feed stage	1	1
AIRHP ₂ CO feed stage	2	2
AIRLPCO feed stage	3	3
N ₂ O ₂ and O ₂ N ₂ product stage	1	1
Heat exchanged gas turbine sub-model		
Parameters	Specified in Table 3.3	
CCS sub-model		
CO ₂ capture efficiency [%]	80	80

(Note: stages are numbered from the top-down) (The initial input values had been adopted for the SMR, WGS, PSA, ASU, heat exchanged gas turbine and CCS sub-models from the references [119-125] (Note: Some sub-models contain features which are not in the references .The initial values of these features are marked by the (*) symbol.)

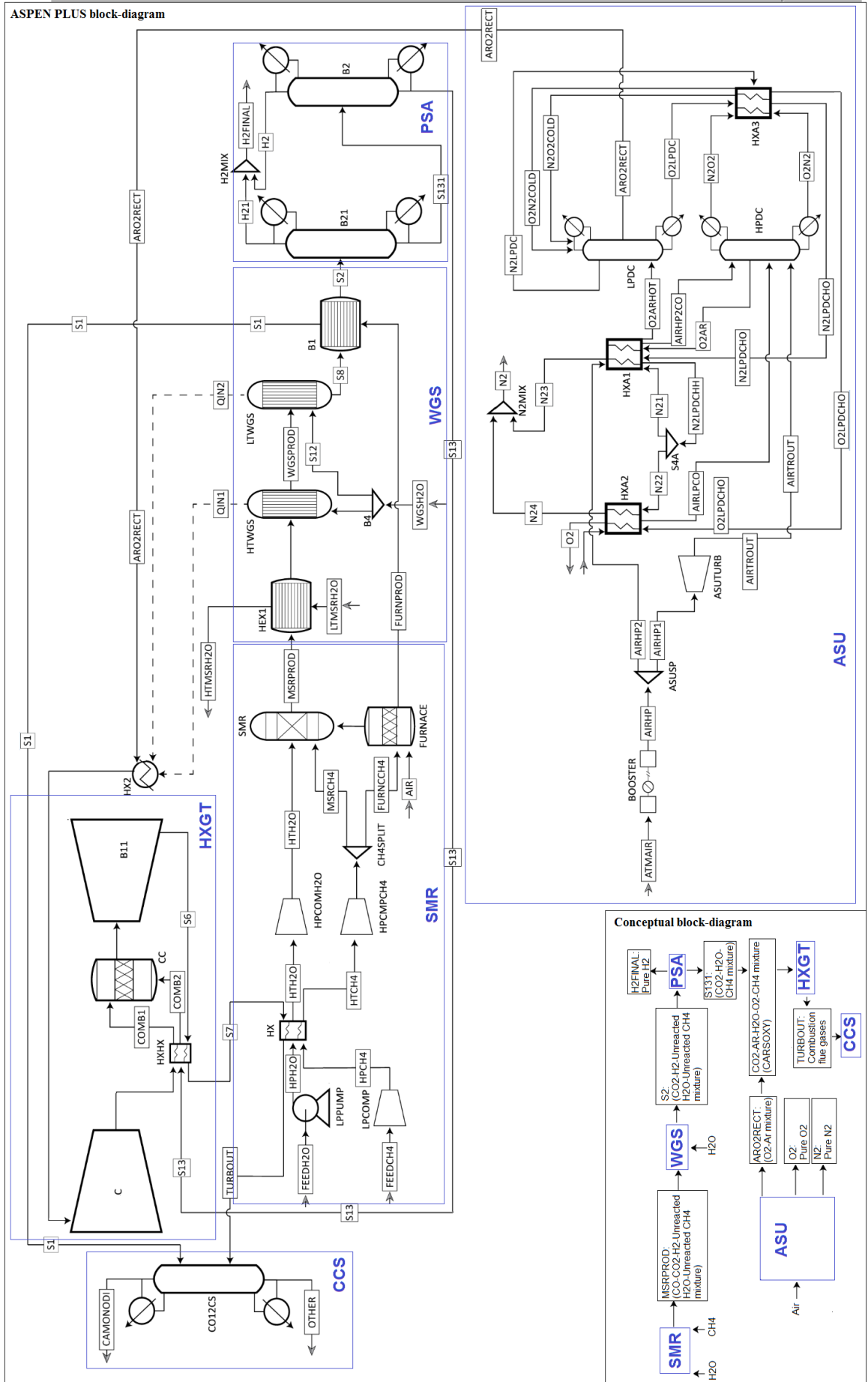
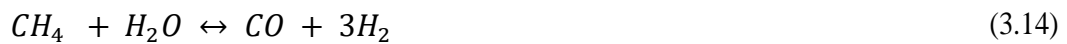


Figure 3.2 ASU-SMR-WGS-PSA-CCS-HXGT model

3.3.2 Steam-Methane Reforming (SMR) modelling

SMR is one of the fully developed technologies used to produce hydrogen [96]. Light hydrocarbon fuels such as methane (CH₄) react with steam to be converted into hydrogen as the main product, carbon monoxide, and carbon dioxide as by-products. In the reforming process, two endothermic reactions take place. Equation (3.14) requires 206 kJ to react to one mole of methane with one mole of steam. This produces hydrogen and a by-product carbon monoxide. Water-gas shift (WGS) reactors utilize steam to convert the by-product carbon monoxide to hydrogen and carbon dioxide [111]. Equation (3.15) requires no WGS as it directly produces hydrogen and carbon dioxide. It consumes 165 kJ and produces hydrogen and carbon dioxide [112].



As shown in Figure 3.2, the SMR process starts by feeding water and methane to the sub-model by the water (FEEDH₂O) and methane (FEEDCH₄) streams. Table 3.2 shows the values of these streams. The water stream is partially compressed to 1.5 bar by the (LPPUMP) pump. Similarly, the methane stream is compressed by the (LPCOMP) compressor. LPCOMP is an isentropic compressor model which has an isentropic efficiency of 85%. Both streams are then heated up in the heat exchanger (HX) by the flue gases of the gas turbine. The final compression stage for water is provided by the (HPCOMP_{H₂O}) compressor and by (HPCOMP_{CH₄}) compressor for methane. Both compressors increase the pressures to 15 bars. Water at this stage is fully converted to steam. The outlet of the methane compressor (HPCOMP_{H₂O}) is split into the (MSRCH₄) and (FURN_{CH₄}) streams to feed the SMR reactor and a furnace, respectively. The (CH₄SPLIT) splitter provides the SMR reactor with 80.8% of the original methane feed. This split ratio (80.85%) allows the SMR reactor to operate at the recommended steam to carbon ratio (S/C=3.5) [120]. The furnace has been modelled using an RSTOIC reactor to simulate stoichiometric combustion of methane with air. The furnace provides the SMR reactor with the required heat to conduct the reforming process via the (QIN) heat stream.

3.3.3 Water Gas Shifting (WGS) Modelling

Water-gas shifting of one mole of carbon monoxide produces approximately 40 KJ. The reaction is typically accelerated by two types of catalysts (namely iron-based and copper-based) [113]. Whenever carbon monoxide is an unwanted by-product gas, water-gas shifting is a scope of interest. It is a very reliable way to purify produced hydrogen via steam reforming of a hydrocarbon fuel such as methane [113]. Removing CO and producing hydrogen, i.e. Equation (3.16), is typically conducted into two stages. These are through high-temperature and low-temperature reactors.



The products of the SMR reactor are cooled down in the (HEX1) heat exchanger before the water gas shift, Figure 3.2. The cooling down process is conducted against the (LTMSRH2O) water stream. The (WGS2O) water stream is used to feed the WGS reactors. The stream is split into the (S9) and (S12) streams to feed the high-temperature water gas shift reactor (HTWGS) and the low-temperature water-gas shift (LTWGS) reactor with a split ratio of 9:1, respectively. Both water gas shift reactors are modelled using (STOIC) reactors to simulate WGS, which are specified in the Equation (3.16). The reactors are connected in series and their final product (S8) is warmed up again in the (B1) heat exchanger using the furnace flue gases. The products exit the heat exchanger. Since both reactors perform exothermic reactions, the heat streams (QIN1) and (QIN2) from the reactors are utilized to heat (AR2RECT) stream. The latter provides the required argon and oxygen supply to the gas turbine unit.

3.3.4 Water Pressure Swing Adsorption (PSA) Modeling

Hydrogen can be separated from a mixture by cryogenic distillation, PSA, or a hybrid combination of the two methods. However, the typical process which is followed in the industry to separate H₂ from the WGS products is PSA. References [114-116] indicate that PSA is insensitive to the changes in molar fractions of the feed stream or to its boundary conditions (i.e. temperature or pressure), where 90% of the Hydrogen is recovered with a 99.99% purity. A detailed description of the process is available somewhere else [115]. The WGS product (S2) has a high hydrogen content. The (H21) stream carries the separated Hydrogen. Stream (S131) carries the remaining contents of the WGS process (i.e. mainly steam, methane and Carbon dioxide). However, stream (S131) still has a relatively high molar fraction of Hydrogen. The (B2) separator further separates the remaining hydrogen coming in the stream (S131), which is then mixed with stream (H21) in (H2MIX). The (S13) stream at this stage carries only steam, methane and carbon dioxide with minor residuals of carbon monoxides. The stream (S13) provides the H₂O-CH₄-CO₂ supply to the CARSOXY turbine unit.

3.3.5 Air Separation Unit (ASU) Modeling

Cryogenic distillation is a more proper choice for CARSOXY gas turbines since it is capable of separating a ternary mixture into its individual components (as discussed in Chapter 2). Air can be separated into Nitrogen, Oxygen, and Argon, with the last two being components of CARSOXY, which can be obtained at once within the same cryogenic distillation unit [116-118].

Figure 3.2 shows the ASU sub-model. It has been modelled using reference [90] as a baseline design. The process starts by compressing the atmospheric air stream (ATMAR) by the isentropic booster. The compressed air is split into the (AIRHP1) and the (AIRHP2) streams. The (AIRHP1) air stream is then fed to the (ASUTRUB) isentropic turbine to expand the air stream before it is finally delivered to the high-pressure distillation column (HPDC) by the (AIRTROUT) stream. The (AIRHP2) stream is cooled down in the (HXA1) against the ASU products in the (N21), (N2LPDCHO) and (O2LPDCHO) streams. The (AIRHP2) stream leaves the (HXA1) heat exchanger as (AIRHP2CO) stream and is fed to the high-pressure distillation column (HPDC). Another atmospheric air stream is also fed to the ASU through the (HXA2) stream. The latter is cooled down against the ASU products in the (N22) and (O2LPDCHO) streams. The flow leaves the heat exchanger as (AIRLPCO) stream and is fed to the high-pressure distillation column (HPDC). The (AIRTROUT), (AIRHP2CO) and (AIRLPCO) streams are therefore at three different pressure levels (all above ambient pressure). As a result, these are fed to the high-pressure distillation column (HPDC) at three different stages. Both the (HPDC) and the (LPDC) are modelled using the ASPEN PLUS RADFRAC model block. The (N2O2) stream and the (O2N2) stream have high molar fractions of nitrogen and oxygen, respectively. Both streams are cooled down in the (HXA3) heat exchanger against the products of the distillation column (LPDC). Only pure oxygen exists in the (O2LPDC) stream, while pure nitrogen is only present in the (N2O2COLD) stream. Stream (ARO2RECT) contains argon and oxygen molecules.

It must be highlighted that the doped process is the baseline process (both are described above). However, the baseline process typically separates the (ARO2RECT) stream into argon and oxygen. In the case of CARSOXY, a well-mixed mixture of oxygen and argon is required and separating oxygen and argon into two different streams is not necessary and thus have been eliminated.

The baseline process parameters have also been re-calibrated from their initial values to the final values (Table 3.2) to provide the required argon and oxygen (Blend 58, Table 3.1) for the CARSOXY turbine unit. The initial values of the ASU parameters have been adjusted to the final values throughout multiple numerical attempts, section 5.2.1.

3.3.6 Carbon Capture and Storage (CCS) Modeling

The CCS unit which is used in the model is a post-combustion unit. This technique removes the Carbon dioxide from the combustion products requiring no major changes to the combustion practice. The process can be easily integrated to currently used power plants in the market [82]. However, this technique incurs in an unsatisfying 70% increase in the electricity bill in most applications [83].

As shown in Figure 3.2 and detailed in Table 3.2, the (CO12CS) is a (SEP2) ASPEN PLUS block model, which captures the produced carbon dioxide and carbon monoxide from the (B11) turbine flue gases. These follow the (S6)-(S7)-(TURBOUT) route to be then captured by the (CO12CS) block. Also, flue gases from the furnace in the SMR unit are captured by (CO12CS) block. These follow the (FURNPROD)-(S1) route.

3.3.7 Heat Exchanged Gas Turbine (HXGT) Cycle Modeling

As discussed in section 3.1, the heat exchanged cycle has been superior among the other cycles (simple cycle, free turbine & simple cycle, evaporative cycle and humidified gas turbine cycle). Therefore, this cycle has been chosen to be adopted to the ASPEN PLUS model. It has been modelled within the assumptions used for the previous work (section 3.2.1) to ensure a consistent approach. As discussed in section 3.2.1, the parametric results have been plotted for a range of operating conditions with respect to the cycle efficiency. The ultimate condition has been identified (section 4) and based on that the HXGT has been modelled. The results from the parametric study (chapter 4) have also shown that dry compression would increase the efficiency more than wet compression. Dry compression refers to the injection of steam to the Carbon dioxide-Argon mixture post the compressor. Therefore, as shown in Figure 3.2, the compressor (C) is fed by the Oxygen-Argon stream (ARO2RECT) instead of a carbon dioxide-argon stream as recommended by the parametric study in chapter 4. An RSTOIC reactor has been used to model the combustion chamber (CC), the compressor (C), the turbine (B11) and the heat exchanger (HXHX) by using their ASPEN-PLUS defined blocks. Table 3.3 concludes the final parameters which have been used to model the HXGT cycle.

Table 3.3 HXGT Parameters.

HXGT Parameters	
Equivalence ratio	1
Turbine Inlet temperature [K]	1900
HX effectiveness	0.8
Compression isentropic efficiency	0.85
Compression pressure ratio	7
Turbine discharge pressure [bar]	2

Expansion isentropic efficiency	0.87
Mechanical efficiency	0.99
Combustion efficiency	0.98
Pressure losses with respect to the stage inlet	
Combustion chamber	0.02
HX cold side	0.03
HX hot side	0.04
Exhaust	0.3

3.3.8 Model Convergence

As illustrated in section 3.3.1, this section discusses the validation of each sub-model of the ASU-SMR-WGS-PSA-CCS-HXGT model (or the CAROXY model). The ASU-SMR-WGS-PSA-CCS-HXGT model is not required to produce the “conventional” molar fractions (i.e. Argon and Oxygen with high purity from the ASU, or high concentrations of Hydrogen from the SMR-WGS-PSA sub-models). Instead, the CARSOXY model produces the required ‘CARSOXY’ molar fraction (i.e. Argon and Oxygen from the ASU and CO₂ from the SMR-WGS-PSA sub-models within the specified CARSOXY molar fractions (Table 3.1, blend 58)). Therefore, the final parameters of each sub-model have diverged for their “conventional” values based on the recommendation from the sensitivity analyses (chapter 5). This essentially means that validation against the literature using the final values (or the calibrated values) is not feasible at this stage of the study. Alternatively, the convergence of the calibrated CARSOXY model (with the final values) is provided in Table 3.4. It is well-known for ASPEN PLUS users that the software typically does not generate results unless the solution converges and complies with thermodynamic and chemical laws. However, to add more certainty, the convergence results had been marked as positive for all streams and blocks. Table 3.4 shows the total convergence results and the total mass balance of the main blocks and the entire model.

Table 3.4 Convergence results.

The relative difference between the inlet and outlet mass flows (Rel.Diff)			
Model/block	Mass Rel.Diff	Model/block	Mass Rel.Diff
Entire model	0.200831E-07	B2	0
SMR	3.06110493E-15	LPDC	4.44654277E-08
Furnace	0.2572E-11	HPDC	4.49540319E-10
HTWGS	3.31185307E-16	CC	0
LTWGS	0	CO12CS	0
B21	1.589198E-16	BOOSTER	0
Convergence tolerance			
0.2572E-11			

To conclude this point, CARSOXY model (with the calibrated parameters) is not an optimization approach, which produces “conventional” products i.e. with higher efficiency or a lower heat duty. It is a novel approach which produces “unconventional” products (CARSOXY molar fractions (Table 3.1, blend 58). The convergence results confirm that the model complies with the theoretical thermodynamic and chemical law. Nevertheless, developing a prototype as a future work would provide valuable data to address concerns of practical application (i.e. coke forming in the SMR unit, efficiency decaying, etc.)

3.4 The methodology of assessing CARSOXY techno-economic

The previous models have demonstrated to produce CH₄, CO₂, H₂O, Ar and O₂ within the required CARSOXY molar fractions, (results in chapter 5 and methodology in section 3.3). Yet the system must prove its economic sustainability to be adopted by industry. A comparison between the CARSOXY and the Air-driven cycles have been performed in this thesis. Both cycles have been modelled using the same modelling technique under the same conditions. The economic sustainability of the CARSOXY gas turbine is judged against standard indicators and evaluators. Table 3.5 defines each evaluator.

Table 3.5 Economic evaluators

Evaluator	Description	Reference
Net Present Value (NPV)	The anticipated current value of the difference between cash inflows and outflows over a future period. If this indicator is positive, then the project is profitable.	[123]
Discounted payout period (DPP)	The period which is required to pay for all the costs included in the project. Thus, the shorter this period the more effective the investment is.	[124]
Profitability Index (PI)	It is the ratio of the present value of the accumulative income (PVI) to the present value of the accumulative outcomes (PVO). If this ratio is greater than one, then the project is profitable.	[124]
Internal rate of return (IRR)	The essential discount rate which zeros the NPV.	[124]
Modified Internal rate of return (MIRR)	A modified version of the IRR which allows a comparison between projects with different sizes. It measures the attractiveness of a project.	[125]
The net rate of return (NRR)	The ratio of the net present value (NPV) to the present value of the cash outflows (PVO) of the last period of a project.	[125]
Engineering, Procurement and Construction (EPC).	This set of processes ensures that the project is at a satisfying level to be handed over to the final owner.	[125]
Start-up period	It specifies the required period to transfer a project into a mature state, in which it meets the market needs. The start-up period converts the project into a scalable business, based on the market demand.	[125]
Capital Cost	It is a one-time expense which is required to bring a project to its operating condition. In other words, it is the expense which	[127]

	covers the EPC period. It is a threshold expense which an investor shall provide.	
Operation Cost	The cost which is paid continuously is referred to as the Total operating cost. It covers all the necessary expenses to maintain the operability of the project. It also covers maintenance and administrative costs daily	[128]

3.4.1 Techno-economic Setup of the CARSOXY model

It is important to highlight that the ASU-SMR-WGS-PSA-CCS-HXGT (or CARSOXY) model (Figure 3.2) is functional in any required capacity provided that the ratios in Table 3.6 are retained. Table 3.6 provides mole flow rates for 1 kmol/h of Methane to produce the required molar fractions of CARSOXY (blend 58, Table 3.1). To assess the techno-economic of the model, it has been modelled such that it consumes 1241[kg/h] of CH₄ (by the FEEDCH₄) and the parameters in Table 3.6 have been updated in the model according to their ratios to methane flow rate. The total mass flow rate of all inlet streams is 441731 [kg/h]. Those specific flow rates are the results of the calibration process (as discussed in section 3.1), where the initial values of the parameters (which are obtained from the literature[119-125]) changed to the final values (Table 3.2) to provide the required argon and oxygen (Blend 58, Table 3.1) for the CARSOXY turbine unit. This has been achieved throughout multiple numerical attempts, section 5.2.1.

Table 3.6: ASU-SMR-WGS-PSA-CCS-HXGT mole flow rates for 1 kmol/h of Methane

Feed Stream	Mole flow Rate [kmol/h]	Product Stream	Mole flow Rate [kmol/h]	LPDC rates	Mole flow Rate [kmol/h]
FEEDCH ₄	1	N ₂	70.93	distillate	70.93
FEEDH ₂ O	0.71	O ₂	17.6		
AIR	0.53	H ₂	2.06		
WGS _H 2O	0.96	S13	1.47	boil-up rate	737.38
ATMIR	79.66	ARO2RECT	1.47		
AIRLP	10.3				

(Note: Rounded for two decimal places)

3.4.2 Techno-economic Setup of an Air-driven HXGT model

To obtain comparable results, an Air-driven-heat-exchanged cycle has been modelled, Figure 3.3. The cycle is provided with air such that the combustion chamber (CCAIR) performs stoichiometric combustion using the same amount of fuel as the CARSOXY model, 1240.8 [kg/h] of CH₄. Both methane and air compressors (CH₄AIR and CAIR, respectively) provide discharge pressures of 10 bar to match the same inlet pressures of the heat exchanger (HXHX) in the CARSOXY model. The heat exchanger (AIRX) transfers heat from the hot side to the cold sides up to the crossover limit (cold sides' outlet

temperatures approach but do not exceed the hot-side inlet temperature). This condition has been considered for the CARSOXY model. The same combustion chamber block as the CARSOXY model has been used. Such that the combustion outlet temperature and pressure are 1900K and 9.95 bar, respectively. Similarly, the turbine (TAIR) has a pressure ratio of 0.1366 to match the performance of the turbine in the CARSOXY model. Same efficiencies as the CARSOXY have been used. Table rev3.7 describes the components of the Air-driven-heat-exchanged cycle.

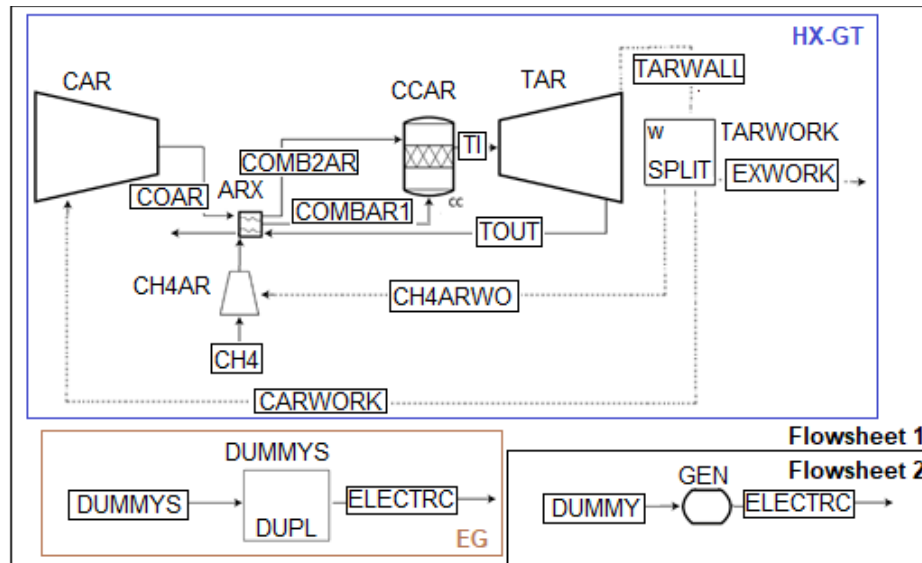


Figure 3.3 Air-driven HX-GT sub-models.

3.4.3 Electricity generation and consumption modelling for the Air-driven gas turbine

As shown in Figure 3.3, a dummy work splitter (TARWORK) has been used to split the work generated by the (TAR) turbine into 3 portions. The first two work portions are those provided to the (CH4AR) methane compressor and the (CAR) air compressor. Excess work is assumed to be used to generate electricity by an ideal electricity generator. The generated electricity is added to the economic analysis as a profit source. This can be added to an ASPEN PLUS model by assigning a price to a material product stream, unbroken streams in Figure 3.3. Prices cannot be assigned to a work product stream, Figure 3.3. The (GEN) block is an ideal block, which operates using electrical work. The block was set to operate using the same amount of excess work generated by the (TAIR) turbine in a separate flowsheet. Thus, the electricity utility of the (GEN) block reflects the same amount of the electricity which would have been generated by the (TAIR) turbine, provided that an ideal generator has been used. After running the model in Figure 3.3-flowsheet 2, the utility cost (which is equal to the produced electricity by the TAIR) has been obtained. The (GEN) block in flowsheet 2 was fed with the (DUMMY) zero-cost value stream. The (ELECTRC) product stream of the block is a (material) product stream. The price of the stream has

been chosen such that it matches exactly the utility cost (which is equal to the produced electricity by the TAR). Both the (DUMMY) and the (ELECTRIC) stream have been transferred to the actual model (flowsheet 1) to include the electricity profits in the economic analysis. Table 3.7 describes the components of the Air-driven-heat-exchanged cycle.

Table 3.7: description of the components of the Air-driven-heat-exchanged cycle.

Name	Description
CAR	Air compressor
ARX	A heat exchanger (between combustion inlets and turbine flue gases)
CCAR	Combustion chamber
TAR	Turbine
TARWORK	Dummy work splitter
CH4AR	Methane compressor
DUMMYS	Dummy block (zero cost, zero energy consumption and production)
GEN	Ideal block (provides a price for the generated power by the Air-driven-heat-exchanged cycle)

As discussed in section 3.4.2, all blocks are modelled under the same assumptions and working conditions of the heat exchanged gas turbine unit, which are available in Table 3.3.

3.4.4 Electricity generation and consumption modelling for the CARSOXY cycle

To assess the techno-economic of the CARSOXY model, electricity generation and consumption have to be included in the CARSOXY model. Therefore, the CARSOXY model in Figure 3.2 has been updated accordingly as shown in Figure 3.4. Electricity generation and consumption of the CARSOXY model has been modelled using the same technique which has been adopted to the Air-driven gas turbine model. As shown in Figure 3.4, the work Generated by the (B11) turbine is added to the work generated by the (ASUTRBI) turbine through a dummy summation block. Then, the total work is split into six portions to supply the necessary work to the (C) compressor, the (LPPUMP) pump, the (LPCOMP) compressor, the (HPCOMH2O) compressor, the (HPCMPCH4) compressor, and the excess work. The same modelling technique which is used for the Air-driven gas turbine has been used to include electricity consumption and generation in the economic analysis for the CARSOXY cycle.

3.4.5 Techno-economic Assumptions

The techno-economic analyses of this thesis have been conducted using the ASPEN PLUS software. It has been conducted using version 9, which has been issued in 2016. Therefore, the 2016 year has been assumed to be the start of basic engineering of the project. Analyses have been performed assuming that the United Kingdom is the location of the plant, thus the 2016 Sterling Pound has been used for these analyses. The operation life of the cycle has been chosen to be 20 years with a 1 year of a startup period.

Moreover, Table 3.8 provides the set of assumptions which has been used in the ASPEN PLUS software to perform the techno-economic analyses.

3.4.6 Raw material and products pricing

CARSOXY production involves four material products. These are nitrogen, carbon dioxide, oxygen and hydrogen. The process also involves three raw materials. These are air, water, and methane. Air is supplied to the process at the atmospheric condition, thus its price has been assumed to be zero. Prices have been obtained from the literature. However, these must be escalated from the literature published dates to the start date of the basic engineering of the project (2016). The escalation has been performed using the Chemical Engineering Plant Cost Index (CEPCI) and Equation (3.6). Moreover, prices with different currencies have been converted to the 2016 Sterling Pound. Tables 3.9 and 3.110 provides the archived and updated CEPCIs and prices.

$$C_{\text{updated}} = \left(\frac{\text{CEPCI}_{\text{updated}}}{\text{CEPCI}_{\text{Archived}}} \right) C_{\text{Archived}} \quad (3.16)$$

Table 3.8 techno-economic assumptions

Economic Analysis Assumptions (provided by Aspen Plus)		
Assumption	Unit (Period= One year)	Value
Number of Weeks per Period	Weeks/period	52
Number of Periods for Analysis	Period	20
Working Capital Percentage	Percent/period	5
Operating Charges	Percent/period	25
Plant Overhead	Percent/period	50
ROR Annuity Factor	--	5
Tax Rate	Percent/period	40
Interest Factor	--	1.2
Economic Life of Project	Period	20
Salvage Value (Percent of Initial Capital Cost)	Percent	20
Project Capital Escalation	Percent/period	5
Products Escalation	Percent/period	5
Raw Material Escalation	Percent/period	3.5
Operating and Maintenance Labor Escalation	Percent/period	3
Utility Escalation	Percent/period	3
Start Period for Plant Startup	Period	1
Desired Return on Project for Sales Forecasting	Percent/Period	10.5
End Period for Economic Life of Project	Period	20
General and Administrative Expenses	Percent/Period	8
Desired Rate of Return/Interest Rate	Percent/period	20
Electricity price [118]	£/KWh	0.1145

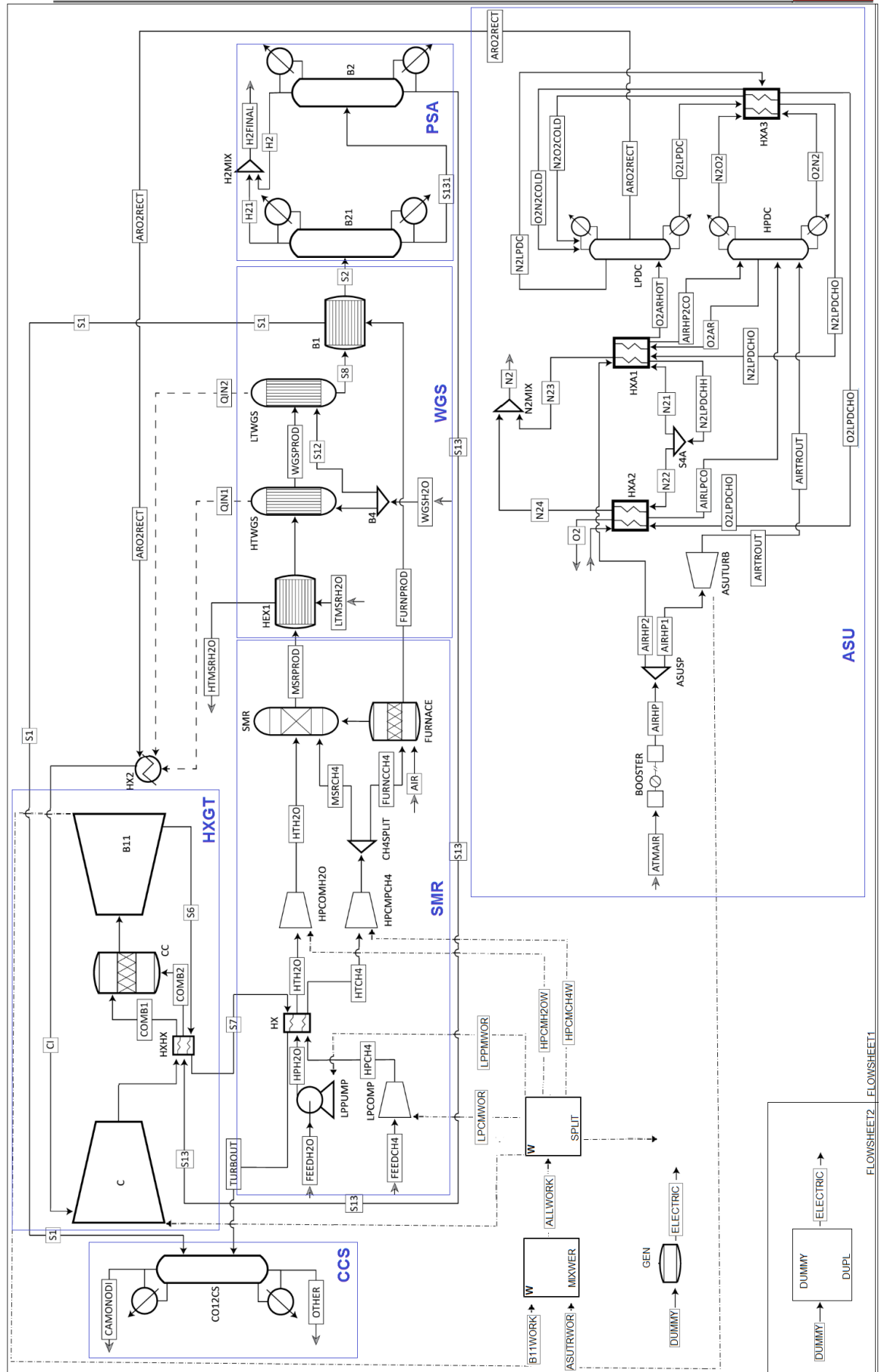


Figure 3.4 ASU-SMR-WGS-PSA-CCS-HXGT model, updated with electricity generation.

Table 3.9 Raw materials prices (€)

Material	Raw material			
		CH ₄	H ₂ O	Air
Archived	€	0.097 [\$/kg]	1.5388 [€/m ³]	zero
	€ Reference and year	Referenced in 2016[130]	Referenced in 2018[131]	
	CEPCI	541.7	567.5	
	CEPCI reference	[132]	[133]	
Updated	Year	2016	2016	
	CEPCI	541.7	541.7	
	CEPCI reference	[133]	[133]	
	€	0.7	1.4588	
Currency change	Exchange rate	1[2016 £] = 1.3346[US\$]	1[2016 £] = 1.3346[US\$]	
	Exchange rate reference	Reference:[134] based on the average exchange rate in the middle of the year (30/June/2016).		
€ [2016 US\$]		0.097 \$/kg	1.96 \$/m ³	0
€ [2016 £]		0.0729 £/kg	1.468605 £/m ³	0

Table 3.10 Products prices (€), the purity and other properties of the components are available in the references [134-136].

Material	Product material				
		Nitrogen	Carbon dioxide	Oxygen	Hydrogen
Archived		14.9 \$/tN ₂	70 \$/tCO ₂	1.3346 \$/kgO ₂	1.49 [USD/Kg]
	€ Reference and year	Referenced in 2011[134]	Referenced in 2000 [135]	Referenced in 2016 [134]	Referenced in 2010 [136]
	CEPCI	585.7	394.1	---	550.8
	CEPCI reference	[132]	[132]	--	[133]
Updated	Year	2016	2016	---	2016
	CEPCI	541.7	541.7	---	541.7
	CEPCI reference	[133]	[133]	---	[133]
	€	13.78066	96.21669	---	1.465
Currency change	Exchange rate	1[2016 £] = 1.3346[US\$]	1[2016 £] = 1.3346[US\$]	1[2016 £] = 1.3346[US\$]	1[2016 £] = 1.3346[US\$]
	Exchange rate reference	Reference: [134]based on the average exchange rate in the middle of the year (30/June/2016).			
€ [2016 US\$]		13.78066 \$/tN ₂	96.21669 \$/ tCO ₂	1.3346 \$/kgO ₂	1.465 \$/kg H ₂
€ [2016 £]		11 £/tN ₂	72.09403 £/tCO ₂	1 £/kg	1.4386 £/kg

3.4.7 Equipment Pricing

The ASPEN PLUS software provides the prices of the used pieces of equipment in the process based on a built-in database. However, some pieces of equipment operate within specifications which are out of the database range. Therefore, quotations must be provided using cost functions for these pieces of equipment. Table 3.11 shows the pieces of equipment which are not included in the database. The remaining pieces of equipment are priced based on the database of the Aspen plus software, Table 3.18.

Table 3.11 Quoted pieces of equipment

CARSOXY- driven Gas turbine			Air-driven Gas turbine
B1	HPCMPCH4	HX2	ARX
B11	HPCOMH2O	Mixers	CH4AR
HX	FURNACE	MSR	CAR
LTWGS and HTWGS	HXHX	HEX1	CCAR
splitters	CC	C	TAR

Equation (3.17) [136] has been used for all heat exchangers in Table 3.11. Based on the reference [136], the material cost factor (f) depends on the metal type and its maximum allowable temperature (T_{max}), Table 3.12. These have been chosen according to the operation conditions of each heat exchanger. The purchased capital cost Ξ_{REC} is a function of $P_{in,REC}^{cold}$, $\dot{m}_{in,REC}^{cold}$, ΔP , r_1 , ε and T_{max} . These parameters are based on operation conditions. Therefore, these are obtained from the ASPEN PLUS model and shown in Tables 3.13. Equation (3.17) provides capital costs in €_{2002} . However, these have to be escalated to 2016 € . This is performed by using Equation (3.16), provided that $CEPCI_{2002}$, $CEPCI_{2016}$ and the $\text{€}/\text{€}_{2016}$ exchange rate are given in Table 3.13

$$\Xi = r_1 \times \dot{m}_{in,REC}^{cold} \times P_{in,REC}^{cold} \times (\Delta P^{-0.5}) \times \frac{\varepsilon}{1-\varepsilon} \times f \quad (3.17)$$

Table 3.12 Heat exchangers material Cost factor vs. Maximum metal temperature[136]

Material	347 stainless steel	Super 347 stainless steel	Inconel 625	Haynes 230	Haynes 214
f	1	1.5	5	7	9
T_{max} [$^{\circ}\text{C}$]	675	750	800	850	900

Table 3.13. HX, HX2, B1, HXHX and AIRX operation conditions and E

CARSOXY Gas turbine							
Heat exchanger	HX		HEX1	HX2	B1	HXHX	
Inlet cold streams	HPCH4	HPH2O	LTMSRH2O	ARO2RECT	S8	S13	CO
$\dot{m}_{in,REC}^{cold}$ [kg/s]	0.34463	0.27444	65.35942	1.142332	0.92664	0.81611	1.1
T_{max} [OC]	560		895	400	800	898	
f	1		9	1	5	9	
r_1 [€, 2002]	625.1[136]						
$p_{in,REC}^{cold}$ [bar]	15	1.5	1	1.445	10	9.97	9.97
ΔP	0.03		0.03	0.03	0.03	0.03	
ε	0.8		0.8	0.8	0.8	0.8	
E €, 2002	120856		1326546	247361	618404	3805767	
CEPCI,2002	395.6 [137]						
CEPCI,2016	541.7 [133]						
E €,2016	165489.9		1816455	338715.5	846789	5211284	
Exchange rate	1[2016 sterling pound] = 1.203[2016 €] Reference: [136] based on the average exchange rate in the middle of the year (30/June/2016).						
E £,2016	137564.3		1509938	281559	703898	4331907	
Air-driven Gas turbine							
Heat exchanger	ARX						
Inlet cold streams	COAIR			CH ₄			
$\dot{m}_{in,REC}^{cold}$ [kg/s]	13.87			0.79			
T_{max} [OC]	1063.156						
f	1						
r_1 [€, 2002]	625.1[136]						
$p_{in,REC}^{cold}$ [bar]	10			10			
ΔP	0.03						
ε	0.8						
E €, 2002	1363682						
CEPCI,2002	395.6 [136]						
CEPCI,2016	541.7 [133]						
E €,2016	1867306						
Exchange rate	1[2016 sterling pound] = 1.203[2016 €] Reference: [138] based on the average exchange rate in the middle of the year (30/June/2016).						
E £,2016	1552208						

The capital costs of the high-temperature water-gas-shift reactor (HTWGS), the low-temperature water-

gas-shift reactor (LTWGS), the steam- methane reformer (SMR) and the Furnace are estimated using Equations (3.18-3.19). Calculations are based on DeCicco's and Ward's method [139-140]. It was originally driven by Zevnik's and Buchanan's method [141]. This method is a function of the material factor, temperature and pressure graph-based factors. References [139-140] replaced the graph-based factors by mathematically calculated factors, which are shown in Table 3.14. Equation (3.18) provides capital costs in €₂₀₀₂. However, these have to be escalated to 2016 £. This is performed by using Equation (3.16), provided that CEPCI₁₉₉₂ and CEPCI₂₀₁₆.

$$C_{DW}^{\wedge} = k_{DW}^{\wedge} \times \dot{N} \times Q^{\dot{0}.6} \times 10^{(F_T + F_P^{\wedge} + F_m^{\wedge})} \tag{3.18}$$

$$\dot{Q} = \dot{m}_p \times \frac{n_H \times n_D}{24 \times 7 \times 10^3} \times 4 \times 12 \tag{3.19}$$

Table 3.14 DeCicco's and Ward's cost factors [139-140]

\hat{F}_T : temperature Factor		
If $T_{max} > 300K$	If $T_{max} = 300K$	If $T_{max} < 300K$
$F_T = 1.8 \times 10^{-4} \times (T_{max} - 300)$	$F_T = 1$	$F_T = 0.57 - (1.9 \times 10^{-2} - T_{min})$
\hat{F}_P : temperature Factor		
If $P_{max} > 1atm$	If $P_{max} = 1atm$	If $P_{max} < 1atm$
$\hat{F}_P = 0.1 \times \log(p_{MAX})$	$\hat{F}_P = 1$	$\hat{F}_P = 0.1 \times \log(\frac{1}{p_{MAX}})$
\hat{F}_m : material Factor		
If $T_{MAX} < 1783 K$		
$\hat{F}_m = 0$		
K constant		
if $Q \leq 4464$ tons per year	$Q > 4464$ tons per year	
$k_{DW}^{\wedge} = 6270$	$k_{DW}^{\wedge} = 4400$	

T_{MAX}, p_{MAX} and \dot{m}_p have been provided from the ASPEN PLUS model and summarized in Table 3.15. n_H and n_D are assumed to be 8 hours/day and 5 days/week, respectively. Table 3.15 also illustrates the calculated capital costs of the SMR the HTWGS, LTWGS and the Furnace

Table 3.15. SMR the HTWGS, LTWGS and the Furnace operation conditions and C_{DW}^{\wedge}

Equipment	MSR	HTWGS	LTWGS	Furnace
T _{MAX} [K]	1175.93	673.15	473.15	1073.15
\hat{F}_T	0.157667	0.067167	0.031167	0.139167
p _{MAX} [atm]	14.80	9.87	9.87	14.80
\hat{F}_P	0.117026	0.099432	0.099432	0.117026
\hat{F}_m	0	0	0	0
\dot{m}_p [kg/h]	1991.795	3201.749	3336.152	1543.396
\dot{Q} [tonne/ year.]	22.76337	36.59141	38.12639	17.63881
k _{DW}	6270	6270	6270	6270
\dot{N}	1	1	1	1
C _{DW} [£,1992]	76974	126428	75266.53	100309.6
CEPCI,1992	369 (By extrapolation) [137]			
CEPCI,2016	541.7 [133]			
C _{DW} [£,2016]	113000	185600	110492	147256.6

The capital costs of all mixers and splitters have been estimated using Equations (3.20-3.21). These are based on Klumpar's, Brown's and Fromme's Method [142]. The claimed accuracy of the method is 94% (i.e. the anticipated price is at least 94% of the actual price). This method can also provide the cost function for compressors, turbines and reactors [142]. The Cost function is a function of temperature and, pressure and material factors, Table 3.16 [142]. Equation (3.20) provides capital costs at \$₁₉₈₁. However, these have to be escalated to 2016 £. This is performed by using Equation (3.16), provided that CEPCI₁₉₈₁, CEPCI₂₀₁₆ and the £/\$₂₀₁₆ exchange rates are given in Table 3.17.

$$\hat{C}_{KBF} = \hat{K}_{KBF} \times \hat{F} \times \hat{N} \times \hat{G}^{\hat{V}} \quad [\$_{1981}] \quad (3.20)$$

$$\hat{F} = 2 \times 10^{(\hat{T} + \hat{P} + \hat{F}_m)} \quad (3.21)$$

Table 3.16. Klumpar's, Brown's and Fromme's cost factors and constants [142]

\hat{T}	
If the temperature (T) $\geq 25^\circ\text{C}$	If the temperature (T) $\geq 25^\circ\text{C}$
$\hat{T} = 1.8 \times 10^{-4} \times (T - 27)$	$\hat{T} = 2 \times 10^{-3} \times (27 - T)$
\hat{P}	
If (P) $\geq 1\text{atm}$	If (P) $\geq 1\text{atm}$
$\hat{P} = 0.1 \times \log(P)$	$\hat{P} = 0.1 \times \log(1/p)$
$\hat{F}_m = 0$	
If T _{MAX} < 1783 K	
$\hat{K}_{KBF} = 1.1 \times 10^2$	$\hat{V} = 0.57$

\hat{T} , \hat{P} and \hat{G} have been provided from the ASPEN PLUS model and summarized in Table 3.17. The calculated capital costs of all mixtures and splitters are also shown in Table 3.17.

Table 3.17. B4, H2MIX, N2MIX, CH4SPLIT, ASUSP, S5, and S4A operation conditions and \hat{C}_{KBF}

Equipment	B4	H2MIX	N2MIX	CH4SPLIT	ASUSP	S5	S4A
T	299	270.7	-192.61	606.75	20	-190	-192.62
\dot{T}	0.0489	0.0438	0.03953	0.04896	0.00126	0.03906	0.0395
p_{MAX} [atm]	0.98	9.87	1.4	14.8	120	6	1.4
\dot{P}	0.0008	0.099432	0.014613	0.117026	0.20791	0.07781	0.0146
\dot{P}_m	0	0	0	0	0	0	0
\dot{G} $\left[\frac{lbs}{h}\right]$	2963.8	11.79874	339343.4	2735.535	393460	305699	339343
\dot{F}	2.2431	2.781855	2.265545	2.931002	3.23748	2.61761	2.2655
\dot{k}_{KBF}	1.1×10^2						
\dot{N}	1						
\dot{C}_{KBF} [1981US\$]	570	20	768	502	7154	1849	768
CEPCI,1981	297 [137]						
CEPCI,2016	541.7 [133]						
\dot{C}_{KBF} [2016 US\$]	1041	37	1401	917	13050	3372	1401
Exchange rate	1[2016 sterling pound] = 1.3346[US\$] Reference [1138] based on the average exchange rate in the middle of the year (30/June/2016).						
\dot{C}_{KBF} [£,2016]	780	28	1050	687	9778	2527	1050

As discussed in section 3.4.5, the techno-economic analysis of this thesis has been conducted using the ASPEN PLUS software. It has been conducted using version 9, which has been issued in 2016. Therefore, the 2016 year has been assumed to be the start of basic engineering of the project.

Averaging Equation (3.20) with Equation (3.18) would add certainty to the anticipated capital costs. This approach has been used to estimate the capital cost of C, CC, B11, HPCOMPCH4 and HPCOMPH2O in the CARSOXY model. Similarly, it has been used for the compressors (CH4AIR and CAIR), the combustion chamber (CCAIR) and the turbine (TAIR) in the Air-driven model. Both equations have been escalated to 2016 using the ratios of CEPCI₂₀₁₆ to CEPCI₁₉₈₁ and CEPCI₁₉₉₂ for Equation (3.20) and Equation (3.18), respectively. Equation (3.20) has been converted to £₂₀₁₆ using the £/\$₂₀₁₆ exchange rate. CEPCI₂₀₁₆ and CEPCI₁₉₉₂ are provided in Table 3.18. While CEPCI₁₉₈₁ and £/\$₂₀₁₆ are provided in Table 3.17. Therefore, the averaged cost function can be written as shown in Equation (3.22). T, P, \dot{m}_p and \dot{G} have been provided from the ASPEN PLUS model and summarized in Table 3.18. The calculated capital costs are also shown in Table 3.18.

$$\dot{C}_{2016} = \frac{CEPCI_{2016}}{2} \left(\frac{[£/\$_{2016}] \times \dot{C}_{KBF}}{CEPCI_{1981}} + \frac{C_{DW}}{CEPCI_{1992}} \right) \quad (3.22)$$

Table 3.18. C, CC, B11, HPCOMPCH4, HPCOMPH2O, CH4AIR, CAIR, CCAIR

and TAIR operation conditions and \dot{C}_{2016}

CARSOXY- driven Gas turbine					
Model	C	CC	B11	HPCOMPCH4	HPCOMP20
T_{MAX} [K]	1341	2173	2173	879.9	1082.76
$\dot{F}_T = \dot{T}$	0.1873	0.33714	0.33714	0.104382	0.140897
p_{MAX} [atm]	9.87	9.81	9.81	14.8	14.8
$\dot{F}_P = \dot{P}$	0.0994	0.09916	0.09916	0.117026	0.117026
\dot{F}_m [30]	0	$\cong 0.2$	$\cong 0.2$	0	0
\dot{m}_p [kg/h]	4113.2	7128.21	7128.21	1240.7	988.2
G [lbs/h]	9067.7	15715.1	15715.1	2735.395	2178.803
\dot{Q} [$\frac{\text{tonne}}{\text{year}}$]	46.868	81.6118	81.61	14.22	11.19248
k_{DW}	6270				
\dot{k}_{KBF}	1.1×10^2				
N	1	1	1	1	1
\dot{F}	3.87	8.65	8.65	3.33	3.62
\dot{C}_{DW} [£,1992]	122286	380332	38033	51250.43	48632
\dot{C}_{KBF} [1981US\$]	76637	234455	234455	33294.4	31808.64
\dot{C} [£, 2016]	141252	436584	436581	60023.53	56700
Air-driven Gas turbine					
Model	CH4AR	CAR	CCAR	TAR	
T_{MAX} [K]	504.45	607.9	1900	1900	
$\dot{F}_T = \dot{T}$	0.036801	0.055422	0.288	0.288	
p_{MAX} [atm]	9.87	9.87	9.87	9.82	
$\dot{F}_P = \dot{P}$	0.099432	0.099432	0.09943	0.09921	
\dot{F}_m [30]	0	0	0	0	
\dot{m}_p [kg/h]	2893.256	49990.28	52883.5	52883.5	
G [lbs/h]	72.75112	1259.387	1332.371	1332.371	
\dot{Q} [$\frac{\text{tonne}}{\text{year}}$]	32.87791	571.2828	604.160	604.160	
k_{DW}	6270				
\dot{k}_{KBF}	1.1×10^2				
N	1	1	1	1	
\dot{F}	2735.55	47264.4	49999	49999	
\dot{C}_{DW} [£,1992]	42123	243017	429413	429195	
\dot{C}_{KBF} [1981US\$]	27401	145131	256016	255885	
\dot{C} [£, 2016]	45514.62	255683.3	451564	451335	

Table 3.19 ASPEN-PLUS database pricing

Equipment	C_{ASPEN} [£, 2016]	Equipment	C_{ASPEN} [£, 2016]	Equipment	C_{ASPEN} [£, 2016]
HPDC-bottoms split	550000	LPCOMP	522600	HXA2	123700
HPDC-condenser and accumulator	550000	LPDC-condenser and accumulator	513500	HXA3	234500
HPDC-overhead split	550000	LPDC-bottoms split	513500	LPPUMP	19400
HPDC-Reboiler	103400	LPDC-overhead split	513500	B2	90000
HPDC-reflux pump	53500	LPDC-Reboiler	666400	B21	90000
HPDC-tower	406100	LPDC-reflux pump	408400	BOOSTER	2.74E+06
HXA1	442800	LPDC-tower	5.79E+06	CO12CS	195400
ASUTURBI	783500				

Finally, Table 3.19 shows the pricing of the pieces of equipment which are provided based on the ASPEN PLUS pricing database.

To sum up this section, the dominant costs of the CARSOXY cycle are those for the BOOSTER, LPDC-tower, the heat exchangers HXHX and HEX1, respectively. The BOOSTER cost ($C_{ASPEN} = \text{£}_{2016} 27400000$) has been estimated using ASPEN PLUS database-Table 3.1-and it has the highest cost amongst all other components of the CARSOXY cycle. It is followed by the cost of the LPDC-tower ($C_{ASPEN} = \text{£}_{2016} 5.790000$), which was also estimated using the ASPEN PLUS database, Table 3.1. Both of costs of the heat exchangers HXHX ($\text{£} = \text{£}_{2016} 4331907$) and HEX1 ($\text{£} = \text{£}_{2016} 1509938$) were estimated using Equation 3.17 and escalated to 2016 using Equation 3.16. The prices of the remaining pieces of equipment –Tables 14, 15, 17, 18 and 19– are insignificant in comparison to the BOOSTER, LPDC-tower, the heat exchangers HXHX and HEX1.

At this stage, this section (3.4) is concluded since ASPEN PLUS is able to perform techno-economic analyses for both models (CARSOXY and Air-driven cycle) using the assumption specified in section 3.4.5, raw material and products prices specified in section 3.4.6 and prices of all pieces of equipment specified in section 3.4.7.

Although techno-economic analyses contribute to understanding the feasibility of adopting CARSOXY

to industry, experimentally assessing its combustibility remains a crucial task. For example, ASPEN PLUS provides results assuming the steady-state condition and does not take into account combustion turbulence. Therefore, the paradox of theoretically showing high techno-economic sustainability while not demonstrating an acceptable combustion behaviour could potentially exist unless it has been proven otherwise. Therefore, experimentally assessing CARSOXY combustion has been performed in this thesis and the following sections (3.5 and 3.6) describe the methodology of characterizing CARSAOXY combustion in comparison to Air/methane.

3.5 The methodology for assessing flame chemiluminescence and emissions.

This thesis attempts to experimentally assess CARSOXY in comparison to a CH₄/air flame. OH chemiluminescence imaging integrated with Abel deconvolution techniques have been utilized to study flame stability, and flame geometry (i.e. Area of highest heat intensity ($A_{\overline{OH}_{Max}}$), Center of highest heat intensity ($C_{\overline{OH}_{Max}}$)) over a range of instability conditions (excitation frequencies [50Hz-700Hz]). Moreover, NO_x and carbon emissions have also been analyzed. The suggested molar fractions of CARSOXY by the reference [102] have been normalized such that it contains zero H₂O molar fraction (Dry combustion).

3.5.1 Chemiluminescence imaging systems

The chemiluminescence imaging in this study is based on the IRO-CCD LaVision setup. A CCD (Figure 3.5.J) camera is integrated to an IRO high-speed gated image intensifier (Figure 3.5.I). The optics associated with the system is an OH filter (Figure 3.5.F) fitted on a 78 mm UV fixed-focal-length relay lens (Figure 3.5.H). The image intensifier is controlled by the I/I control unit (Figure 20.G), which is remotely controlled by the DaVis 7 software. Figure 3.5 shows the electrical and the optical connections of the IRO intensifier, the I/I control unit and the CCD camera to the CPU. The band-pass filter captures the OH radicals concentrated at 315nm±15nm. The light signal is transferred via the 78 mm UV fixed-focal-length relay lens to the IRO intensifier. The intensifier gate signal pulse width time is 400µs with a gain of 85%. The intensified image is finally captured by the 10Hz CCD camera which has a resolution of (688 x 520pixels) at 16 bits. This provides an (X x Y) field of view of (60 x 45 mm) and 11.26667 pixels/mm resolution. The IRO-CCD system is placed perpendicular to the direction of the flow. It captures images through the quartz cylindrical confinement, Figure 3.5.E. The IRO-CCD targets the nozzle exit of the 20-kW generic burner, Figure 3.5.D.

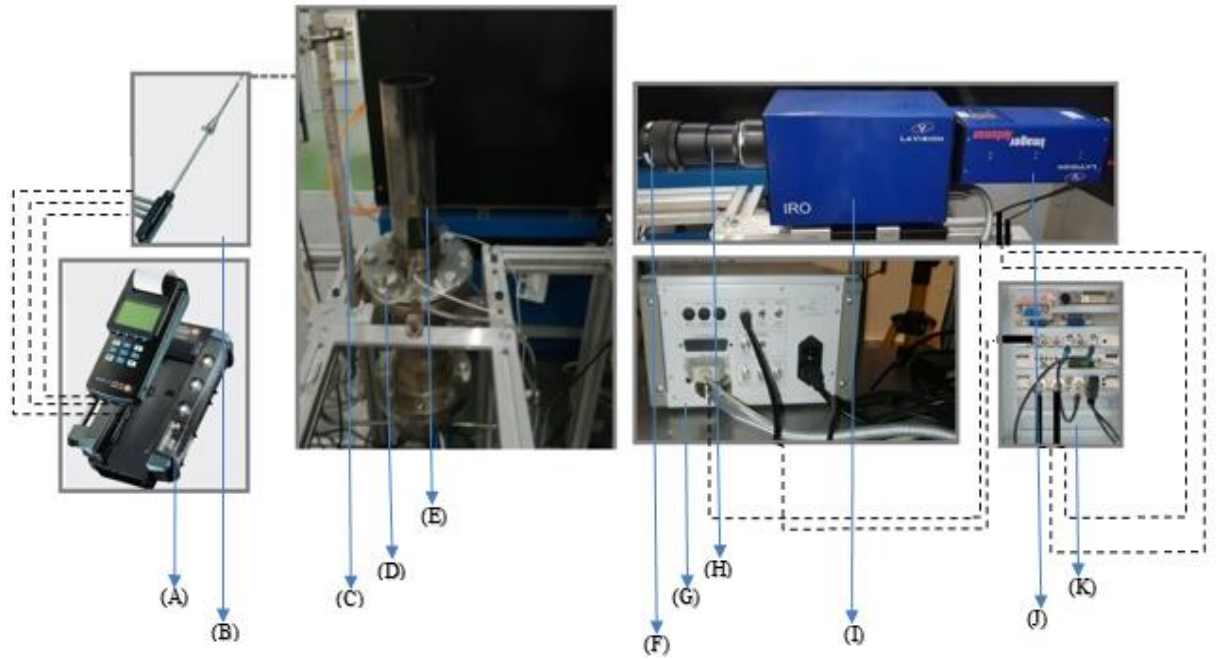


Figure 3.5 Experiment setup;(A:TESTO gas analyzer),(B: Gas analyzer probe),(C: Ignitor pilot),(D: Burner rig),(E: quartz cylindrical confinement),(F: OH filter),(G: Image intensifier control unit), (H: Fixed-focal-length relay lens),(I: IRO image intensifier),(J: CCD camera),(K: LA VISION CPU)

3.5.2 Emission analyses system

As shown in Figure 3.5.A, a TESTO 350 XL gas analyzer has been used to measure exhaust gas emissions from the burner. TESTO 350 XL is capable of detecting oxygen, nitrogen monoxide, sulphur dioxide hydrogen sulphide and unburned hydrocarbon fuel (i.e. methane) using five electrochemical sensors and one infrared sensor to detect carbon dioxide. The device consists of a portable analyzer unit and detachable control unit. Water vapour from exhaust gases is accumulated using a condensation trap in the analyser unit, The condensation trap is drained when water reaches an unacceptable level.

The emission analyzer probe (Figure 3.5.B) has been located at the exit of the confinement and below the ignition pilot, Figure 3.5.C. This location reduces atmospheric air interference. It also records lower emission levels which are related to the ignition pilot.

The device was sent to the manufacturer [148] to be calibrated in order to be used in the experiment to analyse NO_x and carbon emissions. It must be highlighted that the device was reserved to be first used for this experiment and no other uses were between the manufacturer calibration and the experiment. This has been done to ensure that the device provides results within its reported uncertainties (± 10 ppm, ± 2 ppm and ± 2 ppm for CO, NO and NO₂ measurements, respectively [148]).

Using TESTO to quantify NO_x and carbon emissions has been reported in the literature [191-193]. As recommended by the reference [191]; all measurements were taken after a certain period (i.e. 1 minute) to provide repeatable and consistent measurements.

3.5.3 Burner specifications

A diffusive 20-kW generic burner has been used to compare the CARSOXY flame to the Air/Methane flame. The flame is stabilized with a quartz cylindrical confinement together with a swirler. The confinement is 30 cm long with a diameter of 8.5 cm, Figure 3.6.D. The confinement top is open to the surrounding and it fits on top of the confinement base, Figure 3.6.I. A nine-vane swirler with a swirl number of 1.5 (Figure 3.6.E) has been used together with a ninety-degree divergent nozzle (inner diameter =2.8cm), Figure 3.6.F. The swirler fits on its base (outer diameter=5cm), Figure 3.6.H. Fuel is supplied to the burner through the fuel intake (Figure 3.6.B), which is directly connected to the diffusive injector (inner diameter =5mm), Figure 3.6.H. The working fluid is supplied to the burner through the working fluid intake, Figure 3.6.A. Mixing Fuel with the working fluid only occurs at the burner exit, the mixing distance is ~1.5cm

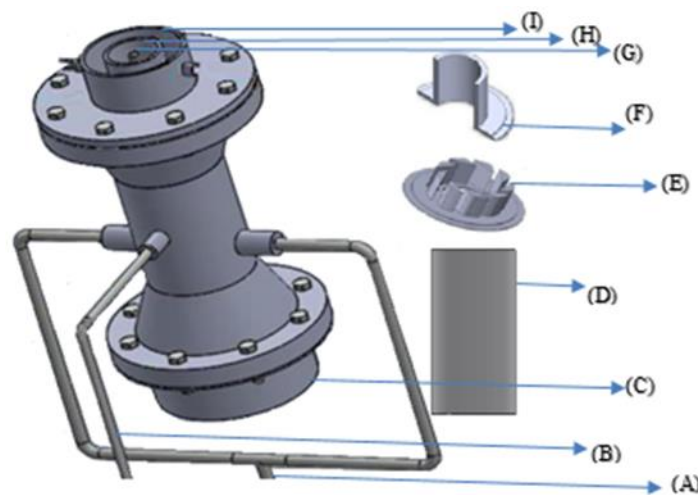


Figure 3.6.A, the 20-kW generic burner system ; (A: Working fluid intake), (B: Fuel intake), (C: speaker container), (D: quartz cylindrical confinement), (E: Swirler, SN=1.5), (F: Swirler/burner nozzle, divergent angle =90°), (G diffusive injector), (H: Swirl base), (I: confinement base).

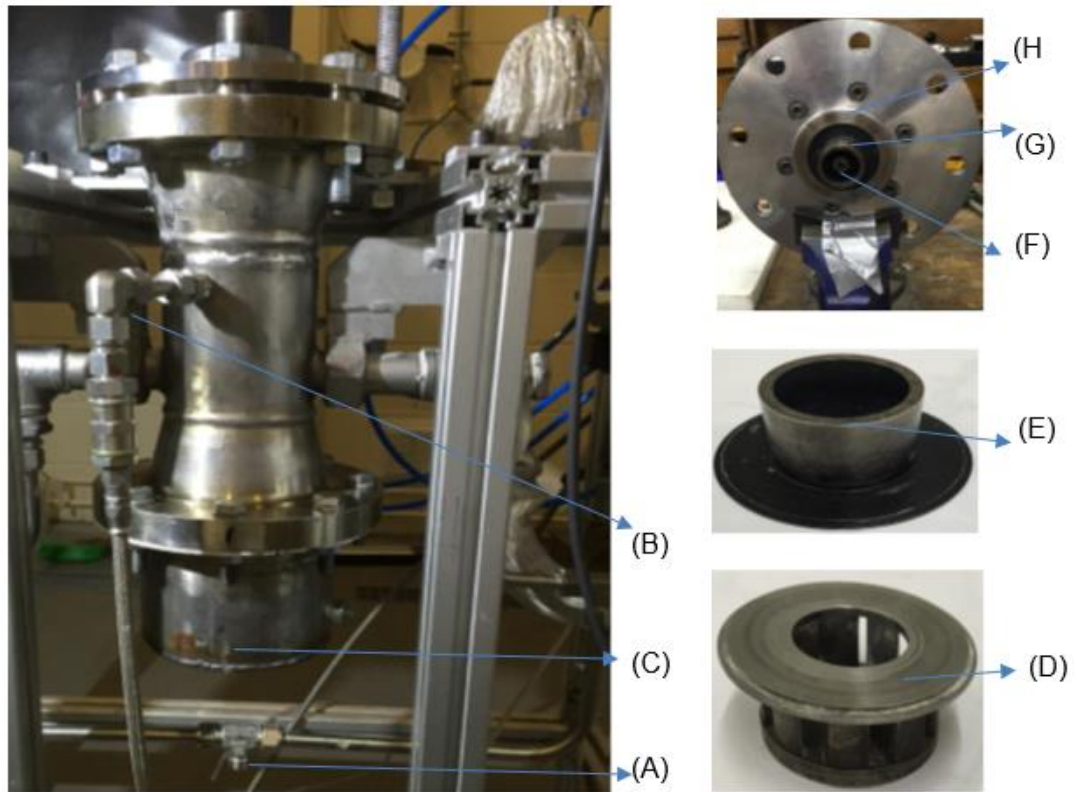


Figure 3.6.B, The 20-kW generic burner system ;(A: Working fluid intake), (B: Fuel intake), (C: speaker container), (D: Swirler, SN=1.5), (E: Swirler/burner nozzle, divergent angle =90⁰), (F diffusive injector), (G: Swirl base), (H: confinement base) [191].

3.5.4 Working fluid calibration

Platon PGS3 calibrated rotameters were installed to control the working fluid flow rates. Since the density of the CARSOXY working fluid varies from that for Air, the rotameters have to be recalibrated such that it supplies CARSOXY working fluid in equivalence to airflow rates. Equation (3.23) [143] has been used to recalibrate the rotameter.

$$q_{v2} = \sqrt{\frac{D_1}{D_2}} \times q_{v1} \quad (3.23)$$

3.5.5 Acoustic properties

The natural frequency of the burner has been identified as 150Hz by the previous study [144]. The burner is equipped with a Visaton WS 17 E Woofers 8 Ω speaker to excite the flame by [50-700] Hz. The speaker is located in the speaker container, Figure 3.6.C. The container cooled by an external air supply to

maintain the temperature of the speaker at a constant level. Moreover, data points of the experiment have been generated with time gaps to allow the speaker to cooldown. The frequency- impedance response of the speaker is provided by the reference [144].

The function of the speaker is to subject both of the CARSOXY and Air/Methane flames to comparable instability conditions to examine the CARSOXY flame stability behaviour about the Air/Methane flame. An explicit statement must be made that this approach has neither been used in literature nor used herein to obtain flame transfer function. It has been used based on the hypothesis that CARSOXY working fluid will have a different response towards excitation frequencies in comparison to air. The hypothesis attributes this to the differences in the physical properties (i.e. viscosity, mass, density, etc.) between air and CARSOXY. Essentially, obtaining flame transfer function would require adjusting the experimental setup in many aspects (i.e. recording frequency must be higher than the excitation frequency; further details can be provided elsewhere [194-196]).

3.5.6 Experiment procedure and matrix

The experiment matrix has been chosen on the ground of comparing CARSOXY flame to Air/Methane flame at constant thermal power (i.e. $P_{th} = 0.556$ kW) using 1 L/min of methane at 1.5 bar and 25°C, Equation (3.25) [145]. Although this low level of P_{th} has diverged from high conventional industrial levels, this ensures comparable results within the burner's capacity (as described in section 3.5.3). By taking into account the limited available CARSOXY reservoir, at this P_{th} (or low methane flow rate), the effect of the working fluid on the flame behaviour becomes more significant at lower flow rates (compared to higher levels of P_{th} or methane flow rates).

Three constant working fluid flow rates have been chosen (40L/min, 60L/min and 80L/min at 4 bar and 25°C). Essentially, the corresponding λ has been calculated using the oxygen mass instead of the working fluid mass since the mass of the CARSOXY working fluid is different from that for air, Equations (3.26-3.28).

The average Reynold's numbers (R_e) of the three flow rates at the burner exit have been calculated as a step towards nondimensionalizing and globalizing this work. Using the thermo-fluid properties (μ , m_{oxygen} , m_{fuel} and ρ) of CARSOXY and Air together with the dimensional properties (A and L) of the burner exit, R_e has been calculated, Equations (3.29-3.31) [145] The thermo-fluid (μ , m_{oxygen} , m_{fuel} and ρ) properties of CARSOXY and Air have been obtained by simulating the three flow rates under the experiment setup conditions using ASPEN PLUS. Table 3.20 shows the corresponding λ , P_{th}

and R_e of the flow rates.

1L/min of methane has been combusted using the three working fluids flow rates of CARSOXY and Air. Each case has been exited throughout ([50 Hz -700 Hz], 8 dB and 10V) and recorded using the chemiluminescence imaging system (described in section 3.5.1).

Emissions have been analyzed under the excitation condition of (200 Hz, 8 dB and 10V), \dot{V}_{WF} of 140L/min and \dot{V}_{CH_4} of [2L/min to 4.5 L/min]. These operation conditions have been chosen to subject both flames to an excitation level while maintaining the flame within the confinement and below the emission analyzer probe, Figure 3.5. This condition reduces atmospheric air interference which reduces measurement errors. Other conditions either forced the flame beyond the confinement or caused early blowouts.

$$P_{th} = \dot{m}_f LHV \quad (3.25)$$

$$\lambda_{oxy} = \frac{OFR_{Act}}{OFR_{stoic}} = \frac{1}{\phi_{oxy}} \quad (3.26)$$

$$OFR_{Act} = \frac{\dot{m}_{oxygen,Act}}{\dot{m}_{fuel,Act}} \quad (3.27)$$

$$OFR_{stoic} = \frac{n_{oxygen,stoic}}{n_{fuel,stoic}} = 2 \quad (3.28)$$

$$R_e = \frac{\rho V L_H}{\mu} = \frac{V L_H}{\nu} \quad (3.29)$$

$$L_H = L_0 - L_i \quad (3.30)$$

$$V = \frac{\dot{V}}{A} \quad (3.31)$$

Table 3.20 $V, R_e, \dot{m}_{oxygen}, \lambda_{oxy}$ and ϕ_{oxy} of the three \dot{V}_{WF} (40,60,80 L/min).

AIR					
\dot{V}_{WF} (L/min)	V (m/s)	R_e	\dot{m}_{oxygen} (g/s)	λ_{oxy}	ϕ_{oxy}
40	0.289	1735	0.805	24.76	0.04
60	0.433	2600	1.21	37.15	0.027
80	0.578	3470	1.61	49.5	0.02
CO ₂ -Ar-O ₂					
\dot{V}_{WF} (L/min)	V (m/s)	R_e	\dot{m}_{oxygen} (g/s)	λ_{oxy}	ϕ_{oxy}
40	0.289	2200	1.25	38.5	0.026
60	0.433	3300	1.875	57.75	0.0173
80	0.578	4400	2.5	77	0.013

3.5.7 Certainty

The used working fluid and CH₄ rotameters in the experiment have an uncertainty of $\pm 1.25\%FSD$ [146], the full ranges are 440L/min and 4.8 L/min, respectively. Constant uncertainty values of ($\pm 1.25\% \times 440L/min = \pm 5.5 L/min$) and ($\pm 1.25\% \times 4.8L/min = \pm 0.06 L/min$) can be concluded for the working fluid and CH₄ flow rates, respectively.

The frequency has been varied with an uncertainty of $\pm 5\%$ [147] certainties of these previously mentioned parameters have been labelled where are related in the results. The gas analyzer has uncertainties of $\pm 10 ppm$, $\pm 2 ppm$ and $\pm 2 ppm$ for CO, NO and NO₂ measurements [148].

As previously mentioned in section 3.5, the suggested molar fractions of CARSOXY by the reference [25] have been normalized such that it contains zero H₂O molar fraction (Dry combustion). Therefore a cylinder of 29% carbon dioxide, 32% oxygen and 39% argon was used to supply the burner with the necessary working fluid. The cylinder has filling relative tolerances of 5% for each component with respect to its molar fraction [198]. Therefore, the actual filled molar fraction values of the components are specified in Table 3.21. The purity of methane (methane CP grade) is 99.5% as reported by the supplier [198], the 0.5 % of impurity is due to the content of other gases, Table 3.22.

Table 3.21 The actual filled molar fraction values of carbon dioxide, oxygen and argon.

Component	Required molar fraction	Absolute tolerance	Available molar fraction
CO ₂	29%	± 1.45	27.55% to 30.45%
O ₂	32%	± 1.65	30.35% to 33.6%
Ar	39%	± 1.95	37.05% to 40.95%

Table 3.22 Methane impurities of methane CP grade [198]

Component	Content (ppmv)
Ethane	150
Nitrogen	5200
Oxygen	150
Other hydrocarbons	150
Moisture	3

3.5.8 Intensifier gate signal pulse width /gain selection

The light signal of OH chemiluminescence is very low to be captured by the filter-fitted CCD camera unless intensified. Therefore, as discussed in section 3.5.1, the IRO image intensifier has been used. However, the light signal must be intensified within acceptable gain and gate signal pulse width (i.e. image saturation is avoided).

The gate signal pulse width and the intensifier gain have been selected for the three cases ($\dot{V}_{WF} = 80\text{L/min}$, 60L/min and 40L/min) such that the maximum light intensity does not exceed (2000 count) to avoid image saturation in any case (based on the equipment-specific settings provided by LaVision [149]). The intensifier gate signal pulse width time has been held constant at $400\mu\text{s}$ while varying the intensifier gain up to 90%. The intensifier gate signal pulse width time has been chosen based on the recommendation provided by a previous study [150]. It has also been chosen such that it is inside the camera exposure interval (0.1 s) (i.e. $t_f > dt_g + dt_d$), Figure 3.7 [149].

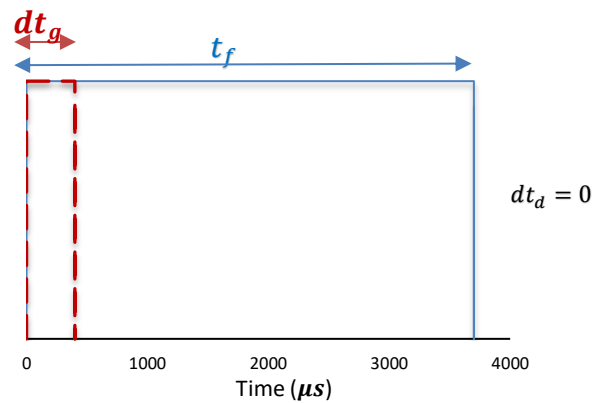


Figure 3.7 Intensifier gate signal pulse width and camera exposure time.

The maximum light intensity has been measured using the averaged images for each case. 300 images have been averaged without background correction in order not to affect the actual maximum intensity. As shown in Figure 3.8, increasing the gain up to 80% has a negligible effect on the image intensity. However, increasing the gain to 85% boosts the maximum intensity of ($\dot{V}_{WF} = 80\text{L/min}$) case to approximately (2000 count). The two remaining cases ($\dot{V}_{WF} = 60$ and 40L/min) are yet below that limit. Further increase of the intensifier gain increases the maximum intensity for the three cases beyond 2000 count. Therefore, the intensifier gain has been chosen to be 85% and held constant for the three cases of \dot{V}_{WF} throughout the experiment.

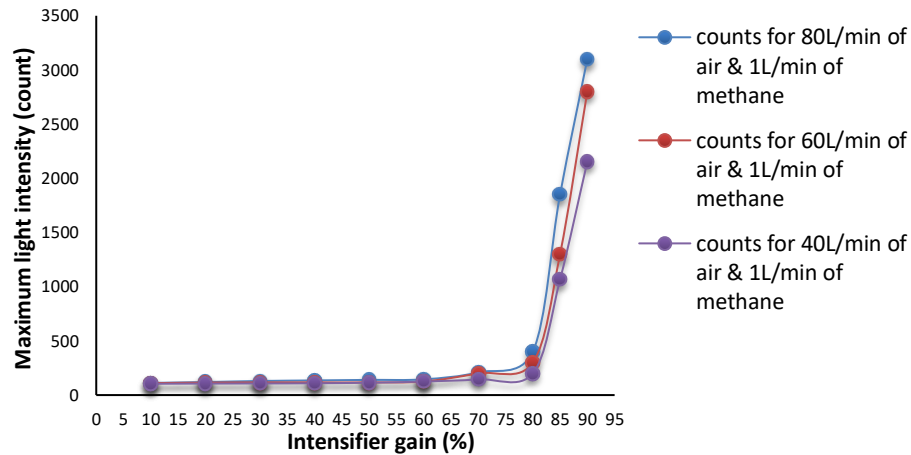


Figure 3.8 image intensifier gain transfer curves.

3.5.9 Number of images justification

Justifying the number of images essentially ensures that the time interval in which the averaged image has been processed is long enough to describe the overall behaviour of the flame. In other words, any additional increase in the number of images will have a negligible effect on the averaged image.

A flame at (\dot{V}_{WF} of 80 L/min and \dot{V}_{CH_4} of 1 L/min) has been captured by 500 images. It has been partially averaged by four different schemes in which the number of averaged images increases until it is fully averaged (i.e. 100/500, 300/500, 400/500 and 500/500). Once the averaged images have been obtained for each scheme, the regional pixel intensities for each image have been plotted, Figure 3.9. Regional pixel intensities refer to the count values at a specific region of pixels [150]. This has been chosen as a horizontal line from the left edge to the right edge of the image (from 0 to 60.88 mm (or 0 to 688 pixel)). The line is located at the centre of the image (at a vertical coordinate of 23 mm (or 260 pixels)). The burner vertical centerline is located at X=33.64mm as shown in Figure 3.9. On a side note, it can be seen that the flame is not perfectly axisymmetric about its vertical burner centerline. This is attributed to the fact that the fuel diffusive injector could be slightly off-centre and thus affecting the flame symmetry.

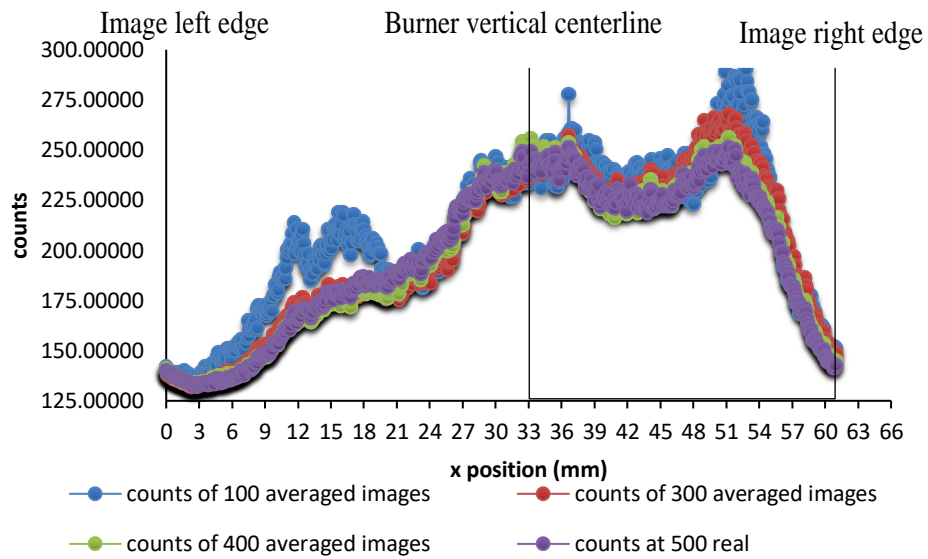


Figure 3.9 Regional pixel intensities of the horizontal edge-to-edge line at a vertical coordinate of 23 mm (or 260 pixels).

Once the regional intensities have been plotted, the error for each pixel has been plotted for the three partially averaged images (100/500, 300/500 and 400/500) relative to the fully averaged image (500/500). Table 3.23 shows the average relative error for each averaging scheme. As the number of images reaches 300, the error becomes negligible ($\sim 3\%$). Therefore, this has justified choosing 300 images as a sufficient interval to describe the overall flame behaviour.

Table 3.23 Average relative error for the partially averaged images

Partially averaged images	Average relative error
100/500	6.8%
300/500	3.03%
400/500	1.23%

3.5.10 Background correction and temporal averaging

Evaluating the image processing techniques in the literature indicates that chemiluminescence images can be utilized by temporal averaging [151] together with background correction [152]. A MATLAB code –Appendix 3.2– has been utilized to subtract the pixel intensities of each instantaneous image of the actual flame-cases from the corresponding pixel intensities of the instantaneous background image, Equation (3.32) [153]. Once it has been applied, the 300 consecutive background-corrected images ($[c_{ij}]_{m=1}^{n=300}$) have been produced. The MATLAB code then produces the temporally averaged image by calculating the mean pixel intensity of the 300 images for each pixel location, Equation (3.33) [153].

Figure 3.10 provides a sample of the temporally resolved and background-corrected images. Bulk flow direction and burner centerline are parallel to the Y-axis and burner exit is located at Y=0mm. X=0 mm and X=60 mm correspond to the left and right edges of the image, respectively. Mixing Fuel with the working fluid only occurs at the burner exit, the mixing distance is ~1.5 cm.

$$[c_{ij}]_{m=1}^{n=300} = [a_{ij}]_{m=1}^{n=300} - [b_{ij}]_{m=1}^{n=300} \quad (3.32)$$

$$\bar{c}_{ij} = \frac{\sum_{m=1}^{n=300} c_{ij}}{n} \quad (3.33)$$

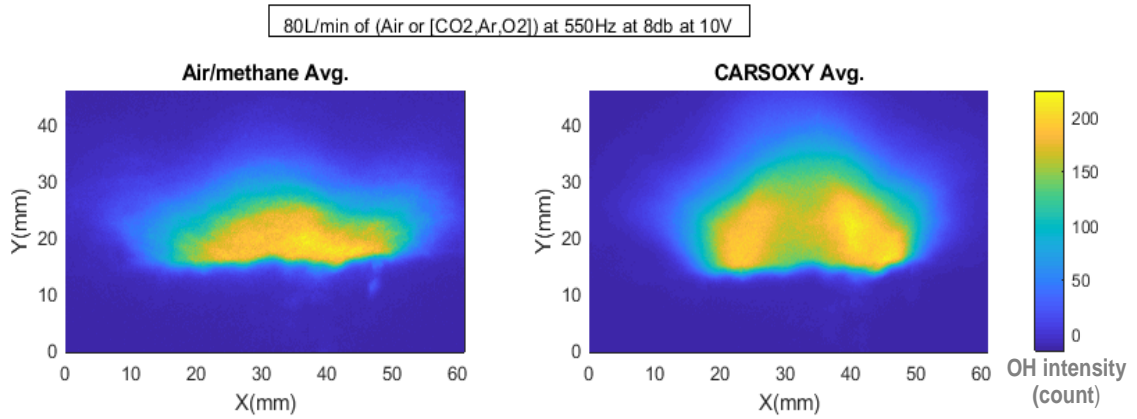


Figure 3.10 a sample of the temporally averaged and background-corrected image (bulk flow direction and burner centerline are parallel to the Y-axis and burner exit is located at, X=0 mm and X=60 mm correspond to the left and right edges of the image, respectively).

3.5.11 Chemiluminescence and heat release fluctuations

The heat release fluctuation has been calculated using the instantaneous and averaged integral pixel intensities (OH^* and \overline{OH} , using a MATLAB code-Appendix 3.2.1- to perform Equations (3.34) and (3.35) respectively). This technique quantifies chemiluminescence based on the summation of all pixel intensities [160].

$$[OH^*]_{m=1}^{n=300} = \left[\sum_{i=1}^{688} \sum_{j=1}^{520} I_{OH,ij}^* \right]_{m=1}^{n=300} \quad (3.34)$$

$$\overline{OH} = \sum_{i=1}^{688} \sum_{j=1}^{520} \bar{I}_{OH,ij} \quad (3.35)$$

This thesis applies the standard deviation concept to quantify the chemiluminescence fluctuation (OH^*/\overline{OH}) over time. Standard deviation is a statistical technique which measures the tendency of data points to be far from the mean value [154]. This thesis utilizes this concept as described in Equation (3.36) [154] by processing the chemiluminescence fluctuation data-points using the built-in standard deviation statistical function in MATLAB. Figure 3.11 provides a sample of the heat release fluctuation data points. (The full set of results is provided in chapter 7).

$$\sigma_{OH^*/\overline{OH}} = \sqrt{\frac{1}{n-1} \sum_{m=1}^n ([OH^*/\overline{OH}]_m - 1)^2} \quad (3.36)$$

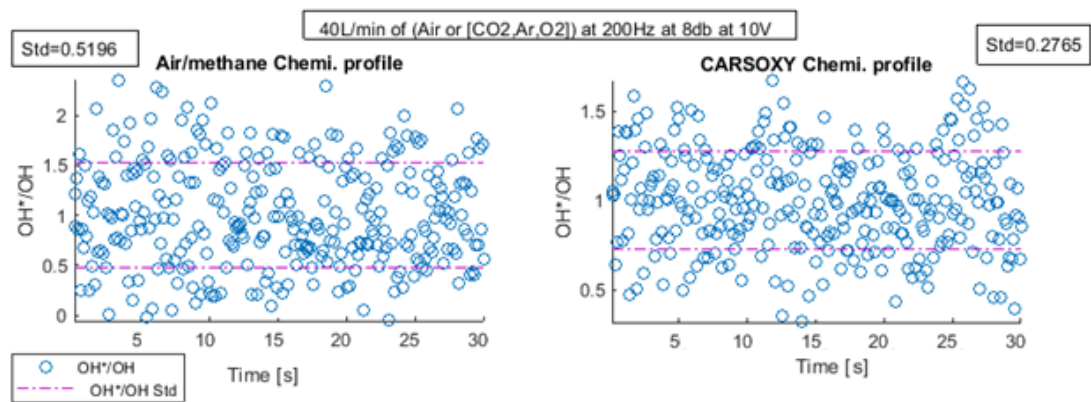


Figure 3.11 Data Sample of the Standard deviation (σ) of the heat release fluctuations (OH^*/\overline{OH}) (40L/min of (Air or [CO₂, Ar, O₂]) at 200Hz at 8db at 10V).

3.5.12 Specially resolved images

This thesis has adopted the Abel deconvolution technique developed by the reference [153] and optimized by [150] to reconstruct the line-of-sight averaged images into a specially-resolved representation such that the pixel intensities are not affected by the signal contribution from both in front of and behind the focal plane of the CCD. Since Abel deconvolution technique assumes axisymmetry, the code has been applied on the averaged image such that the right half (from X=33.64mm to X=33.64mm 60.27mm) is mirrored about the burner centerline(X=33.64 mm). Figure 3.12 provides a sample of the temporally and specially resolved and images. (The full set of results is provided in chapter 7). The MATLAB code is provided in Appendix 3.2.2.

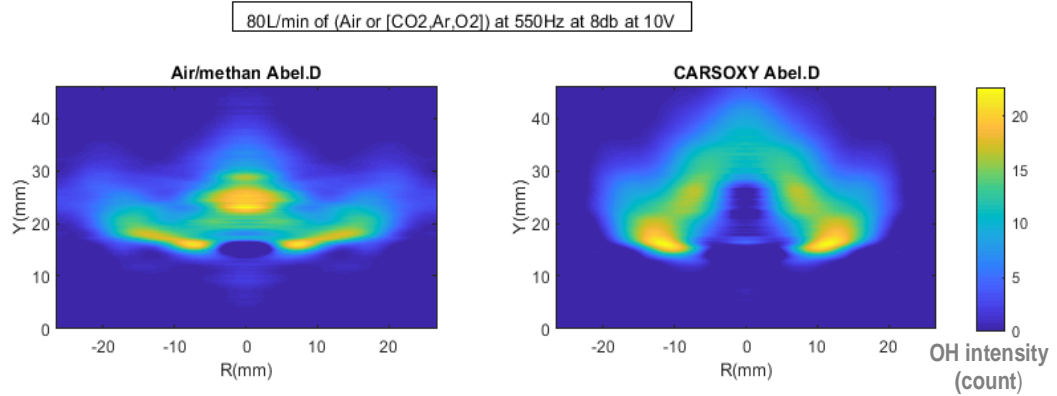


Figure 3.12 A sample of temporally and specially resolved images using Abel deconvolution.

3.5.13 Identifying the location of the highest heat intensity centre

Once the temporally and specially resolved images have been obtained, the location of the highest intensity centre ($C_{\overline{OH}_{Max}}$) has been identified with respect to the burner centerline and base. With the aid of MATLAB interactive tools, ($C_{\overline{OH}_{Max}}$) has been identified as illustrated in Figure 3.13. (The full set of results is provided in chapter 7).

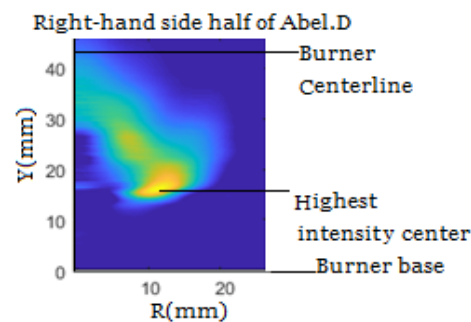


Figure 3.13 Sample of the right-hand side ($C_{\overline{OH}_{Max}}$) with respect to the burner centerline

3.5.14 Identifying the area of the highest heat intensity centre

As discussed in section 3.1, $A_{\overline{OH}_{Max}}$ is defined as the area of the highest heat intensity. This parameter has been studied in the literature (i.e. correlated to theoretical flame geometric characterization [155]).

In the context of this thesis, the temporally and specially resolved images have been rescaled to a binary image relative to the maximum intensity (\overline{OH}_{Max}) using MATLAB. This benchmarks the region with the highest intensity, which allows the MATLAB code to calculate its Area($A_{\overline{OH}_{Max}}$). Figure 3.14 provides a sample of the calculated areas. (The full set of results is provided in chapter 7). A threshold of 70% of the maximum intensity was recommended by the reference [155]; thus, it has been used for this thesis. The geometric characterization allows us to

obtain an area perturbation

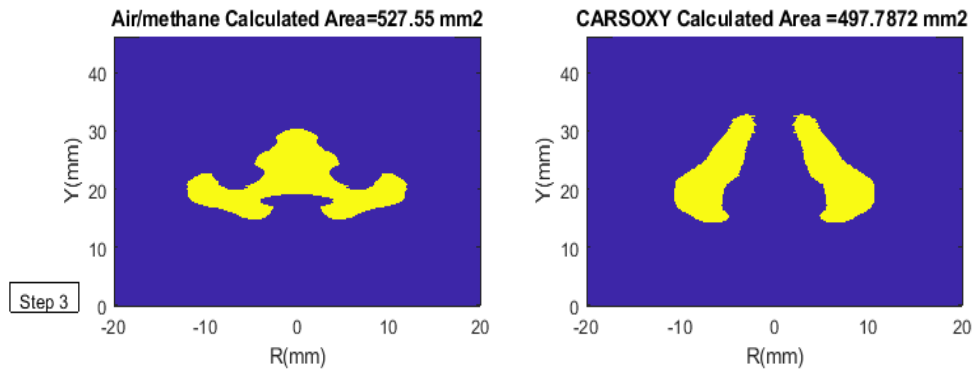


Figure 3.14 sample of the calculated areas

To sum up this section, and as discussed in section 3.1, studying flame shape and geometry in this thesis is limited by the area of the highest heat intensity ($A_{\overline{OH}_{Max}}$) and the centre of the highest heat intensity ($C_{\overline{OH}_{Max}}$). The next section (3.6) illustrates how laser-induced fluorescence techniques have been utilized to perform Damkohler analyses and plot Borghi regime diagrams. In addition, the following section (3.6.3.4) highlights the critical role of obtaining $C_{\overline{OH}_{Max}}$ to perform Damkohler analyses.

3.6 Methodology for assessing flame by laser-induced fluorescence.

At Cardiff University's thermofluids and combustion Lab, an OH Planar Laser-Induced Fluorescence (PLIF) imaging system has been utilised with the diffusive 20-kW generic burner (described in section 3.5.3) to examine the qualitative properties of the CARSOXY flame, which are then used to calculate the Damköhler numbers (Da) under varying operating conditions. The system is provided by LaVision and based on a combination of a dye laser and an Nd:YAG laser. The Nd:YAG laser pumps the dye laser with the fundamental laser, which is frequency-doubled to excite combustion species (i.e. OH). The dye optics tunes the output laser wavelength at the required excitation wavelength before passing through sheet forming optics and eventually into the burner.

The PLIF system is integrated with the LaVision 10 Hz CCD camera –with a resolution of (688 x 520 pixels) at 16 bits - fitted on the 78 mm UV fixed-focal-length relay lens (Figure 3.5.J), the IRO high speed gated image intensifier (Figure 3.5.I), the I/I control unit (Figure 20.G). The CCD camera is associated with a band-pass filter which captures OH radicals fluorescence emission a (315nm+15nm). The IRO-CCD system is placed perpendicular to the direction of the flow. Whereas the intensifier gate signal pulse

width time is 400 μ s with a gain of 85% for the chemiluminescence analyses, these were set at 0.05 μ s and 80%, respectively. These values were provided by LaVision service team who commissioned the OH PLIF system at Cardiff University [164]. The gate time in the PLIF analysis is significantly low compared to the chemiluminescence analyses (i.e. 0.05 μ s compared to 400 μ s) because the lifetime of the OH radical fluorescence signal is extremely short (\sim 2 ns).

3.6.1 PLIF components and setup

As shown in Figure 3.15, the PLIF system consists of a Sirah PrecisionScan dye laser and a Continuum Precision Nd:YAG laser. The latter pumps the dye laser by a 532 nm beam with a shot-to-shot frequency of 10 Hz. The pulse duration range for each shot is 5-10 ns at 532 nm. The linewidth of the Sirah PrecisionScan dye laser is \pm 2.7pm at 570nm using 2400 lines / mm, 60mm long grating. The exact wavelength of the OH radicals excitation is achieved by using a solution of Rhodamine 6G dye powder and ethanol. This dye was recommended by LaVision service team who commissioned the OH PLIF system at Cardiff University [156] to avoid wavelength overlaps and interference of other species. The dye solution has a fundamental wavelength of 562 nm. However, the grating is remotely controlled and can modify the dye laser fundamental wavelength with an accuracy of 0.001 nm. The grating was adjusted such that the fundamental wavelength becomes 566 nm. The laser beam is then directed to a frequency-doubling crystal, which halves the wavelength of the beam (\sim 283 nm) to excite the OH radicals. To take into account for the OH ground state distribution dependence on temperature, the final wavelength of the dye laser beam was tuned to 283.027 nm. This wavelength has the lowest Boltzmann factor (the lowest temperature dependence) for CH₄ combustion at 573 K and 1.1 bar [157] (the operating condition of this PLIF analyses). Sheet-forming optics are utilized to convert the line beam (at 283.027 nm) into an approximately 20 mm wide and 1-2 mm thick laser sheet. Finally, the laser sheet passes through the quartz (described in section 3.5.3). Identical to the chemiluminescence analyses, the camera is located at the side of the quartz, which is perpendicular to the axial fluid flow and the laser sheet. Therefore, the same field of view of chemiluminescence analyses is achieved for PLIF analyses (the (X x Y) field of view of (60 x 45 mm) and 11.26667 pixels/mm resolution. The Nd:YAG laser pumps the dye laser with a 430 mJ/pulse (4.3 W/pulse) beam at a repetition rate of 10 Hz. The energy level significantly drops in the dye laser due to the optics which are used to adjust the wavelength of the laser beam. Therefore, the final PLIF pulse energy drops to 15 mJ/pulse (150mW/pulse) at 283 nm. Finally, the Davis7 software synchronizes the intensifier gate timing with the final PLIF laser pulse through synchronizing the intensifier gate timing with the camera shutter, Nd: YAG flashlamp and Q-switch.



Figure 3.15 PLIF top view, (A: Nd:YAG laser), (B: Dye laser), (C: Rhodamine 6G dye powder and ethanol), (D: Temperature monitor), (E: Sheet forming optics), (F: Grating), (G: Frequency-doubling crystal), (H: burner quartz), (I: IRO intensifier) –(J: CCD camera), (K: Webcam), (45° mirror)

3.6.2 Experiment procedure and matrix

The experiment matrix has been chosen on the ground of comparing CARSOXY flame to Air/Methane flame at constant thermal power (i.e. $P_{th} = 0.556$ kW) using 1 L/min of methane at 1.5 bar and 25°C, Equation (3.25). Working fluids were supplied to the burner at 4.5 bar and 25°C. Eight average Reynold's numbers (R_e) have been maintained constant for the working fluids (air and CO₂-Ar-O₂), (2000-3750, with a step of 250). Moreover, nine oxidizing equivalence ratios (λ_{oxy}) have been maintained constant for CH₄/air and CARSOXY, (35-70, with a step of 4.375).

Using the thermo-fluid properties (dynamic Viscosity (μ), oxygen mass flow rate (m_{oxygen}), fuel mass flow rate (m_{fuel}) and density (ρ)) of CARSOXY and air together with the dimensional properties (cross-sectional areas (A) and diameters (L)) of the burner exit, R_e has been calculated, Equations (3.29-3.31). The thermo-fluid (μ , m_{oxygen} , m_{fuel} and ρ) properties of CARSOXY and Air have been obtained by simulating all attempts under the experiment setup conditions using ASPEN PLUS. Table 3.24 shows the corresponding oxygen mass flow rates (m_{oxygen}), oxygen to fuel equivalence ratios (λ_{oxy}), fuel to oxygen equivalence ratio (ϕ_{oxy}) and flow velocity (V) of the attempts at constant R_e for Air and CARSOXY. Table 3.25 shows the corresponding \dot{m}_{oxygen} , λ_{oxy} and R_e , V of the attempts at constant ϕ_{oxy} for air and CARSOXY.

Table 3.24 V, \dot{V}_{WF} , \dot{m}_{oxygen} , λ_{oxy} and ϕ_{oxy} of the eight R_e (2000-3750).

CO ₂ - Ar -O ₂						
R_e	V (m/s)	$\dot{V}_{WF}(m^3/s)$	$\dot{V}_{WF}(L/min)$	$\dot{m}_{oxygen}(g/s)$	λ_{oxy}	ϕ_{oxy}
2000	0.263	0.00061	36.4	1.1	35.0	0.029
2250	0.296	0.00068	40.9	1.3	39.4	0.025
2500	0.329	0.00076	45.5	1.4	43.8	0.023
2750	0.361	0.00083	50.0	1.6	48.1	0.021
3000	0.394	0.00091	54.6	1.7	52.5	0.019
3250	0.427	0.00098	59.1	1.8	56.9	0.018
3500	0.460	0.00106	63.6	2.0	61.3	0.016
3750	0.493	0.00114	68.2	2.1	65.6	0.015
Air						
R_e	V(m/s)	$\dot{V}_{WF}(m^3/s)_e$	$\dot{V}_{WF}(L/min)$	\dot{m}_{oxygen}	λ_{oxy}	ϕ_{oxy}
2000	0.33	0.0008	46.1	0.93	28.54	0.035
2250	0.38	0.0009	51.9	1.04	32.11	0.031
2500	0.42	0.0010	57.7	1.16	35.67	0.028
2750	0.46	0.0011	63.4	1.28	39.24	0.025
3000	0.50	0.0012	69.2	1.39	42.81	0.023
3250	0.54	0.0012	74.9	1.51	46.38	0.022
3500	0.58	0.0013	80.7	1.62	49.94	0.020
3750	0.63	0.0014	86.5	1.74	53.51	0.019

Table 3.25 $V, \dot{V}_{WF}, \dot{m}_{oxygen}$, and R_e of the nine λ_{oxy} (35-70).

CO ₂ - Ar - O ₂						
λ_{oxy}	V	$\dot{V}_{WF} (m^3/s)$	$\dot{V}_{WF} (L/min)$	\dot{m}_{oxygen}	ϕ_{oxy}	R_e
35	0.26	0.00061	36	1.1	0.029	2000
39.375	0.30	0.00068	41	1.3	0.025	2250
43.75	0.33	0.00076	45	1.4	0.023	2500
48.125	0.36	0.00083	50	1.6	0.021	2750
52.5	0.39	0.00091	55	1.7	0.019	3000
56.875	0.43	0.00098	59	1.8	0.018	3250
61.25	0.46	0.00106	64	2.0	0.016	3500
65.625	0.49	0.00114	68	2.1	0.015	3750
70	0.53	0.00121	73	2.3	0.014	4000
Air						
λ_{oxy}	V	$\dot{V}_{WF} (m^3/s)$	$\dot{V}_{WF} (L/min)$	\dot{m}_{oxygen}	ϕ_{oxy}	R_e
35	0.41	0.0009	57	1.1	0.029	2450
39.375	0.46	0.0011	63	1.3	0.025	2750
43.75	0.51	0.0012	70	1.4	0.023	3050
48.125	0.56	0.0013	77	1.6	0.021	3350
52.5	0.61	0.0014	84	1.7	0.019	3650
56.875	0.66	0.0015	91	1.8	0.018	3950
61.25	0.71	0.0016	98	2.0	0.016	4250
65.625	0.76	0.0018	105	2.1	0.015	4550
70	0.81	0.0019	112	2.3	0.014	4850

PLIF analyses have been performed on each attempt (at $R_e = 2000-3750$ and $\lambda_{oxy}=35-70$) using the described setup in section 3.6.1. Performing Damköhler analyses and plotting Borghi combustion regime diagrams are typically performed with respect to a range of Reynolds numbers and/or equivalence ratios [160]. The chosen Reynolds number range herein is within the studied ranges of non-premixed flames (i.e. $R_e = 1000-5000$) in the literature [162].

Finally, chemiluminescence analyses have been performed on each case using the described chemiluminescence setup in section 3.5.1

3.6.3 PLIF image processing and data analyses

As discussed in section 3.5.15, Abel deconvolution technique has been adopted for the chemiluminescence analyses to spatially resolve images from the signal contribution of OH radicals from both in front of and behind the focal plane of the CCD. However, this is not needed for PLIF analyses since the fluorescence signal is only due to the laser excitation sheet, located at the focal plane. The image processing conducted for the PLIF analyses includes background correction, noise filtering, correction for the laser sheet intensity distribution, correction for shot-to-shot laser energy variation and temporal

averaging. After applying the previously mentioned image corrections, an edge detection algorithm is applied to the final image to examine the qualitative properties of the flame, which are then used to calculate the Damköhler numbers (Da) under varying operating conditions. Image processing was performed using MATLAB codes, Appendix 3.3.

3.6.3.1 Laser energy shot-to-shot variation

500 images were captured for each PLIF case of study, this choice of the number of images is based on the recommendation of the PLIF analyses of the reference [156]. The laser energy for each image was measured using the LaVision energy monitor. The pixel intensities for each image were normalized to the maximum measured laser energy by multiplying the pixel intensities of each instantaneous image by the ratio of its corresponding laser energy to the maximum laser energy. The MATLAB code is available in Appendix 3.3.1.

3.6.3.2 Background and laser sheet image corrections

500 images were captured with laser firing and with the quartz present in the field of view but without a flame in the burner. These 500 images were temporally averaged and subtracted from each instantaneous image of the case of study (image with a flame).

Laser light intensity across the laser sheet follows a Gaussian distribution, which has the highest laser intensity towards the middle of the sheet and intensity decrease towards the edges towards the y-direction of the field of view. Therefore, it was necessary to ensure that the pixel intensities are increased where the laser energy is lower than the maximum laser energy across the laser sheet. This was accomplished by converting the averaged and background corrected laser sheet image-Figure 3.16.A- into an (X-Y-I) MATLAB matrix. Laser sheet profiles (Y-I curves) were plotted across the X directions, which were finally averaged into one curve, Figure 3.16.B. Using the curve-fitting built-in “cftool” function in MATLAB, the normalized laser sheet intensity profile was fitted with a Gaussian distribution, Equation 3.37, where I_{GF} is the Gaussian fitted intensity of the normalized intensity at Y position.

$$I_{GF} = 1.2 * \exp\left(-\left(\frac{Y - 38.3}{7.1}\right)^2\right) \quad (3.37)$$

The Gaussian fit is utilized for laser sheet profiles because it provides a statistically symmetric representation of averaged sheet intensity with significant fluctuating components [158]. Once, the Gaussian fit was obtained, Figure 3.16.B, the absolute gradient was plotted of the Gaussian fit was plotted,

Figure 3.15. The code described in Appendix 3.3.2 was applied to correct images using Gaussian fit at the maximum gradients (where a sudden change of the normalized Gaussian fitted intensity, $Y=38.42$ mm and 12.23 mm, Figure 3.15).

As shown in Figure 3.16, the normalized laser sheet profile does not perfectly match the single-peak Gaussian fitted curve and further optimization of curve fitting is possible, using a multi-peak Gaussian curve fitting. Essentially, additional terms with different coefficients and constants will be added to the fitting equation (i.e. Equation 3.37) if a multi-peak Gaussian curve fitting is used. However, multi-peak Gaussian curve fitting requires significantly higher computational time and processing capacity in comparison to single-peak curve fittings. Therefore, considering the available computational processing capacity and the large experiment matrix (Tables 3.24 and 3.25), the normalized laser sheet profile was approximated to the single-peak Gaussian fitted curve shown in Figure 3.16.

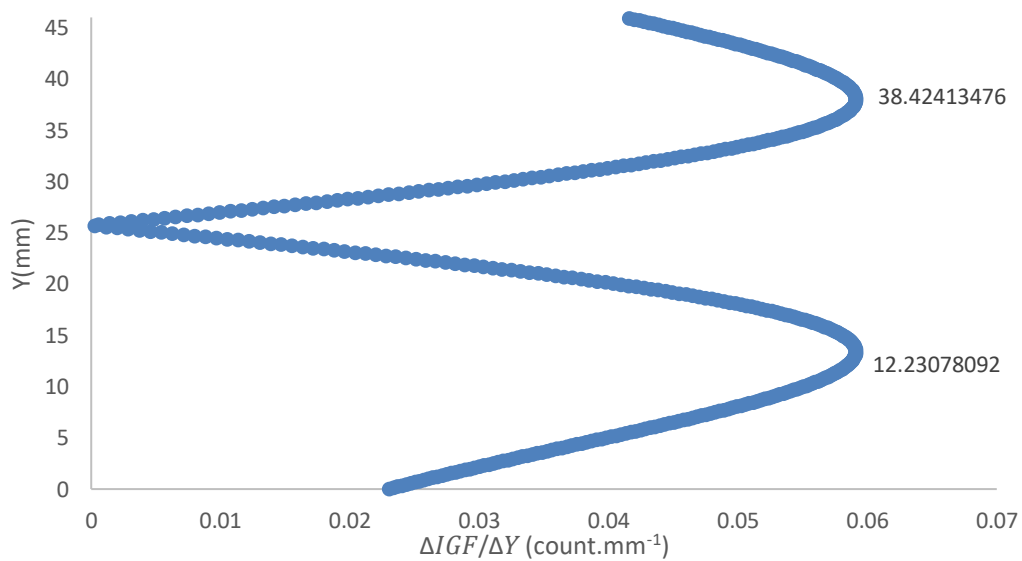


Figure 3.15 Absolute gradient of the Laser sheet Gaussian fit

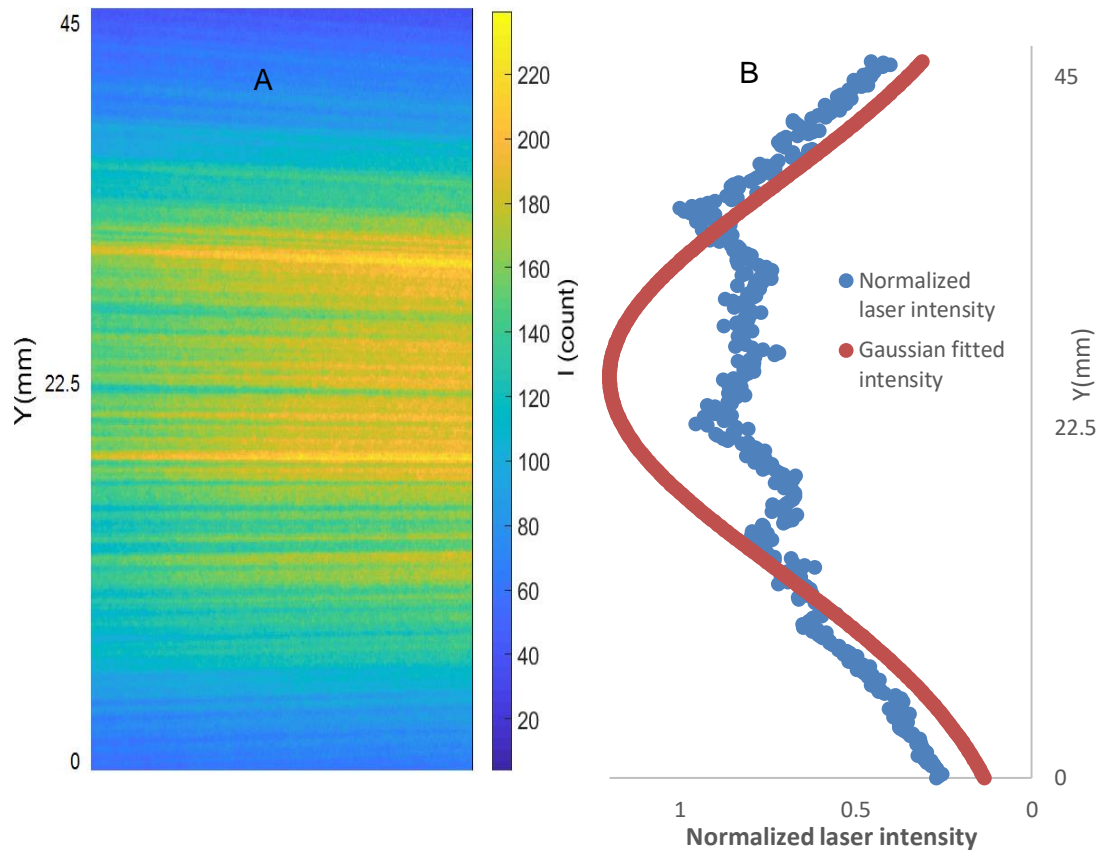


Figure 3.16 PLIF laser sheet intensity (A) and Gaussian fit to intensity distribution (B) for image correction.

3.6.3.3 Flame properties detection

The MATLAB code from the reference [158] -Appendix 3.3.3- has been adopted to characterize the main features of a flame using the temporally averaged image (after laser energy shot-to-shot variation, background and laser sheet corrections have been conducted). This technique initially finds the maximum pixel intensity in each row of the image. Once this location is determined, the maximum directional intensity change (maximum gradient) is identified on either side of the maximum row pixel, depending on the location of the minimum pixel intensity. This generates lines which correspond to the flame brush thickness for each at the highest OH intensity ($\overline{\delta_{ch}}$). The MATLAB code is a function of a reaction progress variable ($0 < c < 0.5$). The line of the maximum OH intensity corresponds to $c = 0$, where the full brush thickness corresponds to $c = 0.5$. This gives the privileges of studying any desired flame surface location. Based on the literature review [159], $c = 0.5$ has been adopted for the PLIF image processing to study the full brush thickness.

3.6.3.4 Damköhler number (Da) estimation for nonpremixed flames

The significance of performing Damköhler analysis in studying alternative working fluid in diffusive combustion is to assess the diffusion rate in comparison to the reaction rate [199]. Essentially, if the Damköhler number is less than one, then the reaction rate between the working fluid and fuel occurs after their diffusion reaches an equilibrium. On the other hand, if the Damköhler number is greater than one, then the reaction is assumed to be instantaneously in equilibrium [200]. For $Da > 1$, the characteristic chemical time (τ_{ch}) is shorter than τ_n the characteristic flow time, which corresponds to a fast chemical reaction that occurs in a thin layer [162]. This implies that the flame can be assumed “thin” and can be called “flamelet” [183]. In other words, the higher the Da , the more laminar and less turbulent the flame becomes.

Therefore, performing Damköhler analysis in this thesis characterizes the diffusivity of CARSOXY components with respect to their reaction rate in comparison to Air/methane. In addition, it benchmarks CARSOXY turbulence in reference to Air/methane.

Damköhler describes the turbulence-chemistry interaction by correlating the characteristic flow time to the characteristic chemical time (τ_{ch}). Typically, the characteristic flow time is described by the integral time scale (τ_n). Infact, Da is described as the ratio between τ_n and τ_{ch} , Equation (3.38) [160].

$$Da = \frac{\tau_n}{\tau_{ch}} \quad (3.38)$$

τ_n is described as the time during which a particle is influenced by its previous position [159]. However, a more specific and numeric definition to describe nonpremixed flame is provided by the reference [162], Equation (3.39).

$$\tau_n = \frac{L_f}{u_F} \quad (3.39)$$

L_f is the flame base location where the maximum OH intensity is found [162] -Figure3.16- and corresponds to the Y magnitude of $C_{\overline{OH}_{Max}}$ in mm.

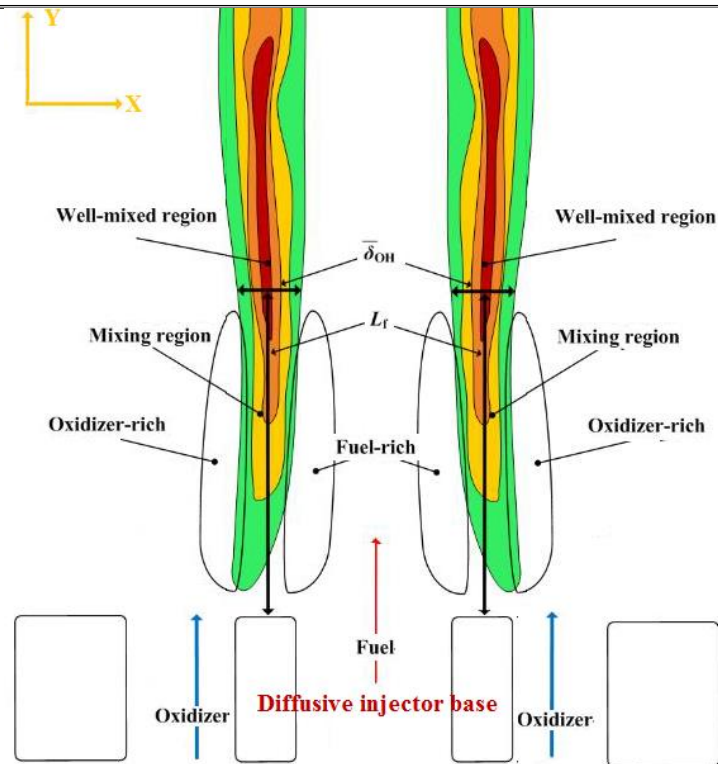


Figure 3.16 Schematic representation of the flame reproduced from the reference [162].

u_F is the injection velocity CH₄ in mm/s. It can be measured for 1l/min ($=3.3334E-05m^3/sec$) at the diffusive injector outlet area ($1.96E-05 m^2$) using Equation 3.31. The corresponding u_F is 1.7m/s. τ_{ch} is numerically described for nonpremixed flame by the reference [170], Equation (3.40).

$$\tau_{ch} = \frac{\bar{\delta}_{Ch}}{S_L} \quad (3.40)$$

As shown in Figure, 3.16, $\bar{\delta}_{Ch}$ is the flame brush thickness at the $Y=L_f$ (in mm). Once L_f is identified, the MATLAB code described in section 3.6.3.3 is applied only to the row with the maximum intensity (at $Y=L_f$, where rows are masked above and below the corresponding row of $Y=L_f$) of the PLIF image.

Finally, similar to the approach suggested by the reference [162], the laminar burning velocity at the stoichiometric condition S_L (559.2mm/s and 398.837 mm/s for CO₂- Ar - O₂/ CH₄ and Air/ CH₄ flames, respectively) was obtained using the CHEMKIN package of the ANSYS software. The 'GRI-Mech 3.0' mechanism was applied on the built-in 'Flame speed freely propagating' sample to obtain S_L . Figure 3.17 shows S_L for a CH₄/air flame and a CH₄/ CO₂- Ar - O₂ flame at a range of equivalence ratios.

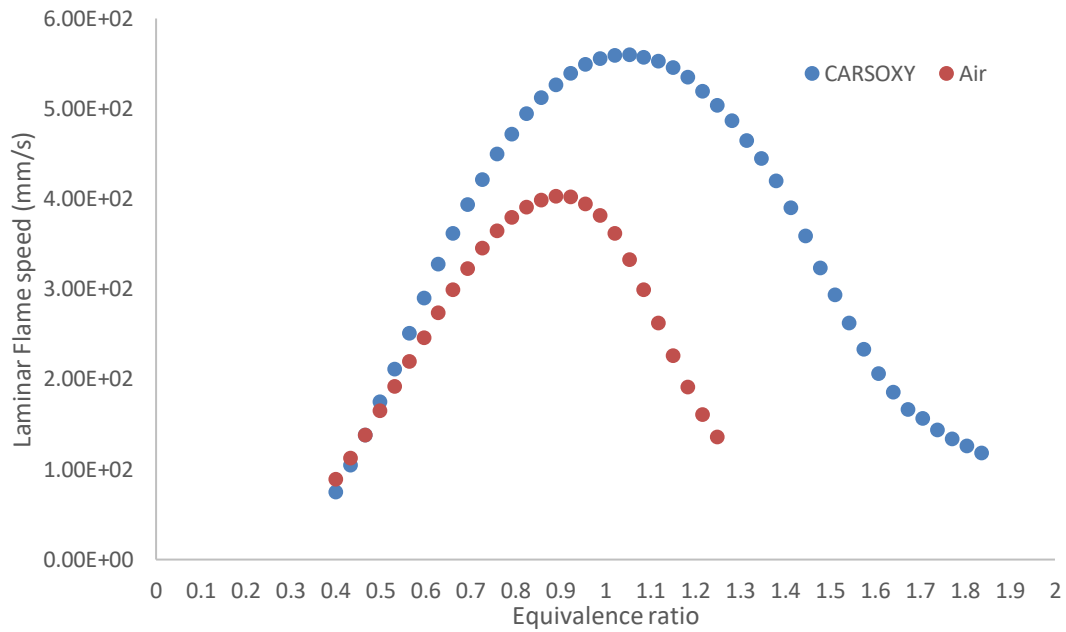


Figure 3.17 S_L for a CH₄/air flame and a CH₄/ CO₂-Ar-O₂ flame at a range of equivalence ratios.

To sum up this section, the raw images obtained from the described PLIF system in section 3.6.1 have been processed (to correct for the laser energy shot-to-shot variation (section 3.6.3.1), background and laser sheet distribution (section 3.6.3.2)). Using the processed images, flame properties (i.e the flame brush thickness the highest OH intensity ($\overline{\delta_{Ch}}$) have been detected as described in (section 3.6.3.3). The flame base location where the maximum OH intensity is found (L_f) corresponds to the Y magnitude of $C_{\overline{OH}_{Max}}$ in mm, thus it has been obtained as described in section (3.5.14) using PLIF images. The laminar burning velocity at the stoichiometric condition (S_L) has obtained using the CHEMKIN package of the ANSYS software. The injection velocity of CH₄ (u_F) has been calculated using Equation 3.3. Finally, those parameters ($\overline{\delta_{Ch}}$, L_f , S_L and u_F) has been utilized to perform Damköhler analyses using Equation 3.38-3.40.

CHAPTER FOUR

A parametric study of various thermodynamic cycles for the use of various CARSOXY blends.

“The temptation to form premature theories upon insufficient data is the bane of our profession.”

~ Arthur Conan Doyle

CHAPTER 4 – A PARAMETRIC STUDY OF VARIOUS THERMODYNAMIC CYCLES FOR THE USE OF VARIOUS CARSOXY BLENDS

The aim of this chapter is to conduct a parametric study for five gas turbine cycles (namely; simple, heat exchanged, free turbine & simple cycle, evaporative and humidified, Figure 3.1) using a CO₂-Argon-Steam-Oxyfuel (CARSOXY) mixture-Table 3.1, blend 58- as working fluid in order to identify their ultimate working conditions with respect to cycle efficiency. The performance of the five cycles using CARSOXY has been estimated for wet and dry compression. A cycle has been suggested for each range of working conditions. The results of this chapter are based on MATLAB codes which are described in section 3.2. This chapter also identifies domains of operating conditions for each cycle, where efficiency can be increased by up to 12% compared to air-driven cycles. Additional 10% increase of the cycle efficiency can be theoretically achieved by using the newly suggested CARSOXY blend. Neither the effect of Steam temperature nor the implementation methods are addressed in this chapter.

4.1 Analyses intervals

The combined effect of varying the compressor pressure ratio and inlet temperature on the cycle efficiency have been studied for Air-driven and CARSOXY gas turbines. Based on the recommendations of the reference [25], blend 58 has been chosen amongst the suggested CARSOXY blends, Table 4.1. The effect of dry and wet compression of the CARSOXY blend has been considered via adjusting the heat capacity of the working fluid in the compression stage, such the heat capacity of steam is included to drive the overall heat capacity of the 'wet' CARSOXY working fluid. On the other hand, it is not included for 'Dry' CARSOXY working fluid, Equations 4.1 and 4.2. Since the heat capacities of the individual components of CARSOXY are functions of temperature, the overall heat capacity, as a result, is adjustable corresponding to temperature variation in the compression and expansion stages. The reference [163] provides the corresponding heat capacities of each individual CARSOXY component at these temperatures intervals.

$$Cp(i) = A + BT'_{0.1} + C T'_{0.1}{}^2 + D T'_{0.1}{}^3 + \frac{E}{T'_{0.1}{}^2} \quad [\text{J/mol.K}] \quad (4.1)$$

$$Cp_{mix} = \sum_i Cp(i)x_i \quad (4.2)$$

The concept of utilizing CARSOXY as a working fluid takes the advantages of using carbon dioxide to

maintain turbine temperature within acceptable ranges, argon to increase specific heat ratio, steam to increase the mass flow rate and oxygen to eliminate NO_x emissions. The reference [191] has proven the combustibility of blend 58 and thus the performances of CARSOXY cycles in the parametric study were evaluated using this blend.

Table 4.1 Blend 58 molar fractions

Wet condition			
Stage	Combustion Inlet (x _i)[%]	Compression stage(x _i)[%]	Expansion stage(x _i)[%]
Argon	25	28.08	25
CO ₂	23	25.8	34
H ₂ O	19	21.34	41
CH ₄	11	0	0
O ₂	22	24.7	0
Dry condition			
Stage	Combustion Inlet (x _i)[%]	Compression stage(x _i)[%]	Expansion stage(x _i)[%]
Argon	30.8	35.7	30.8
CO ₂	28.4	32.85	42
H ₂ O	0	0	27.2
CH ₄	13.58	0	0
O ₂	27.16	31.4	0

(Based on stoichiometric combustion)

Nevertheless, varying compressor inlet temperatures, pressure ratio and CARSOXY compositions (wet/dry) also affect the enthalpy of the combustion reaction which as a result impacts the cycle efficiency, Equation (4.3) [173]. Therefore, identifying the ultimate CARSOXY composition with respect to the cycle efficiency should consider a range of operation conditions (variable temperatures and pressure ratios) and a range of CARSOXY compositions. On this note, the following intervals –Table 4.2– have been chosen to study the cycle efficiency in this chapter.

$$\Delta H_{\text{Reaction}, T'_{0,1}} = \Delta H_{\text{Reaction}, 25^\circ\text{C}} + \int_{25^\circ\text{C}}^{T'_{0,1}} \Delta \bar{C}_p dT \quad (4.3)$$

Table 4.2 Analyses intervals

Parameter	Interval	section
<ul style="list-style-type: none"> Compressor pressure ratio Compressor inlet temperature 	<ul style="list-style-type: none"> [2-10] [250K-600K] Wet/ Dry conditions 	4.2
<ul style="list-style-type: none"> Compressor pressure ratio Turbine inlet temperature 	<ul style="list-style-type: none"> [2-10] [800K-1800K] Dry condition 	4.4
CARSOXY molar fractions	<ul style="list-style-type: none"> A_r: [0.1-0.25] 	4.3

- O₂: [0.1-0.25]
- CO₂: [0.1-0.25]

4.2 Efficiency results with respect to variable compressor inlet temperatures and compressor pressure ratio.

The results of this section are plotted for the cycle efficiency with respect to both the compressor pressure ratio variation within the range of 2-10 and the compressor inlet temperature variation within the range of 250-600K at a constant turbine inlet temperature of 1900K (under the conditions and assumptions provided in section 3.2).

4.2.1 Simple cycle

The CARSOXY-driven simple cycle with wet compression has shown relatively lower efficiency than the air-driven simple cycle, as it falls behind it by almost 2% in all conditions as shown in Figure 4.1.

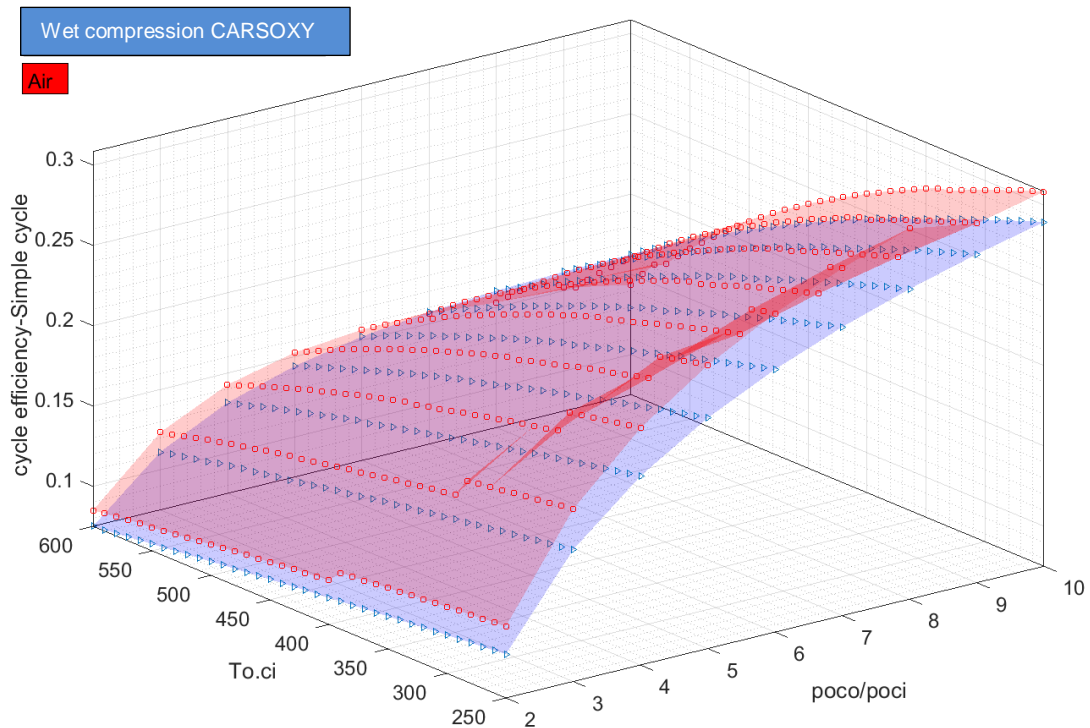


Figure 4.1 Efficiency results for the simple cycle (Wet compression of CARSOXY vs Air).

The dry compression of the CARSOXY-driven simple cycle has maintained a relatively high efficiency in the domain of 300-600K and 6-8 compressor pressure ratio as shown in Figure 4.2. In comparison, the efficiency of the air-driven simple cycle has dramatically dropped at this domain, with the efficiency of the CARSOXY-driven cycle being higher than the air-driven cycle by up to 7%. Nevertheless, at lower

pressure ratios and compressor inlet temperatures, the air-driven simple cycle maintains higher efficiency than the CARSOXY-driven cycle.

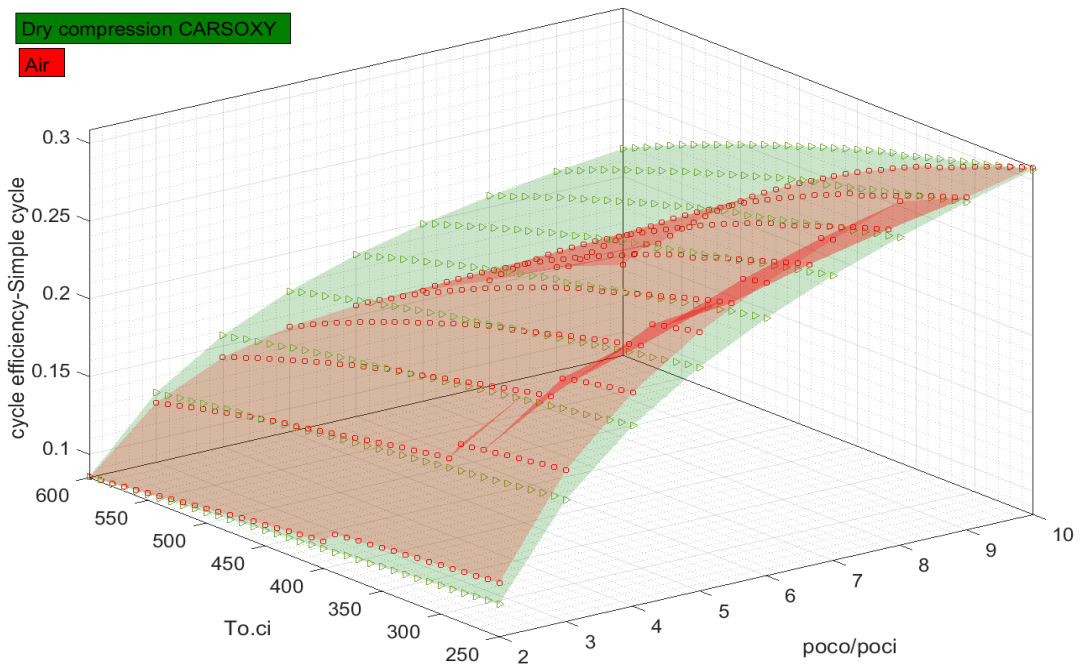


Figure 4.2 Efficiency results for the simple cycle (dry compression of CARSOXY vs Air).

4.2.2 Heat exchanged cycle

Figure 4.3 shows that the CARSOXY-driven heat exchanged cycle with wet compression has higher

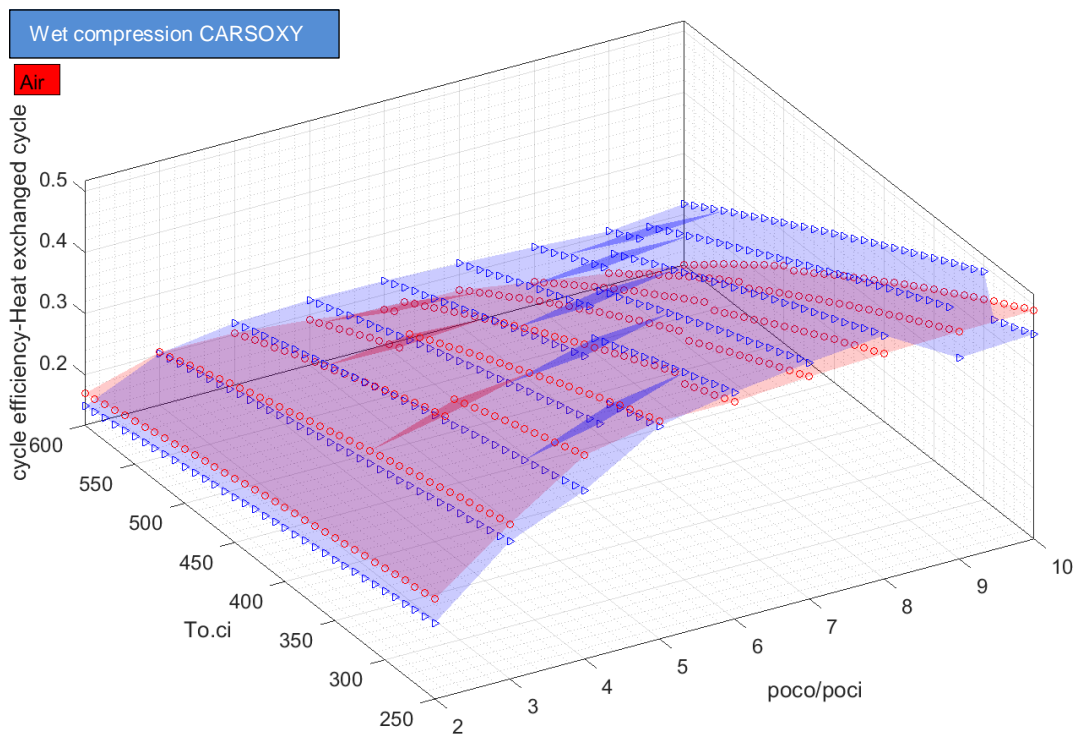


Figure 4.3 Efficiency of the heat exchanged cycle (Wet compression of CARSOXY vs Air).

efficiency by up to 6% relative to the air-driven cycle at the domain of 5-10 compressor pressure ratio and 250-490K compressor inlet temperature. Outside this domain, the air-driven cycle has higher efficiency. The same can be said about Figure 4.4 for dry compression, where the efficiency increased by up to 12% in the higher compressor pressure ratio domain of 4-10. However, it can be said the Air-driven gas turbine has a much smaller interval in which its efficiency is higher than wet CARSOXY gas turbine compared to dry CARSOXY gas turbine (i.e. approximately at pressure ratios of [2-4] at [250-400] K).

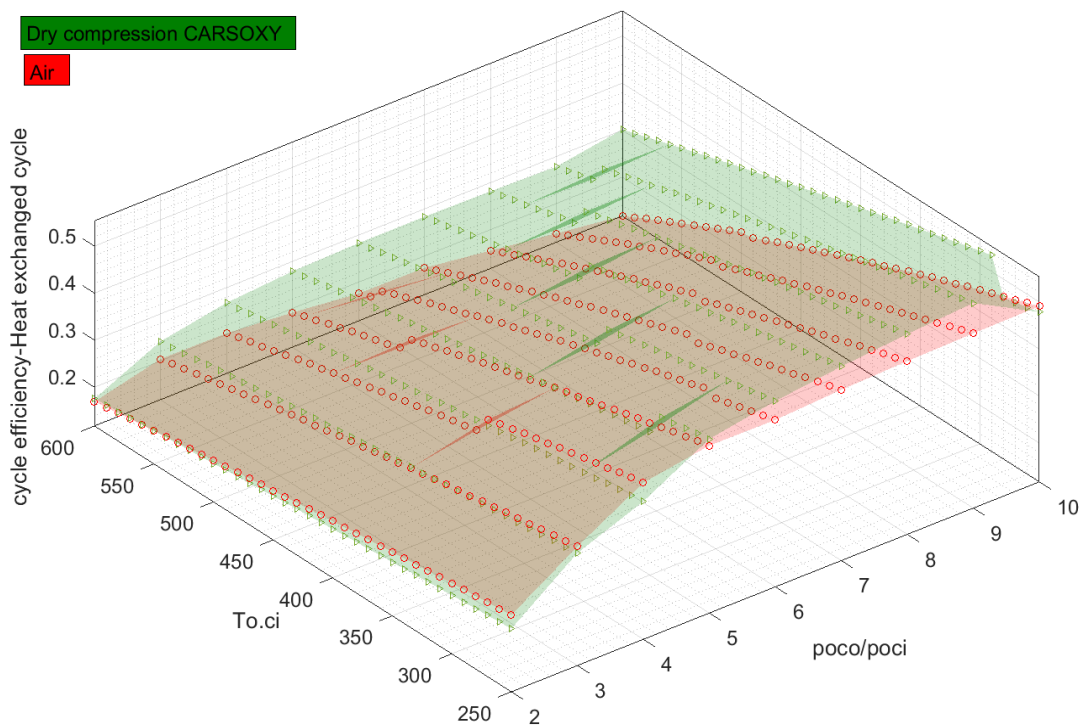


Figure 4.4 Efficiency of the heat exchanged cycle (dry compression of CARSOXY vs Air).

4.2.3 Free turbine & simple cycle

For CARSOXY-driven free turbine & simple cycle, the efficiency relative to the air-driven was higher only at high compressor inlet temperatures above 480K for wet compression for all pressure ratios, Figure 4.5. However, this increase in efficiency is negligible. On the other hand, Air-driven gas turbine illustrated a superior performance in the remaining intervals (i.e. approximately at pressure ratios of [2-10] at [250-470] K, Figure 4.5), where the efficiency increase can approximately reach up to 5% at pressure ratios [5.5-8] at 250 K.

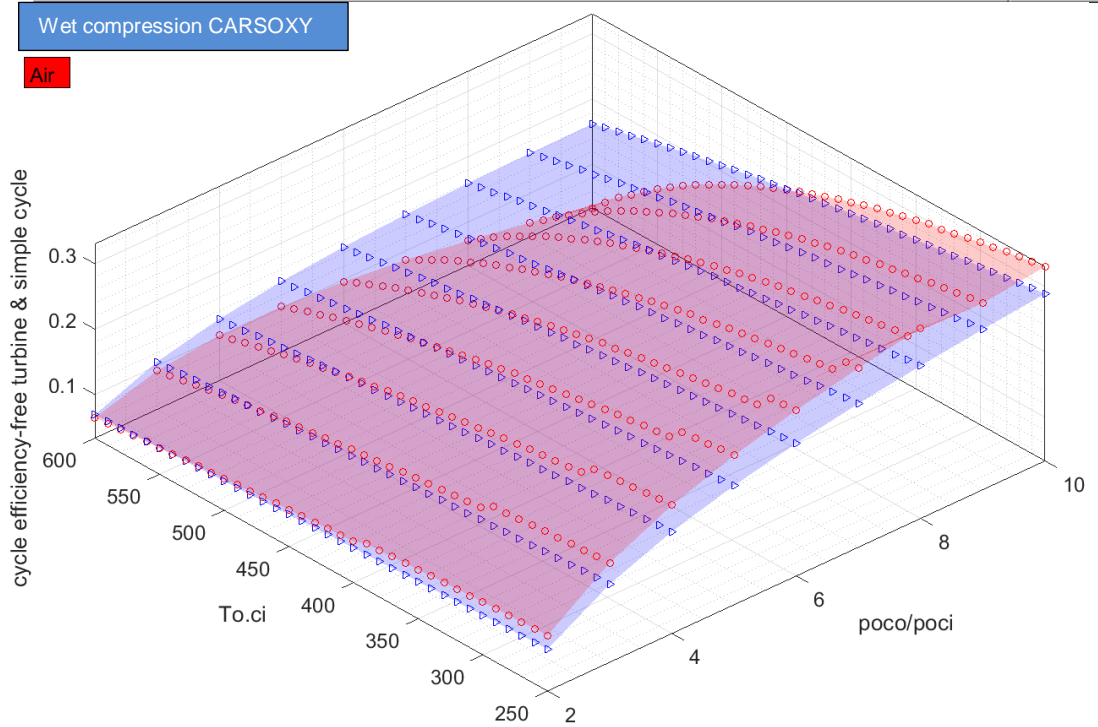


Figure 4.5 Efficiency results for the free turbine-simple cycle arrangement (Wet compression of CARSOXY vs Air)

As shown in Figure 4.6, the efficiency relative to the air-driven was higher only at high compressor inlet temperatures above 360K at all pressure ratios [2-10] for the dry condition of the free turbine- simple

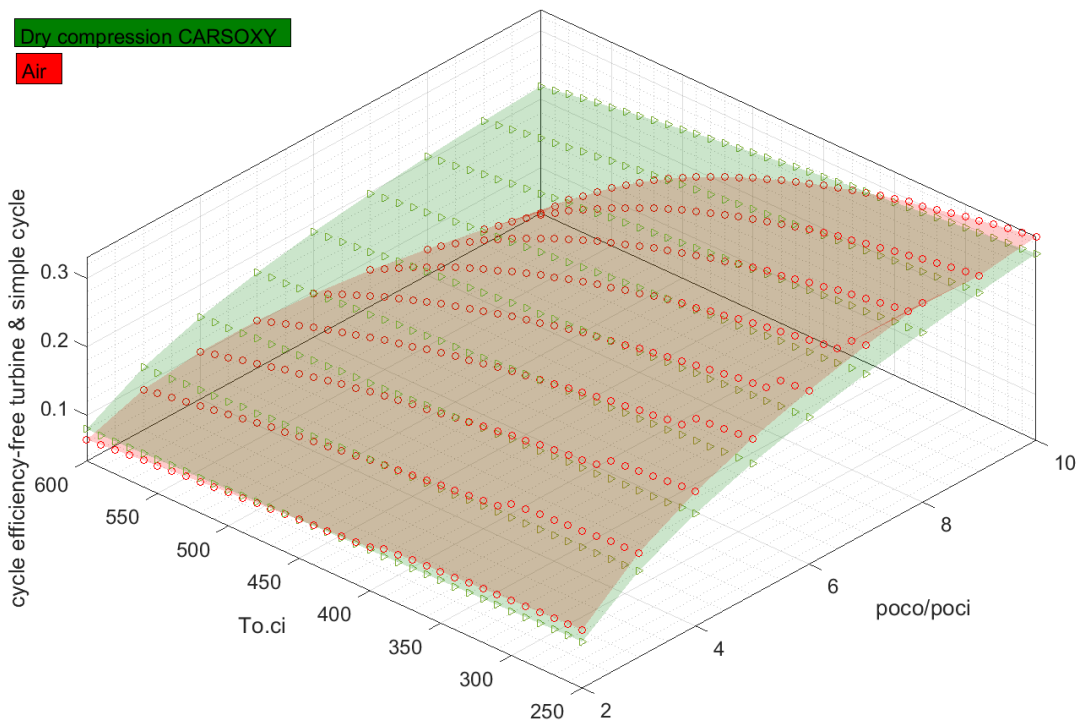


Figure 4.6 Efficiency results for the free turbine-simple cycle arrangement (Dry compression of CARSOXY vs Air)

cycle arrangement. This essentially means that dry condition has increased the interval in which its performance is higher than the Air-driven gas turbine compared to the wet condition. Similarly, Air-driven gas turbine Air-driven gas turbine his higher efficiency in the remaining intervals (i.e. approximately at pressure ratios of [2-10] at [250-360] K, Figure 4.6).

4.2.4 Evaporative cycle

For CARSOXY-driven evaporative cycle, the efficiency has been higher than the air-driven cycle in all conditions by up to 6% for wet compression, Figure 4.7. CARSOXY within this cycle arrangement has boosted the efficiency comparing to the previous cycle (free turbine-simple cycle arrangement at wet). This essentially means that steam molar fraction was capable of increasing turbine power. This increase in power has been capable of compensating the power losses due to wet compression.

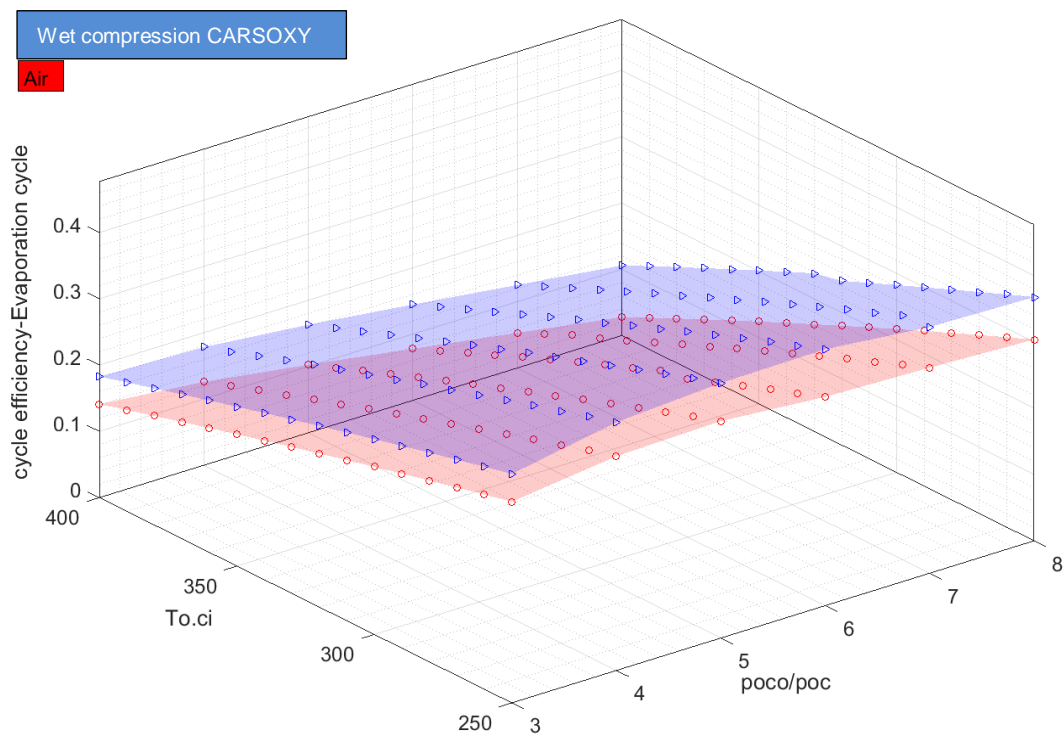


Figure 4.7 Efficiency results for the evaporative cycle (Wet compression of CARSOXY vs Air)

As shown in figure 4.8, the cycle efficiency of CARSOXY is higher than that for the Air driven throughout the entire interval at dry compression. The cycle efficiency is higher by approximately 12%. It is also higher than that of wet compression by approximately 6%. At this point, it is important to highlight that dry compression of the evaporative cycle refers to the implementation of the evaporator after the compressor, whilst before the compressor for wet compression.

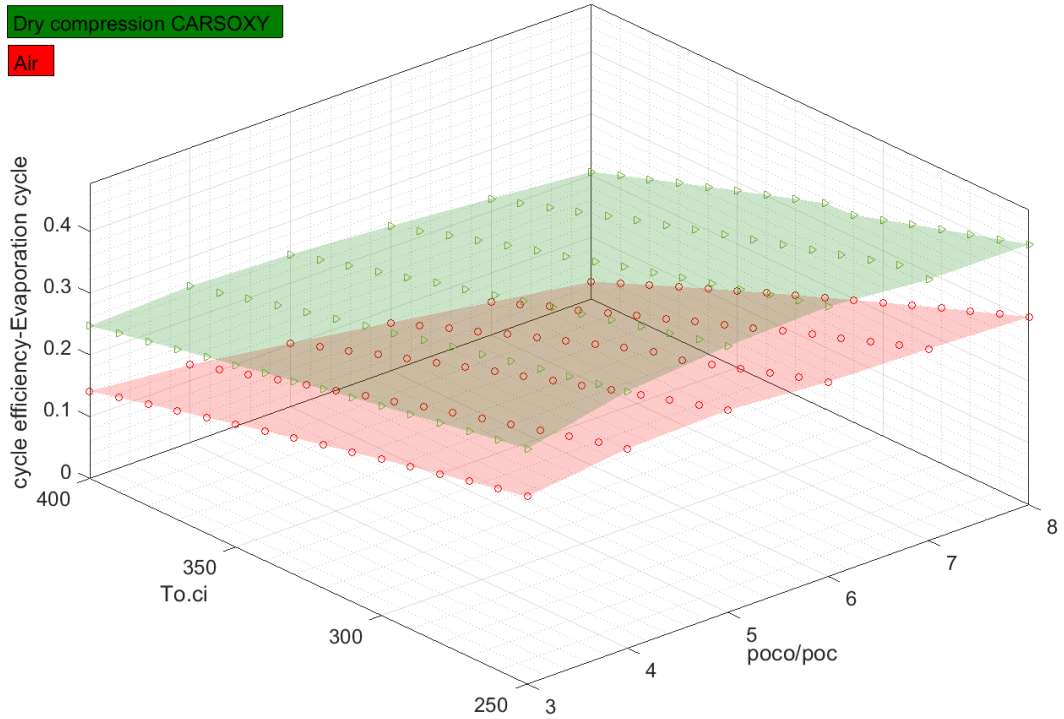


Figure 4.8 Efficiency results for the evaporative cycle (dry compression of CARSOXY vs Air)

4.2.5 Humidified cycle

As can be seen in Figures 4.9 and 4.10, the CARSOXY humidified cycle has higher efficiency at both compression conditions (dry and wet). However, the effect on efficiency becomes more significant

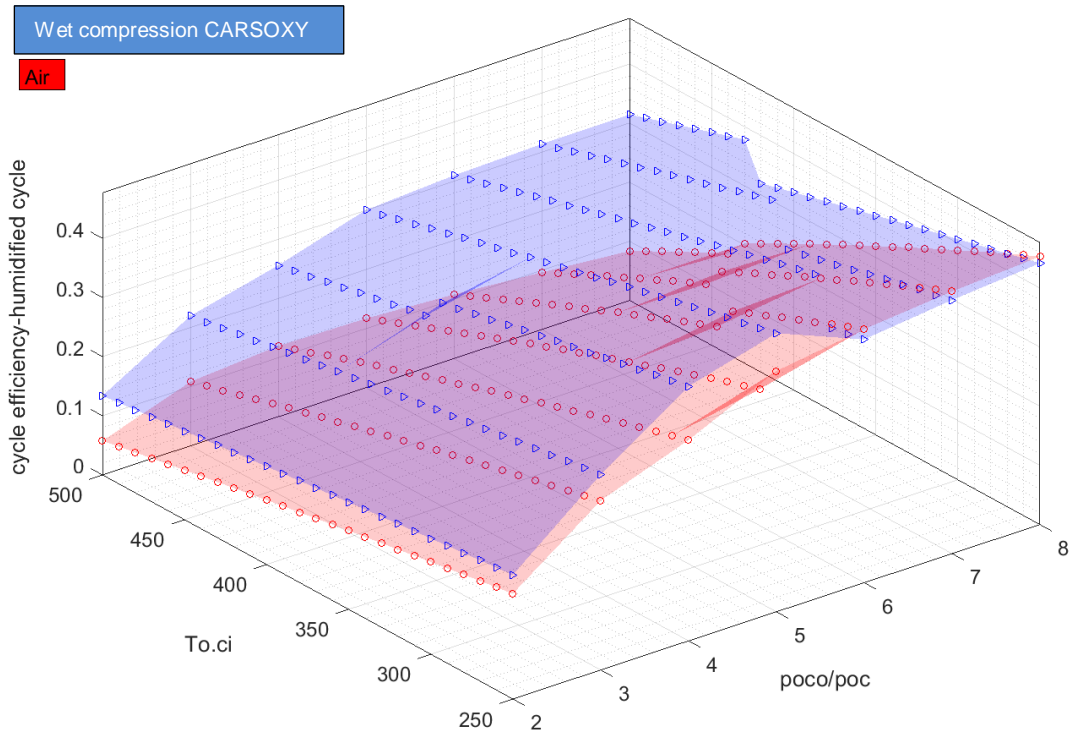


Figure 4.9 Efficiency results for the humidified cycle (Wet compression of CARSOXY vs Air)

as the compressor inlet temperature increases. In fact, the efficiency of the CARSOXY humidified cycle is lower than that for the Air-driven cycle at low temperatures (i.e. at a temperature of 250K and pressure ratios 6-8 bar for wet compression).

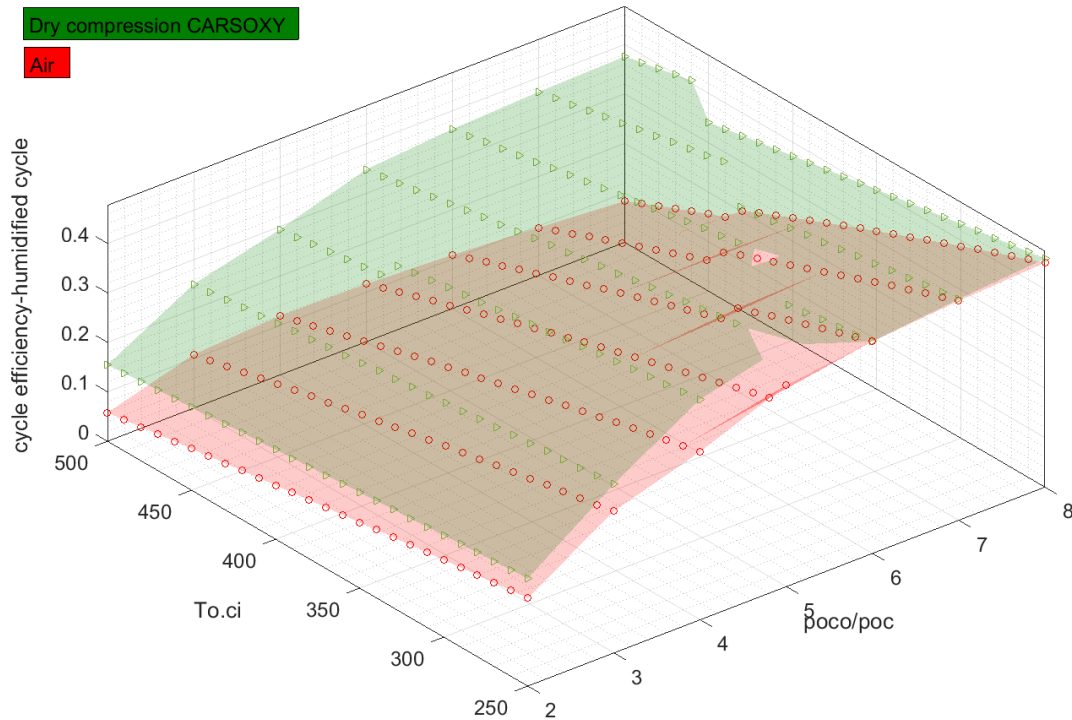


Figure 4.10 Efficiency results for the humidified cycle (Dry compression of CARSOXY vs Air)

4.2.6 Section summary

Complying with the aim of this chapter, the parametric study has been conducted for the five gas turbine cycles (namely; simple, heat exchanged, free turbine & simple cycle, evaporative and humidified, Figure 3.1) using a CO₂-Argon-Steam-Oxyfuel (CARSOXY) mixture-Table 3.1, blend 58- as working fluid in order to identify their ultimate working conditions with respect to cycle efficiency. However, up to this stage of the analysis, those trends could not be attributed to the effect of any specific component of the CARSPXY blend. Instead, the overall performance of the entire CARSOXY blend was assessed to find the ultimate operation CARSOXY within the evaluated cycles. Therefore, section (4.3.6) highlights the effects of CO₂, A_r and H₂O cycle to explain why CARSOXY cycles have shown higher performances in comparison to air-driven cycles.

Table 4.3 provides an approximate summary of the ultimate operation conditions (compressor inlet temperatures and pressure ratio) of CARSOXY-driven cycles under both conditions of wet and dry compression compared to Air-driven gas turbines. The word 'ultimate' refers to the condition where CARSOXY cycle has a higher cycle efficiency in comparison to its own performance in other conditions

while also demonstrating a higher cycle efficiency in comparison to Air-driven gas turbines. To sum up this set of results, dry compression of CARSOXY-driven cycles increases the efficiency in the previously mentioned domains relative to the air-driven cycles. Figure 4.11 compares the five CARSOXY-driven cycles between each other. The heat exchanged cycle has the highest efficiency among the cycles approximately in the pressure ratio intervals of [2-3] (Region 1) and [6-10] (Region 3), whereas at [3-6] (Region 2) the humidified cycle has the highest efficiency. The evaporative cycle has intermediate efficiency values, while the simple cycle and the free turbine-simple cycle has the lowest efficiencies among the five cycles. It is also important to highlight that only the evaporative and humidified cycle consider pressure losses due to steam injection.

Table 4.3 CARSOXY ultimate operation conditions (compressor inlet temperatures and pressure ratio)

Cycle	The ultimate condition of CARSOXY Wet compression		The ultimate condition of CARSOXY Dry Compression	
	Compressor inlet temperature interval [K]	Compressor pressure ratio interval	Compressor inlet temperature interval[K]	Compressor pressure ratio interval
Simple	No interval	No interval	[300-600]	[6-8]
Heat exchanged	[250-490]	[5-10]	[250-600]	[4-10]
Free turbine-simple	[480-600]	[2-10]	[360-600]	[2-10]
Evaporative cycle	[250-600]	[2-10]	[250-600]	[20-10]
Humidified cycle	[340-600]	[2-10]	[240-600]	[2-10]

while the remaining cycles do not consider this effect. This essentially means that including pressure losses due to steam injection would further decrease the efficiency of the simple cycle and the free turbine-simple cycle. In other words, the ideal cases of these two cycles have lower efficiencies than the more realistic cases of the humidified and evaporative cycles. Therefore, these two cycles eliminated for further considerations. Arguably, the heat exchanged cycle does not consider pressure losses due to steam injection while the humidified and the evaporative cycles consider these losses. However, the heat exchanged cycle remains an important perspective for further consideration since a new novel steam injection technique has been suggested (chapter 5) which eliminates the necessity of using the humidified or the evaporative cycles.

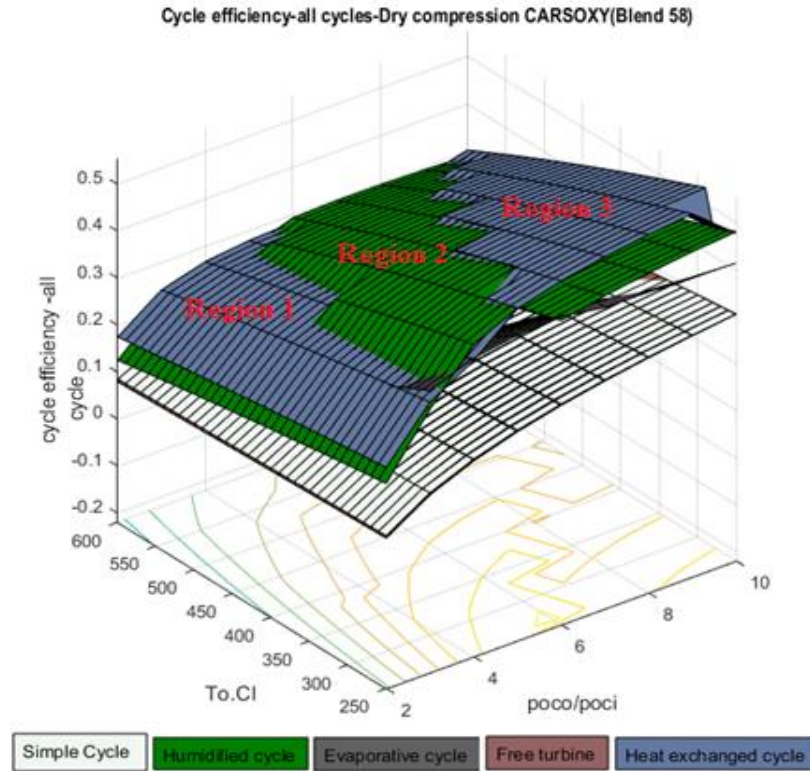


Figure 4.11.Efficiency results for all cycles with dry compression. (Refer to Appendix 4-Figure AP 4.1 for transparent surfaces)

4.3 Efficiency results with respect to variable molar fractions of A_r , CO_2 , and H_2O .

As discussed in section 3.2, the concept of utilizing CARSOXY as a working fluid takes the advantages of using carbon dioxide to maintain turbine temperature within acceptable ranges, argon to increase specific heat ratio, steam to increase the mass flow rate and oxygen to eliminate NO_x emissions. The concept of choosing the ultimate CARSOXY blend was first established by reference [25]. The reference [25] has suggested the use of 150 different CARSOXY blend and studied their effects on cycle efficiency in comparison to an air-driven simple gas turbine cycle. The reference then defined the blend which insures the highest cycle efficiency and defined it as ‘the ultimate’ blend (blend 58, Table 3.1). However, the reference’s choice of the ultimate blend was only compared to a random number of blends with random compositions without identifying the effect of each individual component. Meanwhile, this section studies the combined and individual effect of each component on the cycle efficiency. Based on that, a new ultimate blend is reselected. The choice is based on correlating three intervals of variable molar fractions of carbon dioxide, argon and steam in a three-dimensional efficiency surface, Figure 4.12.

The results have been produced for a range molar fractions of A_r , CO_2 and H_2O where in each case a molar fraction of 25 has been maintained constant for the oxy-fuel (under the conditions and assumptions provided in section 3.2). The results in Figure 4.12 show that the molar fraction of argon is directly proportional to the cycle efficiency and that its effect on increasing the cycle efficiency becomes more significant as the molar fraction of CO_2 decreases. Moreover, the effect of increasing the molar fraction of H_2O is linearly inverse to the cycle efficiency.

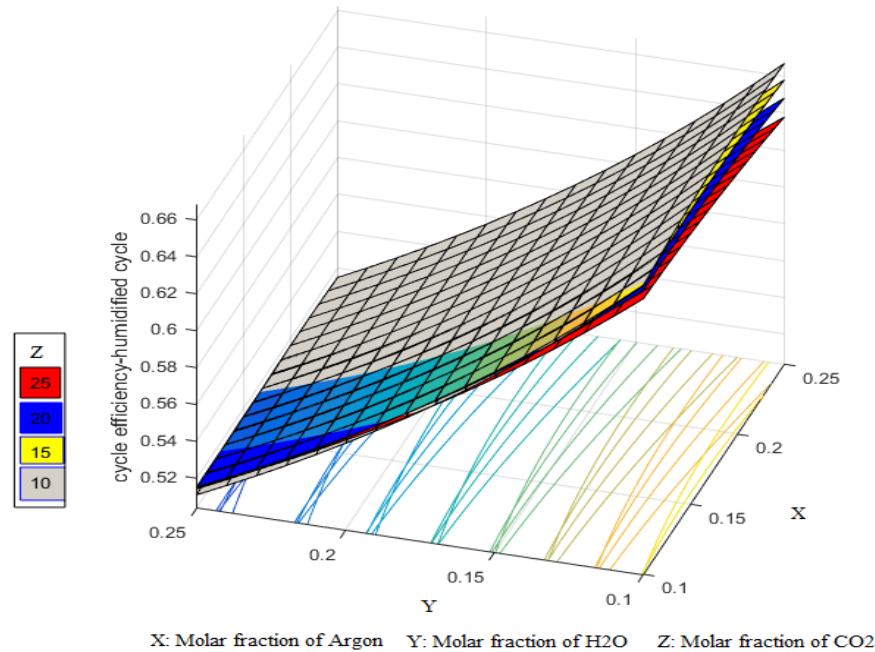


Figure 4.12. Efficiency results with respect to variable molar fractions of Argon, CO_2 , and H_2O (Refer to Appendix 4-Figure AP 4.2 for transparent surfaces).

Therefore, increasing CARSOXY cycle efficiency depends on increasing argon molar fraction while decreasing CO_2 and H_2O . However, this statement shall not be misinterpreted, it does not imply that increasing H_2O molar fraction decreases cycle efficiency (i.e. air-driven cycles). In fact, it is well-known for a fact that injecting steam increase turbine mass flow rate and thus increases cycle efficiency in comparison to other dry cycles, section 2.11.2. However, in the case of CARSOXY, increasing the H_2O molar fraction will be on the cost of reducing argon molar fraction and thus decreasing the cycle efficiency by decreasing the overall specific heat ratio of the working fluid [23-24] (i.e. specific heat ratio of argon is higher than that for steam [163]). Nevertheless, using high levels of argon causes the turbine to overheat [23-24] and dilution becomes a necessity. Therefore, 10% of H_2O molar and 10% of CO_2 molar fractions have been reserved for dilution purposes.

Based on the previous note, a new blend has been suggested with the molar fractions of 47: Argon, 10: H_2O , 10: CO_2 and 33: Oxy-Fuel. This blend has been tested against blend 58 (25: Argon, 23: H_2O , 19: CO_2 and 33: Oxy-Fuel). Results shown in Figure 4.13 indicate that the blend can theoretically increase

the efficiency to greater values than blend (58) by up to an additional 10%. The effect of the suggested blend on increasing efficiency is significant only at low compressor inlet temperatures. In fact, at higher temperatures, i.e. greater than 450K, blend 58 remains superior in terms of cycle efficiency.

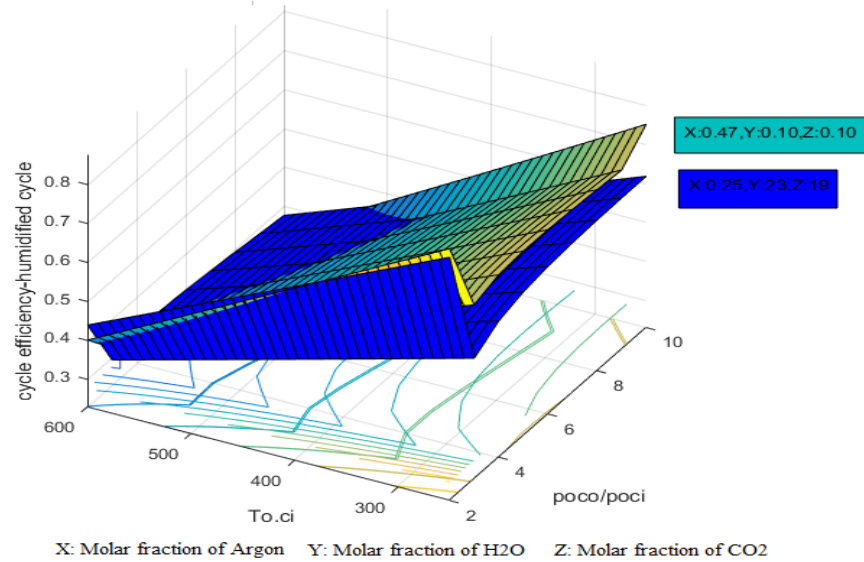


Figure 4.13. Efficiency results for blend 58 and the new suggested blend (Refer to Appendix 4- Figure AP 4.3 for transparent surfaces)

4.4 Efficiency results with respect to the turbine inlet temperature

The effect of increasing the turbine inlet temperature follows the pattern of the conventional air-driven cycles as it increases the cycle efficiency, Figure 4.14. The five cycles remained in the same efficiency ranking order as those plotted with respect to variable compressor inlet temperature, where the heat exchange cycle had the highest efficiency amongst the five cycles. The following results are a sample of increasing turbine temperatures from 800K to 1200K at a compressor pressure ratio of 3 and an inlet temperature of 298K, Table 4.4.

Table 4.4 a sample results of increasing turbine temperatures from 800K to 1200K at a pressure ratio of 3 (Efficiencies at turbine temperature 800K and 1200K (η_{800K} and η_{1200K} , respectively)

Cycle	η_{800K}	η_{1200K}	Absolute increase ($\eta_{1200K} - \eta_{800K}$)	Relative increase $\frac{(\eta_{1200K} - \eta_{800K})}{\eta_{800K}}$
simple cycle	11%	11%	Negligible	Negligible
Heat exchanged cycle	18.75%	26%	7.25%	38.7%
Free turbine & simple cycle	10%	10%	Negligible	Negligible
evaporative cycle	17%	24.6 %	7.60%	44.7%
humidified cycle	12.50%	18.75%	6.25%	50%

However, turbine inlet temperature increases are highly limited by material limitations of the turbine blades at the turbine stage, especially when the temperature is already at a relatively high value.

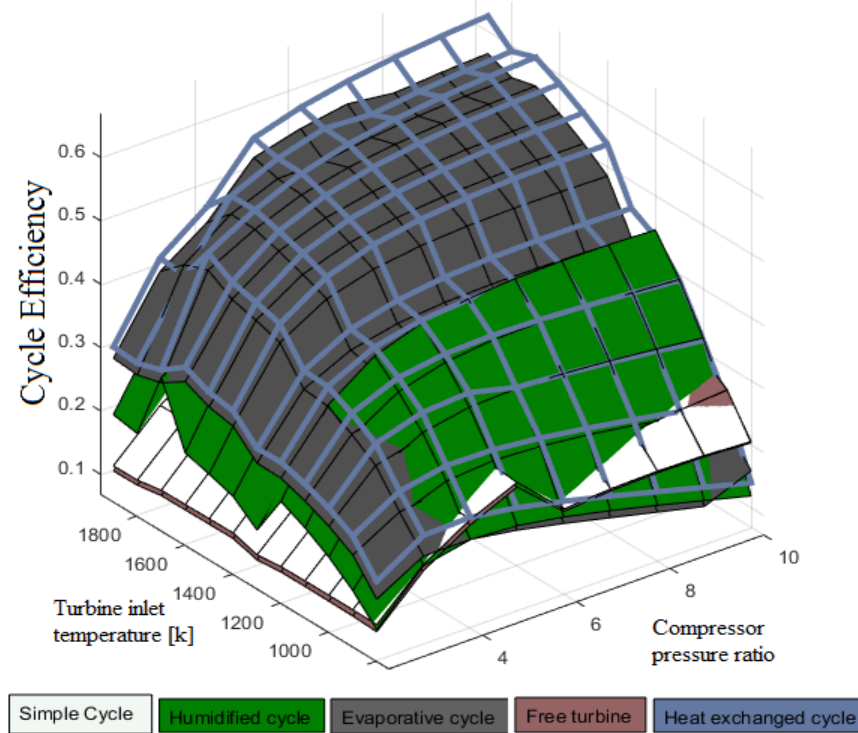


Figure 4.14. Efficiency results for all cycles with respect to turbine inlet temperature variation.
(Refer to Appendix 4-Figure AP 4.4 for transparent surfaces)

Complying with the aim of this chapter, the parametric study has been conducted for the five gas turbine using blend 58 as a working fluid in order to identify their ultimate working conditions with respect to cycle efficiency. However, the cycle response with respect to variable turbine inlet temperature could not be attributed to the effect of any specific component of the CARSPXY blend. Instead, the overall performance of the entire CARSOXY mixture (blend58) was assessed.

4.5 Discussion

The performance of each cycle was determined by plotting the cycle efficiency with respect to the combined effect of varying the compressor inlet temperature and pressure ratio, Figure. 4.11. It can be seen that the Humidified cycle and the heat exchanged cycle have the highest efficiencies amongst cycles. However, neither the heat exchanged cycle nor the Humidified cycle has the ultimate performance over the entire variation domain. The heat exchanged cycle is the ultimate in regions 1 and 3, Figure 4.11. Meanwhile, the Humidified cycle is the ultimate cycle in region 2. It can be concluded that the final CARSOXY gas turbine cycle can use one of the two options (either the heat exchanged or the Humidified cycle). Therefore, cycle efficiencies have been plotted with respect to the combined effect of varying

turbine inlet temperature and compressor pressure ratio, Figure. 4.14. These results played as a decision-making factor for the next stage of development. The heat exchanged cycle has the highest efficiency approximately over the entire variation domain. Therefore, it was chosen to be simulated with Aspen Plus. Arguably, the heat exchanged cycle does not consider pressure losses due to steam injection while the humidified and the evaporative cycles consider these losses. However, the heat exchanged cycle remains an important perspective for further consideration since the new novel steam injection technique which has been suggested (chapter 5) eliminates the necessity of using the humidified or the evaporative cycles.

4.6 Conclusion

CARSOXY-driven cycles can increase the cycle efficiency in the right domains of operating conditions. These domains have been identified for each cycle. Efficiency increase can be up to 12% using a heat exchanged cycle with dry compression. This has been defined as the ultimate arrangement since it is more efficient than an air-driven cycle at any operating condition. The results have shown that the cycle efficiency using CARSOXY blends can be increased as the compressor inlet temperature decreases and the turbine inlet temperature increases. It can be concluded that a compressor inter-cooling system and a turbine re-heater can be used for CARSOXY-driven cycles. However, additional turbine re-heater and compressor inter-cooling systems would penalize the compactness of the cycle. Compressor inter-cooling systems may involve water, which would partially lead to wet compression. Based on the results obtained wet compression reduces the cycle efficiency. Therefore, special care needs to be taken in choosing and implementing the inter-cooling system. Additional 10% increase of the cycle efficiency can be theoretically achieved by a new blend which has the molar fractions of 47% argon, 10% carbon dioxide, 10% H₂O and 33% oxy-fuel at low compressor inlet temperatures. Increasing argon molar fraction and decreasing the molar fraction of H₂O have dominant effects on increasing the overall cycle efficiency. However, increasing argon molar fraction is challenging as air is composed of 78.12% nitrogen, 20.95% Oxygen, and only 0.93% Argon. Therefore, it is crucial to carefully choose the adequate air separation unit in order to provide the necessary amount of argon for the new blend. Finally, an economically sustainable approach shall be adopted to produce CARSOXY within the required molar fractions. Chapter 5 suggests a novel approach to produce CARSOXY whilst chapter 6 evaluates its economic sustainability. The Modified Internal Rate of Return (MIRR) of the CARSOXY cycle –suggested in chapter 5- is approximately 2.2% higher than that for the Air-driven cycle, chapter 6. Moreover, the profitability index (PI) of the CARSOXY cycle is 1.72, while it is only 1.28 for the Air-driven cycle, chapter 6.

CHAPTER FIVE

A novel approach to produce CARSOXY.

“I just want to build great products.”

~ Tim Cook

CHAPTER 5 – A NOVEL APPROACH TO PRODUCE CARSOXY (BLEND 58)

This chapter provides a novel approach to continuously supply a gas turbine with a CARSOXY blend within required molar fractions. The approach involves H₂ and N₂ production, therefore having the potential of also producing ammonia. Thus, the concept allows CARSOXY cycles to be used to support the production of ammonia whilst increasing power efficiency.

An ASPEN PLUS model has been developed to demonstrate the approach. The model involves the integrations of an air separation unit (ASU), a steam methane reformer (SMR), water gas shift (WGS) reactors, pressure swing adsorption (PSA) units and heat exchanged gas turbines (HXGT) with a CCS unit. Sensitivity analyses were conducted on the ASU-SMR-WGS-PSA-CCS-HXGT model. The results provide a baseline to calibrate the model in order to produce the required CARSOXY molar fraction. The MATLAB code (described in section 3.2) provided results to study CO₂ compression effects on the CARSOXY gas turbine compressor.

The chapter provides the conditions in which the sensitivity analyses have been conducted to determine the best operable regime for CARSOXY production with other high valuable gases (i.e. hydrogen). Under these specifications, the sensitivity analyses on the (SMR) sub-model spots the H₂O mass flow rates, which provides the maximum hydrogen level, the threshold which produces significant CO₂ levels. Moreover, splitting the main CH₄ supply to sub-supply an SMR reactor and a furnace reactor correlates to best practices for CARSOXY. The sensitivity analysis has also been performed on the (ASU) sub-model to characterise its response with respect to the variation of airflow rate, distillation/boiling rates, product/feed stage locations and the number of stages of the distillation columns.

The sensitivity analyses have featured the response of the ASU-SMR-WGS-PSA-CCS-HXGT model. In return, the model has been qualified to be calibrated to produce CARSOXY within two operability modes, with Hydrogen and Nitrogen or with Ammonia as by-products. This Chapter provides the adopted numerical attempts to calibrate the model from its initial value to its final values, Table 3.2.

5.1 Sensitivity analyses

The sensitivity analysis in this thesis is provided for the parameters that are the most effective means to control the products molar fractions. These are steam to carbon mole ratio (S/C), steam mole flow rate, and SMR to FURNACE mass split ratio in CH₄SPLIT in the SMR sub-model. Similarly, in the WGS sub-model, water mole flow (WGS_{H2O}) is the most effective method to control the molar fractions of the products. In the ASU sub-model, ATMIR and AIRLP mole flow rates are analyzed, while some of

the parameters in the LPDC have been also modified from their initial values. The following results have been produced within the initial values as specified in Table 3.2 and for the initial sub-models (Figures 5.1 and 5.7).

5.1.1 SMR sub-model sensitivity analysis

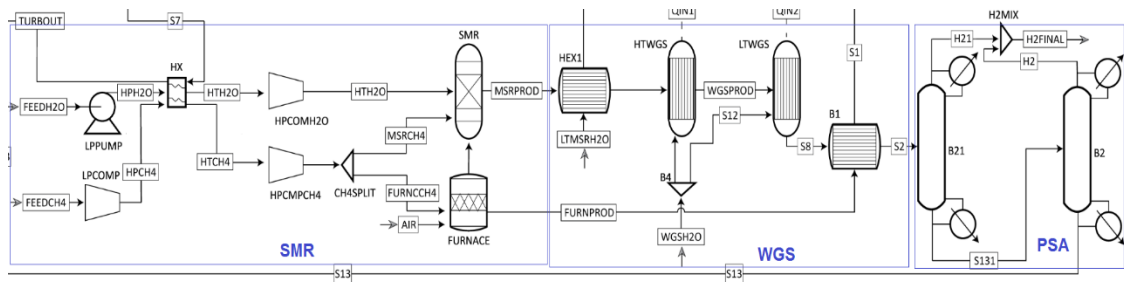


Figure 5.1: Initial SMR, WGS and PSA sub-model, those are parts of the ASU-SMR-WGS-PSA-CCS-HXGT model (this Figure is a part of Figure 3.2)

5.1.1.1 SMR molar fractions vs H2O feed

Figure 5.2 shows the sensitivity analysis when varying the mass flow of water from 10 kg/h to 510 kg/h with respect to the molar fractions of the product stream from the SMR. The remaining parameters are within the initial values as specified in Table 3.2.

It can be seen that increasing the water mass flow increases the molar fraction of hydrogen in the SMR product. However, increasing the water mass flow beyond 350 kg/h has a negligible effect on hydrogen production. Line C (at 350 kg/h of H₂O feed) corresponds to the point in which hydrogen molar fraction remains constant regardless of the increase of the H₂O flow rate. One of the remarkable notes can be seen with the help of Line B (at 225 kg/h of H₂O feed), CO starts to decrease and CO₂ starts to increase. This indicates that a water-gas-shift reaction would partially take place in the reformer after this point (225 kg/h of H₂O). Meanwhile, Line A (at 175 kg/h of H₂O feed) indicates the highest conversion factor of H₂O (at 175 kg/h of H₂O feed).

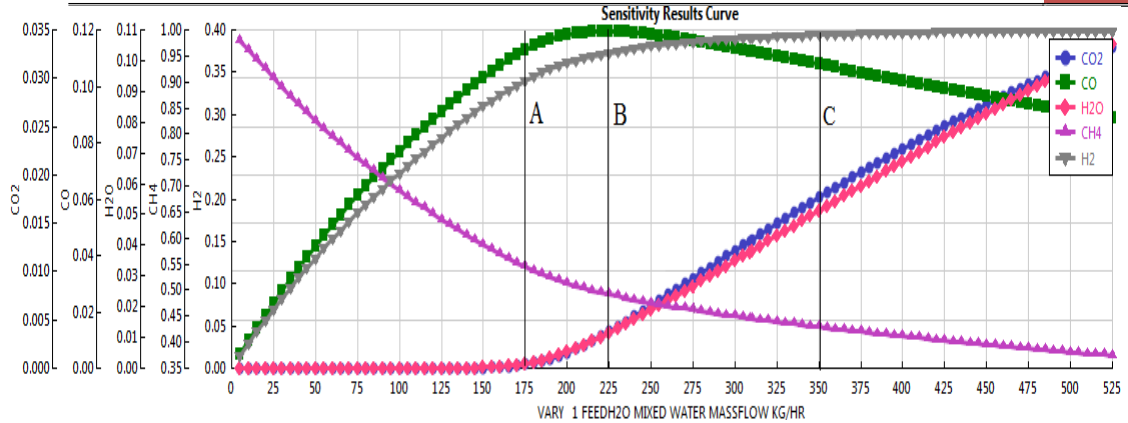


Figure 5.2: SMR sensitivity results (SMR molar fractions vs H₂O feed). Lines A, B and C correspond to the H₂O flow rates of 175, 225 and 350 kg/h, respectively.

5.1.1.2 SMR molar fractions vs CH₄ feed

Figure 5.3 shows the sensitivity analysis when varying the mass flow of methane from 10 kg/h to 950 kg/h with respect to the molar fractions of the product stream from the SMR. The remaining parameters are within the initial values as specified in Table 3.2.

Up to Line D, which corresponds to the H₂O / CH₄ feed mass ratio of 1.54 and methane conversion factor of 0.315, CO₂ increases as the mass flow of CH₄ increases. Beyond this line, CO₂ starts to decrease and CO increases as the CH₄ mass flow increases. High hydrogen molar fraction can be obtained by increasing the CH₄ mass flow rate. However, this would be at the expense of overproducing CO. Moreover, CO₂ production would also be reduced, which is undesirable to the case of CCS or even in the CARSOXY cycles.

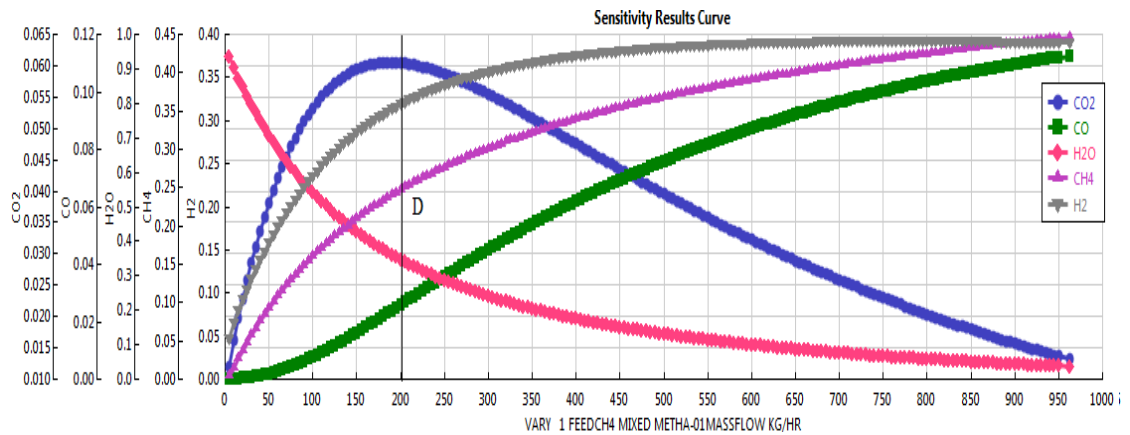


Figure 5.3: SMR sensitivity results (SMR molar fractions vs CH₄ feed). Line D corresponds to the CH₄ flow rate of 200 [kg/h].

5.1.1.3 SMR molar fractions vs CH₄ split ratio

Figure 5.4 shows the sensitivity analysis when varying the split ratio (SMR to FURNACE) of the CH₄SPLIT splitter from 0.925 to 1. The remaining parameters are within the initial values as specified in Table 3.2.

Figure 5.4 shows that carrying the split ratio (SMR to FURNACE) is one of the very effective methods to control the molar fractions of the SMR. The conversion factor of CH₄ decreases as the SMR receives more methane and the furnace receives less methane. This is due to the fact that the SMR becomes less activated as the furnace supplies less heat, which is due to the reduction of furnace feed of methane.

The CO₂ molar fraction in the SMR product has significantly increased. In fact, the increase of the molar fraction curve of CO₂ could be underestimated for the actual increase of CO₂ moles in the products. It must be highlighted that the molar fraction of CO₂ has increased even with the additional increase of the total moles — more CH₄ moles — in the mixture. This is indeed desirable for CARSOXY production since high levels of CO₂ is produced within the minimal conversion of CH₄.

However, the splitting fraction of the SMR methane feed shall not exceed the limit where the CO₂ molar fraction is at the peak since this would be the threshold of the full deactivation of the SMR which is basically neither in favour of the CARSOXY approach (i.e. high molar fractions of CO₂ and CH₄) nor the conventional approach (i.e. high CH₄ conversion factor).

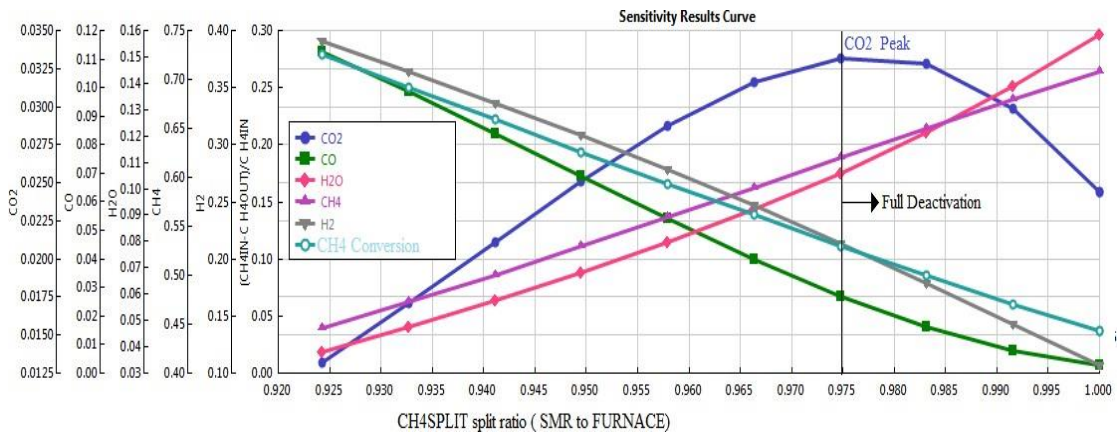


Figure 5.4: SMR sensitivity results (SMR molar fractions vs CH₄ split ratio)

5.1.1.4 SMR molar fractions vs Furnace Air mass flow rate

Figure 5.5 shows the sensitivity analysis of varying the furnace air mass flow from 25 kg/h to 1900 kg/h with respect to the molar fractions of the product stream from the SMR. The remaining parameters are within the initial values as specified in Table 3.2.

As the air mass flow rate increases up to 1000kg/h, the production of hydrogen, carbon dioxide and carbon monoxide increases. However, it can be seen that the molar fraction of CH₄ significantly drops. This is an expected and desirable result for conventional SMR. Unlike the conventional SMR, CARSOXY SMR aims to produce high levels CO₂ within the minimal conversion of CH₄. Therefore, Line E which corresponds to the airflow rate of 650 kg/h could be the ultimate choice to compromise between both requirements.

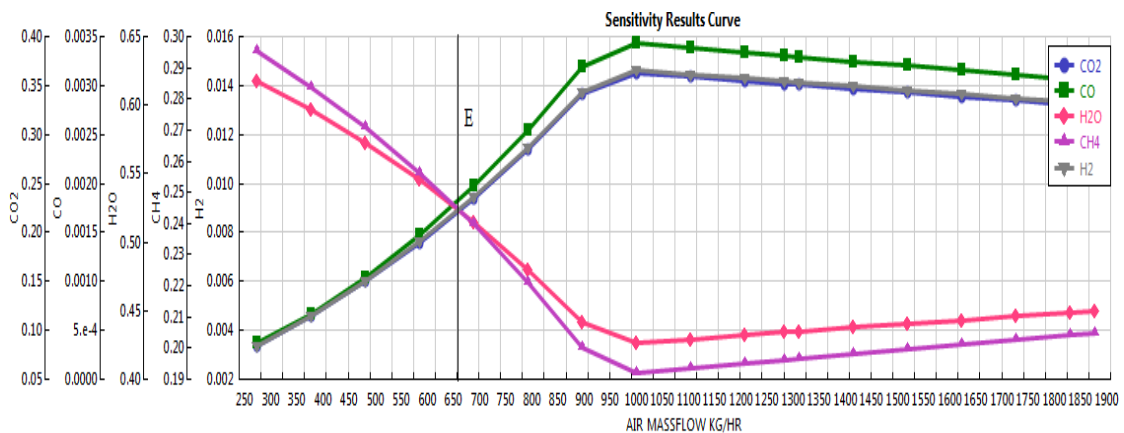


Figure 5.5: SMR sensitivity results (SMR molar fractions vs Furnace Air mass flow rate).Line E corresponds to the airflow rate of 650 kg/h.

5.1.2 WGS sub-model sensitivity analysis

Figure 5.6 shows the molar fraction variation of the WGS product with respect to the variation of the H₂O mole flow rate in the (WGS H₂O) stream. The remaining parameters are within the initial values as in Table 3.2.

It can be seen that increasing H₂O mole flow rate up to 5.25 kmol/h ensures effective WGS. In the effective region, the WGS has zero molar fractions of H₂O. This indicates that all H₂O molecules have reacted with carbon monoxide molecules to produce hydrogen and carbon dioxide. However, increasing the mole flow rate of H₂O beyond 5.25 kmol/h does not increase hydrogen nor carbon dioxide production since the WGS approaches its ineffective region. Unreacted H₂O molecules appear in the WGS product since no further reactions take place in this region. This increases H₂O molar fraction. As a result, CH₄, CO₂, and H₂ molar fractions decrease. However, their actual moles remain constant. The ineffective region allows any desired modification of the H₂O molar fraction in order to match the required H₂O level in any CARSOXY blend.

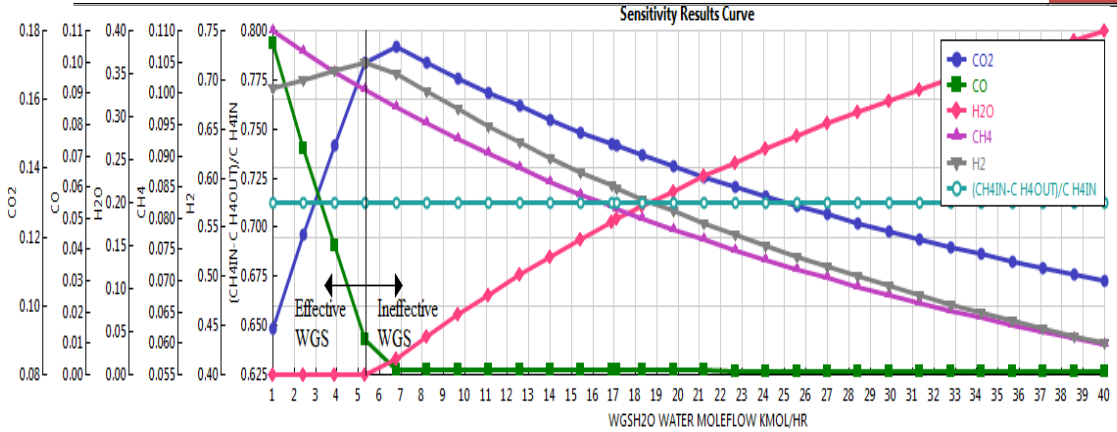


Figure 5.6: WGS sensitivity results (WGS product molar fractions vs WGS H₂O mass flow rate)

5.1.3 ASU sub-model sensitivity analysis

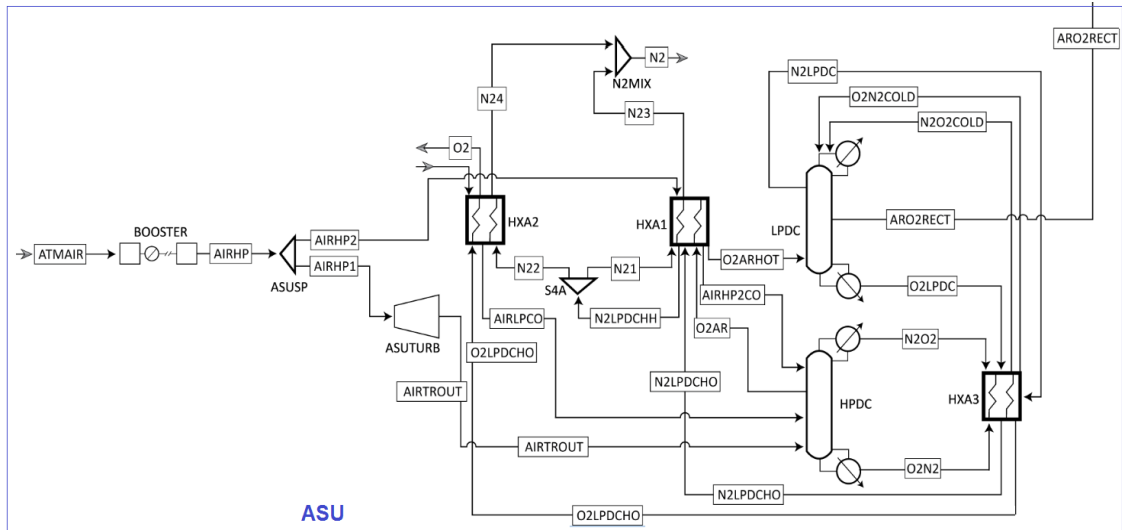


Figure 5.7: ASU initial Model

5.1.3.1 ARO2RECT molar fractions vs BOOSTER discharge pressure

Figure 5.8 shows the results of the molar fractions of the (ARO2RECT) stream with respect to varying the discharge pressure of the (BOOSTER). The remaining parameters are within the initial values as specified in Table 3.2.

It can be seen that the molar fractions of the (ARO2RECT) stream are insensitive towards the variation of the discharge pressure. However, this result shall not be misinterpreted, as the discharge pressure also affects other parameters such as the distillate rate, boil-up rate and other heat duties. It can be seen from Table 2 that the discharge pressure final value is 76 bar, while the initial value is 121.59 bar. Since the results have been plotted for the initial values, the following set of results is only relevant for the 121.59 bar of the (BOOSTER) discharge pressure.

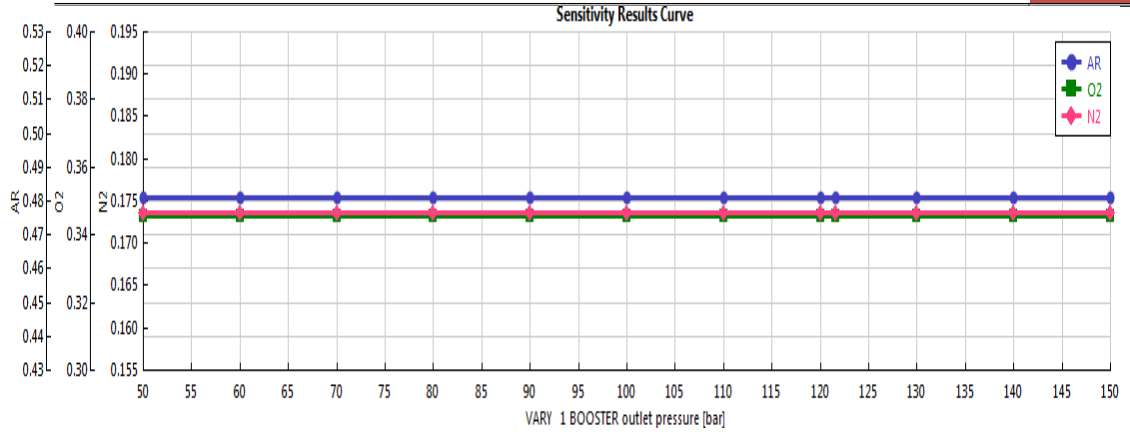


Figure 5.8: ARO2RECT molar fractions vs BOOSTER discharge pressure

5.1.3.2 ARO2RECT molar fractions vs ATMIR mole flow rate

Figure 5.9 shows the molar fractions of A_r, O₂, and N₂ in the (AR) stream. The molar fractions correspond to the variation of the mole flow rates of the (ATMAIR) stream in the interval of 4300-6400 kmol/h. The remaining parameters are within the initial values as specified in Table 3.2.

From 4300 to 4900 kmol/h, the LPDC is incapable of separating argon from oxygen. The separation process starts only when the flow rate of the (ATMAIR) is approximately from 4900 to 5400 kmol/h. The highest purity argon is obtained at 5350 kmol/h with minor residuals of nitrogen and oxygen. Beyond 5400 kmol/h, the (A_r) stream is only composed of nitrogen, which indicates that the number of stages in the LPDC has to be adjusted or the (ARO2RECT) product stage has to be changed.

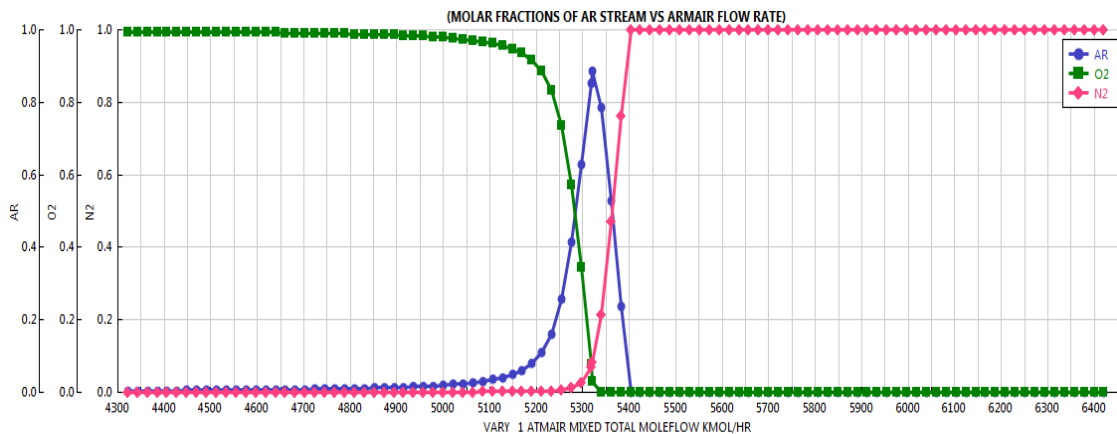


Figure 5.9: ARO2RECT molar fractions vs ATMIR mole flow rate

5.1.3.3 ARO2RECT molar fractions vs AIRLP mole flow rate

Figure 5.10 shows the molar fractions of Ar, O₂, and N₂ in the (AR) stream. The molar fractions correspond to the variation of the mole flow rates of the (AIRLP) stream in the interval of 300-1200 kmol/h. The remaining parameters are within the initial values as in Table 3.2.

The results in Figure 10 followed the same pattern as those in Figure 9. However, the separation process starts only when the flow rate of the (AIRLP) is approximately in the interval of 610-840 kmol/h

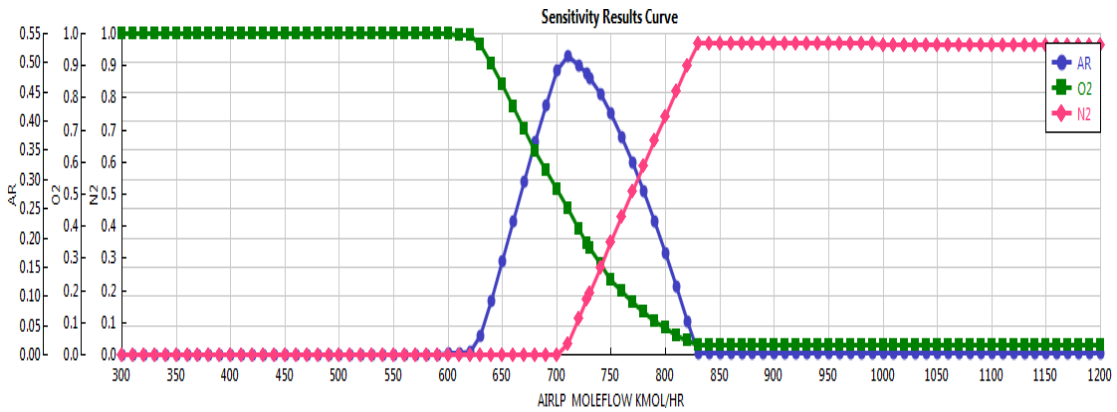


Figure 5.10: ARO2RECT molar fractions vs AIRLP mole flow rate

5.1.3.4 ARO2RECT molar fractions vs LPDC number of stages

As demonstrated in Figure 5.11 the molar fractions of oxygen in the (ARO2RECT) can be maximized if the number of LBDC stages is in the interval of 8-23 stages, while the remaining parameters are within the initial values as specified in Table 3.2.

However, this interval provides a very low level of argon molar fraction. As the number of stages increases beyond 23 stages, the molar fraction of argon increases. Meanwhile, the molar fraction of oxygen decreases and the molar fraction of nitrogen remain approximately unaffected.

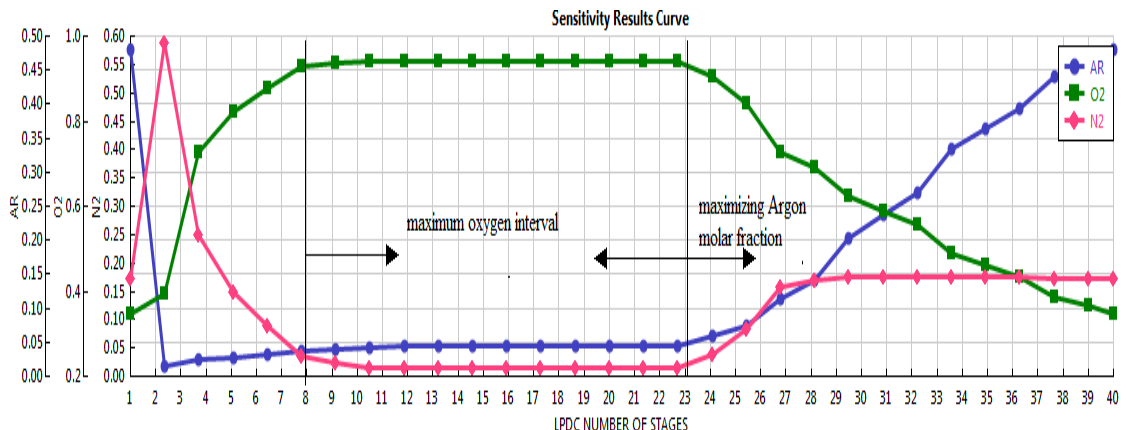
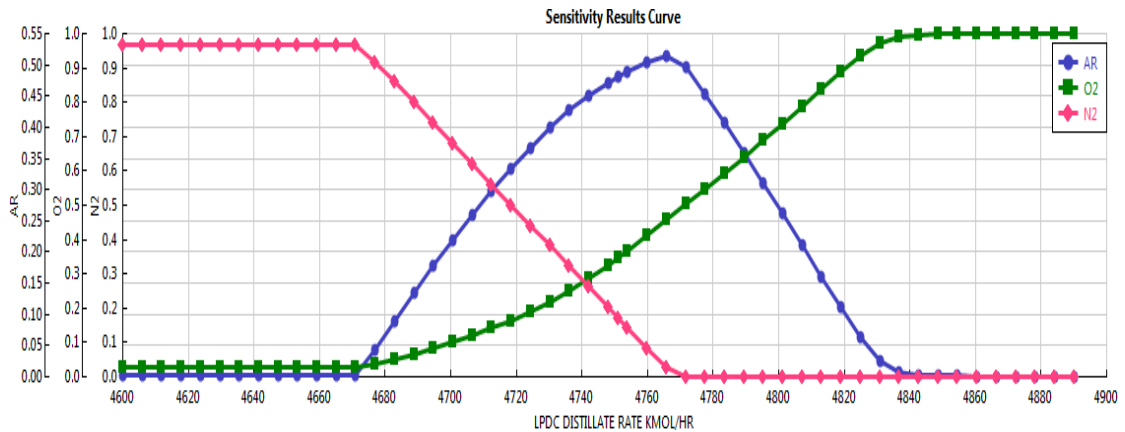


Figure 5.11: ARO2RECT molar fractions vs LPDC number of stages

5.1.3.5 ARO2RECT molar fractions vs LPDC Distillate rate

It can be seen in Figure 5.12 that the (LPDC) has the highest molar fraction of argon at a distillate rate of approximately 4765 kmol/h, The remaining parameters are within the initial values as specified in Table 3.2.

The oxygen and nitrogen molar fraction curves followed approximately the opposite patterns of those in Figure 5.9 and Figure 5.10. It can be generally concluded that the molar fraction of oxygen is directly proportional to the distillate rate of the (LPDC) but inversely proportional to airflow rates in the (ATMIR)



and (AIRLP) streams. In the three cases (i.e. varying the (ATMIR) flow rate, (AIRLP) flow rate, (LPDC) distillate rate), nitrogen molar fraction followed approximately the opposite curve-patterns of oxygen.

Figure 5.12: ARO2RECT molar fractions vs LPDC Distillate rate

5.1.3.6 ARO2RECT molar fractions vs LPDC Boil-up rate

Figure 5.13 illustrates that as the boil-up rate increases in the (LPDC)-while the remaining parameters are within the initial values as specified in Table 3.2-, the molar fractions of oxygen and argon increase in the (ARO2RECT) as well. Meanwhile, the molar fraction of nitrogen decreases.

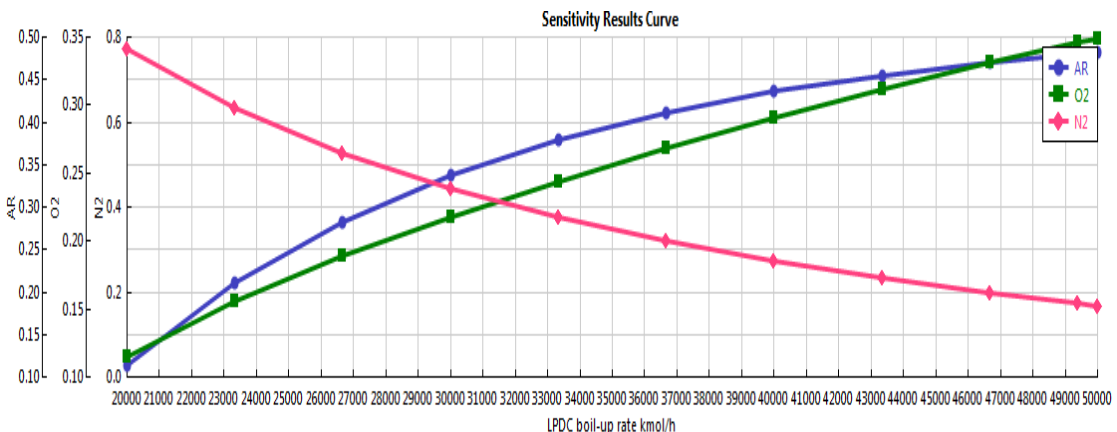


Figure 5.13: ARO2RECT molar fractions vs. LPDC Boil-up rate

5.1.3.7 ARO2RECT molar fractions vs O2ARHOT Feed stage location in the LPDC

Each column in the ASU sub-model is divided into a series of stages, which are numbered from the top down. Figure 5.14 shows that a mixture with high levels of argon and oxygen can be harvested with a zero residual of nitrogen if the feed stage of the (ARO2RECT) is over stage 3. The molar fractions of oxygen and argon can reach approximately 50% each between the third and the fourth stage.

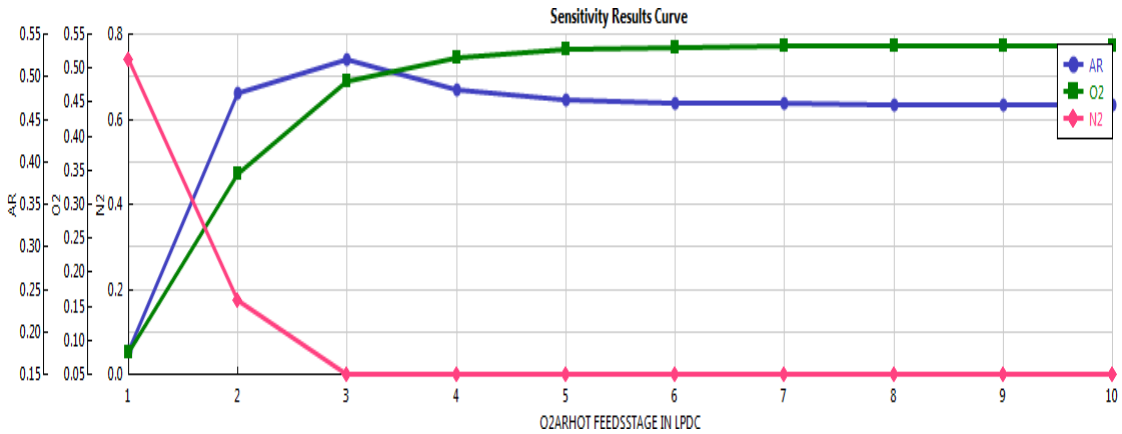


Figure 5.14: ARO2RECT molar fractions vs O2ARHOT Feed stage location in the LPDC

5.1.3.8 ARO2RECT molar fractions vs ARO2RECT and O2LPDC Feed stage location in the LPDC product stage location in the LPDC

It can be seen from Figure 5.15 that a mixture with dominant molar fraction of argon can be obtained in the interval of 7-30 of (ARO2RECT) product stage, while the remaining parameters are within the initial values as specified in Table 3.2. If the mixture is required to contain a dominant molar fraction of oxygen, then the (ARO2RECT) product stage shall be over 30. The molar fractions in the (ARO2RECT) are insensitive of the product stage location of the (O2LPDC) stream.

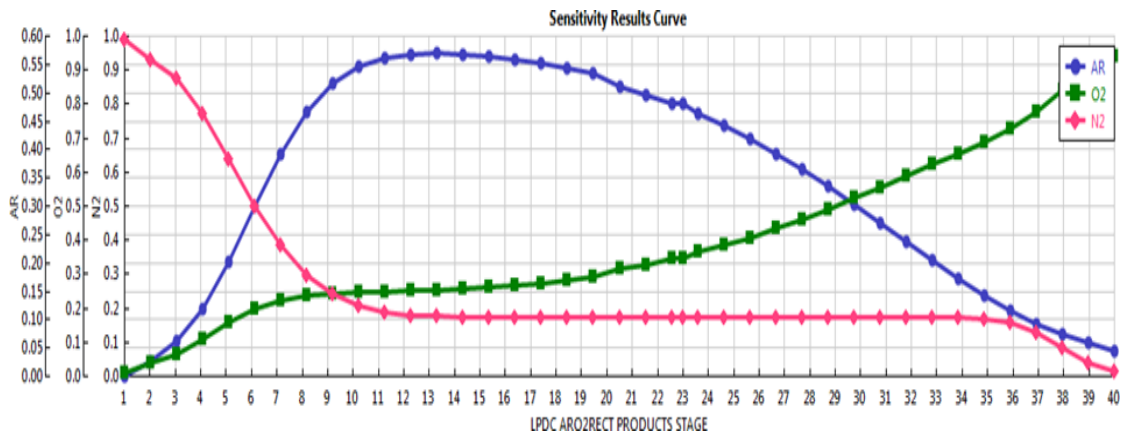


Figure 5.15: ARO2RECT molar fractions vs ARO2RECT product stage location in the LPDC

5.1.3.9 Oxygen-Argon-Carbon dioxide compression vs Oxygen-Argon compression

As it has been discussed previously in section (3.3.7), the compressor is fed by the oxygen- argon stream (ARO2RECT) instead of a carbon dioxide-argon stream. Therefore, the results in Figure 5.16 have been produced using the MATLAB code, discussed in section (3.2), to validate this diversion from the previous parametric study in chapter 4. It can be seen that the oxygen-argon compression theoretically ensures higher cycle efficiency than the oxygen-argon-carbon dioxide compression. It is worth mentioning that the carbon dioxide is supplied to the combustion chamber of the gas turbine by the (S13) stream at the high level of pressure and requires no additional compression. This is another reason for choosing oxygen-argon compression instead of oxygen-argon-carbon dioxide compression.

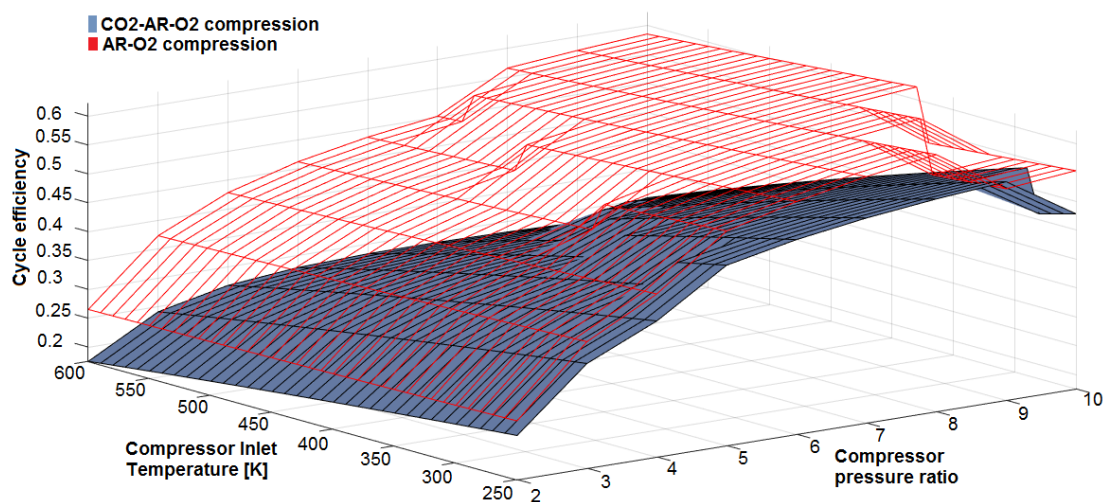


Figure 5.16: Oxygen-Argon-Carbon dioxide compression vs Oxygen-Argon compression

5.2 Calibration and final results

The sensitivity analysis provided guidelines to adjust the ASU-SMR-WGS-PSA-HXGT cycle in order to fulfil the requirements of any desired performance. The initial values of the cycle parameters, which are shown in Table 3.2, have been adjusted to the final values to provide the required molar fractions of CARSOXY. Table 5.1 shows the molar fractions of argon and oxygen which are supplied by the (ARO2RECT) stream together with the molar fractions of methane, carbon dioxide and steam which are supplied by the stream (S13) to the gas turbine cycle. The results have been obtained throughout multiple numerical attempts, section 5.2.1. Errors can be farther decreased using more attempts. Nevertheless, the emphasis is to prove the concept. Hydrogen, nitrogen, and oxygen are also produced with high purity in the ASU-SMR-WGS-PSA-CCS-HXGT cycle by the N₂, H₂FINAL, and O₂ streams, respectively. It must be highlighted that the calibration presented herein is numerical and shall be experimentally validated by

developing a laboratory-scale prototype of the ASU-SMR-WGS-PSA-CCS-HXGT cycle.

Table 5.1: CARSOXY final molar fraction.

Stream	Component	Actual molar fraction	Required molar fraction	Error
ARO2RECT and S12 (required for the CARSOXU)	Ar	0.2683	0.25	0.07
	O ₂	0.2316	0.22	0.05
	CH ₄	0.0980	0.11	0.10
	CO ₂	0.1760	0.19	0.07
	H ₂ O	0.2171	0.23	0.05
N ₂	N ₂	0.9905	-	-
H2FINAL	H ₂	0.9999	-	-
O ₂	O ₂	0.9970	-	-

It is important to highlight that the ASU-SMR-WGS-PSA-CCS-HXGT model is functional in any required capacity (from a laboratory-based scale to a large-scale industry). This can be achieved provided that a constant ratio is used to adjust all mole flow rates, boil-up mole rates and distillate mole rates. On this note, Table 5.2 shows the required mole flow rates of feed streams, the anticipated mole flow rates of product streams, (LPDC) boil-up rate and distillate rates for 1 kmol/h of methane.

Table 5.2: ASU-SMR-WGS-PSA-CCS-HXGT mole flow rates for 1 kmol/h of Methane

Feed Stream	Mole flow rate [kmol/h]
FEEDCH4	1
FEEDH2O	0.71
AIR	0.53
WGS _{H2O}	0.96
ATMIR	79.66
AIRLP	10.3
Product Stream	Mole flow Rate [kmol/h]
N ₂	70.93
O ₂	17.57
H ₂	2.06
S13	1.47
ARO2RECT	1.47
LPDC rates	Mole flow Rate [kmol/h]
distillate	70.93
boil-up rate	737.38

5.2.1 SMR-WGS-PSA Calibration

The equivalent molar fraction of CO₂, H₂O and CH₄ in SMR-WGS-PSA to the CARSOXY blend (Table 5.3) can be calculated by assuming that the molar fractions of O₂ and argon have been provided by ASU. Therefore, the molar fractions of O₂ and Argon shall be excluded from the actual CARSOXY blend in

order to calculate required equivalent MSRWGSPSA molar fractions. This is demonstrated in Equations 5.1-5.4.

Table 5.3 CARSOXY molar fraction, blend 58

(A: CH ₄)(B: O ₂)(X: Ar)(Y: H ₂ O)(Z: CO ₂)	
A	11
B	22
X	25
Y	23
Z	19

$$B + X = 22 + 25 = 47 \tag{5.1}$$

$$A' = \frac{A}{(100 - (B + X))} \times 100\% = \frac{11}{(100 - 47)} \times 100\% = 20.75\% \tag{5.2}$$

$$Y' = \frac{Y}{(100 - (B + X))} \times 100\% = \frac{23}{(100 - 47)} \times 100\% = 43.4\% \tag{5.3}$$

$$Z' = \frac{Z}{(100 - (B + X))} \times 100\% = \frac{19}{(100 - 47)} \times 100\% = 35.85\% \tag{5.4}$$

A', Y' and Z' are the equivalent molar fractions of CH₄, H₂O and CO₂, respectively. These molar fractions are the target molar fractions of the SMR-WGS-PSA product. As demonstrated in the sensitivity analysis, there are various methods of manipulating the molar fractions of the final product. Table 5.4 summarizes these methods.

Table 5.4 SMR-WGS-PSA calibration methods

Method symbol	Method	Figure	Effects on the molar fractions	
(A)	Increase 1 kg/h of H ₂ O mass flow rate (FEEDH ₂ O stream)	5.1	CO ₂	Increase
			CO	Concaves down at 225 kg/h of H ₂ O
			H ₂ O	Increase
			CH ₄	Decrease
			H ₂	Increase
(B)	Increase 1 kg/h of CH ₄ mass flow rate (FEEDCH ₄ stream)	5.2	CO ₂	Concave down at 200 Kg/h of CH ₄
			CO	Increase
			H ₂ O	Decrease
			CH ₄	Increase
			H ₂	Increase
(C)	Increase 1% of SMR to Furnace CH ₄ split ratio (CH ₄ SPLIT)	5.3	CO ₂	Concaves down at a 0.975 of split ratio
			CO	Decrease
			H ₂ O	Increase
			CH ₄	Increase
			H ₂	decrease
(D)	Increase 1 kg/h of Furnace air mass flow rate	5.4	CO ₂	Increase
			CO	Decrease
			H ₂ O	Increase

(E)	Increase 1 kmol/h of H ₂ O through (WGS _{H2O} stream)	5.5	CH ₄	Increase
			H ₂	Decrease
			CO ₂	Decreases from the ineffective WGS limit
			CO	Decrease
			H ₂ O	Increases from the ineffective WGS limit
			CH ₄	Decreases from the ineffective WGS limit
			H ₂	Decreases from the ineffective WGS limit

The molar fractions which correspond to the uncalibrated model are summarized in Table 5.5. These molar fractions are initially monitored via the H21 and S131 streams, Figure 5.1.

As demonstrated in Table 5.5, the uncalibrated S131 molar fractions of CO₂, H₂O and CH₄ shall be increased, increased and decreased, respectively. Method (A) satisfies these requirements, thus it has been chosen to be the first attempt of matching the required molar fractions. The results of this attempt are shown in Table 5.6 for H₂O mass flow rate of 580 kg/h.

Table 5.5 uncalibrated molar fractions of the SMR-WGS-PSA

Stream	Component	uncalibrated molar %	Required%
(S131)	CO ₂	17.1904	Z' = 35.85
	CO	0.1552	Zero
	H ₂ O	14.2125	Y' = 43.4
	CH ₄	61.5188	A' = 20.75
	H ₂	6.9227	Zero
(H21)	CO ₂	0	Zero
	CO	0	Zero
	H ₂ O	0	Zero
	CH ₄	0	Zero
	H ₂	1	To store

Table 5.6.A: Attempt 1: Calibrating the SMR-WGS-PSA sub-models

Attempt 1: Adjust the H ₂ O mass flow rate to 580 kg/h			
Component in S131 stream	Molar fraction at this attempt %	Required molar fraction %	Required action
CO ₂	17.2433	Z' = 35.85	Increase
CO	0.1051	Zero	Be zero
H ₂ O	17.4764	Y' = 43.4	Increase
CH ₄	58.1945	A' = 20.75	Decrease
H ₂	6.9807	Zero	Be zero

(Note: each attempt depends on the updated values of the previous attempt)

It can be seen that Attempt 1 has contributed to approach the desired molar fraction. However, actions are still required. Method (B) has been chosen based on Table 10 to be the Next required actions. Table 5.6.B shows the results of attempt 2, where the CH₄ mass flow rate has been adjusted to 315kg/h.

Table 5.6.B: Attempt 2: Calibrating the SMR-WGS-PSA sub-models

Attempt 2: Adjust the CH ₄ mass flow rate to 315 kg/h			
Component in S131 stream	Molar fraction at this attempt %	Required molar fraction %	Required action
CO ₂	9.28692	Z' = 35.85	Increase
CO	0.1451	Zero	Be zero
H ₂ O	65.3823	Y' = 43.4	Decrease
CH ₄	21.5798	A' = 20.75	Minor decrease
H ₂	3.60588	Zero	Be zero

(Note: each attempt depends on the updated values of the previous attempt)

Attempt 2 has nearly hit the target of the required CH₄ molar fraction with only 0.8298 % to be decreased. However, CO₂ and H₂O molar fractions have to be significantly increased and decreased, respectively. Therefore, Method (C) has been chosen for attempt 3. Table 5.6.C shows the results of attempt 3, where the split fraction adjusted to 0.86.

Table 5.6.C: Attempt 3: Calibrating the SMR-WGS-PSA sub-models

Attempt 3: Adjust the CH ₄ SPLIT split to 0.86			
Component in S131 stream	Molar fraction at this attempt %	Required molar fraction %	Required action
CO ₂	16.8146	Z' = 35.85	Increase
CO	0.1151	Zero	Be zero
H ₂ O	60.8675	Y' = 43.4	Decrease
CH ₄	15.4735	A' = 20.75	Increase
H ₂	6.7293	Zero	Be zero

(Note: each attempt depends on the updated values of the previous attempt)

Attempt 3 has managed to increase the molar fraction of CO₂ compared to attempt 2. However, H₂O and CH₄ molar fractions diverged from the target. As the H₂O molar fraction has to be decreased and the CH₄ molar fraction has to be decreased, the reverse of Method A (decrease the H₂O mass flow rate) can be a good option to fulfil the required actions in Table 5.6.C. Table 5.7 shows the results of the attempt 4. The H₂O mass flow rate has been decreased to 255Kg/h.

Table 5.7: Attempt 4: Calibrating the SMR-WGS-PSA sub-models

Attempt 4: Adjust H ₂ O mass flow rate to 225 kg/h			
Component in S131 stream	Molar fraction at this attempt %	Required molar fraction %	Required action
CO ₂	21.1474	Z' = 35.85	Increase
CO	0.1711	Zero	Be zero
H ₂ O	44.5399	Y' = 43.4	Minor increase
CH ₄	25.627	A' = 20.75	Minor Decrease
H ₂	8.5146	Zero	Be zero

(Note: each attempt depends on the updated values of the previous attempt)

Attempt 4 has almost fulfilled the required molar fractions of H₂O and CH₄. Although it has contributed to approach the CO₂ molar fraction, it is still below the target of the CO₂ molar fraction. Table 5.8 shows

the results of attempt 5, where the split fraction of CH₄SPLIT is adjusted to 0.802769.

Table 5.8: Attempt 5: Calibrating the SMR-WGS-PSA sub-models

Attempt 4: Adjust the split fraction CH ₄ SPLIT to 0.802769			
Component in S131 stream	Molar fraction at this attempt %	Required molar fraction %	Required action
CO ₂	34.9767	Z' = 35.85	Minor increase
CO	0.3310	Zero	Minor Residual
H ₂ O	33.5906	Y' = 43.4	Increase
CH ₄	17.0117	A' = 20.75	Minor increase
H ₂	14.090	Zero	Decrease

(Note: each attempt depends on the updated values of the previous attempt)

Table 5.9: Attempt 6: Calibrating the SMR-WGS-PSA sub-models

Attempt 5: Adjust H ₂ O mass flow rate to 379 kg/h			
Component in S131 stream	Molar fraction at this attempt %	Required molar fraction %	Required action
CO ₂	0.306588	Z' = 35.85	Minor increase
CO	0.257713	Zero	Minor Residual
H ₂ O	44.0498	Y' = 43.4	Increase
CH ₄	126928	A' = 20.75	Minor increase
H ₂	12.3408	Zero	Decrease

(Note: each attempt depends on the updated values of the previous attempt)

It can be seen from Table 5.8 and Table 5.9 that attempts 5 and 6 are the only attempts which managed to raise the CO₂ molar fraction nearly to the required level. However, Increasing CO₂ accompanies a significant increase in the molar fraction of H₂. Therefore, it has become essential to add another separation unit post (B2) the S131 stream in order to extract the H₂ from it, Figure 3.2 (final model). This step will contribute to obtain the desired CARSOXY blend with higher purity and utilises the H₂ by-production.

Table 5.10: Attempt 7: Calibrating the SMR-WGS-PSA sub-models

Attempt 7: additional separation block (B2)			
Component in S13 stream	Molar fraction at this attempt %	Required molar fraction %	Required action
CO ₂	34.4894	Z' = 35.85	Minor increase
CO	0.2899	Zero	Minor Residual
H ₂ O	49.5536	Y' = 43.4	Minor decrease
CH ₄	14.2787	A' = 20.75	Increase
H ₂	1.3882	Zero	Minor residual

(Note: each attempt depends on the updated values of the previous attempt)

Table 5.10 shows the molar fractions of the S13 stream after adding the additional separation block. H₂ has been extracted from the S13 stream where a residual molar fraction of 1.3882 has remained in the stream. The CO₂ molar fraction has almost met the required level where only 1.3606 % has to be increased. H₂O and CH₄ molar fractions have to be decreased and increased, respectively. Therefore, attempt 8 will be to decrease the H₂O mass flow rate. The final equivalent molar fractions of CO₂, H₂O and CH₄ throughout the sequence of attempts described in Tables 5.11-5.15.

Table 5.11: Attempt 8: Calibrating the SMR-WGS-PSA sub-models

Attempt 8: Adjust H ₂ O mass flow rate of to210 kg/h			
Component in S13 stream	The molar fraction at this attempt %	Required molar fraction %	Required action
CO ₂	0.41.429	Z' = 35.85	Decrease
CO	0.48268	Zero	Minor residual
H ₂ O	34.0924	Y' = 43.4	Decrease
CH ₄	22.4009	A' = 20.75	Decrease
H ₂	16.6941	Zero	Minor residual

(Note: each attempt depends on the updated values of the previous attempt)

Table 5.12: Attempt 9: Calibrating the SMR-WGS-PSA sub-models

Attempt 9: Adjust the CH ₄ mass flow rate to 275 kg/h			
Component in S13 stream	The molar fraction at this attempt%	Required molar fraction %	Required action
CO ₂	36.3899	Z' = 35.85	Minor residual
CO	348053	Zero	Minor residual
H ₂ O	43.0278	Y' = 43.4	Minor residual
CH ₄	18.7682	A' = 20.75	Increase
H ₂	1.46604	Zero	Minor residual

(Note: each attempt depends on the updated values of the previous attempt)

Table 5.13: Attempt 10: Calibrating the SMR-WGS-PSA sub-models

Attempt 10: Adjust the split fraction of CH ₄ SPLIT to 0.808727			
Component in S13 stream	The molar fraction at this attempt %	Required molar fraction %	Required action
CO ₂	34.5211215525241	Z' = 35.85	Minor residual
CO	0.327254338543147	Zero	Minor residual
H ₂ O	44.02197198667	Y' = 43.4	Increase
CH ₄	19.7389896300055	A' = 20.75	Increase
H ₂	1.39066249225725	Zero	Minor residual

(Note: each attempt depends on the updated values of the previous attempt)

Table 5.14: Attempt 11: Calibrating the SMR-WGS-PSA sub-models

Attempt 11: Adjust CH ₄ mass flow rate to 285kg/h			
Component in S13 stream	The molar fraction at this attempt%	Required molar fraction %	Required action
CO ₂	35.7844	Z' = 35.85	Minor residual
CO	0.342388	Zero	Minor residual
H ₂ O	41.8177	Y' = 43.4	Increase
CH ₄	20.6139	A' = 20.75	Minor residual
H ₂	1.44165	Zero	Minor residual

(Note: each attempt depends on the updated values of the previous attempt)

Table 5.15: Attempt 12: Calibrating the SMR-WGS-PSA sub-models

Attempt 12: Adjust H ₂ O mass flow rate to 227 kg/h			
Component in S13 stream	The molar fraction at this attempt%	Required molar fraction %	Required action
CO ₂	35.2126	Z' = 35.85	Minor residual
CO	0.33069	Zero	Minor residual
H ₂ O	43.4235	Y' = 43.4	Minor residual
CH ₄	19.6147	A' = 20.75	Minor residual
H ₂	1.41843	Zero	Minor residual

(Note: each attempt depends on the updated values of the previous attempt)

5.2.2 ASU Calibration

The equivalent molar fractions A' , Y' and Z' of CH_4 , H_2O and CO_2 , respectively from the SMR-WGS-PSA have been obtained as demonstrated in section 5.2.1. The molar fractions of CH_4 , H_2O and CO_2 shall be excluded from the actual CARSOXY blend in order to calculate required equivalent Oxygen and Argon molar fractions from the ASU (B' and X' , respectively),. This is shown in Equations 5.5 and 5.6.

$$B' = \frac{B}{(100 - (A + Y + Z))} \times 100\% = \frac{22}{(100 - 53)} \times 100\% = 46.8\% \quad (5.5)$$

$$X' = \frac{X}{(100 - (A + Y + Z))} \times 100\% = \frac{25}{(100 - 52)} \times 100\% = 53.2\% \quad (5.6)$$

The uncalibrated molar fractions of the ASU (Figure 5.7) are summarized in Table 5.16. It can be seen that (ARO2RECT) stream is highly expected to fulfil the requirements of the B' and X' molar fractions since the O_2 molar fraction is only required to be decreased by 1.0757 % to match the required molar fraction ($B' = 46.8\%$). Similarly, A_r molar fraction is only required to be increased by 5.5306 % to match the required molar fraction ($X' = 53.2\%$). Therefore, the following attempt focuses on (ARO2RECT) stream.

Table 5.16: Uncalibrated molar fractions of the ASU (initial model)

Stream	Component	Uncalibrated molar fraction%	Require action
(A _r)	A _r	88.6303	Eliminated
	O ₂	3.0869	
	N ₂	8.2827	
(O ₂)	A _r	3.5700E-18	Pure O ₂
	O ₂	99.9953	
	N ₂	3.5700E-18	
(N ₂)	A _r	0.2826	Pure N ₂
	O ₂	0.3741	
	N ₂	99.3432	
(ARO2RECT)	A _r	47.6694	$X' = 53.2\%$
	O ₂	47.8757	$B' = 46.8\%$
	N ₂	4.4548	Zero

5.17 Calibrating the ASU unit

Attempt 1: Adjust the flow rate of the (ATMAIR) stream to 5336 kmol/h

Stream	Component	Molar fraction at this attempt %	Required action
(ARO2RECT)	A _r	53.4	Minor residual
	O ₂	36.2553	Increase
	N ₂	10.3447	Be zero

(Note: each attempt depends on the updated values of the previous attempt)

Attempt 1 has successfully matched the required A_r with minor residual. However, the O_2 and N_2 molar fractions have significantly diverged from the required molar fractions ($B' = 46.8\%$ and zero N_2). It must be mentioned that the 5336 kmol/h of (ATMAIR) flow rate approximately provides the peak of the A_r molar fraction where any increase or decrease of the ATMAIR airflow rate would decrease the A_r molar fraction. This can be seen in Figure 5.9. Furthermore, in order to increase the molar fraction of O_2 to match the required molar fraction (B') the flow rate has to be decreased. This will not provide the required A_r molar fraction (X'). In other words, manipulating the flow rate of the (ATMAIR) stream can either ensure the required A_r molar fraction or the O_2 molar fraction separately but cannot provide both molar fractions at the same time. In order to increase the O_2 molar fraction and decrease the N_2 molar fraction, the (ARO2RECT) stream must be located near the high concentration of O_2 , which is towards the bottom stage of the distillation column. Table 5.18 summarizes results of the attempts of modifying the stage of the (ARO2RECT) stream. Attempt 17(ATMAIR stream stage is 23) managed to obtain approximately the required molar fractions of A_r and O_2 . However, a zero molar fraction of N_2 could not be achieved in any of these attempts (Table 5.18). Decreasing the flow rate of the (AIRLP) stream can decrease the N_2 molar fraction in the (ARO2RECT) stream. Table 5.19 shows the result of modifying the AIRLP flow rate to 690 kmol/h. In the next set of attempts (19-23), the number of stages in the (LPDDC) distillation column is modified. Table 5.20 summarizes results of the attempts.

Table 5.18 Calibrating the ASU unit

Attempt	(ARO2RECT) stream stage	A_r molar fraction	O_2 molar fraction	N_2 molar fraction
2	39	0.074922	0.91931	0.005768
3	38	0.098548	0.88866	0.012792
4	37	0.126594	0.85359	0.019816
5	36	0.131197	0.841126	0.027676
6	35	0.162392	0.80826	0.029348
7	34	0.196444	0.773703	0.029853
8	33	0.23231	0.737716	0.029975
9	32	0.268933	0.701089	0.029978
10	31	0.305331	0.664723	0.029946
11	30	0.340674	0.629422	0.029904
12	29	0.374302	0.595835	0.029863
13	28	0.405741	0.564437	0.029822
14	27	0.434674	0.535542	0.029784
15	26	0.460906	0.509344	0.02975
16	25	0.484367	0.485914	0.029719
17	24	0.505032	0.465275	0.029693
18	23	0.522988	0.447341	0.02967

(Note: each attempt depends on the updated values of the previous attempt)

Table 5.19 Calibrating the ASU unit

Attempt 18: Adjust the flow rate of the (AIRLO) stream to 690 kmol/h			
Stream	Component	Molar fraction at this attempt	Required action
(ARO2RECT)	A _r	1.1051E-06	Minor residual
	O ₂	48.75	Increase
	N ₂	51.25	Be zero

(Note: each attempt depends on the updated values of the previous attempt)

Table 5.20 Calibrating the ASU unit

Attempt	number of stages in the (LPDDC)	A _r molar fraction	O ₂ molar fraction	N ₂ molar fraction
19	38	0.477462	0.522537	1.09E-06
20	39	0.496402	0.503597	1.10E-06
21	40	0.512487	0.487512	1.11E-06
22	41	0.525823	0.474176	1.11E-06
23	42	0.536737	0.463261	1.11E-06

(Note: each attempt depends on the updated values of the previous attempt)

Attempt 23 in Table 5.20 shows that the molar fractions of the (ARO2RECT) stream have matched exactly the required equivalent molar fractions B' , X' and zero nitrogen. This essentially means that rectifier (RECT)-Figure 5.7- can be eliminated (as shown in Figure 3.2). This will reduce (the cost, complexity, etc.) of the CARSOXY ASU unit compared to conventional ASU.

5.3 Discussion

The ASU-SMR-WGS-PSA-CCS-HXGT cycle has two modes of operability. As shown in Table 5.1 and Table 5.2, the first mode produces the CARSOXY within the required molar fraction with hydrogen and nitrogen as by-products. The second mode reacts nitrogen with hydrogen to produce ammonia (Haber-Bosch process). As shown in Table 5.2 approximately 2 kmol/(kmol CH₄) of hydrogen is by-produced in order to produce CARSOXY within the required molar fractions. Enough nitrogen to convert 2kmol/h of hydrogen to ammonia is also produced. Ammonia can be used for many applications, including fertilizing or fueling of cycles [164]. Figure 5.17 shows the necessarily detailed flowsheet which can be added to the ASU-SMR-WGS-PSA-CCS-HXGT (Figure 3.2) cycle in order to convert it to the second mode (producing ammonia).

The second mode establishes an easier introduction of CARSOXY to the market in the near future. The second mode allows the CARSOXY cycle to be used where ammonia is produced. The processes involved in the ASU-SMR-WGS-PSA-CCS-HXGT have diverged from the conventional processes in many aspects. To name a few, after the sensitivity analysis the final parameters of the WGS model have been chosen to ensure low methane conversion factor (enough to produce the required carbon dioxide

and maintain the required methane level as unreacted). In addition, conventional argon production involves a rectifying process, while it has been eliminated in the ASU-SMR-WGS-PSA-CCS-HXGT cycle by customizing the operation conditions of the ASU. This shall decrease the capital cost and provides better matching between the ASU and the gas turbine unit. Moreover, the integration of all the involved sub-models has utilized the waste energy (i.e. using the HX heat exchanger) between the gas turbine model and the SMR model.

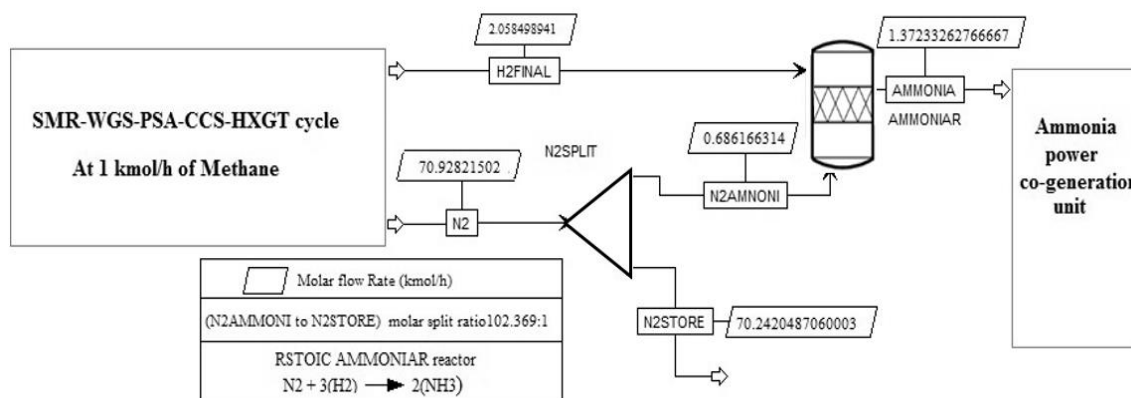


Figure 5.17: Ammonia production (Second mode).

As observed from tables 5.1 and 5.2, hydrogen and nitrogen are produced from the process. These gases can be used either as separate by-products or to produce ammonia. If the latter is selected, the process could be defined as in Figure 5.17. It is estimated that using 1 kmol/hr of methane in the process, 1.37 kmol/hr of ammonia could be produced. It must be remembered that the production of this ammonia would come with an energy excess from the CARSOXY process, which eventually would also lead to the recovery of CO₂ via CCS technologies. Therefore, the process has the potential to deliver an appreciated commodity whilst delivering extra power via efficient and clean cycles.

Essentially, Lowering the S/C ratio decreases catalysts lifetime whilst increasing the process efficiency. Amongst the possible solutions is the utilization of platinum group metals (PGM). However, this approach requires an additional cost [165]. Despite the economic challenges, the process remains applicable at an S/C ratio which can be lower than 0.7 (i.e. 0.1-0.4) [165]. Finally, the increased efficiency indirectly contributes to compensating for the cost of (PGM) catalyst.

Maintaining the S/C ratio within the marginal conventional value (~2) can also provide the required CARSOXY molar fractions. The reader is directed to the previously published work [166] for the full details.

5.4 Conclusion

This chapter has provided a sensitivity analysis to study the behaviour of the involved sub-models in the ASU-SMR-WGS-PSA-CCS-HXGT cycle. This has enabled the modification of the operating conditions

in order to provide the required CARSOXY molar fractions for power, CCS and ammonia production purposes. The utilisation of waste heat amongst the sub-models and the elimination of some facilities which would have existed in conventional processes have the potential to decrease both the operation and the capital cost of such a cycle. This chapter has shown various methods in order to obtain the required CARSOXY molar fractions. Some methods stand out from the crowd. The sensitivity analyses on the (SMR) sub-model spots the H₂O mass flow rates most appropriate for the use of CARSOXY and recovery of other gases, namely nitrogen and hydrogen, for further processes. These are 350 kg/h, 225kg/h and 175 kg/h of H₂O, respectively within a variation interval of [10-510] kg/h of H₂O. In addition, varying the CH₄ mass flow rate within the interval of [10-950] kg/h identifies the point which peaks the CO₂ product level, 200 kg/h of CH₄. This has identified the CH₄ mass splitting ratio which activates/deactivates the (SMR) sub-model, 0.975 SMR to furnace CH₄ mass ratio. A 650 kg/h of air to the furnace has been identified as a compromise point between both of the conventional and CARSOXY demands. Similarly, a 5.25 kmol/h of H₂O supply to the (WGS) sub-model has been identified as the activation/deactivation point of the sub-model. The next chapter (6), conducting techno-economic analyses on the cycle is essential in order to prove economic sustainability.

5.5 Future work

The sensitivity analyses provide a visualization of how the involved sub-models in the CARSOXY plant may have (or have not) diverged from conventional sub-models. Moreover, the sensitivity analyses evaluate the cycle performance over various intervals of operation conditions. Once this has been specified, a mathematical optimization approach can be employed as future work, exergy analysis and mathematical modelling can further optimize the waste heat utilization for real, profitable applications. It must be highlighted that the calibration presented herein is numerical and all the other suggested theoretical tasks shall be experimentally validated by developing a laboratory-scale prototype of the ASU-SMR-WGS-PSA-CCS-HXGT cycle.

CHAPTER SIX

CARSOXY Techno-economic.

“Economics is too important to leave to economists.”

~ Steve Keen

CHAPTER 6 –CARSOXY TECHNO-ECONOMIC

Due to strict emission control regulations on gas turbines, power generation industries are liable for maintaining CO₂ and NO_x emission levels within allowable tolerance margins. However, compromising between energy demands and the emission control regulations is indeed one of the economic challenges in the industry. Therefore, emission control techniques must be innovatively introduced to the industry, such that high economic sustainability and efficiency are retained. The developed CARSOXY gas turbine cycle (ASU-SMR-WGS-PSA-CCS-HXGT, analyzed in chapter 5) eliminates NO_x emissions by replacing Air/fuel combustion with CO₂-Argon-Steam/oxyfuel combustion in the HXGT unit. In addition, the developed CARSOXY gas turbine model control carbon emissions by the CCS unit. Yet this technique must prove economic sustainability in order to be adopted by the industry. This chapter performs comparable techno-economic analyses between CARSOXY and Air-driven gas turbine cycles using the same amount of CH₄ fuel. Both cycles have been modelled and economically analyzed using ASPEN PLUS. The CARSOXY cycle has demonstrated to payout all costs way before the Air-driven cycle. In fact, 85.5% of the CARSOXY project's life is profitable (positive NPV), while only 69.5% is profitable for the Air-driven cycle. The Modified Internal Rate of Return (MIRR) of the CARSOXY cycle is approximately 2.2% higher than that for the Air-driven cycle. Moreover, the profitability index (PI) of the CARSOXY cycle is 1.72, while it is only 1.28 for the Air-driven cycle.

6.1 Capital costs and operation costs

In order to understand the parameters of the investment results, it is crucial to highlight the definition of the total project capital cost. It is a one-time expense, which is required to bring the project to its full operating condition. In other words, it is the expense, which covers the EPC period. According to reference [129], “It is used to evaluate new projects of a company. It is the minimum return that investors expect for providing capital to the company, thus setting a benchmark that a new project has to meet”. Another important term is the working capital percentage. It refers to the cash percent of the capital cost. It is crucial to overcome urgent circumstances or unplanned obligations. According to reference [167], “Working capital is a measure of operation liquidity and refers both to cash on hand and assets a business can quickly convert to cash”. The results of the section are based on the assumption that the working capital percentage is 5 percent/year, (section 3.4.5, Table 3.7). As discussed in section 3.4.2, the Air-driven-heat-exchanged cycle has been supplied with air to perform stoichiometric combustion using the same amount of fuel as the CARSOXY model, 1240.8 [kg/h] of CH₄. Further details of the Air-driven-heat-exchanged cycle are provided in Tables 3.3 and rev3.7. The details of CARSOXY cycle are available

in Table 3.2 (Final values). As shown in Figure 6.1.A, the total project cost of the CARSOXY plant (7.78E+07 [£]) far-exceeds what is required for the Air-driven cycle (3.21E+06 [£]). These results are expected since more pieces of equipment in the CARSOXY plant are used (i.e. additional MSRWGS unit and additional ASU).

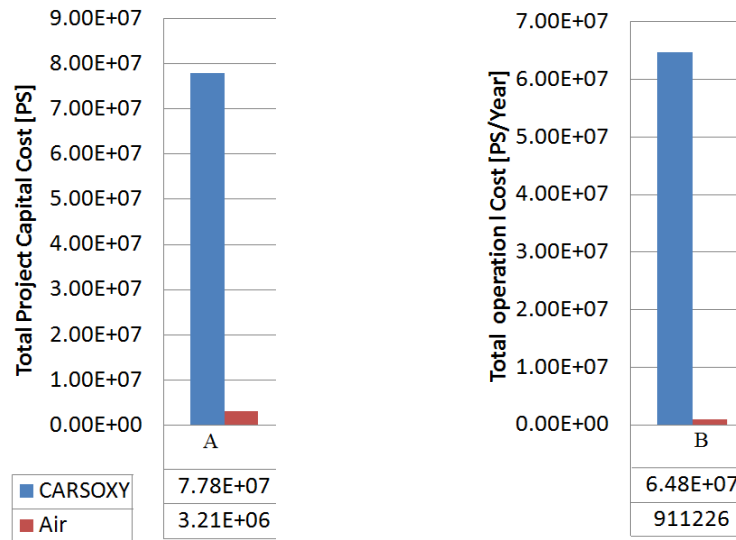


Figure 6.1 Total project cost and operational costs.

The breakdown of the total project capital cost of the CARSOXY cycle is shown in Figure 6.2. The dominant costs of the CARSOXY cycle are those to cover the EPC period, the BOOSTER, LPDC-tower, the heat exchangers HXHX and HEX1, respectively. The EPC costs ($C_{ASPEN} = \pounds_{2016} 2.86E+07$) and the BOOSTER cost ($C_{ASPEN} = \pounds_{2016} 2.74E+07$) had been estimated using ASPEN PLUS database. Those were followed by the cost of the LPDC-tower ($C_{ASPEN} = \pounds_{2016} 5.79E+06$), which was also estimated using the ASPEN PLUS database, Table 3.1. Both of costs of the heat exchangers HXHX ($\pounds = \pounds_{2016} 4.33E+06$) and HEX1 ($\pounds = \pounds_{2016} 1.51E+06$) were estimated using Equation 3.17 and escalated to 2016 using Equation 3.16. The costs of the remaining pieces of equipment –Tables 12, 14, 16, 17 and 18- are insignificant in comparison to the BOOSTER, LPDC-tower, the heat exchangers HXHX and HEX1.

The breakdown of the total project capital cost of the Air-driven cycle is shown in Figure 6.3. The dominant costs of the Air-driven cycle are those to cover the EPC period, the heat exchanger ARX, the combustion chamber (CCAR), the turbine (TAR), the compressors (CAR) and (CH4AR), respectively. The EPC costs ($C_{ASPEN} = \pounds_{2016} 2.01E+06$) and heat exchanger ARX cost ($\pounds = \pounds_{2016} 1.55E+06$) had been estimated using ASPEN PLUS database and Equation 3.16, respectively. Those were followed by the costs of the combustion chamber (CCAR) ($\hat{C}_{2016} = \pounds_{2016} 4.52E+05$), the turbine (TAR) ($\hat{C}_{2016} = \pounds_{2016} 4.51E+05$), the compressors (CAR) ($\hat{C}_{2016} = \pounds_{2016} 2.56E+05$) and (CH4AR) ($\hat{C}_{2016} =$

£₂₀₁₆4.55E+04), respectively. Those were estimated using Equation 3.22, as demonstrated in Table 3.17.

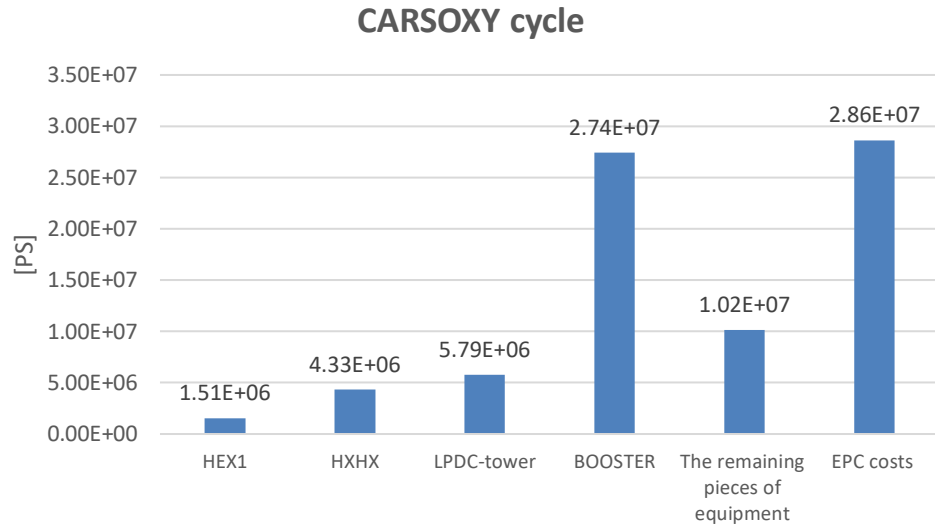


Figure 6.2. The breakdown of the total project capital cost of the CARSOXY cycle

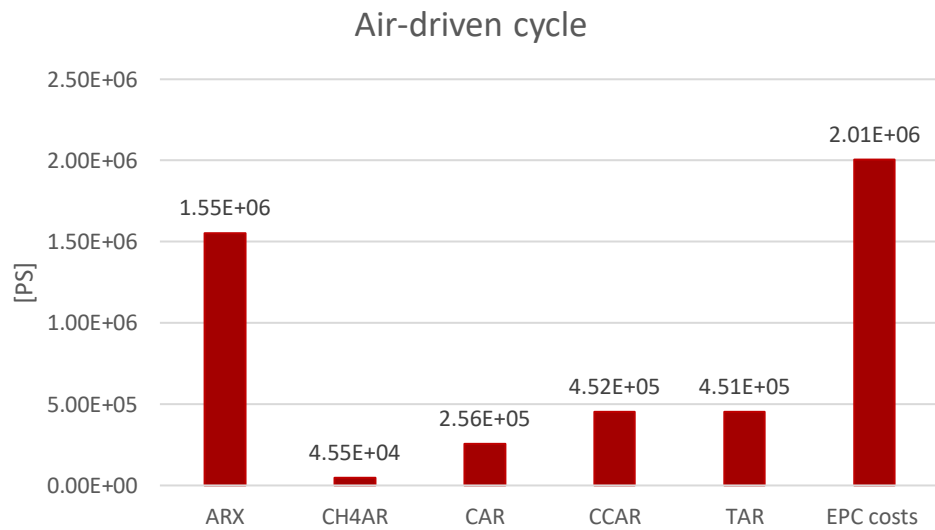


Figure 6.3. The breakdown of the total project capital cost of the Air-driven gas turbine cycle

The cost, which is paid on a continuous basis, is referred to as the total operation cost. It covers all the necessary expenses in order to maintain the operability of the project. According to the reference [167], “It is defined as expenses associated with the maintenance and administration of a business on a day-to-day basis”. It does not cover anything related the capital expenses. It includes the utility cost (such as electricity, heating, cooling, etc.) and the raw materials costs. Similar to the capital costs results; because the CARSOXY model has additional pieces of equipment (i.e. additional MSRWS unit and additional ASU); the total operation cost of the CARSOXY plant is higher than that for the Air-driven cycle. As shown in Figure 6.1.B, the total operational costs are 6.48+07 [£/Year] and approximately 911,200 [£/Year] for the CARSOXY plant and the Air-driven cycle, respectively. The total operation cost has the

general and administrative (G&A) expenses as sub-categories. According to reference [168], “General and administrative expenses (G&A) are expenditures related to the day-to-day operations of a business. General and administrative expenses pertaining to operation expenses rather than to expenses that can be directly related to the production of any goods or services, including rent, utilities, insurance, and managerial salaries. The results of the section are based on the assumption that the G&A cost is 8 percent/year, (section 3.4.5, Table 3.7). Therefore, as shown in Figure 6.4.A, the G&A results are approximately 5.18E6 [£/Year] and 73000 [£/Year] for the CARSOXY plant and the Air-driven cycle, respectively.

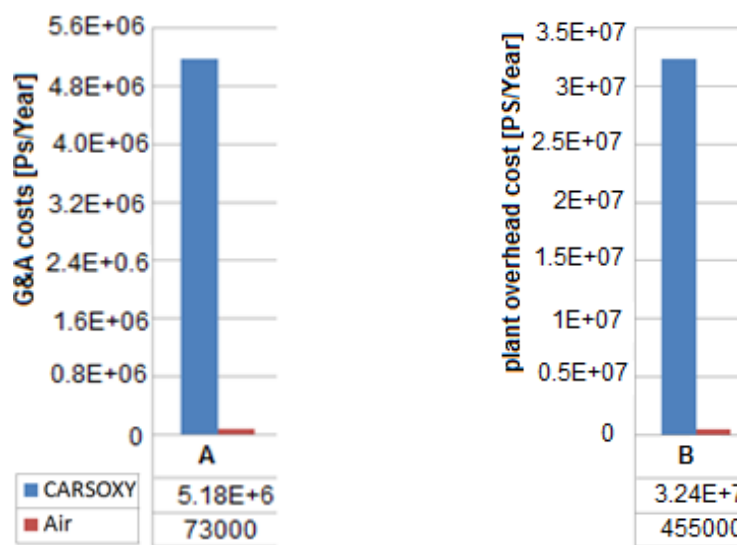


Figure 6.4 G&A and Plant overhead costs.

The percent of operation labour is the continuous payroll for employees, which is expressed as a percentage of gross sales [169]. While the plant overhead is essentially the percentage of the operation labour in addition to expenses which cannot be tracked directly such as the maintenance cost. According to reference [170], “Factory overhead, also called manufacturing overhead or work overhead or American English factory burden is the total cost involved in operation all production facilities of a manufacturing business that cannot be traced directly to a product”. The results of the section are based on the assumption that the plant overhead is 50 percent/year, (section 3.4.5, Table 3.8). Therefore, as shown in Figure 6.4.B, the plant overhead results are approximately 3.24E7 [£/Year] and 455000 [£/Year] for the CARSOXY plant and the Air-driven cycle, respectively. These results are expected since more pieces of equipment in the CARSOXY plant are used (i.e. additional SMR, WGS unit and additional ASU) causing higher Total project, operational, G&A and Plant overhead costs.

6.2 Raw material costs and product sales

The total raw material costs for both systems are similar since the same amount of CH₄ fuel has been fed to both systems, as shown in Figure 6.5.A. The total raw material cost of the Air-driven cycle is approximately 594,000 [£/Year]. Since the Air-driven cycle has only CH₄ as raw material, then the total raw material cost (594,000 [£/Year]) corresponds to the cost of the consumed CH₄. It also represents the CH₄ cost consumed by the CARSOXY plant since both the Air-driven and the CARSOXY plants have been modelled such that both consume the same amount of CH₄. The total raw material cost of the CARSOXY plant is approximately 619,000 [£/Year]. It can already be anticipated that the CARSOXY plant must have much higher total product sales than the Air-driven cycle in order to pay out for the high project cost and the operation cost. As shown in Figure 6.5.B, the total product sales of the CARSOXY plant is 3.04E+08 [£/Year], while it is only 2.92E+06 for the Air-driven heat cycle.

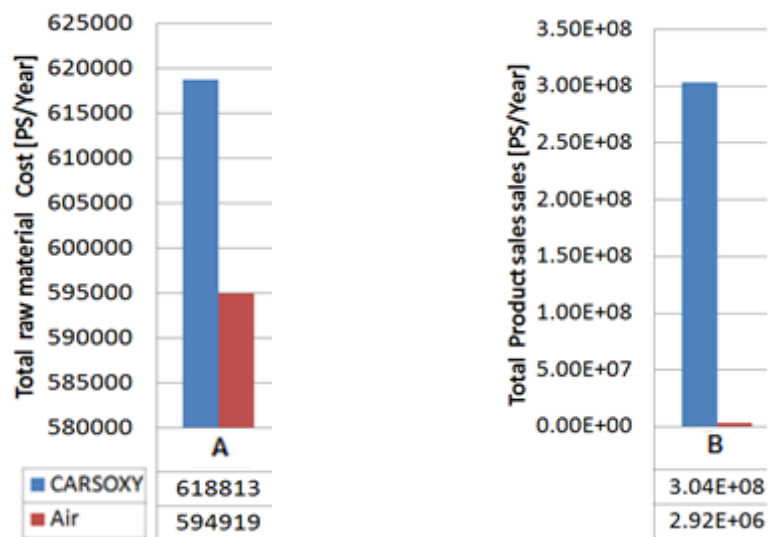


Figure 6.5 Total raw material cost and product sales.

Knowing that the only raw material costs for the CARSOXY plant are water and CH₄, then the cost of water is calculated as the difference between the total cost (619,000 [£/Year]) and the CH₄ methane (594,000 [£/Year]). The value is equal to 25,000 [£/Year], Figure 6.6 (Raw material cost breakdown).

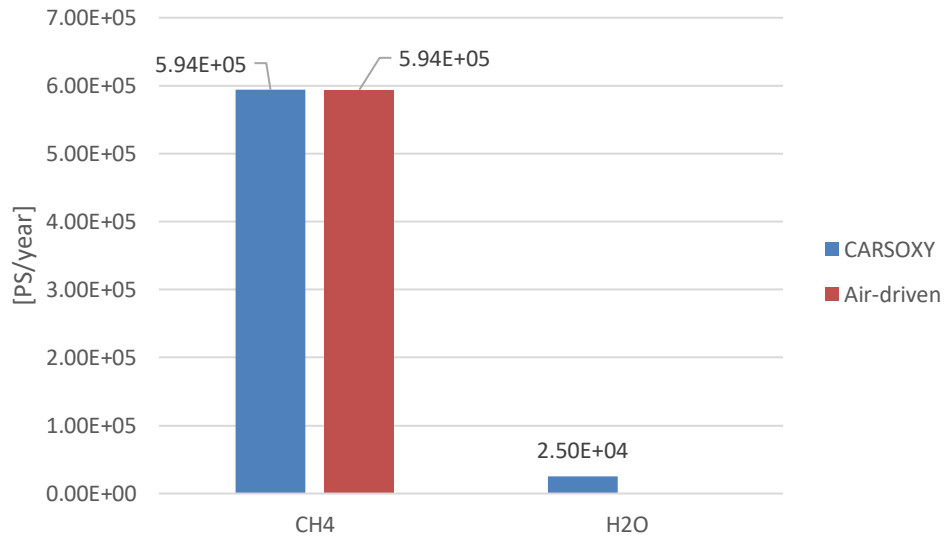


Figure 6.6 Raw material cost breakdown

Figure 6.7 shows the breakdown of sales. It can be seen that CARSOXY cycle is capable to payback its high capital cost mainly by the products of its gases O₂, N₂, H₂ and CO₂ sales. In fact, those products explain how CARSOXY cycle is economically sustainable (as discussed in the following chapter), despite of its high capital and operational costs (as explained in the previous section).

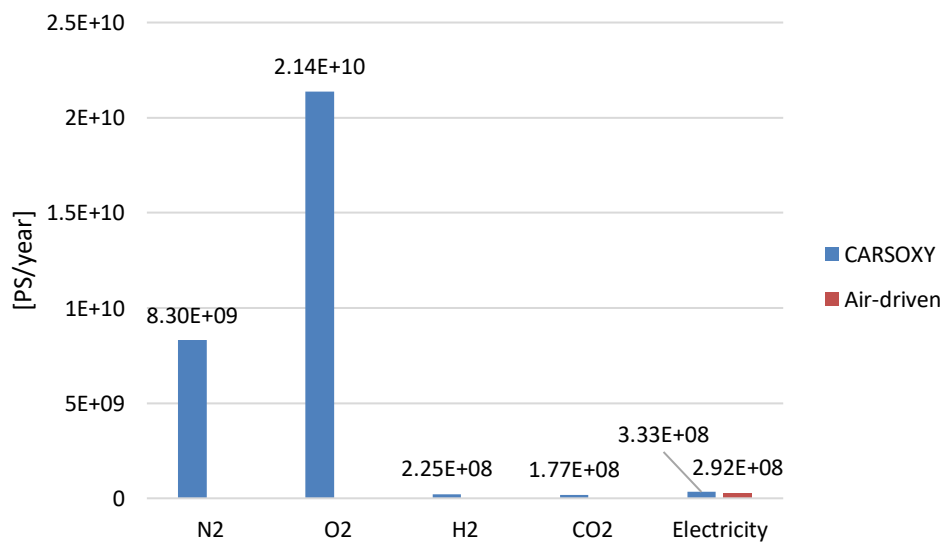


Figure 6.7 Sales breakdown

6.3 Payout period and Engineering, procurement and construction (EPC) period

The preliminary processes of a project are engineering, procurement and construction (EPC). According to reference [127], “It is defined as all the activities involved in order to hand over the project to the final owner. Such activities include design, procurement, construction, commissioning and handover”. The EPC is specified by two time-milestones. These are the start date for engineering and the completion date for construction. The EPC period is followed by the start-up period. It specifies the required period to transfer a project into its mature state, in which it meets the market needs. According to reference [128], “The Start-up period is defined as the period which is designed to develop a scalable business model to meet a marketplace need”. Payout period (P.O) is the period, which is required to pay for all the costs included in the project. Thus, the shorter this period the more effective the investment is.

As discussed previously, the CARSOXY plant has much higher total product sales than the Air-driven cycle, which as a result pays out for the high project cost and the operation cost. In fact, the CARSOXY plant is capable of paying out for all costs before the Air-driven cycle. As shown in Figure 6.8.A, the payout (P.O) periods are approximately 2.9 years and 6.1 years for the CARSOXY plant and the Air-driven cycle, respectively. Finally, the duration of the EPC period for the CARSOXY is approximately 0.83 year, which is higher than the 0.289 of the Air-driven cycle, Figure 6.8.B. This is due to the complexity involved in the EPC period of the CARSOXY plant.

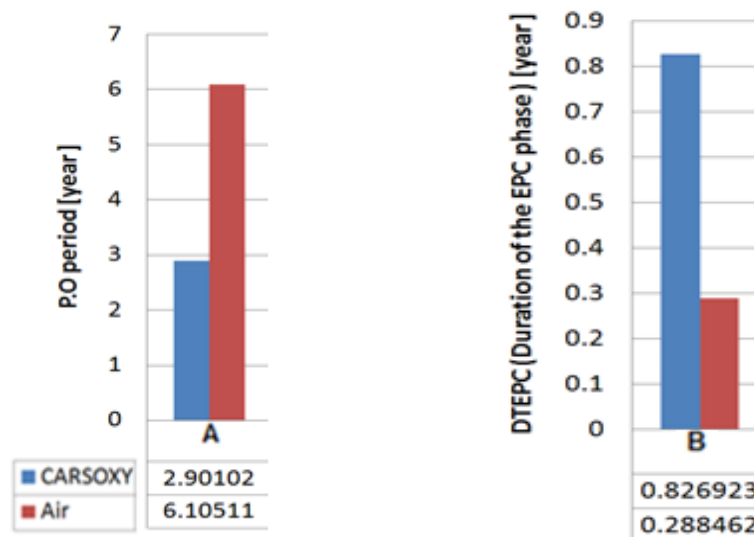


Figure 6.8 Payout period and Engineering, procurement and construction (EPC) period

6.4 Operation cost and product sales breakdowns throughout the project's life

As discussed in section 6.3 the operation costs and the product sales of the CARSOXY plant far exceed those for the Air-driven heat exchanged cycle. However, there are a few remarkable points.

The results displayed previously are the overall value throughout the project's life. The results of this section are the breakdown for each year and throughout the project's life. As shown in Figures 6.9 and 6.6, the operation costs in the first year for both systems are very low compared to other years. This is due to the EPC phase, which takes place in the first year.

Since the Duration of the EPC of the CARSOXY plant is more than that for the Air-driven heat exchanged cycle (approximately 0.83 and 0.289 of the first year, respectively), it can be noted that the operation cost of the CARSOXY plant in the first year is very low (compared to the second year).

Meanwhile, the operation cost in the first year is relatively higher (compared to the second year) for Air-driven heat exchanged cycle. This is because it will be in the operation phase before the CARSOXY cycle. From the second year until the last year, the operation costs approximately increase with constant rates for both cycles.

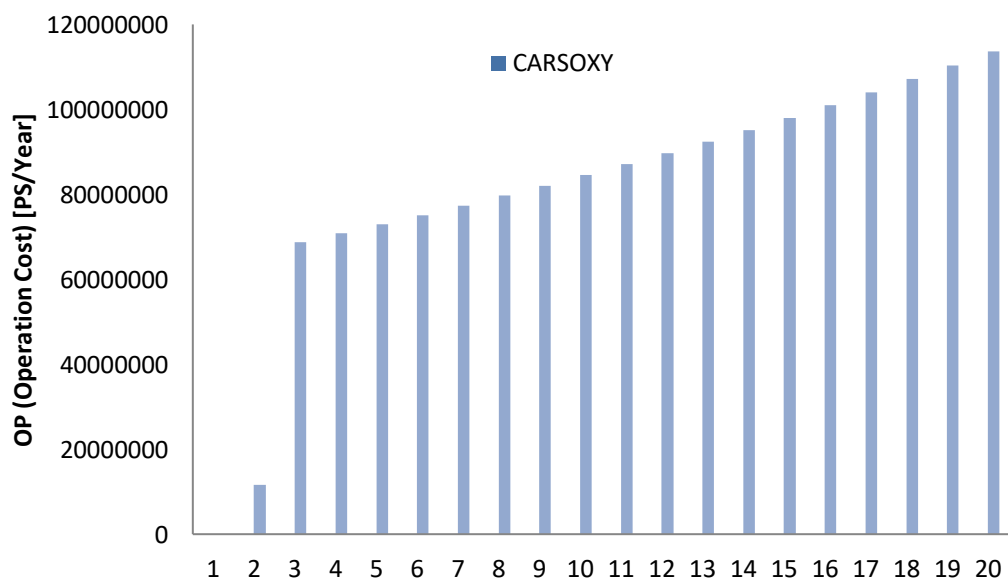


Figure 6.9 CARSOXY operation cost breakdown

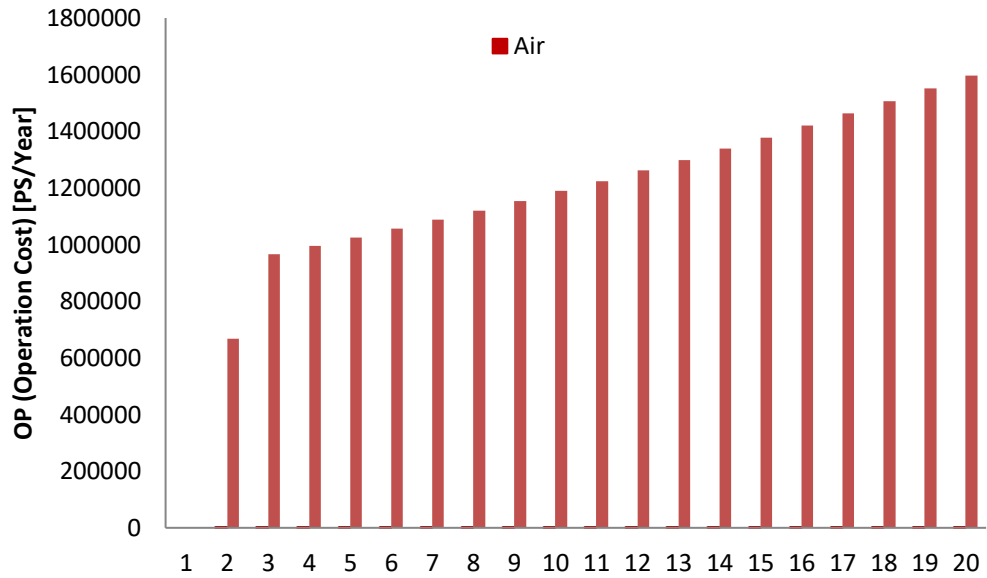


Figure 6.10 Air-driven operation cost breakdown

Patterns of the product sales are very similar to those for of the Operation costs. However, there is one major difference. It can be seen in Figures 6.11 and 6.12 that the large difference between the years is between the second and the third year (instead of the first and the second year). This is because of the fact that one additional start-up year is required after the EPC period in order to bring both systems to the production phase. It should be highlighted that the product sale is not the final revenue. The latter is subjected to the subtractions of expenses (such as operation costs, taxes, depreciation expenses, etc.). These are discussed in the following section.

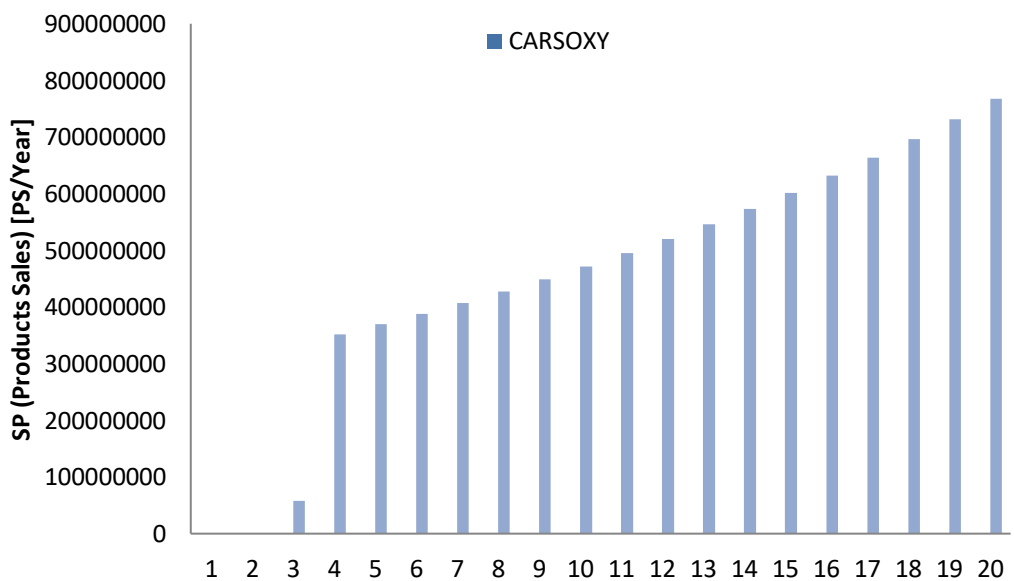


Figure 6.11 CARSOXY product sales breakdown

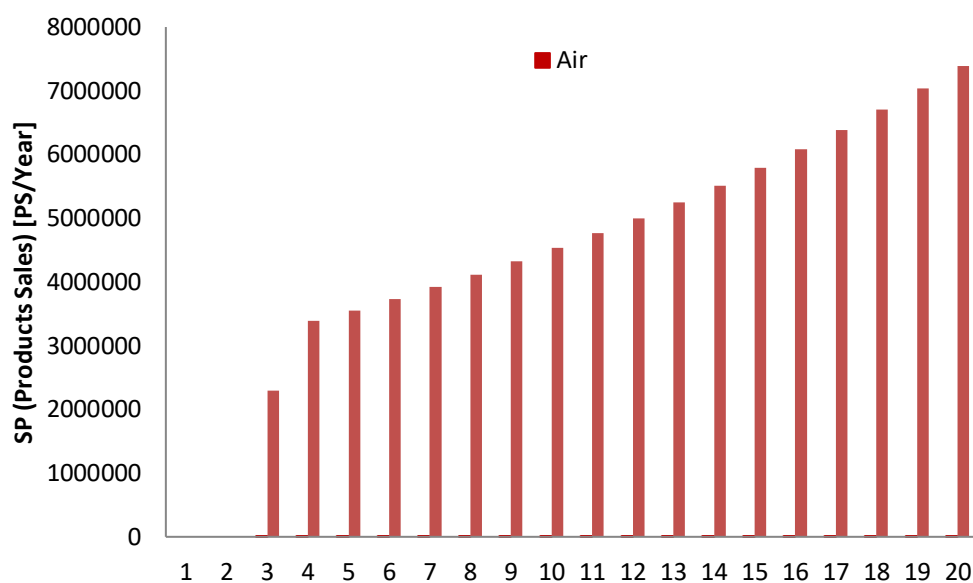


Figure 6.12 Air-driven product sales breakdown

6.5 Revenue Breakdown

Table 6.1 provides the definitions of other important economic parameters, which are involved in the revenue breakdown.

Table 6.1 Economic terms

Term	Definition	Reference
Revenue	“Revenue is the amount of money that a company actually receives during a specific period, including discounts and deductions for returned merchandise. It is the top line or gross income figure from which costs are subtracted to determine net income”	[177]
depreciation expense	“A depreciation expense is the amount deducted from gross profit to allow for a reduction in the value of something because of its age or how much it has been used. When you buy and own equipment, your business may be entitled to deduct a depreciation expense”	[178]
Earnings	“Earnings typically refer to after-tax net income, sometimes known as the bottom line, or a company's profits. Earnings are the main determinant of a company's share price because earnings and the circumstances relating to them can indicate	[177]

	whether the business will be profitable and successful in the long run”	
Tax	Business earnings are subjected to the tax system, which is imposed by governmental regulations. According to the reference [185], “A Tax Rate is the percentage at which a corporation is taxed. The tax rate is the tax imposed by the federal government and some states based on an individual's taxable income or a corporation's earnings”.	[172]

Figures 6.13 and 6.14 show the results of the revenue breakdown. After subtracting the depreciation expenses from the revenue, it is equal to the "Earning before taxes". Subtracting taxes from the revenue is equal to the "Total Earnings". Subtracting the "Earning before taxes" from the taxes is referred to as the "Net Earnings". It can be seen that the taxes are imposed for the CARSOXY plant only after the second year, Figure 6.13. Meanwhile, it is imposed for the Air-driven heat exchanged cycle directly after the first year with a very low amount, Figure 6.14. One of the Remarkable points is the TEX (Total expenses Excludes Taxes and Depreciation). As shown in Figure 6.14. In the first year of the Air-driven heat exchanged cycle, the TEX is very high. In fact, it is higher than any revenue value throughout the first 13 years of the project's life.

The same cannot be said about the CARSOXY plant. As shown in Figure 6.14, the revenue starts to exceed the TEX from the third year. Since then, the TEX neither exceeds the revenue nor exceeds the total (Or/and Net) Earnings. In fact, Net Earnings are approximately three to two times higher than the TEX from the third year and throughout the project's life.

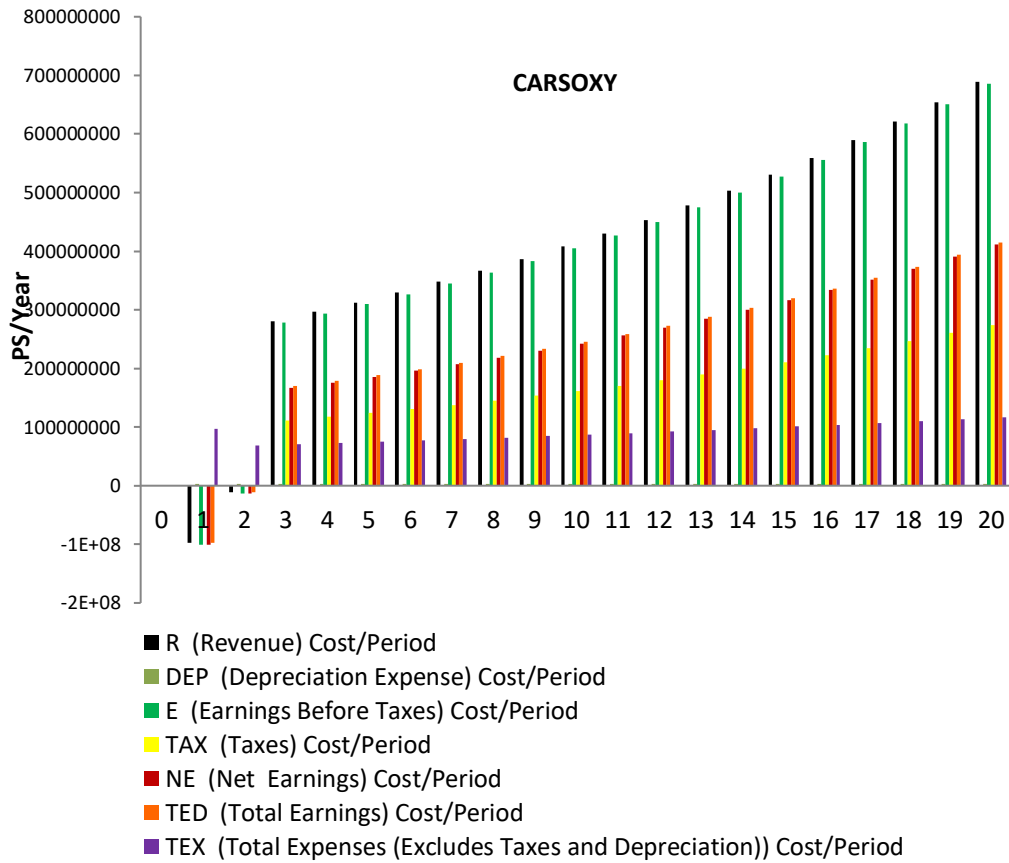


Figure 6.13 CARSOXY Revenue Breakdown (Note: Depreciation is negligible)

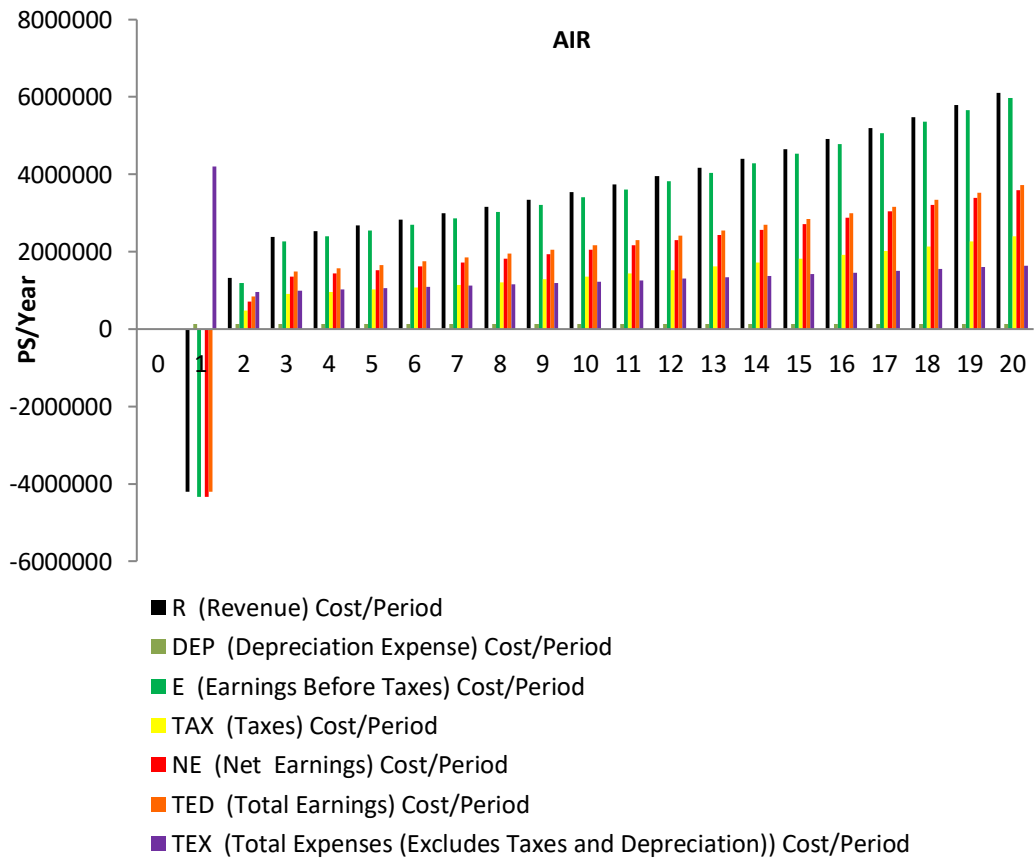


Figure 6.14 Air-driven Revenue Breakdown (note: Depreciation is negligible)

6.7 Net present value

According to the reference [172], “Present value (PV) is the current value of a future sum of money or stream of cash flows given a specified rate of return”. However, this term must be distinguished from the Net Present Value. According to the reference [124], “Net present value (NPV) is the difference between the present value of cash inflows and the present value (PVI) of cash outflows (PVO) over a period of time”. If the net present value of a year has a positive value, then the project can be considered profitable for this year. If NPV has a negative value, then the project is not yet profitable.

Perhaps the Net Present value is one of the most important parameters, if not the most important. Based on Figure 6.15, the NPVs of the CARSOXY plant for the first two years are negative. Then, it remains positive for the rest of the project's life. The Negative NPVs are relatively small compared to the remaining Positive NPVs. As highlighted in the figure, the NPV transfers from the negative region to the positive region after 2.9 years (P.O) period. Based on Figure 6.16, the NPVs of the Air-driven cycle are negative for 6 years. It transfers to the positive region exactly after 6.105 years, which is 30.5% of the projects life. This means that only 69.5 % of the projects life is profitable. On the other hand, the NPVs of the CARSOXY plant are negative for the first 2.9 years of the project's life. This is only 14.5% of the project's life, while 85.5% is considered profitable.

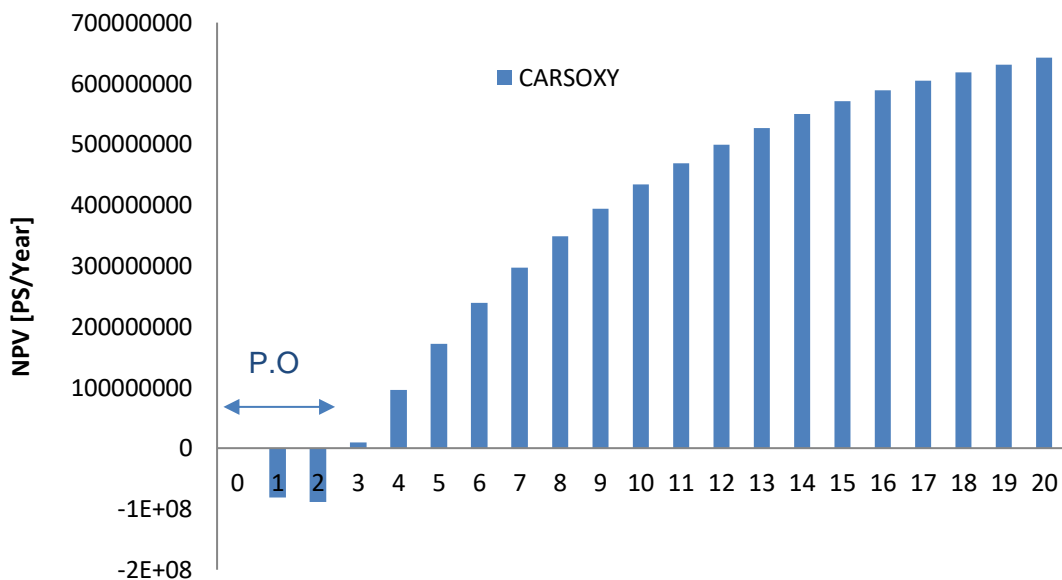


Figure 6.15 CARSOXY NPV.

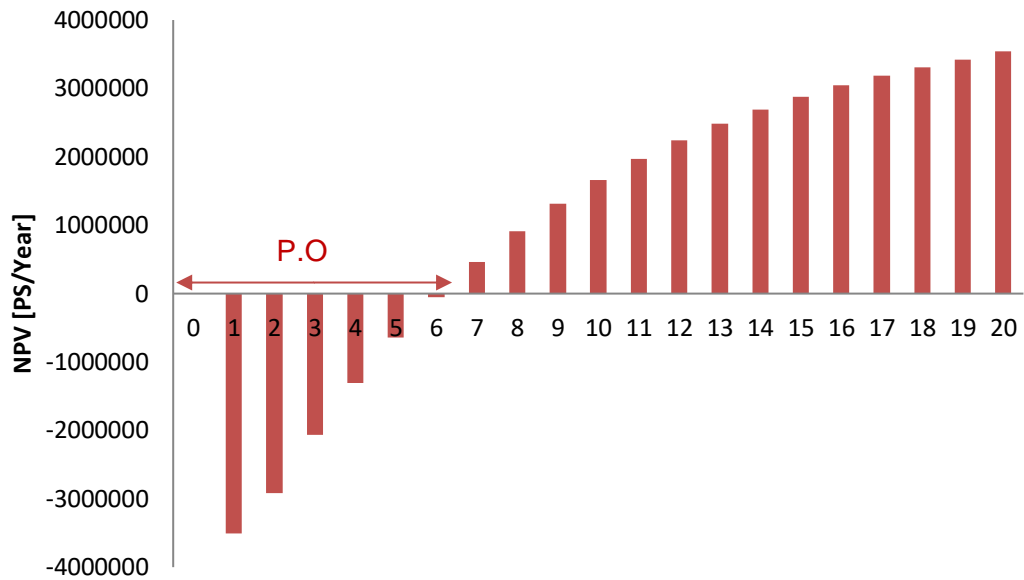


Figure 6.16 Air-driven NPV.

6.8 Rates of return and profitability index Results

According to the reference [124], “Internal rate of return is a discount rate that makes the net present value (NPV) of all cash flows from a particular project equal to zero”. If the Net present value is high (desirable), then a high IRR is required to bring it to zero. Therefore, if the IRR is high, then this is a (desirable) indicator. According to the reference [175], “The modified internal rate of return (MIRR) is a financial measure of an investment's attractiveness”. It is a very reliable tool to compare projects of different sizes. As shown in Figure 6.17.A, the IRRs of the CARSOXY plant and the Air-driven cycle are approximately 91.58% and 35.77%, respectively. This indicator is in favour of the CARSOXY plant. However, it is not yet what investors fully rely on. The MIRR is a very conservative and strict indicator. It takes into account the positive and negative cash flows. Based on Figure 6.17.B, the MIRR of the CARSOXY plant is approximately 2.2% higher than that for the Air-driven cycle.

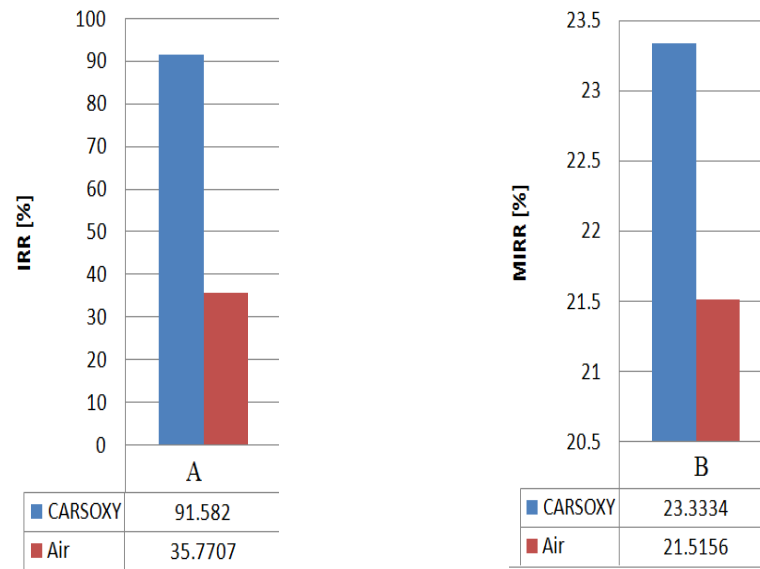


Figure 6.17 IRR and MIRR results.

The NRR indicator in Figure 6.18.A represents the ratio of the Net present value and the present value of all cash outflows in the last year of the project's life. The NRRs are approximately 73% and 28.7% for the CARSOXY and the Air-driven cycle, respectively. This indicates how mature and productive investment has become within the project's life [173]. Therefore, it can be concluded that the CARSOXY plant has managed to reach an acceptable productive and mature state. However, the Air-driven cycle would still require more time to reach a more mature state. The profitability index (PI) correlates the present values of the cash inflows and outflows. In fact, it is the ratio of both values. The project is considered profitable only if the (PI) is greater than one [172]. It can be seen in Figure 6.18.B that the Air-driven cycle is considered profitable with a PI of 1.28. However, it would have a higher PI if the project's life is longer. On the other hand, the PI of the CARSOXY cycle is 1.72.

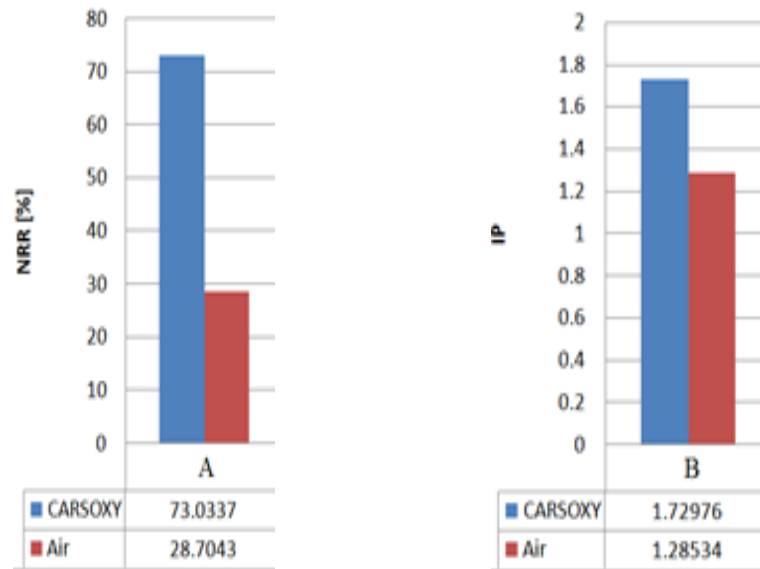


Figure 6.18 NRR and IP results.

6.9 Conclusion

On the ground of performing comparable techno-economic analyses between the CARSOXY and the Air-driven cycles, the same amount of CH₄ fuel (1240.8 [kg/h]) has been used for both cycles. Both cycles have been modelled using the same modelling technique under the same techno-economic conditions which are specified in sections 3 and 4, respectively. Due to the complexity involved in the CARSOXY cycle the total project cost, the total operation cost and the EPC (7.78E+07 [£], 6.48+07 [£/Year] and 0.83 Year, respectively) went beyond the limits of those for the Air-driven cycle. At first glance, these "unattractive" indicators would categorize the CARSOXY cycle as a risky project. However, high risks come with high gains. The high total product sales of the CARSOXY cycle do not only make up for those "unattractive" indicators but also entitle the CARSOXY cycle to payout all costs way before the Air-driven cycle.

The Net Present Value (NPV) is defined as the anticipated current value of the difference between cash inflows and outflows over a future period. If this indicator is positive, then the project is profitable [123]. 85.5% of the CARSOXY project's life is profitable (positive NPV), while only 69.5% is profitable for the Air-driven cycle. Moreover, very strict indicators such as the MIRR, IRR and NRR have examined the economic sustainability of the CARSOXY cycle. The MIRR is used to compare investments with different sizes of cash flows, and it has been in favour of the CARSOXY cycle by approximately 2.2% higher than that for the Air-driven cycle. On that note, it is highly important to highlight that the

CARSOXY cycle is fractional, such that it can be scaled to any capacity size to match the industry demand (from a laboratory-based scale to a large-scale industry) provided that a constant ratio is used to adjust all flow rates, Table 5. Furthermore, the Internal Rate of Return (IRR) indicators have also been on the side of the CARSOXY cycle. IRR is defined as The essential discount rate which zeros the NPV[124]. The Internal Rates of Return (IRR) were approximately 91.58% and 35.77% for the CARSOXY cycle and the Air-driven, respectively. Finally, the CARSOXY cycle is anticipated to become more productive investment than the Air-driven cycle as the NRRs are 73% and 28.7% for the CARSOXY and the Air-driven, respectively. Therefore, based on the figures it can be concluded that the CARSOXY cycle has the potential to be adopted by the industry in the near future.

Finally, it is important to highlight that the techno-economic analyses presented in this chapter are based on several assumptions, section 3.4.5. Those assumptions become less valid as the operation life of the project increases. Moreover, as discussed in section 3.4.6, while price escalation between past and present using the Chemical Engineering Plant Cost Index could be used with a high level of certainty [133], escalation between present and future shall be used with a lower level of certainty as those are based on anticipation functions performed by ASPEN PLUS [125]. In addition, as discussed in section 6.1, there are some costs, which cannot be traced directly (i.e. plant overhead) and can only be anticipated. Therefore, it is wise to use the results of this chapter as anticipations rather than facts.

CHAPTER SEVEN

Chemiluminescence imaging and emission analyses of CARSOXY combustion. (Experimental)

“The test of all knowledge is an experiment.”

~ Richard Feynman

CHAPTER 7 – CARSOXY CHEMILUMINESCENCE IMAGING AND EMISSION ANALYSES.

Strict regulations and Acts have been imposed to limit NO_x and carbon emissions. Innovative techniques have become resorts for the power generation industry to overcome such a low level of tolerance. CO₂-Argon-Steam Oxy-Fuel (CARSOXY) gas turbines have theoretically proven to offer an economically sustainable solution whilst retaining high efficiency, chapters 4, 5 and 6. This chapter attempts to experimentally assess CARSOXY in comparison to an Air/Methane flame. OH chemiluminescence imaging integrated with Abel deconvolution techniques [153] have been utilized to study flame stability, and flame geometry (i.e. Area of highest heat intensity ($A_{\overline{OH}_{Max}}$), Center of highest heat intensity ($C_{\overline{OH}_{Max}}$) over a range of instability conditions (excitation frequencies [50Hz-700Hz]). Moreover, NO_x and carbon emissions have also been analyzed. The standard deviation of heat release fluctuations ($\sigma_{OH^*/\overline{OH}}$) has been utilized as the base-criteria to compare the stability performance of CARSOXY to Air/Methane combustion. The results of this chapter are obtained explained in the methodology section (3.5). The definitions of the assessed parameters are present in section 3.5.

Essentially, higher stability performance has been demonstrated by CARSOXY as the average $\sigma_{OH^*/\overline{OH}}^{CARSOXY}$ is 0.711, 0.65 and 0.54, whilst $\sigma_{OH^*/\overline{OH}}^{Air}$ is 1.99, 0.72 and 0.86 over the excitation interval [50Hz-700Hz] for the working fluid flow rates (\dot{V}_{WF}) of 40L/min, 60L/min and 80L/min, respectively. These results have been further confirmed by the $C_{\overline{OH}_{Max}}$ results. CARSOXY has shown both lower sensitivity towards both variable flow rates and excitation frequencies compared to Air/Methane. In addition, CARSOXY reduced CO emissions approximately to 10% of those of Air/methane, while having negligible levels of NO_x emissions. Finally, CARSOXY flame is anticipated to be more compact than Air/Methane, such that $\bar{A}_{\overline{OH}_{Max},CARSOXY}$ is 334 mm² and 228mm², while $\bar{A}_{\overline{OH}_{Max},Air}$ is 399mm² and 24 mm² at $\dot{V}_{WF}=80L/min$ and 60L/min and 40L/min, respectively. However, CARSOXY flame has a higher area of the highest heat intensity in comparison to Air/Methane at $\dot{V}_{WF}=40L/min$ (571 mm² and 385.9mm², respectively).

As discussed in section 3.5, the suggested molar fractions of CARSOXY (blend 58, Table 3.1) by the reference [25] have been normalized such that it contains zero H₂O molar fraction (Dry combustion). Therefore, the result of this chapter corresponds to this blend.

7.1 NO, NO₂ and NO_x emissions

Corresponding the methodology of emission analyses (section 3.5.2), Figure 7.1 shows the NO, NO₂ and NO_x emissions of the methane/Air and methane CO₂-A_r-O₂ flames. The experimental NO, NO₂ and NO_x emission results matched the expectation, such as those for the CARSOXY flame are lower than those for the Air/Methane flame. Nevertheless, CARSOXY flame must theoretically have zero NO, NO₂ and NO_x as it does not contain Air. The captured levels of NO, NO₂ and NO_x are because the confinement is not fully enclosed from the atmospheric air. Besides, these emission levels are also related to the ignition pilot.

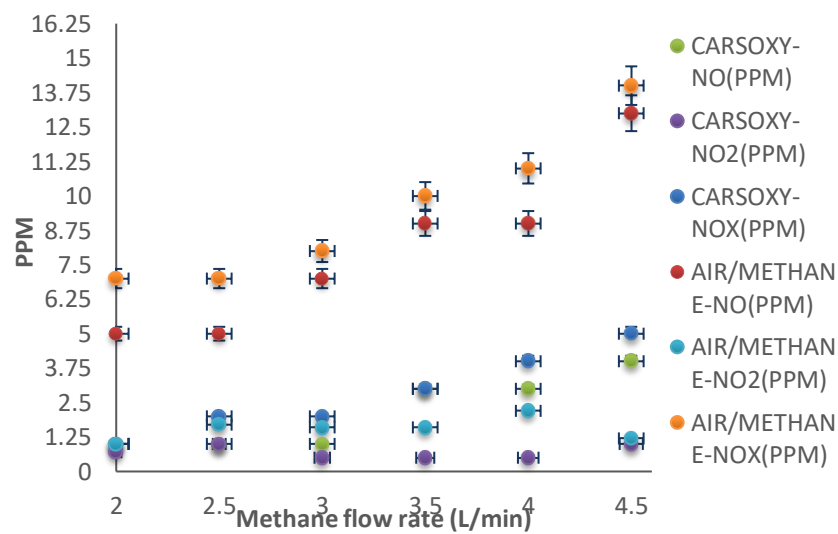


Figure 7.1 NO, NO₂ and NO_x flue gases at 140 L/min of \dot{V}_{WF} .

7.2 CO emissions

Corresponding the methodology of emission analyses (section 3.5.2), Figure 7.2 shows the CO emission levels, the CO levels of the CARSOXY flame is significantly lower than those for the Air/Methane flame. This is indeed one of the major advantages of CARSOXY combustion. The reduced levels of CO can be explained by the high levels of oxygen in the CARSOXY blend which enhances the conversion of CO to CO₂. It is worth mentioning that high conversion of CO to CO₂ facilitates easier CO₂ capturing by CCS units.

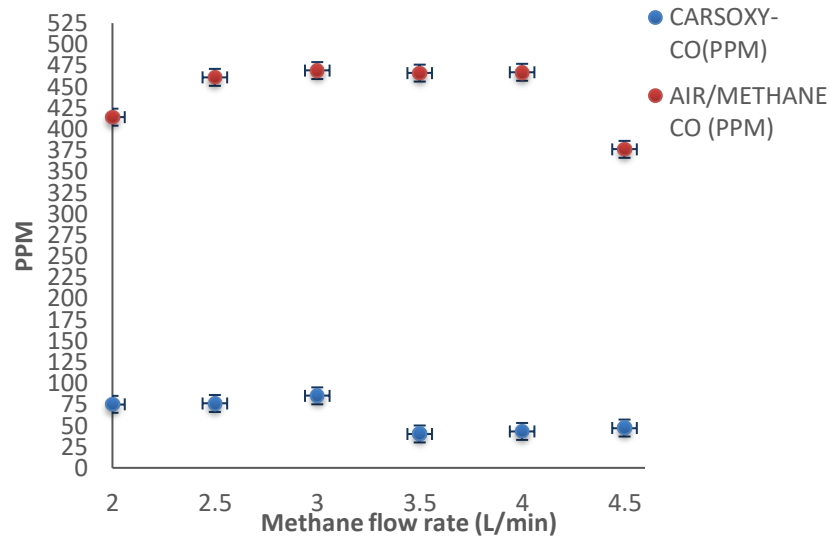


Figure 7.2 CO emissions at 140 L/min of \dot{V}_{WF} .

7.3 $\sigma_{OH^*/\overline{OH}}$ at \dot{V}_{WF} of 80 L/min and \dot{V}_{CH_4} of 1L/min.

As discussed in section 3.5.10, each instantaneous background image has been subtracted from its corresponding instantaneous flame image. Similarly, the averaged background image has been subtracted from its corresponding averaged flame image. As discussed in section 3.5.11, heat release fluctuation has been calculated using the background-corrected instantaneous and averaged integral pixel intensities (OH^* and \overline{OH} , using a MATLAB code -Appendix 3.2.1- to perform Equations (3.34) and (3.35) respectively). This thesis applies the standard deviation concept to quantify the chemiluminescence fluctuation (OH^*/\overline{OH}) over time. Standard deviation is a statistical technique which measures the tendency of data points to be far from the mean value [162]. Therefore, each instantaneous image has its own instantaneous standard deviation in reference to the averaged image (as shown in Figure 3.11). Those instantaneous standard deviations have been averaged to represent the overall averaged standard deviation of each flame condition (i.e. \dot{V}_{WF} of 40L/min, 60L/min and 80 L/min over [50Hz-700Hz]).

Since the standard deviation is a non-dimensional parameter, it has been utilized to compare the chemiluminescence fluctuation (OH^*/\overline{OH}) of CARSOXY flame in comparison to Air/methane. This technique has not been utilized for this thesis and there is no evidence of use in the evaluated combustion literature.

Figure 7.3 shows the standard deviation (σ) of the heat release fluctuations (OH^*/\overline{OH}) over the excitation interval of ([50 Hz -700 Hz], 8 dB and 10V) at \dot{V}_{WF} and \dot{V}_{CH_4} of 80 L/min and 1 L/min, respectively. The standard deviation (σ) of the CARSOXY flame was lower than that for the Air/flame throughout the entire interval. CARSOXY is significantly more stable than Air/Methane at 100Hz and 150 Hz such that $\sigma_{OH^*/\overline{OH}}^{CARSOXY}$ is 0.93 and 0.503 while $\sigma_{OH^*/\overline{OH}}^{Air}$ is 1.62 and 1.08, respectively. Therefore, it can be concluded that the CARSOXY flame has a superior stability performance over the Air/Methane flame within this domain.

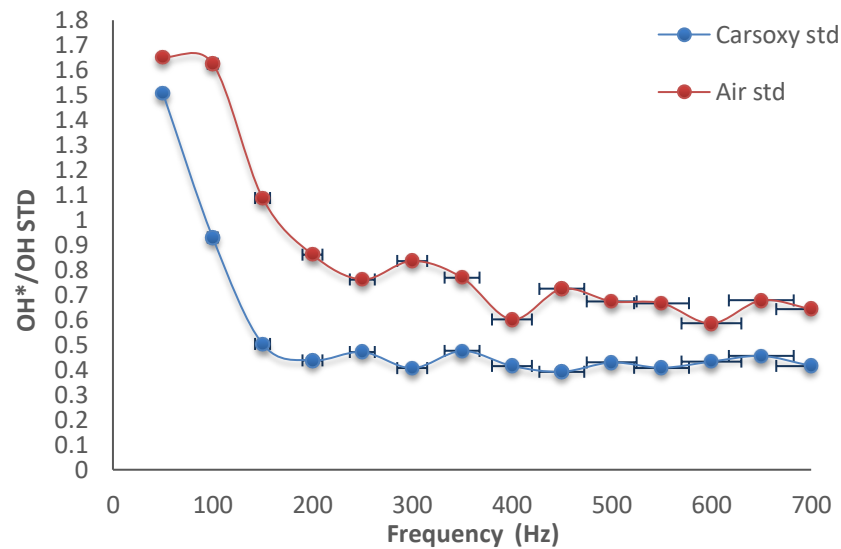


Figure 7.3 $\sigma_{OH^*/\overline{OH}}$ at \dot{V}_{WF} of 80 L/min.

7.4 $\sigma_{OH^*/\overline{OH}}$ at \dot{V}_{WF} of 60 L/min and \dot{V}_{CH_4} of 1L/min.

Figure 7.4 shows the standard deviation (σ) of the heat release fluctuations (OH^*/\overline{OH}) over the excitation interval of ([50 Hz -700 Hz], 8 dB and 10V) at \dot{V}_{WF} and \dot{V}_{CH_4} of 60 L/min and 1 L/min, respectively. As \dot{V}_{WF} dropped from 80 L/min to 60 L/min, the CARSOXY become less stable compared to its performance at \dot{V}_{WF} of 80 L/min. In fact, CARSOXY flame is less stable than the Air/Methane flame beyond 250 Hz. However, CARSOXY flame still has a high stability performance to offer within the excitation interval of [50 Hz to 250 Hz]. Remarkably, the Air/Methane flame at 100 Hz exhibits an instable performance with a $\sigma_{OH^*/\overline{OH}}^{Air}$ of 2.09. Meanwhile, $\sigma_{OH^*/\overline{OH}}^{CARSOXY}$ is only 0.771.

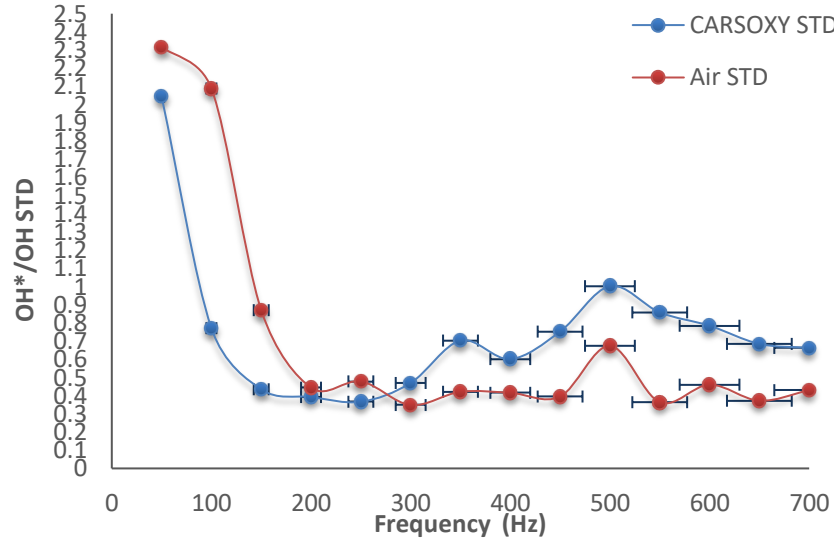


Figure 7.4 $\sigma_{OH^*/\overline{OH}}$ at \dot{V}_{WF} of 60 L/min.

7.5 $\sigma_{OH^*/\overline{OH}}$ at \dot{V}_{WF} of 40 L/min and \dot{V}_{CH_4} of 1L/min.

At $\dot{V}_{WF}=40\text{L/min}$ (Figure 7.5), it can be seen that the Air/Methane flame is extremely unstable at 100 Hz with a $\sigma_{OH^*/\overline{OH}}^{Air}$ of 17.55. At this frequency (100 Hz), CARSOXY can be used as a good substitute for Air/Methane to avoid this extreme condition of instability since $\sigma_{OH^*/\overline{OH}}^{CARSOXY}$ is only 1.02. However, $\sigma_{OH^*/\overline{OH}}^{CARSOXY}$ at 400 Hz is higher than that for the Air/Methane flame (i.e. 2.5 and 0.37, respectively). As a trade-off, CARSOXY flame would still have a better overall stability performance throughout this interval compared to the Air/Methane flame.

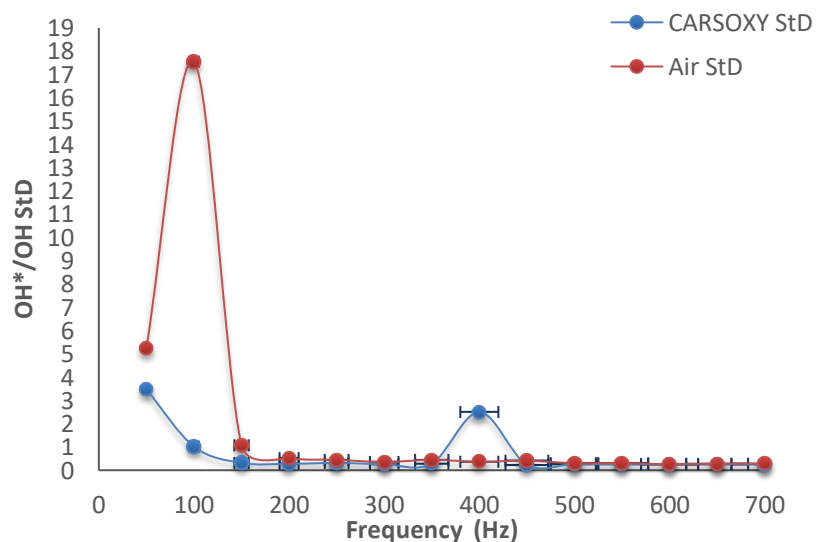


Figure 7.5 $\sigma_{OH^*/\overline{OH}}$ at \dot{V}_{WF} of 40 L/min.

Evaluating the overall stability trends, it can be seen that approximately at the [50-150] Hz region, both flames (CARSOXY and Air/methane) illustrate the highest peaks of instability. This can be essentially explained by the fact that the natural frequency of the burner is located in this region (150Hz). Moreover, the speaker at this region provides escalated levels of impedance. It must be highlighted that the excitation frequencies [50-100] Hz are not within the linear frequency- impedance response of the speaker (i.e. [150-1000] Hz) [199]. However, essentially, the function of the speaker is to subject both of the CARSOXY and Air/Methane flames to comparable instability conditions to examine the CARSOXY flame stability behaviour in reference to the Air/Methane flame.

7.6 $\sigma_{OH^*/\overline{OH}}$ functions of frequency ($\sigma_{OH^*/OH}(f)$)

The experimentally obtained data points of $\sigma_{OH^*/\overline{OH}}$ in Figures 7.3, 7.4 and 7.5 have been curve-fitted using 6th order polynomial functions. These have provided good curve fitting for the \dot{V}_{WF} of (80 and 60 L/min) throughout the entire excitation domain. However, at the \dot{V}_{WF} of 40 L/min the polynomial function provided poor fitting for the entire excitation interval. Therefore, the interval has been divided into three different regions -as shown in Table 7.1- and have been fitted using three different polynomial functions to provide better curve fitting. Table 7.1 provides $\sigma_{OH^*/\overline{OH}}^{CARSOXY}(f)$ of the three \dot{V}_{WF} (40, 60 and 80 L/min) at a \dot{V}_{CH_4} of 40 L/min. This approach provides the heat release standard deviation functions $\sigma_{OH^*/\overline{OH}}^{CARSOXY}(f)$ to establish numerical anticipations of the flame stability response for CARSOXY within the tested frequency (f) interval ([50-700] Hz at 8 dB and 10V). It would also provide a computational simulation baseline for further studies on CARSOXY.

Table 7.1 $\sigma_{OH^*/OH}(f)$ at [50 Hz -700 Hz]

\dot{V}_{WF} [L/min]	Frequency (f) interval [Hz]	$\sigma_{OH^*/OH}^{CARSOXY}(f)$	$\sigma_{OH^*/OH}^{Air}(f)$
80	[50-700]	$\sigma_{OH^*/\overline{OH}}^{CARSOXY} = (-2 \times 10^{-16} \times f^6) + (3 \times 10^{-13} \times f^5) + (4 \times 10^{-11} \times f^4) - (2 \times 10^{-7} \times f^3) + (1 \times 10^{-4} \times f^2) - (2.79 \times 10^{-3} \times f) + 2.6285$	$\sigma_{OH^*/\overline{OH}}^{Air} = (-2 \times 10^{-15} \times f^6) + (4 \times 10^{-12} \times f^5) - (4 \times 10^{-9} \times f^4) + (2 \times 10^{-6} \times f^3) - (0.0003 \times f^2) + (0.0249 \times f) + 1.0893$
60	[50-700]	$\sigma_{OH^*/\overline{OH}}^{CARSOXY} = (2 \times 10^{-15} \times f^6) - (5 \times 10^{-12} \times f^5) + (5 \times 10^{-9} \times f^4) - (2 \times 10^{-6} \times f^3) + (6 \times 10^{-4} \times f^2) - (8.61 \times 10^{-2} \times f) + 5.03$	$\sigma_{OH^*/\overline{OH}}^{Air} = (3 \times 10^{-15} \times f^6) + (7 \times 10^{-12} \times f^5) - (6 \times 10^{-9} \times f^4) + (3 \times 10^{-6} \times f^3) - (0.0005 \times f^2) + (0.0329 \times f) + 1.763$
40	[50-150]	$\sigma_{OH^*/\overline{OH}}^{CARSOXY} = (0.0004 \times f^2) - (0.1019 \times f) + 7.6938$	$\sigma_{OH^*/\overline{OH}}^{Air} = (0.0058 \times f^2) + (1.1091 \times f) - 35.811$

40	[150-400]	$\sigma_{OH^*/\overline{OH}}^{CARSOXY} = (4 \times 10^{-11} \times f^6) - (5 \times 10^{-8} \times f^5) + (2 \times 10^{-11} \times f^3) - (0.0055 \times f^2) + (0.6184 \times f) - 26.587$	$\sigma_{OH^*/\overline{OH}}^{Air} = -(3 \times 10^{-11} \times f^5) + (4 \times 10^{-8} \times f^4) - (2 \times 10^{-5} \times f^3) + (0.0065 \times f^2) - (0.8635 \times f) + 45.767$
40	[400-700]	$\sigma_{OH^*/\overline{OH}}^{CARSOXY} = (2 \times 10^{-13} \times f^6) - (7 \times 10^{-11} \times f^5) + (1 \times 10^{-6} \times f^4) - (0.0008 \times f^3) + (0.3307 \times f^2) - (74.775 \times f) + 7010.5$	$\sigma_{OH^*/\overline{OH}}^{Air} = -(9 \times 10^{-14} \times f^6) + (3 \times 10^{-10} \times f^5) - (4 \times 10^{-7} \times f^4) + (0.0003 \times f^3) - (0.1293 \times f^2) + (27.946 \times f) - 2497.4$

7.7 Area of highest heat intensity ($A_{\overline{OH}_{Max}}$) at \dot{V}_{WF} of 80 L/min and \dot{V}_{CH_4} of 1L/min.

As discussed in section 3.5.12, $A_{\overline{OH}_{Max}}$ results have been obtained for specially resolved images. Figures 7.6 and 7.7 show some the cases at \dot{V}_{WF} of 80 L/min and \dot{V}_{CH_4} of 1L/min. $A_{\overline{OH}_{Max}}$ results are summarized in Figure 7.8.

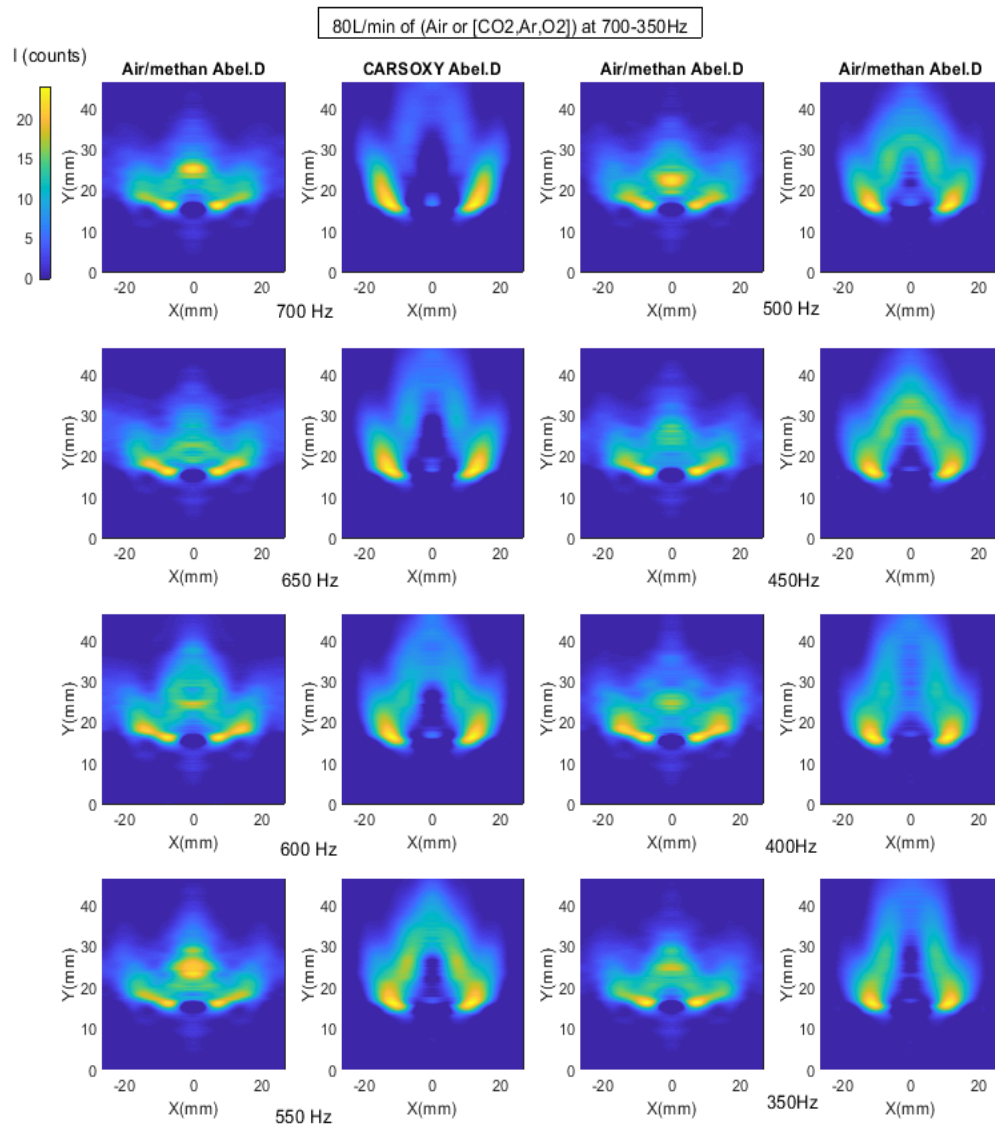


Figure 7.6 temporally and specially resolved images (at \dot{V}_{WF} of 80 L/min and \dot{V}_{CH_4} of 1L/min, 700-350) Hz.

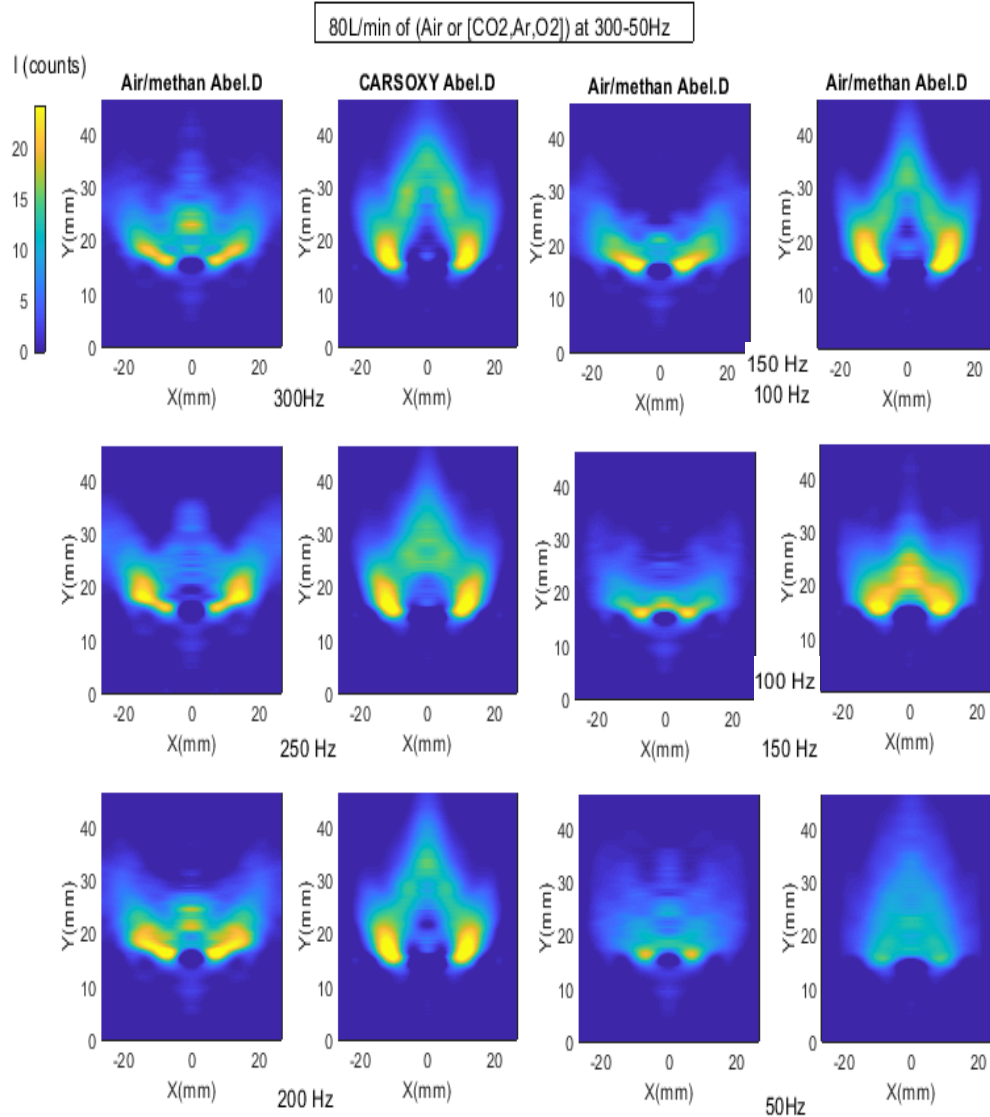


Figure 7.7 temporally and specially resolved images (at \dot{V}_{WF} of 80 L/min and \dot{V}_{CH_4} of 1L/min, 300-50) Hz.

As shown in Figure 7.8, $A_{\overline{OH}_{Max}}$ of CARASOXY is higher than that for the Air/Methane flame in the excitation interval of [50 Hz -150 Hz] and \dot{V}_{WF} of 80 L/min and \dot{V}_{CH_4} of 1 L/min. Nevertheless, the flame area of CARSOXY is lower than that for the Air/Methane flame beyond 150 Hz, except for 450 Hz. In fact, the Average area of the entire excitation interval is lower for CARSOXY than that for the Air/Methane flame (334 mm² and 399 mm², respectively). It is crucial to highlight that both flames produce the same amount of thermal power as both consume the same amount of fuel (1 L/min of CH₄). This essentially means that the CARSOXY flame is more likely to require a more compact burner while producing the same amount of thermal power as the Air/Methane flame.

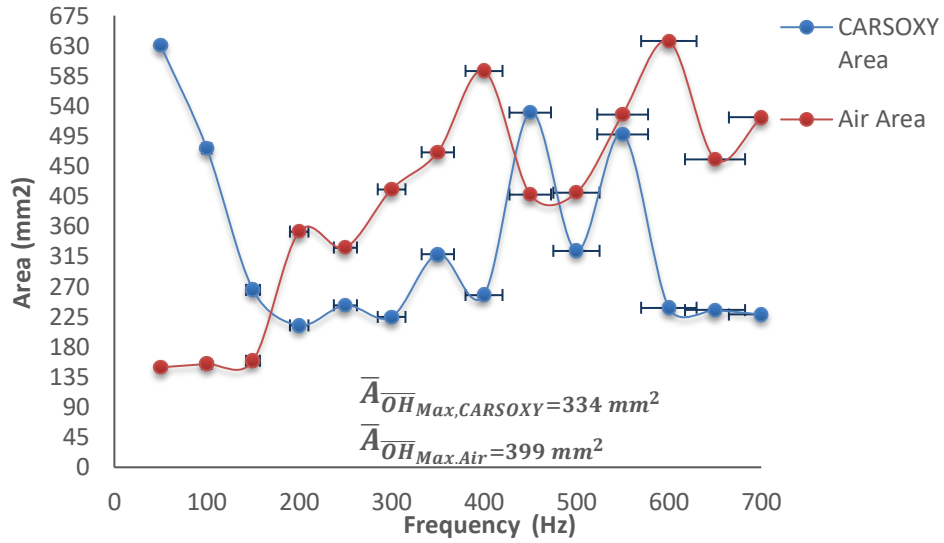


Figure 7.8 Area of highest heat intensity ($A_{\overline{OH}_{Max}}$) at \dot{V}_{WF} of 80 L/min.

7.8 Area of highest heat intensity ($A_{\overline{OH}_{Max}}$) at \dot{V}_{WF} of 60 L/min and \dot{V}_{CH_4} of 1L/min.

As shown in Figure 7.9, as \dot{V}_{WF} decreases to 60L/min, the $A_{\overline{OH}_{Max}}$ patterns approximately retained the same behaviour as those at 80 L/min (Figure 6.A). However, by comparing the average area of both flow rates (\dot{V}_{WF} of 80l/min and 60L/min) it can be seen that the difference between CARSOXY and Air/Methane flame average area ($\bar{A}_{\overline{OH}_{Max,Air}} - \bar{A}_{\overline{OH}_{Max,CARSOXY}}$) decreases as \dot{V}_{WF} decreases from 80l/min to 60L/min.

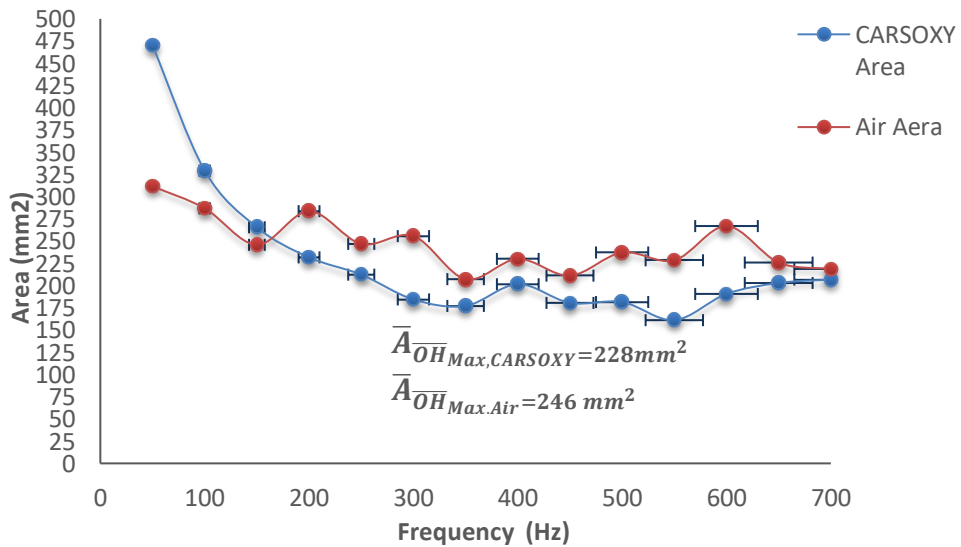


Figure 7.9 Area of highest heat intensity ($A_{\overline{OH}_{Max}}$) at \dot{V}_{WF} of 60 L/min.

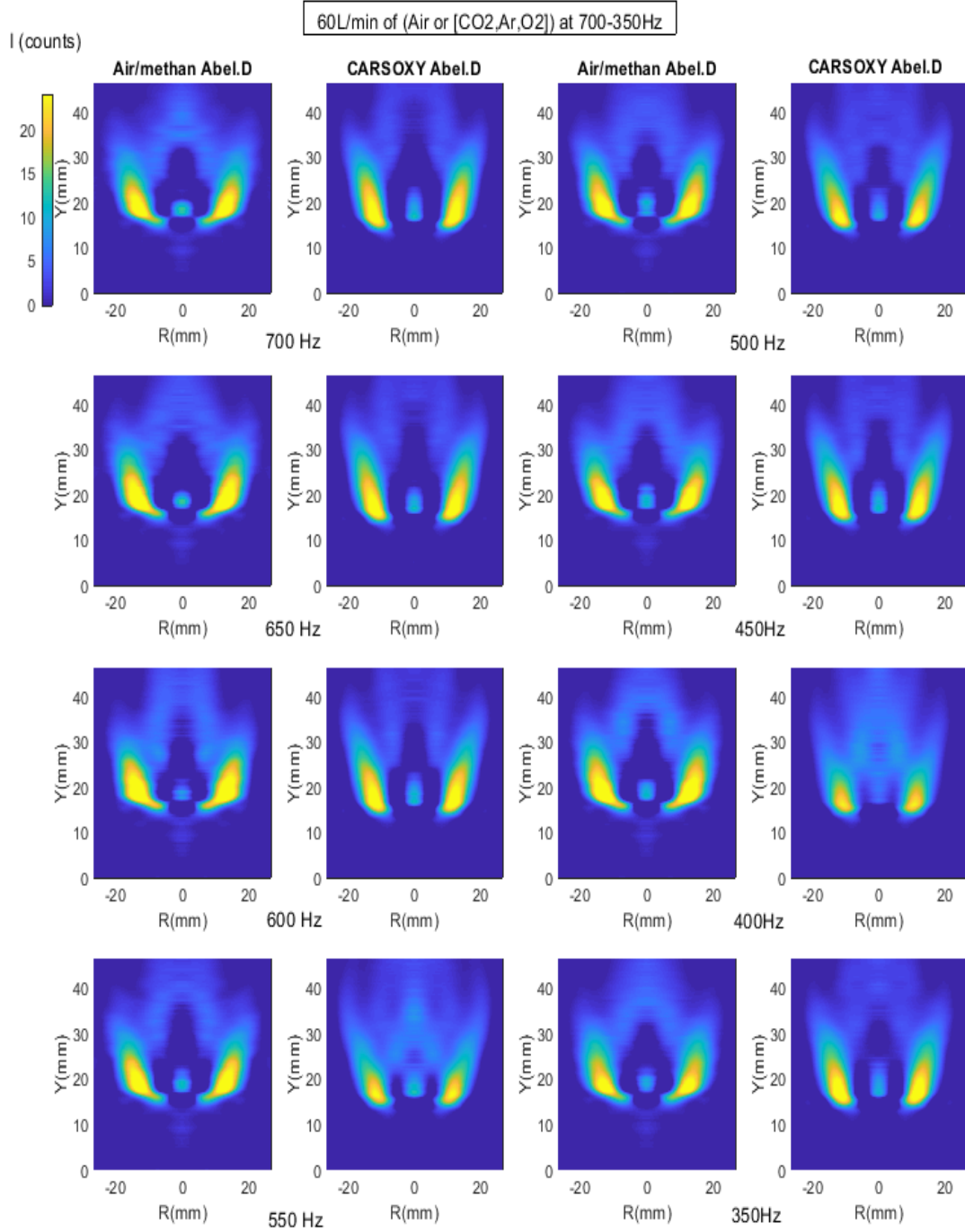


Figure 7.10 temporally and specially resolved images (at \dot{V}_{WF} of 60 L/min and \dot{V}_{CH_4} of 1L/min, 700-350) Hz.

Figures 7.10 and 7.11 show some the cases at \dot{V}_{WF} of 80 L/min and \dot{V}_{CH_4} of 1L/min. $A_{OH_{Max}}$ results are summarized in Figure 7.8.

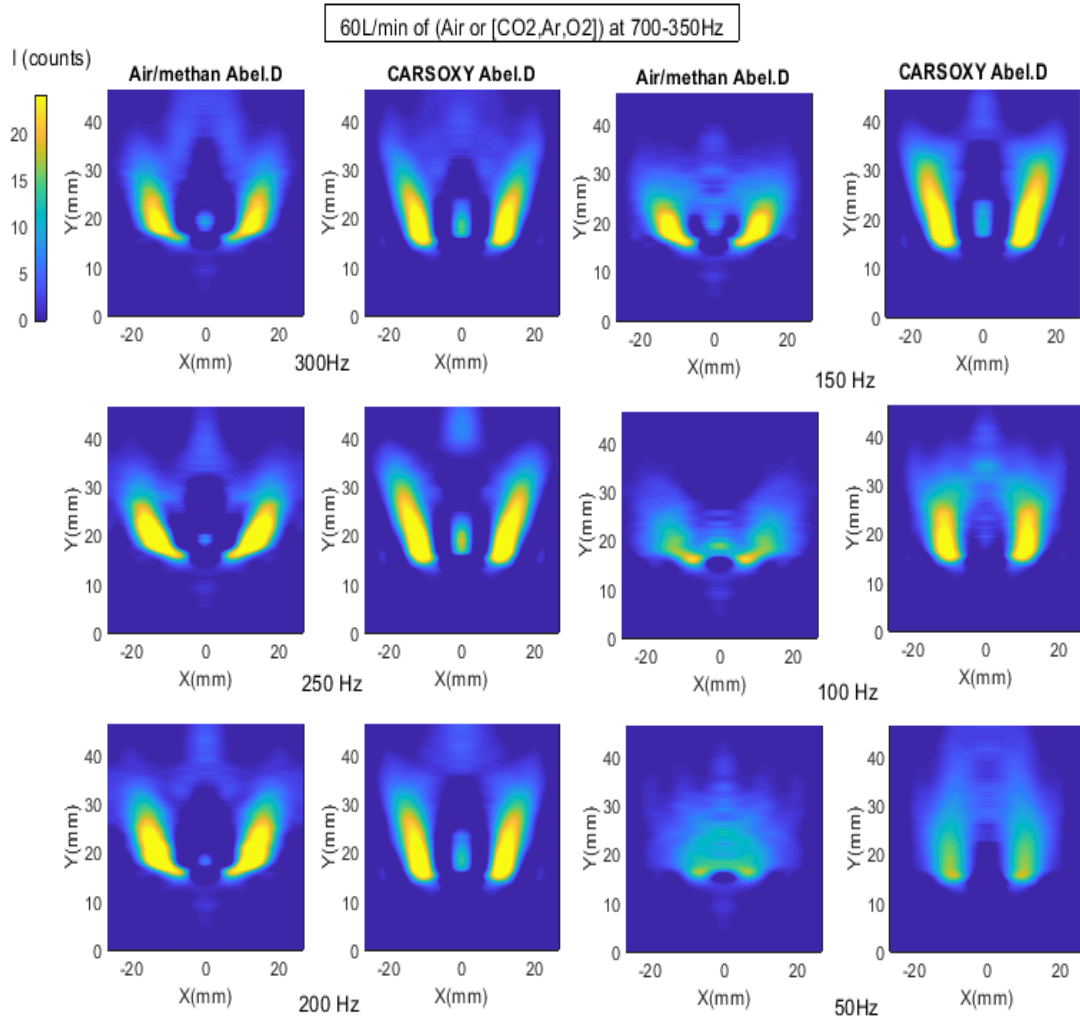


Figure 7.11 temporally and specially resolved images (at \dot{V}_{WF} of 60 L/min and \dot{V}_{CH_4} of 1L/min, 300-50) Hz.

7.7 Area of highest heat intensity ($A_{\overline{OH}_{Max}}$) at \dot{V}_{WF} of 40 L/min and \dot{V}_{CH_4} of 1L/min.

Figures 7.12 and 7.13 show some of the cases at \dot{V}_{WF} of 40 L/min and \dot{V}_{CH_4} of 1L/min. $A_{\overline{OH}_{Max}}$ results are summarized in Figure 7.14. As shown in Figure 7.14, decreasing \dot{V}_{WF} even to a lower level (40L/min) approximately increases $A_{\overline{OH}_{Max}}$ beyond that for the Air/Methane flame. In fact, the flame average areas are 571 mm² and 386 mm² for the CARSOXY and Air/Methane flames, respectively.

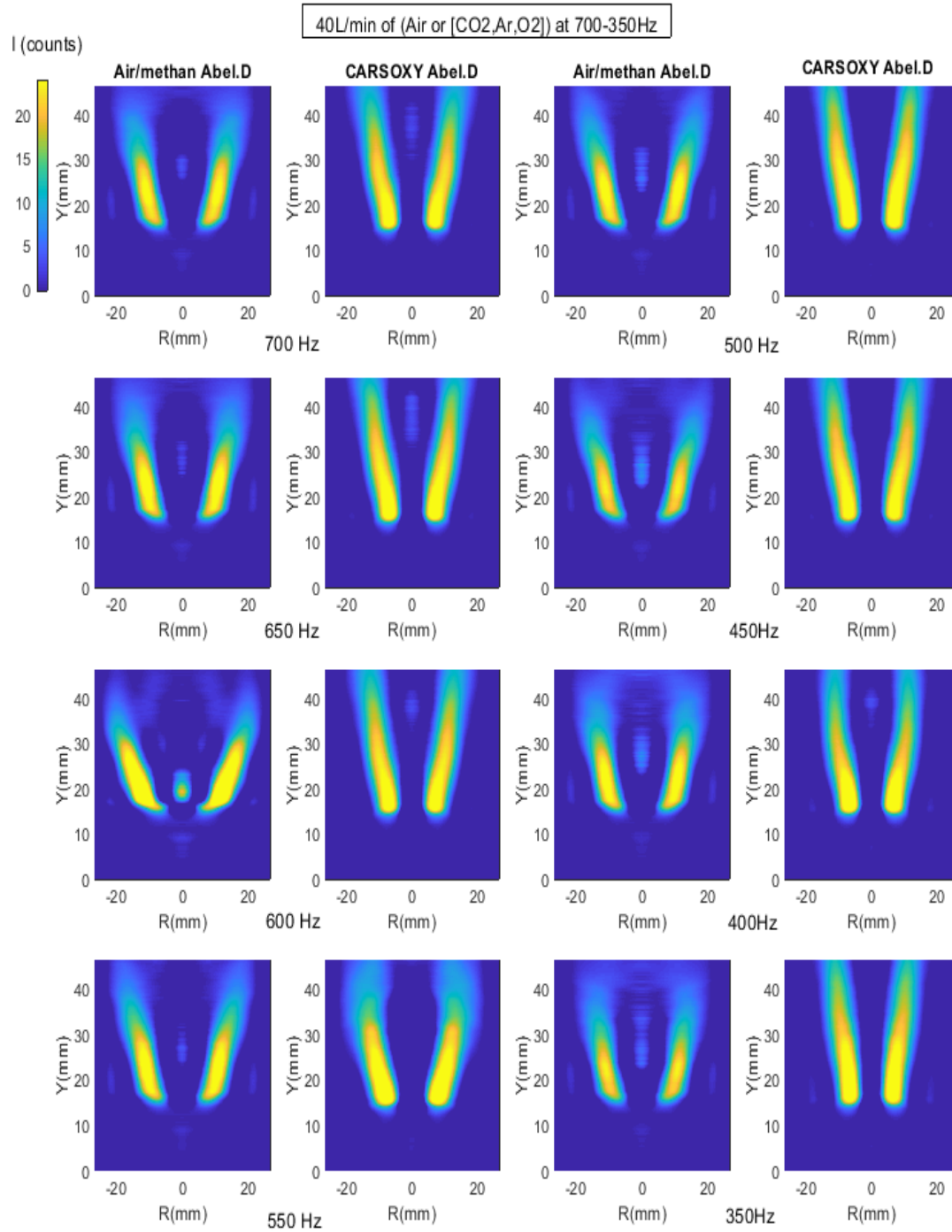


Figure 7.12 temporally and spatially resolved images (at \dot{V}_{WF} of 40 L/min and \dot{V}_{CH_4} of 1L/min, 700-350) Hz.

Therefore, it can be generally concluded that CARSOXY would require a more compact burner compared to Air/Methane combustion while providing the same amount of thermal power, provided that high \dot{V}_{WF} is retained.

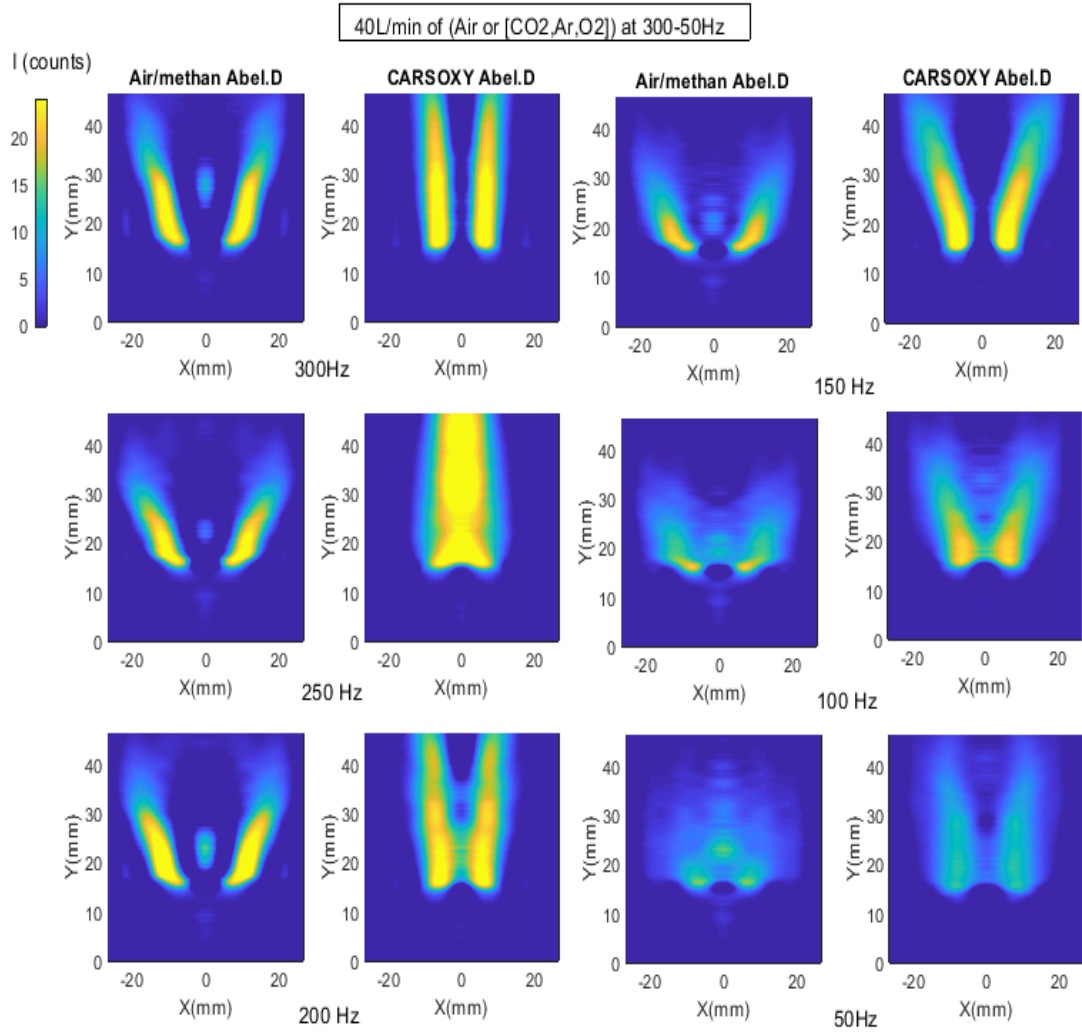


Figure 7.13temporally and specially resolved images (at \dot{V}_{WF} of 40 L/min, 300-50Hz).

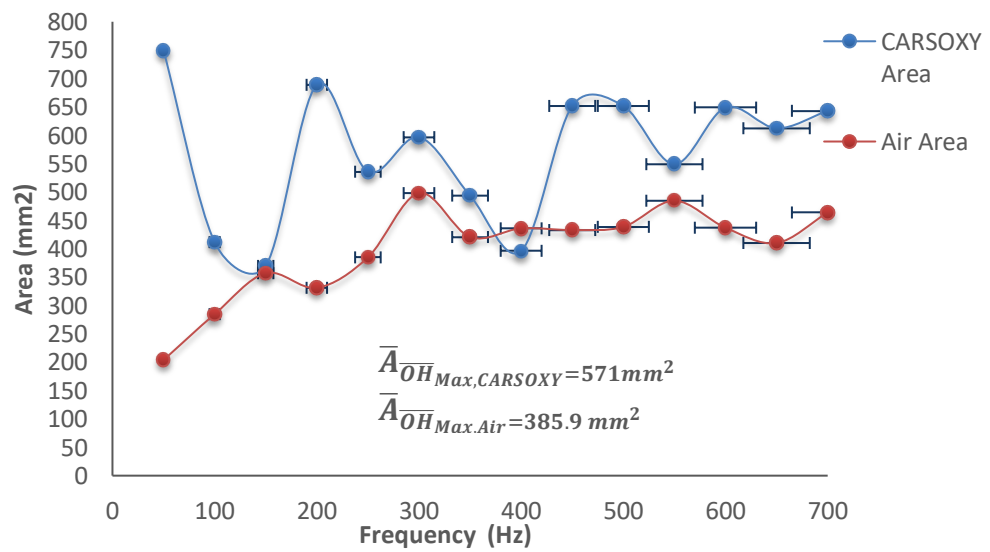


Figure 7.14 Area of highest heat intensity ($A_{OH_{Max}}$) at \dot{V}_{WF} of 40 L/min.

7.8 Centre of highest heat intensity ($C_{\overline{OH}_{Max}}$) at \dot{V}_{WF} of 80 L/min and \dot{V}_{CH_4} of 1L/min.

Figure 7.15 shows ($C_{\overline{OH}_{Max}}$) distribution at 80 L/min and \dot{m}_{CH_4} of 1 L/min. It can be generally said that both flames of Air/Methane and CARSOXY have concentrated $C_{\overline{OH}_{Max}}$. This indicates that both flames are not easily disturbed by the excitation frequencies and the location of $C_{\overline{OH}_{Max}}$. However, at 500Hz and 550Hz, the Air/Methane flame diverged from its highest intensity concentration zone (Y: [15-17] mm, R: [4-5] mm) towards the burner centerline. Similarly, at 250 Hz the Air/Methane flame diverged from the concentration zone but towards the confinement.

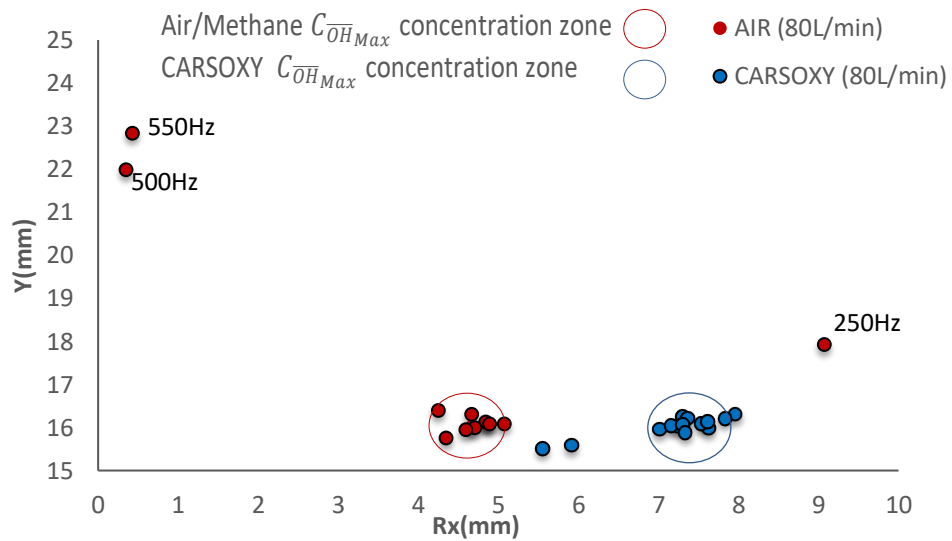


Figure 7.15 Centre of highest heat intensity ($A_{\overline{OH}_{Max}}$) at \dot{V}_{WF} of 80 L/min.

7.9 Centre of highest heat intensity ($C_{\overline{OH}_{Max}}$) at \dot{V}_{WF} of 60 L/min and \dot{V}_{CH_4} of 1L/min.

At \dot{V}_{WF} of 60 L/min (Figure 7.16), it can also be said that $C_{\overline{OH}_{Max}}$ concentration zone of CARSOXY approximately was retained at the same location and size (Y: [16-17] mm, R: [7-8] mm) as that for \dot{V}_{WF} of 80 L/min despite the change in \dot{V}_{WF} . On the other hand, as \dot{V}_{WF} changed from 80L/min to 60 L/min, the $C_{\overline{OH}_{Max}}$ concentration zone of the Air/Methane flame changed its location from (Y: [15-17] mm, R: [4:5] mm) to (Y: [17.5-19] mm, R: [7.5:8.5] mm). This indicates that the $C_{\overline{OH}_{Max}}$ of the Air/Methane flame has a higher sensitivity towards \dot{V}_{WF} compared to that of CARSOXY.

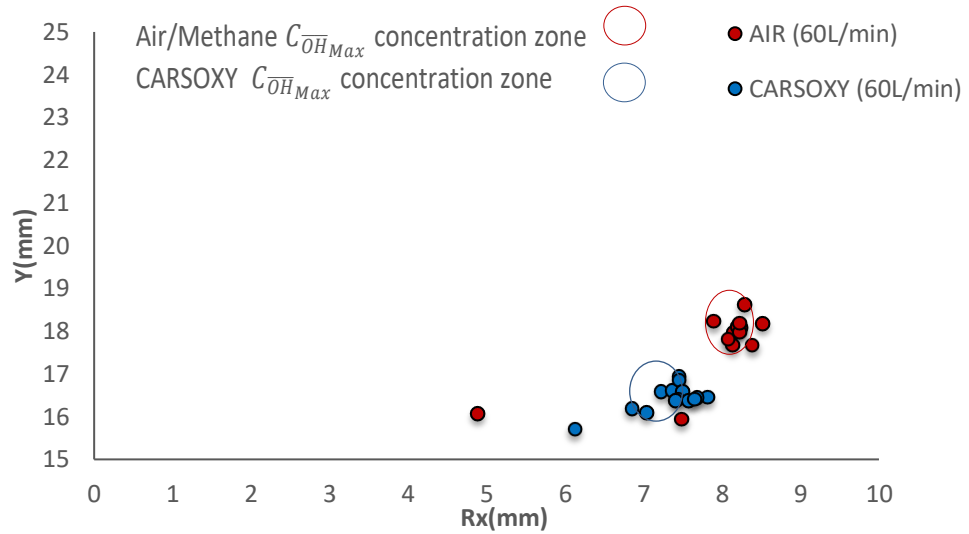


Figure 7.16 Centre of highest heat intensity ($A_{\overline{OH}_{Max}}$) at \dot{V}_{WF} of 60 L/min.

7.10 Center of highest heat intensity ($C_{\overline{OH}_{Max}}$) at \dot{V}_{WF} of 40 L/min and \dot{V}_{CH_4} of 1L/min.

The conclusion of the previous section is further supported by Figure 7.18 as \dot{V}_{WF} further decreases to 40L/min. The concentration zone of the Air/Methane flame has both changed its size and location showing higher sensitivity compared to CARSOXY towards frequency and \dot{V}_{WF} .

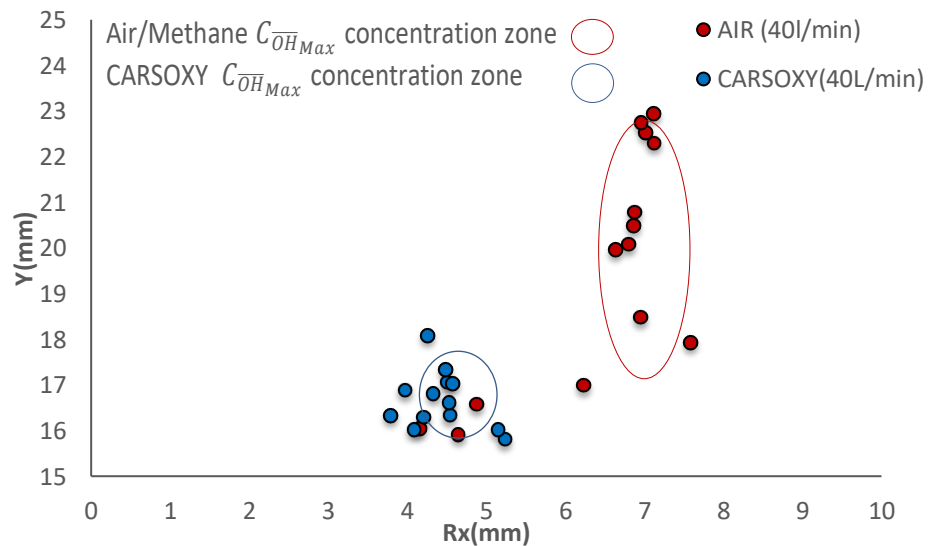


Figure 7.11 Centre of highest heat intensity ($A_{\overline{OH}_{Max}}$) at \dot{V}_{WF} of 40 L/min.

7.11 Discussion

It must be pointed out that the Air/fuel diffusive injection had been an international combustion method which eventually was relegated due to high NO_x emissions [179]. Because CARSOXY does not contain nitrogen molecules, the NO, NO₂ and NO_x emissions were negligible, as those recorded were residuals due to the ignition pilot and surrounding air interference. These anticipated and experimentally proven results can bring back diffusive burners to the industry at a large scale using CARSOXY. Moreover, it is highly important to mention that compact flames are desirable as these would essentially require more compact burners. Nevertheless, compact Air/Methane flames have high NO_x rates [180-181]. Meanwhile, this should not be a concern for CARSOXY flames as these have negligible NO_x emissions. Correlating this to the results obtained for the area of highest heat intensity, CARSOXY generally has a more compact area compared to Air/Methane flame, while both flames produced the same thermal power (0.556 kW or ($\dot{V}_{WF}=1\text{L/min}$)), i.e. $\bar{A}_{OH_{Max,CARSOXY}} = 334 \text{ mm}^2$, 228 mm^2 and 571 mm^2 , while $\bar{A}_{OH_{Max,Air}} = 399 \text{ mm}^2$, 246 mm^2 and 385.9 mm^2 at $\dot{V}_{WF}=80\text{L/min}$, 60L/min and 40L/min , respectively. Therefore, CARSOXY is anticipated to produce the same level of thermal power as Air/Methane within a much more compact burner, while eliminating NO_x emissions. High Oxygen molar fraction in CARSOXY has contributed to reducing CO levels to the tenth of those of Air/Methane and increased CO₂ emission levels. As previously mentioned, the experimental CARSOXY blend has been normalized such that it contains zero H₂O molar fraction (Dry combustion). If the theoretical H₂O molar fractions have been added to the experimental blend (Wet combustion), the CO levels would have been even lower. This expectation has been proven by previous studies in the literature [181]. Before summarizing the overall stability performances, it is essential to emphasize on the used technique. The function of the speaker is to subject both of the CARSOXY and Air/Methane flames to comparable instability conditions to examine the CARSOXY flame stability behaviour about the Air/Methane flame. An explicit statement must be made that this approach has neither been used in literature nor used herein to obtain flame transfer function. It has been used based on the hypothesis that CARSOXY working fluid will have a different response towards excitation frequencies in comparison to air. The hypothesis attributes this to the differences in the physical properties (i.e. viscosity, mass, density, etc.) between air and CARSOXY. Essentially, obtaining flame transfer function would require to adjust the experimental setup in many aspects (i.e. recording frequency must be higher than the excitation frequency, further details can be provided elsewhere [194-196]).

As discussed in section 3.5.10, each instantaneous background image has been subtracted from its corresponding instantaneous flame image. Similarly, the averaged background image has been subtracted

from its corresponding averaged flame image. As discussed in section 3.5.11, heat release fluctuation has been calculated using the background-corrected instantaneous and averaged integral pixel intensities (OH^* and \overline{OH} , using a MATLAB code-Appendix 3.2.1- to perform Equations (3.34) and (3.35) respectively). This thesis applies the standard deviation concept to quantify the chemiluminescence fluctuation (OH^*/\overline{OH}) over time. Standard deviation is a statistical technique which measures the tendency of data points to be far from the mean value [162]. Therefore, each instantaneous image has its own instantaneous standard deviation in reference to the averaged image(as shown in Figure 3.11). Those instantaneous standard deviations have been averaged to represent the overall averaged standard deviation of each flame condition (i.e. \dot{V}_{WF} of 40L/min, 60L/min and 80 L/min over [50Hz-700Hz]).

Since the standard deviation is a non-dimensional parameter, it has been utilized to compare the chemiluminescence fluctuation (OH^*/\overline{OH}) of CARSOXY flame in comparison to Air/methane. This technique has not been utilized for this thesis and there is no evidence of use in the evaluated combustion literature.

By evaluating the overall stability performances of both flames over the excitation interval [50Hz-700Hz] for the three flow rates \dot{V}_{WF} =80L/min, 60L/min and 40L/min, it can be concluded that the CARSOXY flame has a more stable performance compared to Air/Methane flame. As shown in Table 7.2, the average $\sigma_{OH^*/\overline{OH}}^{CARSOXY}$ over the excitation interval for the three flow rates are lower than $\sigma_{OH^*/\overline{OH}}^{Air}$. Therefore, it can be concluded that CARSOXY has better overall stability performance. Furthermore, this has been confirmed by the $C_{\overline{OH}_{Max}}$ results (Figure 7) as the Air/ methane demonstrated higher sensitivity towards both of the excitation frequency and \dot{V}_{WF} . Finally, due to the (experimentally negligible and theoretically zero) NO_x emissions of CARSOXY, the relatively more stable diffusive burners compared to premixed can be used for CARSOXY, whilst not for Air/methane. This is indeed another major stability advantage in favour of CARSOXY combustion.

Table 7.3 Average $\sigma_{OH^*/\overline{OH}}^{CARSOXY}$ and $\sigma_{OH^*/\overline{OH}}^{Air}$ over the excitation interval [50Hz-700Hz] for \dot{V}_{WF} =80L/min, 60L/min and 40L/min.

\dot{V}_{WF} [L/min]	Average $\sigma_{OH^*/\overline{OH}}^{CARSOXY}$	Average $\sigma_{OH^*/\overline{OH}}^{Air}$
40	0.711	1.99
60	0.65	0.72
80	0.54	0.86

7.12 Conclusion

The chemiluminescence and emission analyses conducted in this chapter have proven that a more compact flame is achieved using CARSOXY. Such that $\bar{A}_{\overline{OH}}_{Max,CARSOXY} = 334 \text{ mm}^2, 228\text{mm}^2$ and 571 mm^2 , while $\bar{A}_{\overline{OH}}_{Max,Air} = 399 \text{ mm}^2, 246 \text{ mm}^2$ and 385.9mm^2 at $\dot{V}_{WF} = 80\text{L}/\text{min}, 60\text{L}/\text{min}$ and $40\text{L}/\text{min}$, respectively. Moreover, CO levels in CARSOXY have been reduced to the tenth of those of Air/Methane. Finally, the average $\sigma_{OH^*/\overline{OH}}^{CARSOXY}$ was lower than $\sigma_{OH^*/\overline{OH}}^{Air}$ which illustrates a stable performance of CARSOXY flame (i.e. Average $\sigma_{OH^*/\overline{OH}}^{CARSOXY}$ is 0.711, 0.65 and 0.54 compared to $\sigma_{OH^*/\overline{OH}}^{Air}$ of 1.99, 0.72 and 0.86 at \dot{V}_{WF} of 80L/min, 60L/min and 40L/min, respectively).

CHAPTER EIGHT

Planar Laser-Induced Fluorescence and Chemiluminescence Analyses of CARSOXY combustion. (Experimental)

*“Progress in science depends on new techniques, new discoveries
and new ideas, probably in that order.”*

~ Sydney Brenner

CHAPTER 8 – PLANAR LASER-INDUCED FLUORESCENCE AND CHEMILUMINESCENCE ANALYSES OF CARSOXY COMBUSTION.

CARSOXY flame has been assessed in comparison to CH₄/air flame under various conditions (i.e. at (working fluid Reynold's numbers [2000-3750] and fuel volumetric flowrate \dot{V}_{CH_4} of 1 L/min) and at equivalence ratios λ_{oxy} [35-70]). OH chemiluminescence imaging has been utilized to plot the standard deviation of heat release fluctuation $\sigma_{OH^*/\overline{OH}}$. PLIF imaging has been utilized to study several flame properties (i.e. Area of highest heat intensity ($A_{\overline{OH}_{Max}}$), the centre of highest heat intensity ($C_{\overline{OH}_{Max}}$)). Moreover, Damkohler analyses have been performed and Borghi regime diagrams have been produced for both types of flames.

For each plotted data point of CARSOXY, a CH₄/air data point at has been plotted at the same equivalence ratio. This has been performed over a range of equivalence ratio (i.e. λ_{oxy} of CARSOXY = λ_{oxy} of CH₄/air=35... λ_{oxy} of CARSOXY = λ_{oxy} of CH₄/air=70). These conditions are referred to in the following sections as 'constant equivalence ratios'. Similarly, For each plotted data point of CARSOXY, a CH₄/air data point at has been plotted at the same working fluid Reynold's number This has been performed over a range of Reynold's number (i.e. Re of CARSOXY=Re of CH₄/air=2000... Re of CARSOXY =Re of CH₄/air=3750. These conditions are referred to in the following sections as 'constant Reynolds numbers.

8.1 $\sigma_{OH^*/\overline{OH}}$ of CARSOXY and CH₄/air flames at constant Reynolds numbers/chemiluminescence

Figure 8.1.A shows the standard deviation (σ) of the heat release fluctuations (OH^*/\overline{OH}) over the working fluid Reynolds number interval of ([2000-3750] at \dot{V}_{CH_4} of 1 L/min and Figure 8.1.B shows samples cases of the chemiluminescence images of this interval. The standard deviation (σ) of the CARSOXY flame was lower than that for the CH₄/air flame throughout the entire interval. The average OH^*/\overline{OH} standard deviation of CARSOXY and CH₄/air are 0.117 and 0.242, respectively. CARSOXY becomes significantly more stable than CH₄/air as Reynold's number increases in the interval of [2750-3750] such that $\sigma_{OH^*/\overline{OH}}^{CARSOXY}$ is lower than $\sigma_{OH^*/\overline{OH}}^{Air}$ by approximately 16%. Therefore, it can be concluded that the CARSOXY flame has a less fluctuating heat release performance over this interval.

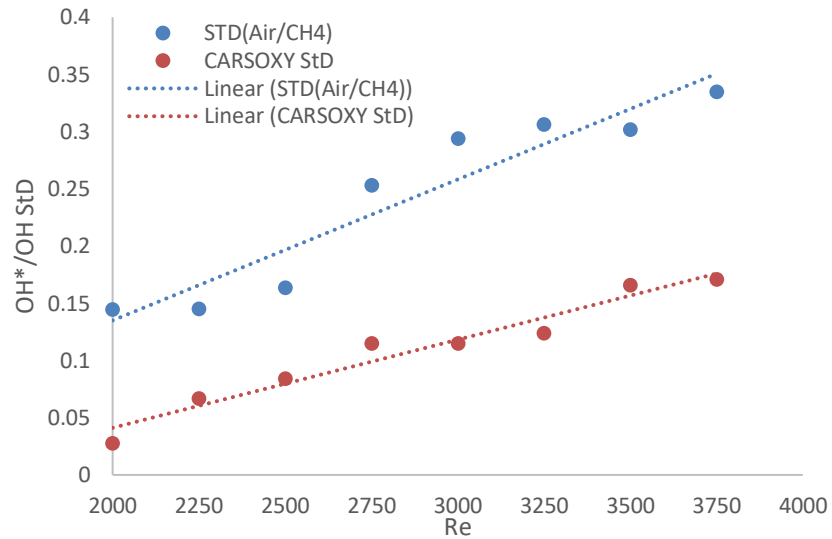


Figure 8.1.A $\sigma_{OH^*/\overline{OH}}$ at constant working fluid Reynold's numbers at \dot{V}_{CH_4} of 1L/min

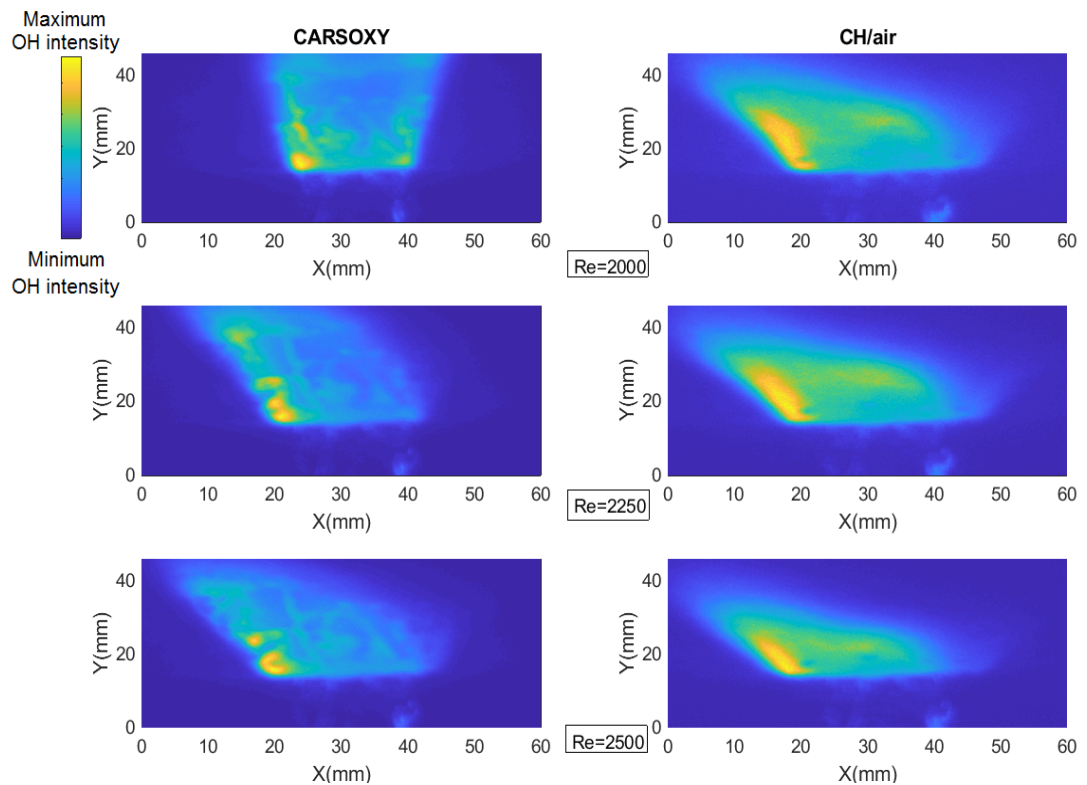


Figure 8.1.B Sample cases of the chemiluminescence images at constant Re

8.2 $\sigma_{OH^*/\overline{OH}}$ of CARSOXY and CH₄/air flames at constant λ_{oxy} / chemiluminescence

Figure 8.2.A shows the standard deviation (σ) of the heat release fluctuations (OH^*/\overline{OH}) over the equivalence ratio interval λ_{oxy} of [35-70] or (ϕ_{oxy} of [0.0286-0.0143]) and Figure 8.2.B shows samples

cases of the chemiluminescence images of this interval. As the air to fuel equivalence ratio λ_{oxy} increases (or the fuel to air equivalence ratio ϕ_{oxy} decreases), both flames become more unstable and the standard deviations of OH^*/\overline{OH} increase in an approximately linear trend. However, similar to the $\sigma_{OH^*/\overline{OH}}$ patterns over Reynold's number interval of [2000-3750], the standard deviation (σ) of the CARSOXY flame was lower than that for the CH₄/air flame throughout the entire λ_{oxy} interval. The difference between the average standard deviations of both flames ($\overline{\sigma_{OH^*/\overline{OH}}}^{CARSOXY} = 0.117$ and $\overline{\sigma_{OH^*/\overline{OH}}}^{Air} = 0.276$) has increased. Remarkably, as indicated by the black dashed line, the $\sigma_{OH^*/\overline{OH}}$ of the CARSOXY flame at the maximum λ_{oxy} (70) has approximately the same value as that for the CH₄/air flame at the lowest λ_{oxy} (35). Moreover, by approximating both patterns to linear trends, the $\sigma_{OH^*/\overline{OH}}$ slope of the CARSOXY is less than that for the CH₄/air flame (i.e. $\overline{\sigma_{OH^*/\overline{OH}}}^{CARSOXY} = 0.0042\lambda_{oxy} - 0.1044$ and $\overline{\sigma_{OH^*/\overline{OH}}}^{CARSOXY} = 0.0054\lambda_{oxy} - 0.0085$). This indicates that the difference between the standard deviations of both flames is anticipated to become more significant as λ_{oxy} increase (i.e. $\lambda_{oxy} > 70$)

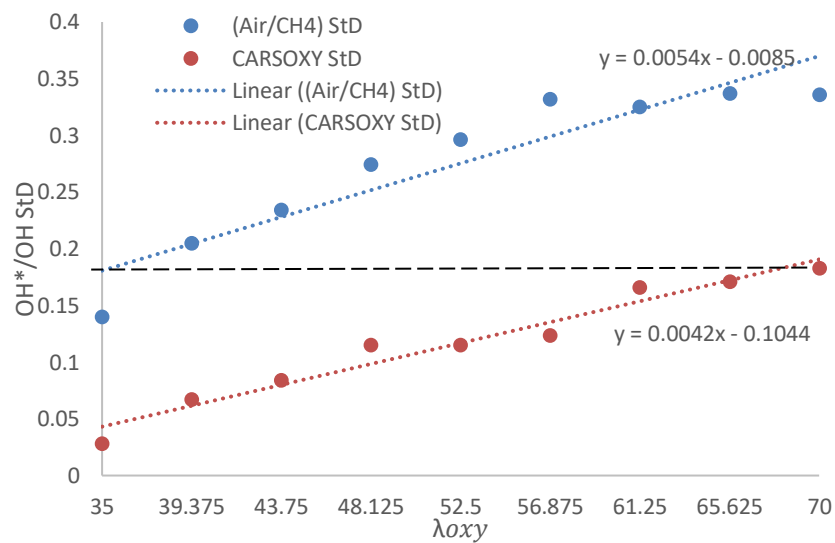


Figure 8.2.A $\sigma_{OH^*/\overline{OH}}$ at λ_{oxy} of [35-70].

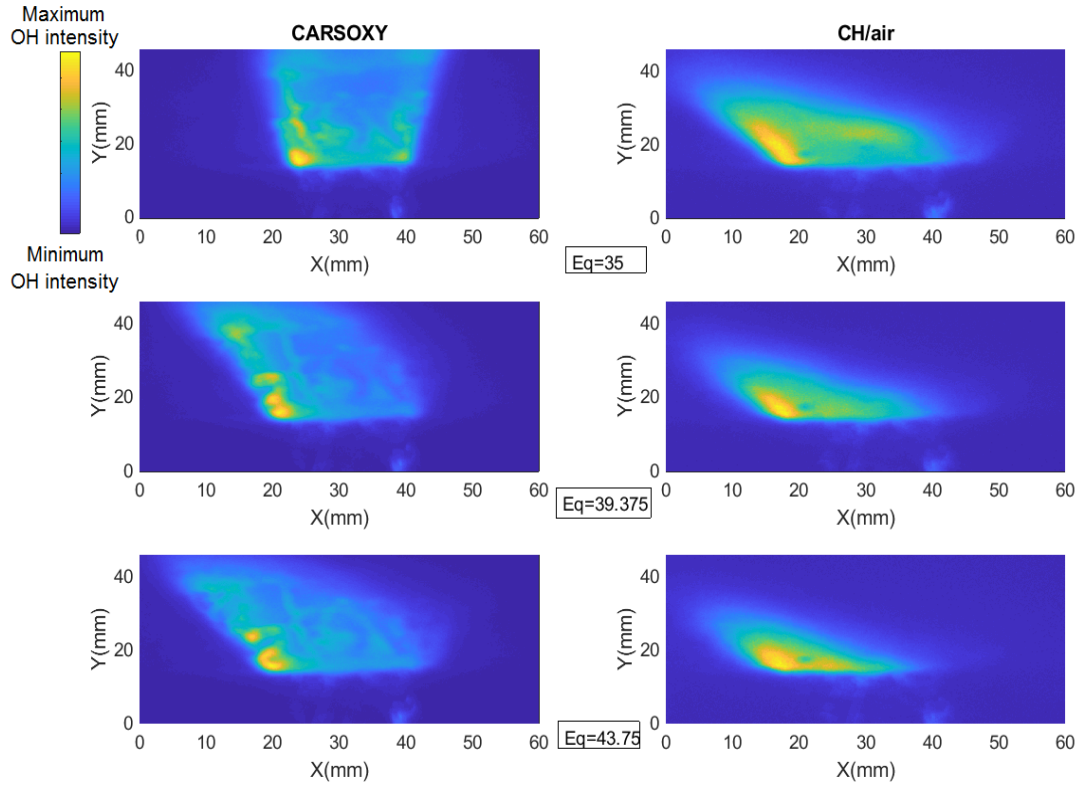


Figure 8.2.B Sample cases of the chemiluminescence images at constant λ_{oxy}

8.3 $\sigma_{OH^*/\overline{OH}}$ functions of Re and λ_{oxy} ($\sigma_{OH^*/\overline{OH}}(Re)$ and $\sigma_{OH^*/\overline{OH}}(\lambda_{oxy})$) / chemiluminescence

The experimentally obtained data points of $\sigma_{OH^*/\overline{OH}}$ in Figures 8.1 and 8.2 have been curve-fitted using 6th order polynomial functions. Table 8.1 and 8.2 provide $\sigma_{OH^*/\overline{OH}}(\lambda_{oxy})$ and $\sigma_{OH^*/\overline{OH}}(Re)$ at a \dot{V}_{CH_4} of 1 L/min, respectively. This approach provides the heat release standard deviation functions $\sigma_{OH^*/\overline{OH}}(Re)$ and $\sigma_{OH^*/\overline{OH}}(\lambda_{oxy})$ to establish numerical anticipations of the flame stability response for CARSOXY within the tested intervals. Curve fittings are shown in Figure 8.3.

Table 8.1 $\sigma_{OH^*/\overline{OH}}(Re)$ at Re of [2000 -3750], \dot{V}_{CH_4} of 1L/min.

Flame type	$\sigma_{OH^*/\overline{OH}}(Re)$
CH ₄ /air	$\sigma_{OH^*/\overline{OH}}^{Air} = -7E(-19)Re^6 + 1E(-14)Re^5 - 8E(-11)Re^4 + 3E(-7)Re^3 - 0.0008Re^2 - 0.8466Re - 387.58$
CARSOXY	$\sigma_{OH^*/\overline{OH}}^{CARSOXY} = -7E(-19)Re^6 + 1E(-14)Re^5 - 9E(-11)Re^4 + 4E(-7)Re^3 - 0.0006Re^2 - 0.6914Re - 311.3$

Table 8.2 $\sigma_{OH^*/OH}$ (λ_{oxy}) at λ_{oxy} of [35-70].

Flame type	$\sigma_{OH^*/OH}$ (λ_{oxy})
CH ₄ /air	$\sigma_{OH^*/OH}^{Air} = -5E(-9)\lambda_{oxy}^6 + 1E(-6)\lambda_{oxy}^5 - 0.0002\lambda_{oxy}^4 + 0.0138\lambda_{oxy}^3 - 0.5408\lambda_{oxy}^2 + 11.175\lambda_{oxy} - 95.106$
CARSOXY	$\sigma_{OH^*/OH}^{CARSOXY} = 3E(-9)\lambda_{oxy}^6 + 1E(-6)\lambda_{oxy}^5 - 0.0001\lambda_{oxy}^4 - 0.0095\lambda_{oxy}^3 + 0.3638\lambda_{oxy}^2 - 7.3356\lambda_{oxy} + 60.484$

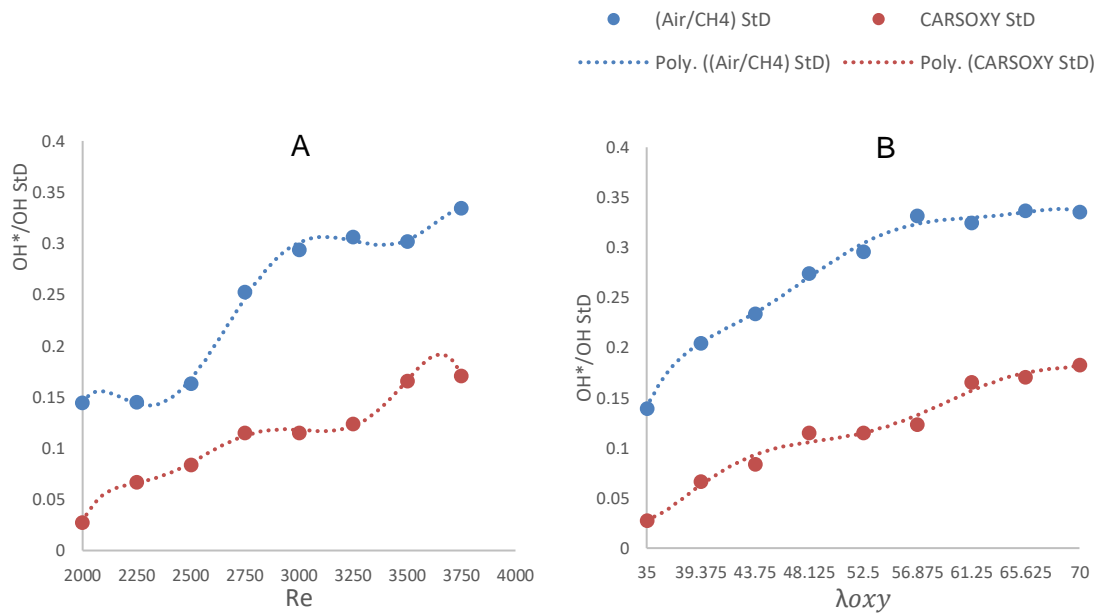


Figure 8.3. $\sigma_{OH^*/OH}$ Curve fittings at (A: Re of [2000 -3750]) and (B: λ_{oxy} of [35-70]).

8.4 Area of the highest heat intensity ($A_{\overline{OH}_{Max}}$) of CARSOXY and CH₄/air flames at constant Reynolds numbers/ PLIF

As discussed in section 3.6.32, the area of the highest heat intensity $A_{\overline{OH}_{Max}}$ results of the PLIF images have been obtained for laser energy shot-to-shot and laser-sheet corrected images. Figures 8.4 show sample cases at constant Reynold's numbers (i.e. 2000-2750). The $A_{\overline{OH}_{Max}}$ results of the entire Re interval of [2000-3750] are summarized in Figure 8.3.

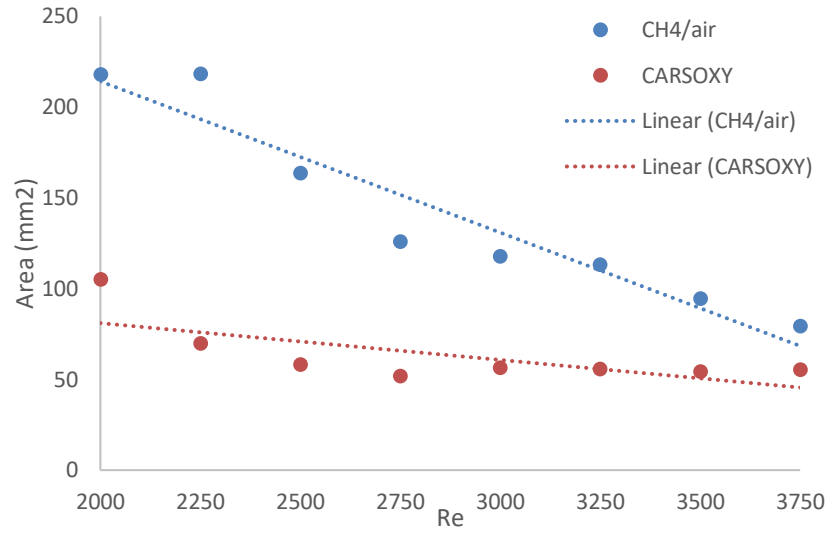


Figure 8.3 $A_{\overline{OH}_{Max}}$ at Re of [2000-3750] and \dot{V}_{CH_4} of 1L/min

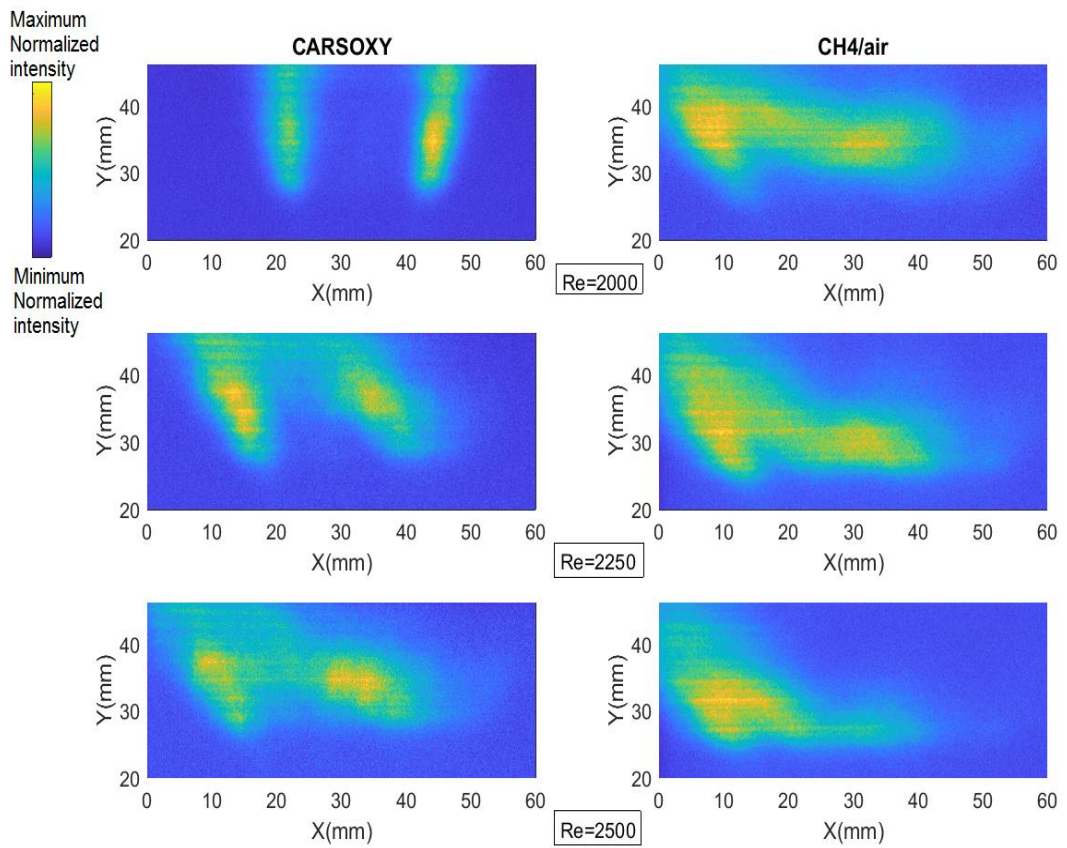


Figure 8.4 Temporally averaged and energy shot-to-shot and laser-sheet corrected PLIF images at Re of [2000-2250] and \dot{V}_{CH_4} of 1L/min

As shown in Figure 8.3, $A_{\overline{OH}_{Max}}$ of the CARSOXY flame is lower than that for CH₄/air flame. The average $A_{\overline{OH}_{Max}}$ of the CARSOXY flame is 45% of the CH₄/air flame. However, as Re increases the difference in $A_{\overline{OH}_{Max}}$ between both flames decreases (i.e. at $Re = 3750$, $A_{\overline{OH}_{Max}}$ of CARSOXY is only 70% of that of CH₄/air). By correlating the linearized $A_{\overline{OH}_{Max}}$ pattern to the linearized $\sigma_{OH^*/\overline{OH}}$ pattern at constant Re (Figure 8.3 and 8.1, respectively), it can be seen that $A_{\overline{OH}_{Max}}$ of the CH₄/air flame has the opposite trend of its $\sigma_{OH^*/\overline{OH}}$ trend, such that the linearized $A_{\overline{OH}_{Max}}$ of converges to the CH₄/air flame linearized $A_{\overline{OH}_{Max}}$ of the CARSOXY flame in a negative slope as Re increases, while the linearized $\sigma_{OH^*/\overline{OH}}$ of the CH₄/air flame diverges from the CARSOXY flame on a positive slope.

8.5 Area of the highest heat intensity ($A_{\overline{OH}_{Max}}$) at constant λ_{oxy} / PLIF

Figures 8.6 shows sample cases at constant λ_{oxy} s (i.e. 35-43.75). The $A_{\overline{OH}_{Max}}$ results of the entire λ_{oxy} interval of [35-70] are summarized in Figure 8.5. The $A_{\overline{OH}_{Max}}$ pattern at constant λ_{oxy} approximately followed the same pattern as those at constant Re . Nevertheless, as the working fluid increases (i.e. $\lambda_{oxy} = 70$), $A_{\overline{OH}_{Max}}$ of the CH₄/air flame is less than that for the CARSOXY flame. However, as it has been experimentally observed, further reduction in the $A_{\overline{OH}_{Max}}$ of the CH₄/Air flame is only anticipated up to the λ_{oxy} of 85 since the flame blows out at this limit.

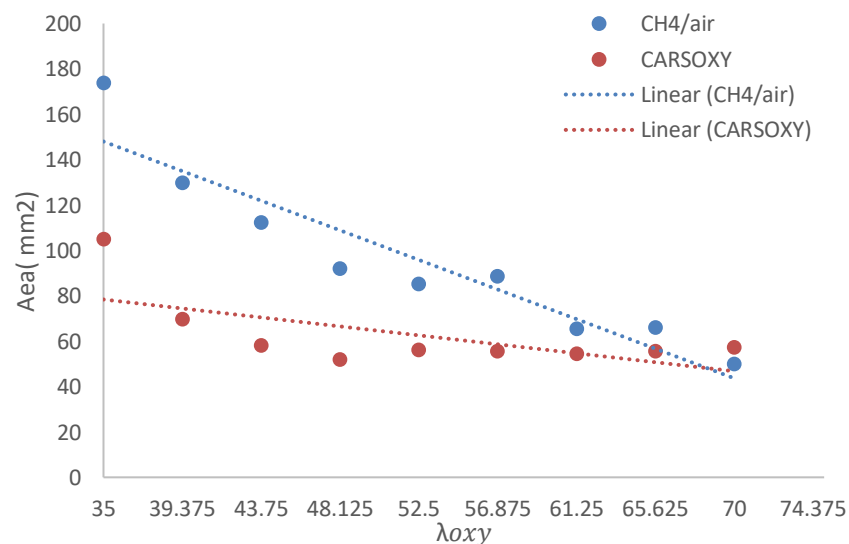


Figure 8.5 $A_{\overline{OH}_{Max}}$ at λ_{oxy} of [35-70].

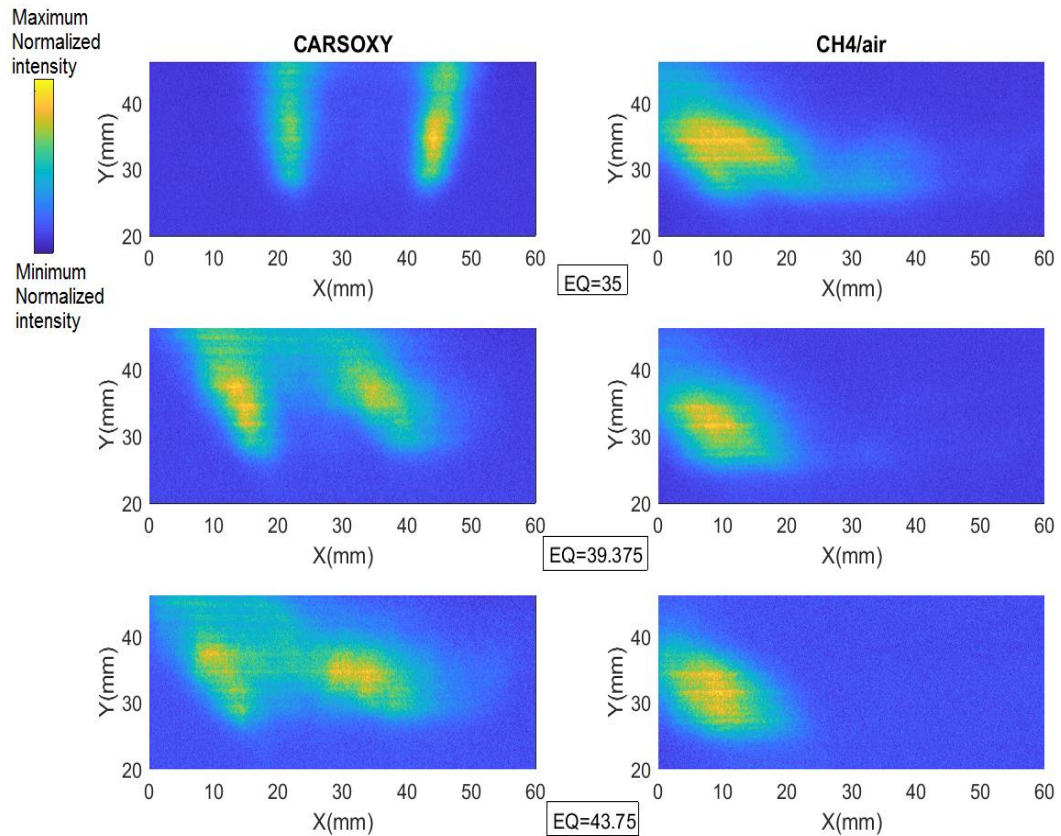


Figure 8.6 Temporally averaged and energy shot-to-shot and laser-sheet corrected PLIF images at λ_{oxy} of [35-70].

8.6 Centre of the highest heat intensity ($C_{\overline{OH}_{Max}}$) at constant Re and \dot{V}_{CH_4} of 1L/min/ PLIF

Figure 8.7 shows the centre of the highest heat intensity ($C_{\overline{OH}_{Max}}$) distribution at constant working fluid Reynold's numbers [2000-3750] and \dot{V}_{CH_4} of 1 L/min. It can be generally said that both flames of CH_4/air and CARSOXY have concentrated $C_{\overline{OH}_{Max}}$. The $C_{\overline{OH}_{Max}}$ of CARSOXY flames were approximately concentrated closer to the burner centerline than those for the CH_4/air flames. However, the $C_{\overline{OH}_{Max}}$ of CARSOXY flames were approximately farther from the burner base compared to the CH_4/air . Remarkably, as the working fluid Reynold's number increases, the $C_{\overline{OH}_{Max}}$ of both flames approach towards the burner base. However, $C_{\overline{OH}_{Max}}$ of the CARSOXY flames diverge from the burner centerline. Meanwhile, the $C_{\overline{OH}_{Max}}$ of the CH_4/air flames converge towards the burner centerline. Finally, as the Reynold's number increases, $C_{\overline{OH}_{Max}}$ of the CAROXY flames converge towards that for the CH_4/air flame at the corresponding Reynold's number. In fact, at $Re = 3750$, both of the CARSOXY and the CH_4/air flame approximately have the same $C_{\overline{OH}_{Max}}$ (21.24 mm and 29.52 mm from the burner centerline and base, respectively). By correlating the $C_{\overline{OH}_{Max}}$ to the $\sigma_{OH^*/OH}$ results, it can be generally said that

as Re increases, $\sigma_{OH^*/OH}$ increases and the distance between the burner base and $C_{\overline{OH}_{Max}}$ decreases.

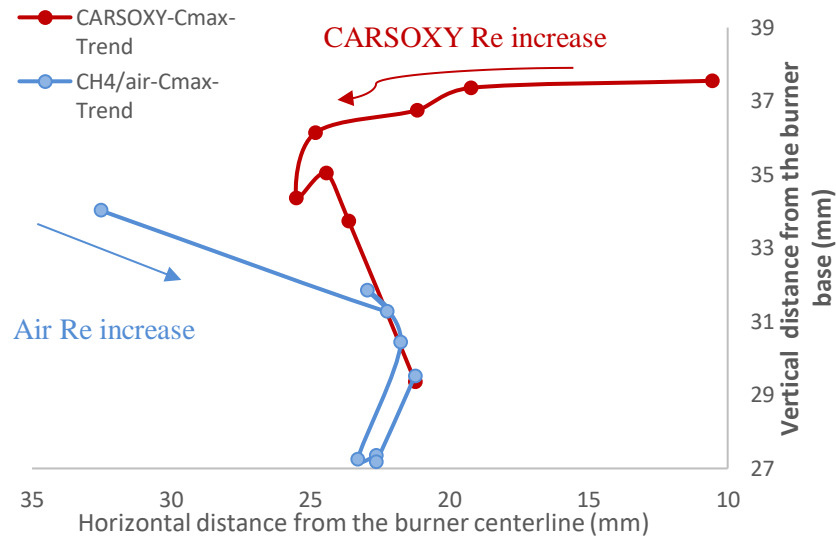


Figure 8.7 ($C_{\overline{OH}_{Max}}$) distribution at constant working fluid Reynold's numbers [2000-3750] and \dot{V}_{CH_4} of 1 L/min

8.7 Centre of the highest heat intensity ($C_{\overline{OH}_{Max}}$) at constant λ_{oxy} / PLIF

As shown in Figure 8.8, the $C_{\overline{OH}_{Max}}$ trends for the increase of λ_{oxy} generally followed the same behaviour as that for Reynold's number increase in Figure 8.7. However, increasing λ_{oxy} does not necessarily lead both of the CARSOXY and CH₄/air flames to have the same $C_{\overline{OH}_{Max}}$ (i.e. $C_{\overline{OH}_{Max}}$ of the CARSOXY flame is located at 21.24 mm and 29.52 mm from the burner centerline and base, respectively. Whereas, $C_{\overline{OH}_{Max}}$ of the CARSOXY flame is located at 26.9 mm and 28.42 mm from the burner centerline and base).

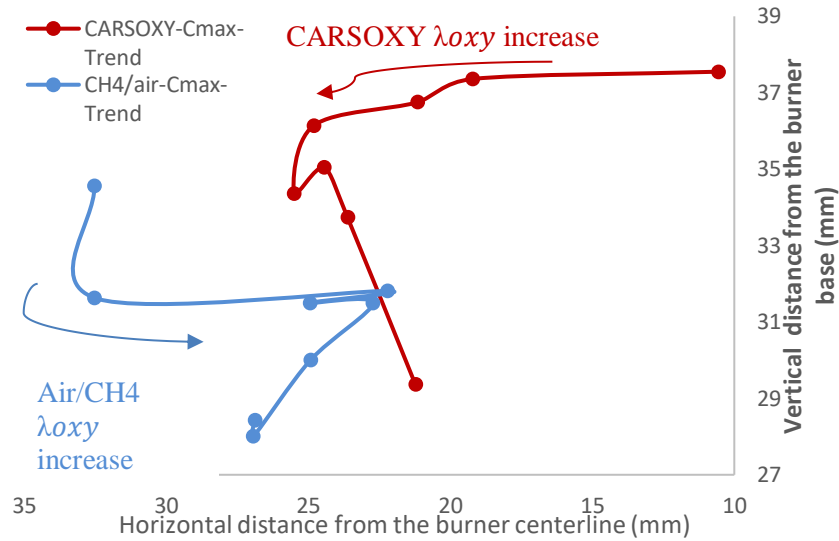


Figure 8.8 ($C_{OH_{Max}}$) distribution at constant λ_{oxy} [35-70].

8.8 Damkohler number (Da) and combustion diagrams/ PLIF

As mentioned in section 3.6.3.4, the Damkohler number Da describes the turbulence-chemistry interaction, depending on the ratio of the characteristic flow time (τ_n) to the characteristic chemical time (τ_{ch}). For $Da > 1$, τ_{ch} is shorter than τ_n , which corresponds to a fast chemical reaction that occurs in a thin layer [200]. This implies that the flame can be assumed “thin” and can be called “flamelet” [201]. In other words, the higher the Da , the more laminar and less turbulent the flame becomes. The reference [200] defined τ_n as the ratio of the distance between the burner base and the centre of the highest heat intensity (L_f) to the fuel injection velocity (u_F). However, as discussed in section 3.6.2, the fuel injection flow rate was maintained constant (\dot{V}_{CH_4} of 1 L/min), and thus u_F was constant. This implies that any increase in τ_n is only due to an increase in L_f . Similarly, the reference [200] defined τ_{ch} as the ratio of flame brush thickness at the highest heat intensity location $\overline{\delta_{ch}}$ to the laminar flame speed (δ_L) at the stoichiometric condition. However, as discussed in section 3.6.2, the experiment was conducted at constant pressures and temperatures, and thus the stoichiometric δ_L was constant. This implies that any increase in τ_{ch} is only due to an increase in $\overline{\delta_{ch}}$. Therefore, based on the reference [200] definitions of τ_{ch} and τ_n and the specific setup of the experiment, Da patterns are only correlated to L_f and $\overline{\delta_{ch}}$. Such that Da increases (the flame becomes more laminar) if L_f and/or $\overline{\delta_{ch}}$ increases and/or decreases, respectively.

8.8.1 Damkohler number (Da)

As shown in Figure 8.9, Da of the CARSOXY is greater than one in all conditions, indicating thin uniform flames throughout the Re interval ([2000-3750]). This indicates that chemical reaction is performed in a short period, such that it is shorter than the flow characteristic time. At $Re = 3000$, the CARSOXY flame has shown the ultimate turbulence-chemical interaction with $Da = 4.74$. This indicates that the flame at this condition has a chemical reaction that is 4.74 times faster than radicals turbulence. However, Da rapidly decreases beyond $Re = 3000$ (i.e. $Da = 1.18$ at $Re = 3750$). On the other hand, Da of the CH_4 /air flame was lower than that for the CARSOXY flame throughout the Re interval. In fact, at $Re = 2000, 2500, 3500$ and 3750 , $Da < 1$, which indicates that the reaction at these conditions is not fast enough to be conducted before particles change their places. The ultimate combustion condition of the CH_4 /air flame was identified at $Re = 2750$, where $\tau_n = 1.32\tau_{ch}$.

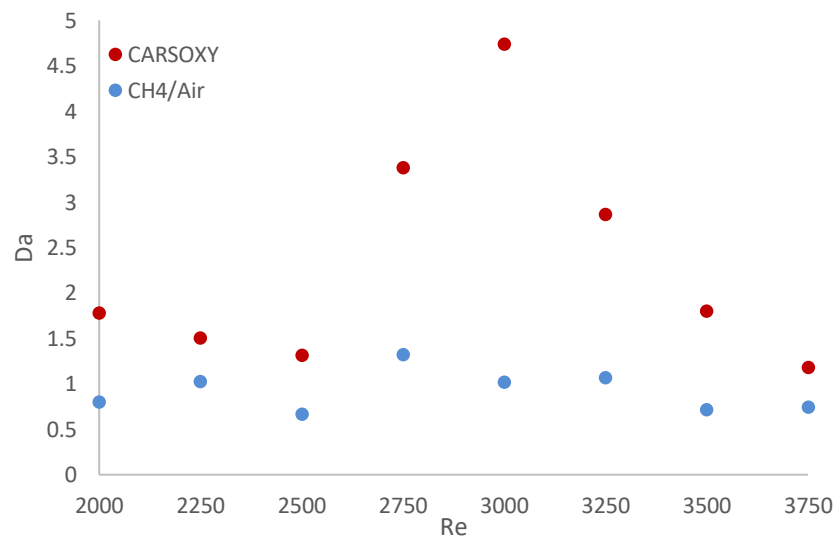


Figure 8.9 Da at constant working fluid Reynold's numbers [2000-3750] and \dot{V}_{CH_4} of 1 L/min

As shown in Figure 8.10, the Da patterns for the increase of λ_{oxy} generally followed the same behaviours as those for Reynold's number increase in Figure 8.9. However, at certain λ_{oxy} conditions (i.e. $\lambda_{oxy}=35, 43.75$ and 65.625), Da of the CH_4 /air flame was significantly low (i.e. $Da \ll 1$).

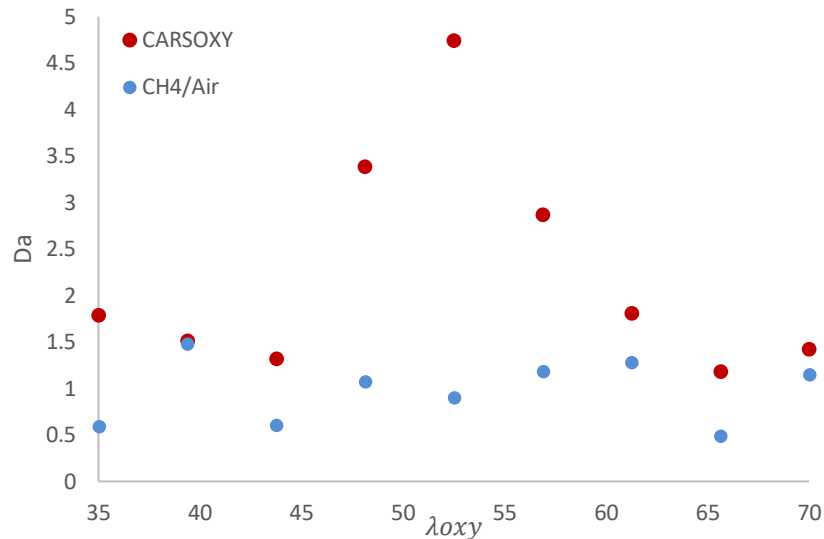


Figure 8.10 Da at constant λ_{oxy} [35-70].

8.8.2 Borghi regime diagram

A regime diagram has been plotted with axes of the relative velocity (u_F/S_L) versus the relative length scale ($L_f/\overline{\delta_{ch}}$) based on the Borghi proposal [184]. Regions

As suggested by the reference [162], the Borghi diagram for nonpremixed flames can be divided into two regions, concentrated reaction zone and broken reaction zone. As the relative length scale decreases and/or the relative velocity increases, the flame exhibits a more broken reaction zone. Similarly, as the relative length scale increases and/or the relative velocity decreases, the flame exhibits a more concentrated reaction zone.

As discussed in section 3.6.2, the fuel injection flow rate was maintained constant (\dot{V}_{CH_4} of 1 L/min), and thus u_F was constant and the experiment was conducted at constant pressures and temperatures, and thus the stoichiometric δ_L was constant. However, as discussed in section 3.6.3.4, each flame type (CARSOXY and CH₄/Air) has its own laminar speed at stoichiometric condition (i.e. $\delta_L=559.2$ mm/s and 398.837 mm/s for CO₂- Ar - O₂/ CH₄ and CH₄/air flames, respectively). Since δ_L of the CARSOXY flame is higher than that for the CH₄/air flame, the relative velocity of the CARSOXY flame was lower than for CH₄/air. This has shifted CARSOXY data points below those for CH₄/air and towards the concentrated reaction zone in the Borghi diagram, which was plotted for CARSOXY and CH₄/flames at constant Re [2000-3750] and \dot{V}_{CH_4} of 1L/min, Figure 8.11. Nevertheless, the CARSOXY flame also approached the concentrated reaction zone in the Borghi diagram as it exhibits a high relative length scale (i.e. at $Re=3000, 3250$ and 2750).

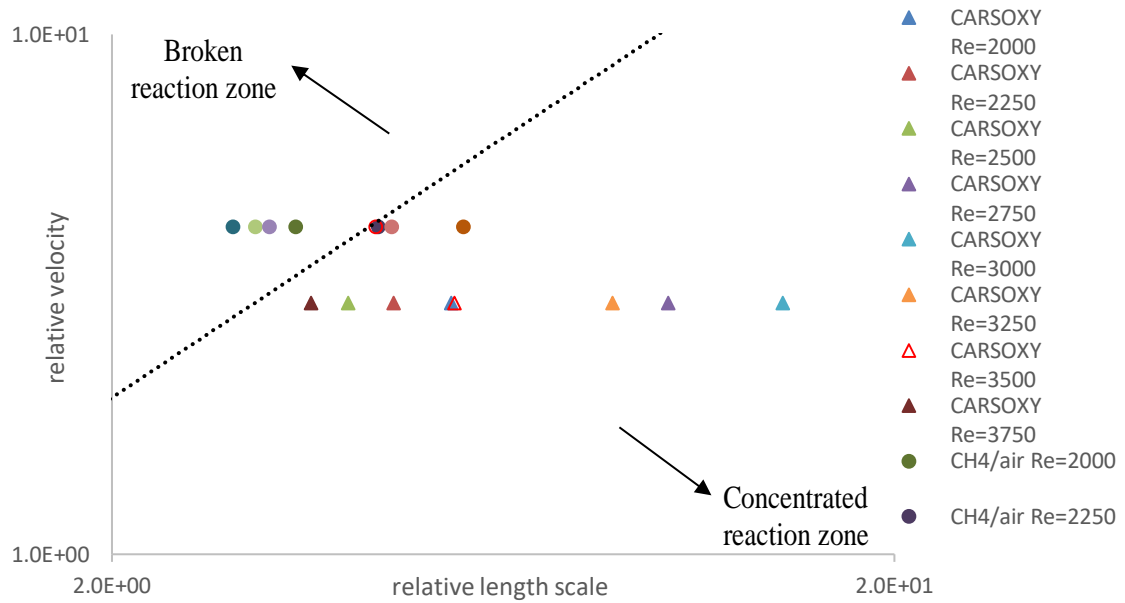


Figure 8.11 Borghi regime at constant working fluid Reynold's numbers [2000-3750] and \dot{V}_{CH_4} of 1 L/min

Figure 8.12 shows the Borghi diagram for CARSOXY and CH₄/air flames at constant λ_{oxy} [35-70]. The relative length scale to the relative velocity ratio patterns for the increase of λ_{oxy} generally followed the same behaviour as those for Reynold's number increase in Figure 8.11. At $\lambda_{oxy} = 65.625$, both of the CH₄/ air and CARSOXY flames exhibit the highest tendency of approaching the broken reaction zone.

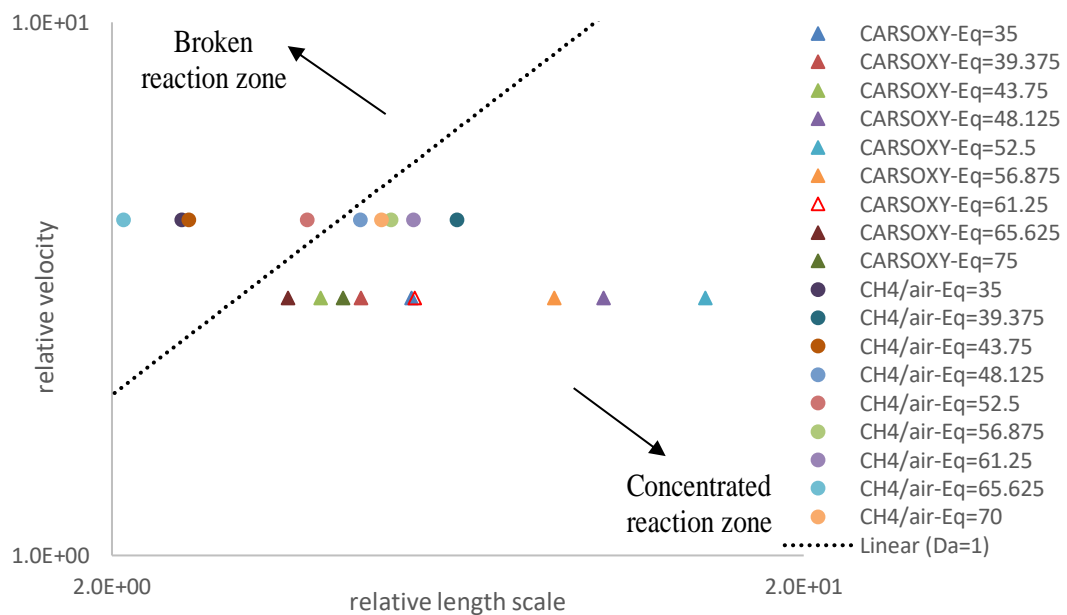


Figure 8.12 Borghi regime at constant λ_{oxy} [35-70].

8.9 Modified Damkohler number (Da) and Borghi regime diagram

The reference [162] defined the characteristic flow time (τ_n) as the ratio of the L_f to u_F as it was observed that L_f decreases with increasing u_F , Equation 8.1. The same behaviour of L_f was also observed with increasing the working fluid velocity V_{wf} (increasing Reynold's number), Figure 8.7. Therefore, it is suggested to modify τ_n to $\tau_{n,mod}$, Equation 8.2. The suggested equation of $\tau_{n,mod}$ was obtained using the "Buckingham π theorem", which is a mathematical approach that correlates physical variables (i.e. L_f , u_F and V_{wf}) to a dimensionless parameter (i.e. the modified Damkohler number $Da_{,mod}$). Similarly, the relative velocity u_F/S_l was adjusted to $\sqrt{u_F V_{wf}}/S_l$ to modify the Borghi diagram.

$$\tau_n = \frac{L_f}{u_F} \tag{8.1}$$

$$\tau_{n,mod} = \frac{L_f}{\sqrt{u_F V_{wf}}} \tag{8.2}$$

As shown in Figure 8.13, $\tau_{n,mod}$ has shifted all data points upwards in $Da_{,mod}$ axes in the same order of magnitude as those plotted for the unmodified Da for the increase of Re, Figure 8.9. Nevertheless, since the modified relative velocities $\sqrt{u_F V_{wf}}/S_l$ were lower than the unmodified relative velocity u_F/S_l , data points in the Borghi diagram (Figure 8.14) were redistributed towards the concentrated reaction zone in variable magnitudes, depending on V_{wf} of each case (Tables 3.21 and 3.22).

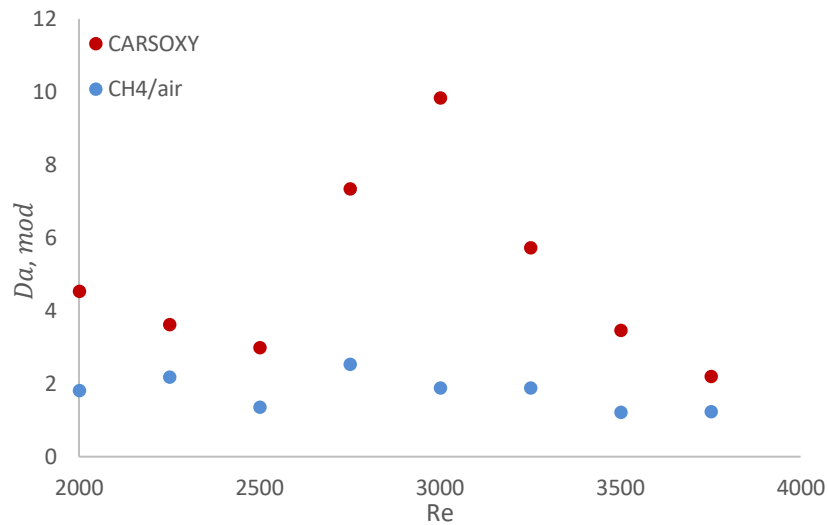


Figure 8.13 $Da_{,mod}$ at constant working fluid Reynold's numbers [2000-3750] and \dot{V}_{CH_4} of 1 L/min

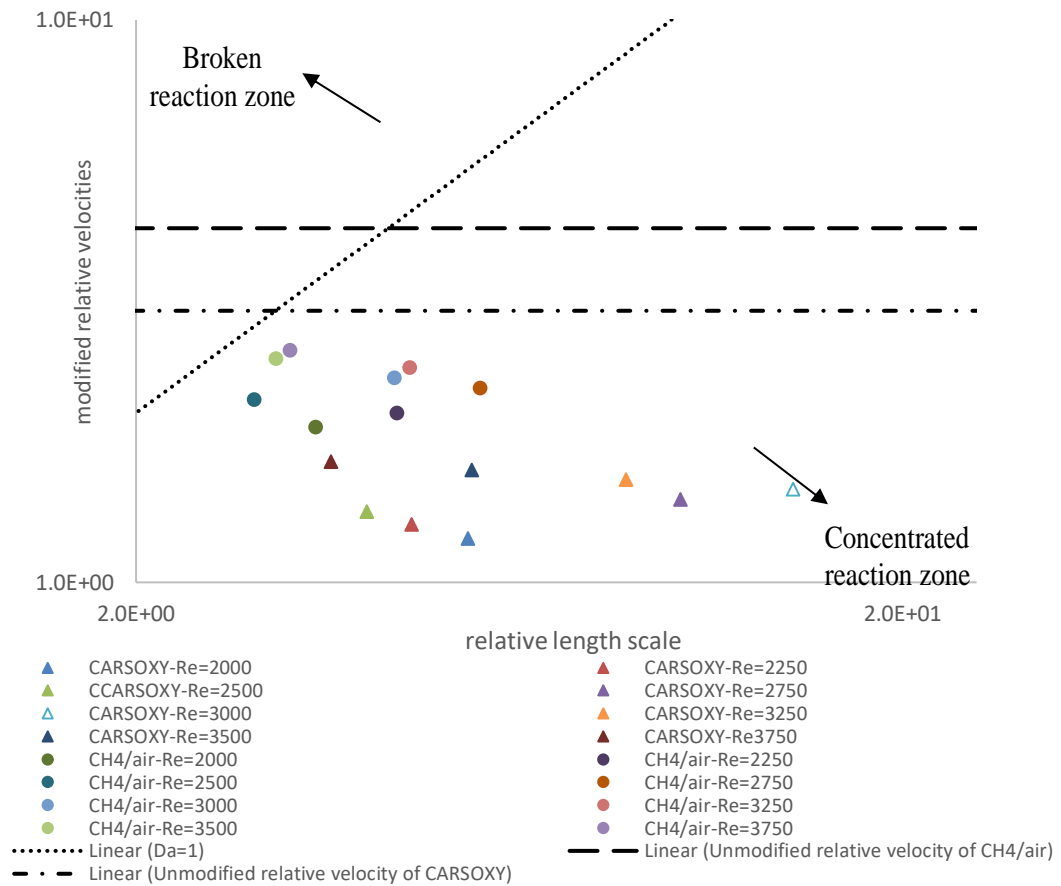


Figure 8.14 Modified Borghi regime at constant working fluid Reynold’s numbers [2000-3750] and \dot{V}_{CH_4} of 1 L/min

The same effects of the modified characteristic flow time ($\tau_{n,mod}$) and relative velocity $\sqrt{u_F V_{wf}}/S_l$ for increasing Re were observed on Da and Borghi diagram for increasing λ_{oxy} , Figures 8.15 and 8.16.

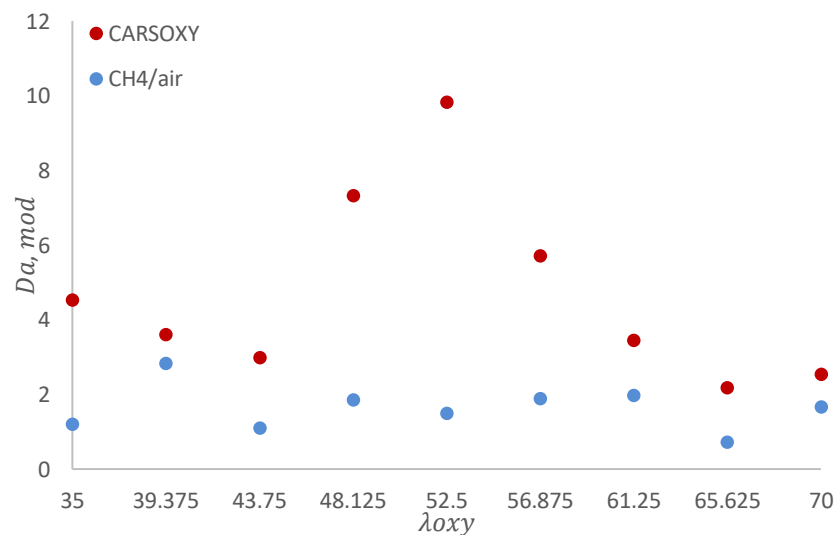


Figure 8.15 Da, mod at constant λ_{oxy} [35-70].

is anticipated to become more significant as Re increase (i.e. $Re > 3750$). To establish numerical anticipations of the flame stability response for CARSOXY within the tested intervals, $\sigma_{OH^*/OH}$ functions of Re and λ_{oxy} ($\sigma_{OH^*/OH}(Re)$ and $\sigma_{OH^*/OH}(\lambda_{oxy})$) have been generated based on the obtained experimental results.

In the interval of $Re=[2000-3750]$, the average $A_{\overline{OH}_{Max}}$ of the CARSOXY flame is 45% of the CH_4/air flame. However, as Re increases, the difference in $A_{\overline{OH}_{Max}}$ between both flames decreases. By plotting $C_{\overline{OH}_{Max}}$ results for $Re=[2000-3750]$, it can be generally said that both flames of CH_4/air and CARSOXY have concentrated $C_{\overline{OH}_{Max}}$. The $C_{\overline{OH}_{Max}}$ of CARSOXY flames were approximately concentrated closer to the burner centerline than those for the CH_4/air flames. As Reynold's number increases, the $C_{\overline{OH}_{Max}}$ of the CARSOXY flames converge towards the same location as that for the CH_4/air . This can be correlated to the $A_{\overline{OH}_{Max}}$ results, where the difference in $A_{\overline{OH}_{Max}}$ decreases. Thus, $C_{\overline{OH}_{Max}}$ of the CARSOXY flame is limited in a smaller area, which is similar to that for CH_4/air flame. Although the $\sigma_{OH^*/OH}$ criteria provide an indication of flame stability, it does not highlight the flame turbulence-chemistry interaction. Therefore, Damkohler analyses suggested by the reference [200] for nonpremixed combustion have been performed. Da of the CARSOXY flame was greater than one and greater than that for the CH_4/air in all conditions, indicating more uniform CARSOXY flames in comparison to CH_4/air flames throughout the Re interval ([2000-3750]).

By plotting the Borghi regime diagram suggested by the reference [162], it has been found that the tendency of the CARSOXY flame of approaching the concentrated reaction zone is greater than that for the CH_4/air flame since the relative velocity of the CARSOXY flame was lower than for CH_4/air . Nevertheless, the CARSOXY flame also approached the concentrated reaction zone in the Borghi diagram as it exhibits a high relative length scale.

The modified Damkohler number (Da) and Borghi regime diagram which take into account the effect of V_{wf} have been plotted. Da, mod of both flames have been higher than the unmodified Da while minting the same order of magnitude. Since the modified relative velocities $\sqrt{u_F V_{wf}}/S_l$ were lower than u_F/S_l , data points in the Borghi diagram were redistributed towards the concentrated reaction zone in variable magnitudes, depending on V_{wf} of each case.

Finally, assessing the performance of the CARSOXY flame against CH_4/air flame at constant λ_{oxy} eliminates the role of high O_2 content in CARSOXY and highlights the combined effect of CO_2 and argon in CARSOXY. At constant λ_{oxy} , CARSOXY patterns in comparison to CH_4/air followed approximately the same patterns as those plotted at constant Re (i.e. higher oxygen levels in CARSOXY compared to

CH₄/air). Therefore, it can be concluded that CO₂ and argon have the most significant effect of changing the CARSOXY flame behaviour in comparison to the CH₄/air flame. However, quantifying the effect of each individual CARSOXY component on the flame behaviour is recommended as a future work by testing CH₄/CO₂-O₂, CH₄/A_r-O₂ flames against CH₄/air flame at constant equivalence ratios to identify the role of CO₂ and A_r, respectively.

8.11 Limitations

As shown in the Figures 8.1B, 8.2B and 8.4, the full ranges of the flames were not captured since the distance between the CCD camera (with a fixed focal length) and the exit of the burner was fixed and thus only a finite part of the flame was captured. Capturing the full range of the visible flame could be obtained if this distance is increased. However, this would affect the resolution of the captured images such that the (pixel/mm) ratio will be decreased.

Nevertheless, increasing the distance between the exit of the burner and the CCD camera only captures a larger part of the visible flame but not necessarily a larger part of the OH fluoresce. Provided that the CCD captures the full range of the visible flame, the laser sheet must cover the full range of the flame. This could be obtained by increasing the distance between the PLIF system (or the laser sheet-forming optics) and the exit of the burner. However, this will decrease the laser power (received by the flame), thus, tracking OH fluoresces becomes more difficult.

To sum up, the results of this chapter are only for a finite zone. Therefore, those results do not characterize the flames in their full range. It is recommended to perform a parametric study to find the optimum PLIF setup (i.e. finding the ultimate distances amongst the exit of the burner, CCD camera and sheet laser sheet-forming optics to find acceptable image resolutions and laser power (received by the flame), while capturing the full range of OH fluorescence of the flame.

CHAPTER NINE

Discussion and Future work

“Progress in science depends on new techniques, new discoveries and new ideas, probably in that order.”

~ Sydney Brenner

CHAPTER 9 – DISCUSSION AND FUTURE WORK

This thesis aimed to conduct baseline investigations to characterize CARSOXY gas turbines, towards facilitating a higher level of technology maturity. The investigations included a parametric study for five gas turbine cycles using CARSOXY as working fluid, a novel approach of producing CARSOXY, a techno-economic study and experimental analyses. This chapter provides a summary of the main findings and provides recommendations for future work. The reader is directed to the discussions and conclusions at the end of the five core chapters (4, 5, 6, 7 and 8) for more detailed discussions.

9.1 Outcomes of the parametric study

The performance of the five cycles (namely; simple, heat exchanged, free turbine & simple cycle, evaporative and humidified) using CARSOXY has been estimated in comparison to CH₄/air for wet and dry compression by plotting the cycle efficiency with respect to the combined effect of varying the compressor inlet temperature and pressure ratio. Amongst the five cycles, the heat exchanged cycle was identified as the ultimate CARSOXY cycle. Efficiency increase can be up to 12% using CARSOXY heat-exchanged cycle with dry compression compared to air-driven cycles. Therefore, it was chosen to be simulated with Aspen Plus. Additional 10% increase of the cycle efficiency can be theoretically achieved by a new blend, which has the molar fractions of 47% argon, 10% carbon dioxide, 10% H₂O and 33% oxy-fuel.

9.2 Outcomes of analyzing the novel approach of producing CARSOXY

An ASPEN PLUS model has been developed to demonstrate the approach of producing CARSOXY. The model involves the integrations of an air separation unit (ASU), a steam methane reformer (SMR), water gas shift (WGS) reactors, pressure swing adsorption (PSA) units and heat exchanged gas turbines (HXGT) with a CCS unit. Sensitivity analyses were conducted on the ASU-SMR-WGS-PSA-CCS-HXGT model to feature its response. Two modes of operability have been achieved, the first mode produces the CARSOXY within the required molar fraction with hydrogen and nitrogen as by-products. The second mode reacts nitrogen with hydrogen to produce ammonia (Haber-Bosch process). The processes involved in the ASU-SMR-WGS-PSA-CCS-HXGT have diverged from the conventional processes in many aspects. To name a few, after the sensitivity analysis the final

parameters of the WGS model have been chosen to ensure low methane conversion factor (enough to produce the required carbon dioxide and maintain the required methane level as unreacted). In addition, conventional argon production involves a rectifying process, while it has been eliminated in the ASU-SMR-WGS-PSA-CCS-HXGT cycle by customizing the operation conditions of the ASU.

9.3 Outcomes of the Techno-economic assessment of the ASU-SMR-WGS-PSA-CCS-HXGT cycle

The suggested technique of producing CARSOXY (the ASU-SMR-WGS-PSA-CCS-HXGT cycle) must prove economic sustainability in order to be adopted by the industry. Comparable techno-economic analyses have been performed between CARSOXY and Air-driven gas turbine cycles using the same amount of CH₄ fuel. The CARSOXY cycle has demonstrated to payout all costs way before the Air-driven cycle. In fact, 85.5% of the CARSOXY project's life is profitable (positive NPV), while only 69.5% is profitable for the Air-driven cycle. The Modified Internal Rate of Return (MIRR) of the CARSOXY cycle is approximately 2.2% higher than that for the Air-driven cycle. Moreover, the profitability index (PI) of the CARSOXY cycle is 1.72, while it is only 1.28 for the Air-driven cycle. Due to the complexity involved in the CARSOXY cycle the total project cost, the total operation cost and the EPC (7.78E+07 [£], 6.48+07 [£/Year] and 0.83 Year, respectively) went beyond the limits of those for the Air-driven cycle. At first glance, these "unattractive" indicators would categorize the CARSOXY cycle as a risky project. However, high risks come with high gains. The high total product sales of the CARSOXY cycle do not only make up for those "unattractive" indicators but also entitle the CARSOXY cycle to payout all costs way before the Air-driven cycle. Therefore, based on the figures it can be concluded that the CARSOXY cycle has the potential to be adopted by the industry in the near future.

9.4 Outcomes of the chemiluminescence imaging and emission analyses over a range of instability conditions (excitation frequencies [50Hz-700Hz]) and variable volumetric flowrates

OH chemiluminescence imaging integrated with Abel deconvolution techniques have been utilized to study flame stability, and flame geometry (i.e. Area of highest heat intensity ($A_{OH_{Max}}$), Center of highest heat intensity ($C_{OH_{Max}}$)) over a range of instability conditions (excitation frequencies [50Hz-700Hz]). Moreover, NO_x and carbon emissions have also been analyzed. The standard deviation of

heat release fluctuations ($\sigma_{OH^*/\overline{OH}}$) has been utilized as the base-criteria to compare the stability performance of CARSOXY to Air/Methane combustion.

CARSOXY is anticipated to produce the same level of thermal power as Air/Methane within a much more compact burner while eliminating NO_x emissions. High oxygen molar fraction in CARSOXY has contributed to reducing CO levels to the tenth of those of Air/Methane and increased CO₂ emission levels. Thus, CCS in CARSOXY-driven plant can be implied with a lower efficiency penalty compared to those in Air-driven plants.

By evaluating the overall stability performances of both flames over the excitation interval [50Hz-700Hz] for the three flow rates $\dot{V}_{WF}=80\text{L}/\text{min}$, $60\text{L}/\text{min}$ and $40\text{L}/\text{min}$, it can be concluded that the CARSOXY flame has a more stable performance compared to Air/Methane flame. The average $\sigma_{OH^*/\overline{OH}}^{CARSOXY}$ over the excitation interval for the three flow rates are lower than $\sigma_{OH^*/\overline{OH}}^{Air}$. Therefore, it can be concluded that CARSOXY has better overall stability performance. Furthermore, this has been confirmed by the $C_{\overline{OH}_{Max}}$ results (Figure 7) as the Air/ methane demonstrated higher sensitivity towards both of the excitation frequency and \dot{V}_{WF} . Finally, due to the (experimentally negligible and theoretically zero) NO_x emissions of CARSOXY, the relatively more stable diffusive burners compared to premixed can be used for CARSOXY, whilst not for Air/methane. This is indeed another major stability advantage in favour of CARSOXY combustion.

9.5 Outcomes of PLIF and Chemiluminescence analyses over a range of λ_{oxy} and fluid Reynold's numbers

After analysing CARSOXY in comparison to CH₄/air over variable volumetric flowrates, it was essential to perform the analyses over a range of λ_{oxy} and fluid Reynold's numbers. OH chemiluminescence integrated with PLIF imaging has been utilized to study several flame properties at Re of [2000-2250] and \dot{V}_{CH_4} of 1L/min and λ_{oxy} of [35-70] (i.e. Area of highest heat intensity ($A_{\overline{OH}_{Max}}$), the centre of highest heat intensity ($C_{\overline{OH}_{Max}}$)). Moreover, Damkohler analyses have been performed and Borghi regime diagrams have been produced for both types of flames.

Essentially, the standard deviation ($\sigma_{OH^*/\overline{OH}}$) of the CARSOXY flame was lower than that for the CH₄/air flame throughout the entire interval of $Re = [2000 - 3750]$ by approximately 16%, indicating higher heat release stability than that for the CH₄/air flame.

In the interval of $Re=[2000-3750]$, the average $A_{\overline{OH}_{Max}}$ of the CARSOXY flame is 45% of the CH_4/air flame. By plotting $C_{\overline{OH}_{Max}}$ results for $Re=[2000-3750]$, it can be generally said that both flames of Air/Methane and CARSOXY have concentrated $C_{\overline{OH}_{Max}}$. The $C_{\overline{OH}_{Max}}$ of CARSOXY flames were approximately concentrated closer to the burner centerline than those for the CH_4/air flames.

Damkohler analyses for nonpremixed combustion have been performed. Da of the CARSOXY flame was greater than one and greater than that for the CH_4/air in all conditions, indicating more uniform CARSOXY flames in comparison to CH_4/air flames throughout the Re interval ([2000-3750]).

By plotting the Borghi regime diagram, it has been found that the tendency of the CARSOXY flame of approaching the concentrated reaction zone is greater than that for the $CH_4/flame$ since the relative velocity of the CARSOXY flame was lower than for CH_4/air . Nevertheless, the CARSOXY flame also approached the concentrated reaction zone in the Borghi diagram as it exhibits a high relative length scale.

Finally, assessing the performance of the CARSOXY flame against CH_4/air flame at constant λ_{oxy} eliminates the role of high O_2 content in CARSOXY and highlights the combined effect of CO_2 and Argon in CARSOXY. At constant λ_{oxy} , CARSOXY patterns in comparison to CH_4/air followed approximately the same patterns as those plotted at constant Re (i.e. higher oxygen levels in CARSOXY compared to CH_4/air). Therefore, it can be concluded that CO_2 and Argon have the most significant effect of changing flame behaviour in comparison to CH_4/air flame.

9.6 Future work

As discussed in chapter 4, the efficiency of CARSOXY gas turbines can be further increased by additional 10% by a new blend, which has the molar fractions of 47% argon, 10% carbon dioxide, 10% H_2O . Therefore, it is recommended to theoretically assess this blend to answer questions related to the feasibility of producing this blend in an economically sustainable approach. It is also suggested to experimentally identify the combustion mechanism of this blend.

As discussed in chapter 5, the concept of producing CARSOXY has been demonstrated computationally using the simulation software ASPEN PLUS. However, in order to promote this concept to the industry, a laboratory-scale prototype is advised to be commissioned. While the model

has been calibrated to produce the required CARSOXY molar fractions, exergy analysis and mathematical modelling can further optimize the waste heat utilization for real, profitable applications.

CARSOXY flame was experimentally examined against CH₄/air flame and the differences between both flames were related to the combined effects of CARSPXY components. Quantifying the effect of each individual CARSOXY component on the flame behaviour is recommended as a future work by testing CH₄/ CO₂- O₂, CH₄/A_r- O₂ and CH₄/ H₂O- O₂ flames against CH₄/air flame at constant equivalence ratios to identify the role of CO₂, A_r and H₂O, respectively.

CARSOXY balances the three factors of combustion stability, cycle efficacy and turbine temperature. Once the exact effects of each component on these factors are determined, balancing these factors over variable conditions (i.e. variable gas turbine inlet temperature and pressure) can be optimized by utilizing a control unit integrated with temperature sensors, pressure sensors and mass flow controllers. This could be a leading step towards automated combustion.

Finally, studying CARSOXY gas dynamics and its interaction with turbine/compressor blades and cascades remains a crucial task, which can be fulfilled by utilizing CFD models together with wind tunnel-based experiments. It must be pointed out that local Mach numbers on turbine blades can reach the supersonic level, which is an extremely critical point that is highly sensitive to the working fluid properties.

REFERENCES

- [1] Lefebvre, Arthur H., and Dilip R. Ballal. Gas turbine combustion: alternative fuels and emissions. CRC press, 2010.
- [2] Morris, A., B. Cacciapuoti, and Wei Sun. "The role of small specimen creep testing within a life assessment framework for high temperature power plant." *International Materials Reviews* 63, no. 2 (2018): 102-137.
- [3] United Kingdom Department for Business, Energy and Industrial Strategy. Digest of UK Energy Statistics. London; 2016.
- [4] International Energy Agency. World Energy Outlook 2016 Executive Summary. Paris; 2016.
- [5] Goto, Kazuya, Katsunori Yogo, and Takayuki Higashii. "A review of efficiency penalty in a coal-fired power plant with post-combustion CO₂ capture." *Applied Energy* 111 (2013): 710-720.
- [6] Scheffknecht, G., Al-Makhadmeh, L., Schnell, U., & Maier, J. (2011). Oxy-fuel coal combustion—A review of the current state-of-the-art. *International Journal of Greenhouse Gas Control*, 5, S16-S35.
- [7] Álvarez, J. F. G., & de Grado, J. G. (2016). Study of a modern industrial low pressure turbine for electricity production employed in oxy-combustion cycles with CO₂ capture purposes. *Energy*, 107, 734-747..
- [8] Tuttle, S. G., Chaudhuri, S., Kostka Jr, S., Kopp-Vaughan, K. M., Jensen, T. R., Cetegen, B. M., & Renfro, M. W. (2012). Time-resolved blowoff transition measurements for two-dimensional bluff body-stabilized flames in vitiated flow. *Combustion and Flame*, 159(1), 291-305..
- [9] Nemitallah, M. A., Rashwan, S. S., Mansir, I. B., Abdelhafez, A. A., & Habib, M. A. (2018). Review of novel combustion techniques for clean power production in gas turbines. *Energy & Fuels*, 32(2), 979-1004.
- [10] Fu, Q., Kansha, Y., Song, C., Liu, Y., Ishizuka, M., & Tsutsumi, A. (2016). A cryogenic air separation process based on self-heat recuperation for oxy-combustion plants. *Applied Energy*, 162, 1114-1121.
- [11] Abou-Arab, T. W. Experimental Investigation of Oxy-Fuel Combustion of CNG Flames Stabilized Over a Perforated-Plate Burner.
- [12] Jonsson, M., & Yan, J. (2005). Humidified gas turbines—a review of proposed and implemented cycles. *Energy*, 30(7), 1013-1078.
- [13] Giampaolo, T. (2003). *The gas turbine handbook: Principles and practices*. The Fairmont Press, Inc..
- [14] He, Y., Zou, C., Song, Y., Chen, W., Jia, H., & Zheng, C. (2016). Experimental and numerical study of the effect of high steam concentration on the oxidation of methane and ammonia during oxy-steam combustion. *Energy & Fuels*, 30(8), 6799-6807.
- [15] Richards, G. A., Casleton, K. H., & Chorpening, B. T. (2005). CO₂ and H₂O diluted oxy-fuel combustion for zero-emission power. *Proceedings of the Institution of Mechanical Engineers, Part A: Journal of Power and Energy*, 219(2), 121-126.
- [16] Jin, B., Zhao, H., Zou, C., & Zheng, C. (2015). Comprehensive investigation of process characteristics for oxy-steam combustion power plants. *Energy conversion and management*, 99, 92-101.
- [17] Xiong, J., Zhao, H., Chen, M., & Zheng, C. (2011). Simulation study of an 800 MWe oxy-combustion pulverized-coal-fired power plant. *Energy & Fuels*, 25(5), 2405-2415.
- [18] Xiong, J., Zhao, H., & Zheng, C. (2011). Exergy analysis of a 600 MWe oxy-combustion

- pulverized-coal-fired power plant. *Energy & Fuels*, 25(8), 3854-3864.
- [19] Xiong, J., Zhao, H., & Zheng, C. (2012). Thermoeconomic cost analysis of a 600 MWe oxy-combustion pulverized-coal-fired power plant. *International Journal of Greenhouse Gas Control*, 9, 469-483.
- [20] Jin, B., Zhao, H., & Zheng, C. (2014). Dynamic modeling and control for pulverized-coal-fired oxy-combustion boiler island. *International Journal of Greenhouse Gas Control*, 30, 97-117.
- [21] Singh, J. (1999). *Sterling Dictionary of Physics*. Sterling Publishers Pvt. Ltd.
- [22] Shahsavan, M., & Mack, J. H. (2017). The effect of heavy working fluids on hydrogen combustion.
- [23] No, H. C., Kim, J. H., & Kim, H. M. (2007). A review of helium gas turbine technology for high-temperature gas-cooled reactors. *Nuclear Engineering and Technology*, 39(1), 21-30.
- [24] Nayagam, V., Haggard Jr, J. B., Colantonio, R. O., Marchese, A. J., Dryer, F. L., Zhang, B. L., & Williams, F. A. (1998). Microgravity n-heptane droplet combustion in oxygen-helium mixtures at atmospheric pressure. *AIAA journal*, 36(8), 1369-1378.
- [25] Al-Doboon, Ali, Milana Gutesa, Agustin Valera-Medina, Nick Syred, Jo-Han Ng, and Cheng Tung Chong. "CO₂-argon-steam oxy-fuel (CARSOXY) combustion for CCS inert gas atmospheres in gas turbines." *Applied Thermal Engineering* 122 (2017): 350-358.
- [26] Paris Agreement. "United Nations Framework Convention on Climate Change, Paris Agreement." (2015).
- [27] Single Market Act. "Communication from the commission to the European parliament, the council, the economic and social committee and the committee of the regions." (2012).
- [28] Reid, Colin T. "Climate law in the United Kingdom." In *Climate Change and the Law*, pp. 537-549. Springer, Dordrecht, 2013. United Kingdom Parliament. *Climate Change Act 2008*. Chapter 27. London; 2008.
- [29] UK Parliament. "The Carbon Plan: Delivering our low carbon future." *Energy* (2011): 218.
- [30] V. Smil, *Energy at the crossroads: global perspectives and uncertainties*: MIT press, 2005.
- [31] Conti, John, Paul Holtberg, Jim Diefenderfer, Angelina LaRose, James T. Turnure, and Lynn Westfall. *International energy outlook 2016 with projections to 2040*. No. DOE/EIA-0484 (2016). USDOE Energy Information Administration (EIA), Washington, DC (United States). Office of Energy Analysis, 2016.
- [32] Clerici, Alessandro, and G. Alimonti. "World energy resources." In *EPJ Web of Conferences*, vol. 98, p. 01001. EDP Sciences, 2015.
- [33] Demirbas, A. "Methane Gas Hydrate: Springer Science & Business Media." London, England (2010).
- [34] MacLeay, Iain. *Digest of United Kingdom energy statistics 2010*. The Stationery Office, 2010.
- [35] Qadrdan, Meysam, Modassar Chaudry, Nick Jenkins, Pranab Baruah, and Nick Eyre. "Impact of transition to a low carbon power system on the GB gas network." *Applied energy* 151 (2015): 1-12.
- [36] Wolsky, A. M., E. J. Daniels, and B. J. Jody. "CO₂ capture from the flue gas of conventional fossil-fuel-fired power plants." *Environmental Progress* 13, no. 3 (1994): 214-219.
- [37] Pavri, Roointon, and Gerald D. Moore. "Gas turbine emissions and control." *General Electric Report* No. GER-4211 (2001).
- [38] Choi, Gyung-Min, and Masashi Katsuki. "Advanced low NO_x combustion using highly preheated air." *Energy conversion and Management* 42, no. 5 (2001): 639-652.
- [39] Generation, GE Power. "Gas Turbine NO_x Emissions Approaching Zero—Is it Worth the Price?."

- [40] Hendricks, R. C., D. T. Shouse, and W. M. Roquemore. "Water injected turbomachinery." (2005).
- [41] Docquier, Nicolas, and Sébastien Candel. "Combustion control and sensors: a review." *Progress in energy and combustion science* 28, no. 2 (2002): 107-150.
- [42] Rao, Anand B., and Edward S. Rubin. "A technical, economic, and environmental assessment of amine-based CO₂ capture technology for power plant greenhouse gas control." *Environmental science & technology* 36, no. 20 (2002): 4467-4475.
- [43] Breeze, Paul. *Power generation technologies*. Newnes, 2019.
- [44] ASME Codes and Standards Committee B133, Subcommittee 2. "Environmental Standards for Gas Turbine, Low NO_x Measurement: Gas Turbine Plants, Turbines", Report No. 9855-3 (1998).
- [45] Chiesa, Paolo, and Stefano Consonni. "Natural gas fired combined cycles with low CO₂ emissions." *J. Eng. Gas Turbines Power* 122, no. 3 (2000): 429-436.
- [46] Zhang, Zhiguo, Dan Zhao, Siliang Ni, Yuze Sun, Bing Wang, Yong Chen, Guoneng Li, and S. Li. "Experimental characterizing combustion emissions and thermodynamic properties of a thermoacoustic swirl combustor." *Applied Energy* 235 (2019): 463-472.
- [47] Zhao, Ruikai, Shuai Deng, Li Zhao, Shuangjun Li, Yue Zhang, and Bowen Liu. "Performance analysis of temperature swing adsorption for CO₂ capture using thermodynamic properties of adsorbed phase." *Applied Thermal Engineering* 123 (2017): 205-215.
- [48] Xing, Fei, Arvind Kumar, Yue Huang, Shining Chan, Can Ruan, Sai Gu, and Xiaolei Fan. "Flameless combustion with liquid fuel: A review focusing on fundamentals and gas turbine application." *Applied Energy* 193 (2017): 28-51.
- [49] Self, Stuart J., Marc A. Rosen, and Bale V. Reddy. "Effects of Oxy-Fuel Combustion on Performance of Heat Recovery Steam Generators." *European Journal of Sustainable Development Research* 2, no. 2 (2018): 22.
- [50] Hu, Yue, Gang Xu, Cheng Xu, and Yongping Yang. "Thermodynamic analysis and techno-economic evaluation of an integrated natural gas combined cycle (NGCC) power plant with post-combustion CO₂ capture." *Applied Thermal Engineering* 111 (2017): 308-316.
- [51] Herranz Puebla, Luis Enrique, José Ignacio Linares Hurtado, and Beatriz Yolanda Moratilla Soria. "Power cycle assessment of nuclear high temperature gas-cooled reactors." (2009).
- [52] McDonald, Colin F. "Helium turbomachinery operating experience from gas turbine power plants and test facilities." *Applied Thermal Engineering* 44 (2012): 108-142.
- [53] Prisyazhniuk, Vitaly A. "Alternative trends in development of thermal power plants." *Applied Thermal Engineering* 28, no. 2-3 (2008): 190-194.
- [54] Bammert, K., and R. Klein. "The influence of He-Ne, He-N₂, and He-CO₂ gas mixtures on closed-cycle gas turbines." In *ASME 1974 International Gas Turbine Conference and Products Show*, pp. V01BT02A041-V01BT02A041. American Society of Mechanical Engineers, 1974.
- [55] Glarborg, Peter, and Line LB Bentzen. "Chemical effects of a high CO₂ concentration in oxy-fuel combustion of methane." *Energy & Fuels* 22, no. 1 (2007): 291-296.
- [56] Markewitz, Peter, Wilhelm Kuckshinrichs, Walter Leitner, Jochen Linszen, Petra Zapp, Richard Bongartz, Andrea Schreiber, and Thomas E. Müller. "Worldwide innovations in the development of carbon capture technologies and the utilization of CO₂." *Energy & environmental science* 5, no. 6 (2012): 7281-7305.
- [57] Bibrzycki, J., and T. Poinso. "Reduced chemical kinetic mechanisms for methane combustion in O₂/N₂ and O₂/CO₂ atmosphere." Working note ECCOMET WN/CFD/10 17 (2010).
- [58] Zhang, S. J., S. To, G. Q. Zhang, and Z. W. Zhu. "A review of machine-tool vibration and its influence upon surface generation in ultra-precision machining." *International journal of machine*

- tools and manufacture 91 (2015): 34-42.
- [59] Ameel, Bernd, Christophe T'Joel, Kathleen De Kerpel, Peter De Jaeger, Henk Huisseune, Marnix Van Belleghem, and Michel De Paepe. "Thermodynamic analysis of energy storage with a liquid air Rankine cycle." *Applied Thermal Engineering* 33, no. 1 (2013): 130-140.
- [60] Pilavachi, P. A. "Mini-and micro-gas turbines for combined heat and power." *Applied thermal engineering* 22, no. 18 (2002): 2003-2014.
- [61] Heppenstall, T. "Advanced gas turbine cycles for power generation: a critical review." *Applied Thermal Engineering* 18, no. 9-10 (1998): 837-846
- [62] De Sa, Ashley, and Sarim Al Zubaidy. "Gas turbine performance at varying ambient temperature." *Applied Thermal Engineering* 31, no. 14-15 (2011): 2735-2739.
- [63] Beck, Douglas, and David G. Wilson. *Gas-turbine regenerators*. Springer Science & Business Media, 2012.
- [64] Bassily, Ashraf M. "Effects of evaporative inlet and aftercooling on the recuperated gas turbine cycle." *Applied thermal engineering* 21, no. 18 (2001): 1875-1890.
- [65] Bhargava, R., and C. B. Meher-Homji. "Parametric analysis of existing gas turbines with inlet evaporative and overspray fogging." In *ASME Turbo Expo 2002: Power for Land, Sea, and Air*, pp. 387-401. American Society of Mechanical Engineers, 2002.
- [66] McDonald, Colin F., and David Gordon Wilson. "The utilization of recuperated and regenerated engine cycles for high-efficiency gas turbines in the 21st century." *Applied Thermal Engineering* 16, no. 8-9 (1996): 635-653.
- [67] Luo, Xiaobo, and Meihong Wang. "Optimal operation of MEA-based post-combustion carbon capture for natural gas combined cycle power plants under different market conditions." *International Journal of Greenhouse Gas Control* 48 (2016): 312-320.
- [68] Kanniche, Mohamed, René Gros-Bonnivard, Philippe Jaud, Jose Valle-Marcos, Jean-Marc Amann, and Chakib Bouallou. "Pre-combustion, post-combustion and oxy-combustion in thermal power plant for CO₂ capture." *Applied Thermal Engineering* 30, no. 1 (2010): 53-62.
- [69] Saravanamuttoo, Herbert IH, Gordon Frederick Crichton Rogers, and Henry Cohen. *Gas turbine theory*. Pearson Education, 2001.
- [70] Pielke Jr, Roger A. "The British Climate Change Act: a critical evaluation and proposed alternative approach." *Environmental research letters* 4, no. 2 (2009): 024010.
- [71] Liu, C. Y., G. Chen, N. Sipöcz, Mohsen Assadi, and Xue-Song Bai. "Characteristics of oxy-fuel combustion in gas turbines." *Applied Energy* 89, no. 1 (2012): 387-394.
- [72] Li, Hailong, Jinyue Yan, and M. Anheden. "Impurity impacts on the purification process in oxy-fuel combustion based CO₂ capture and storage system." *Applied Energy* 86, no. 2 (2009): 202-213.
- [73] Stein-Brzozowska, Gosia, Jörg Maier, and Günter Scheffknecht. "Impact of the oxy-fuel combustion on the corrosion behavior of advanced austenitic superheater materials." *Energy procedia* 4 (2011): 2035-2042.
- [74] Huang, Ying, and Vigor Yang. "Dynamics and stability of lean-premixed swirl-stabilized combustion." *Progress in energy and combustion science* 35, no. 4 (2009): 293-364.
- [75] Xie, Yongliang, Jinhua Wang, Meng Zhang, Jing Gong, Wu Jin, and Zuohua Huang. "Experimental and numerical study on laminar flame characteristics of methane oxy-fuel mixtures highly diluted with CO₂." *Energy & Fuels* 27, no. 10 (2013): 6231-6237.
- [76] Gibbins, Jon, and Hannah Chalmers. "Carbon capture and storage." *Energy policy* 36, no. 12 (2008): 4317-4322.

- [77] Yokoyama, R., K. Ito, and Y. Matsumoto. "Optimal sizing of a gas turbine cogeneration plant in consideration of its operational strategy." *Journal of engineering for gas turbines and power* 116, no. 1 (1994): 32-38.
- [78] Cogen-Turbo, A. S. M. E. "vol. 6, A Study on Modified Gas Turbine Systems with Steam Injection or Evaporative Regeneration, K." Annerwall and G. Svedberg (1991).
- [79] Agren, N. D., Mats O. Westermark, Michael A. Bartlett, and Torbjörn Lindquist. "First experiments on an evaporative gas turbine pilot power plant: Water circuit chemistry and humidification evaluation." *Transactions of the ASME-A-Engineering for Gas Turbines and Power* 124, no. 1 (2002): 96-102.
- [80] Wyszynski, M. L., T. Megaritis, and R. S. Lehrle. "Hydrogen from Exhaust Gas Fuel Reforming: Greener." In *Leaner and Smoother Engines'*, Presentation in H2Net Meeting. 2017.
- [81] Najjar, Yousef SH. "Gas turbine cogeneration systems: a review of some novel cycles." *Applied thermal engineering* 20, no. 2 (2000): 179-197.
- [82] Wall, Terry F. "Combustion processes for carbon capture." *Proceedings of the combustion institute* 31, no. 1 (2007): 31-47.
- [83] Kaur, Manmeet. "Carbon Capturing and Storage Technology & current CCS initiatives in India (Emerging Technology in the field of Environmental Engineering)." *International Journal of Advanced Research in Computer Science* 8, no. 4 (2017).
- [84] Leung, Dennis YC, Giorgio Caramanna, and M. Mercedes Maroto-Valer. "An overview of current status of carbon dioxide capture and storage technologies." *Renewable and Sustainable Energy Reviews* 39 (2014): 426-443.
- [85] Stanger, Rohan, and Terry Wall. "Sulphur impacts during pulverised coal combustion in oxy-fuel technology for carbon capture and storage." *Progress in Energy and Combustion Science* 37, no. 1 (2011): 69-88.
- [86] Aaron, Douglas, and Costas Tsouris. "Separation of CO₂ from flue gas: a review." *Separation Science and Technology* 40, no. 1-3 (2005): 321-348.
- [87] Bernardo, Paola, Enrico Drioli, and G. Golemme. "Membrane gas separation: a review/state of the art." *Industrial & Engineering Chemistry Research* 48, no. 10 (2009): 4638-4663.
- [88] Khalel, Zeinab AM, Ali A. Rabah, and Taj Alasfia M. Barakat. "A new cryogenic air separation process with flash separator." *ISRN Thermodynamics* 2013 (2013).
- [89] Agrawal, R., D. W. Woodward, and T. F. Yee. "Argon production from air distillation: use of a heat pump in a ternary distillation with a side rectifier." *Gas separation & purification* 8, no. 1 (1994): 37-43.
- [90] Kerry, F. "Industrial gas handbook gas separation." *Gas Sep Purif* (2006).
- [91] Smith, A. R., and J. Klosek. "A review of air separation technologies and their integration with energy conversion processes." *Fuel processing technology* 70, no. 2 (2001): 115-134.
- [92] Cheung, Harry. "Moderate-pressure cryogenic air separation process." *Gas separation & purification* 5, no. 1 (1991): 25-28.
- [93] King, C. Judson. *Separation processes*. Courier Corporation, 2013.
- [94] Kansha, Yasuki, Akira Kishimoto, Tsuguhiko Nakagawa, and Atsushi Tsutsumi. "A novel cryogenic air separation process based on self-heat recuperation." *Separation and Purification Technology* 77, no. 3 (2011): 389-396.
- [95] Cornelissen, R. L., and G. G. Hirs. "Exergy analysis of cryogenic air separation." *Energy Conversion and Management* 39, no. 16-18 (1998): 1821-1826.
- [96] Barelli, L., G. Bidini, F. Gallorini, and S. Servili. "Hydrogen production through sorption-enhanced

- steam methane reforming and membrane technology: a review." *Energy* 33, no. 4 (2008): 554-570.
- [97] Sircar, Shivaji, and Timothy C. Golden. "Pressure swing adsorption technology for hydrogen production." *Hydrogen and syngas production and purification technologies* 10 (2009): 414-450.
- [98] LeValley, Trevor L., Anthony R. Richard, and Maohong Fan. "The progress in water gas shift and steam reforming hydrogen production technologies—a review." *International Journal of Hydrogen Energy* 39, no. 30 (2014): 16983-17000.
- [99] RJ, Byron Smith, Muruganandam Loganathan, and Murthy Shekhar Shantha. "A review of the water gas shift reaction kinetics." *International Journal of Chemical Reactor Engineering* 8, no. 1 (2010).
- [100] George W., Mildred S. Dresselhaus, and Michelle V. Buchanan. "The hydrogen economy." *Physics today* 57, no. 12 (2004): 39-44.
- [101] Twigg, Martyn V. *Catalyst handbook*. Routledge, 2018.
- [102] David S. "The water-gas shift reaction." *Catalysis Reviews Science and Engineering* 21, no. 2 (1980): 275-318.
- [103] Bracht, M., P. T. Alderliesten, R. Kloster, R. Pruschek, G. Haupt, E. Xue, J. R. H. Ross, M. K. Koukou, and N. Papayannakos. "Water gas shift membrane reactor for CO₂ control in IGCC systems: techno-economic feasibility study." *Energy Conversion and Management* 38 (1997): S159-S164.
- [104] Kazuo Matsumoto, and Susumu Noda. "Liftoff heights of turbulent non-premixed flames in co-flows diluted by CO₂/N₂." *Combustion and Flame* 161, no. 11 (2014): 2890-2903.
- [105] Zhu, Xuren, Xi Xia, and Peng Zhang. "Near-field flow stability of buoyant methane/air inverse diffusion flames." *Combustion and Flame* 191 (2018): 66-75.
- [106] Zhang, Ting, Qinghua Guo, Xudong Song, Zhijie Zhou, and Guangsuo Yu. "The chemiluminescence and structure properties of normal/inverse diffusion flames." *Journal of Spectroscopy* 2013 (2012).
- [107] Syred, Nicholas. "A review of oscillation mechanisms and the role of the precessing vortex core (PVC) in swirl combustion systems." *Progress in Energy and Combustion Science* 32, no. 2 (2006): 93-161
- [108] Osvaldo, Viguera-Zúñiga Marco, Syred Nicholas, Valera-Medina Agustín, and De la Rosa-Urbalejo Daniel. "Flashback avoidance in swirling flow burners." *Ingeniería, Investigación y Tecnología* 15, no. 4 (2014): 603-614.
- [109] Glassman, Irvin, Richard A. Yetter, and Nick G. Glumac. *Combustion*. Academic press, 2014.
- [110] Annamalai, Kalyan, Ishwar K. Puri, and Milind A. Jog. *Advanced thermodynamics engineering*. CRC press, 2011
- [111] Ding, Y., and E. Alpay. Adsorption-enhanced steam-methane reforming. *Chemical Engineering Science*, 55 (2000), pp. 3929-3940.
- [112] Hufton, J. R., S. Mayorga, and S. Sircar. Sorption-enhanced reaction process for hydrogen production. *AIChE Journal*, 45 (1999), pp. 248-256.
- [113] Mendes, D., A. Mendes, L. M. Madeira, A. Iulianelli, J. M. Sousa, and A. Basile. The water-gas shift reaction: from conventional catalytic systems to Pd-based membrane reactors—a review. *Asia-Pacific Journal of Chemical Engineering*, 5 (2010), pp. 111-137.
- [114] Tarun, Cynthia B., Eric Croiset, Peter L. Douglas, Murlidhar Gupta, and Mohammad HM Chowdhury. Techno-economic study of CO₂ capture from natural gas based hydrogen plants.

- International Journal of Greenhouse Gas Control, 1 (2007), pp.55-61.
- [115] Barg, Christian, José Maria Pinto Ferreira, Jorge Otávio Trierweiler, and Argimiro Resende Secchi. Simulation and optimization of an industrial PSA unit. *Brazilian Journal of Chemical Engineering*, 17 (2000), pp. 695-704.
- [116] Yang, Ralph T. *Gas separation by adsorption processes*. Butterworth-Heinemann., New York, USA, 2013.
- [117] UK Department for business, Energy and Industrial strategy. (2018). Industrial electricity prices in the EU. [online] Available [Accessed 7 May 2019].
- [118] Johnsen, K., Grace, J.R., Elnashaie, S.S., Kolbeinsen, L. and Eriksen, D., 2006. Modeling of sorption-enhanced steam reforming in a dual fluidized bubbling bed reactor. *Industrial & engineering chemistry research*, 45(12), pp.4133-4144.
- [119] Hajjaji, Noureddine, Marie-Noëlle Pons, Ammar Houas, and Viviane Renaudin. "Exergy analysis: An efficient tool for understanding and improving hydrogen production via the steam methane reforming process." *Energy Policy* 42 (2012): 392-399.
- [120] Odi Alrebei, Agustin Valera-Madeina, Parametric Study of Carbon dioxide-Argon -Steam Oxy-fuel (CARSOXY) Gas Turbines, Proceedings of the 13th Conference on Sustainable Development of Energy, Water, and Environment Systems, SDEWES2018.0479, 1-12
- [121] Hoffmann, Stéphanie, Michael Bartlett, Matthias Finkenrath, Andrei Evulet, and Tord Peter Ursin. "Performance and cost analysis of advanced gas turbine cycles with precombustion CO₂ capture." *Journal of Engineering for Gas Turbines and Power* 131, no. 2 (2009): 021701.
- [122] Understanding the Present Value Interest Factor. [online] Investopedia. Available at: <https://www.investopedia.com/terms/p/pvif.asp> [Accessed 7 May 2019].
- [123] Al-Malah, Kamal IM. *Aspen plus: chemical engineering applications*. John Wiley & Sons, 2016
- [124] Beaves, Robert G. "Net present value and rate of return: implicit and explicit reinvestment assumptions." *The Engineering Economist* 33, no. 4 (1988): 275-302.
- [125] Hosie, Jonathan. "Turnkey contracting under the FIDIC Silver Book: What do owners want? What do they get?." London, UK (2007).
- [126] Katila, Riitta, Eric L. Chen, and Henning Piezunka. "All the right moves: How entrepreneurial firms compete effectively." *Strategic Entrepreneurship Journal* 6, no. 2 (2012): 116-132.
- [127] Brealey, Richard, Stewart Myers, Franklin Allen, and Pitabas Mohanty. *Principles of Corporate Finance*, 11e. McGraw-Hill Education, 1988.
- [128] University of Oxford., 2015, "Our World in Datas", Available Online <https://ourworldindata.org/grapher/natural-gas-prices?time=1984..2016>. [Accessed 20th March 2019]
- [129] Ccwater.org.uk. Water Meter Calculator | Consumer Council for Water. [online] Available at: <https://www.ccwater.org.uk/watermetercalculator/> [Accessed 30 Oct. 2019].
- [130] Peters, Max Stone, Klaus D. Timmerhaus, Ronald E. West, Klaus Timmerhaus, and Ronald West *Plant design and economics for chemical engineers*. Vol. 4. New York: McGraw-Hill, 1968.
- [131] Lozowski, D. (2019). *The Chemical Engineering Plant Cost Index - Chemical Engineering*. [online] Chemengonline.com. Available at: <https://www.chemengonline.com/pci-home> [Accessed 6 May 2019].
- [132] Xe.com. (2019). XE Currency Converter - Live Rates. [online]

- Available at: <https://www.xe.com/currencyconverter/> [Accessed 7 May 2019].
- [133] Xe.com. (2019). XE Currency Converter - Live Rates. [online]
Available at: <https://www.xe.com/currencyconverter/> [Accessed 7 May 2019].
- [134] Government of India, 2016, "Ministry of Finance Department of Revenue Central Board of Excise & Customs.," F. No. 296/4/2016- CX-9. (Note : Oxygen price was determined using sample data, obtained from Indian Trade (Import/Export))
- [135] Wong, Sam, W. D. Gunter, and M. J. Mavor. "Economics of CO₂ sequestration in coalbed methane reservoirs." In SPE/CERI Gas Technology Symposium. Society of Petroleum Engineers, 2000.
- [136] Galanti, Leandro, and Aristide F. Massardo. "Micro gas turbine thermodynamic and economic analysis up to 500 kW size." *Applied Energy* 88, no. 12 (2011): 4795-4802.
- [137] Folk.ntnu.no. (2019). [online] Available at: http://folk.ntnu.no/magnehi/cepci_2011_py.pdf [Accessed 7 May 2019].
- [138] PoundSterling Live. (2019). Historical Rates for the GBP/EUR currency conversion on 30 June 2016 (30/06/2016).. [online] Available at: <https://www.poundsterlinglive.com/best-exchange-rates/british-pound-to-euro-exchange-rate-on-2016-06-30> [Accessed 7 May 2019].
- [139] DeCicco, Robert W. "Economic evaluation of research projects-by computer." *Chem. Eng* 75, no. 12 (1968): 84.
- [140] Ward, Thomas J. "Predesign estimating of plant capital costs." *Chemical Engineering* 91, no. 19 (1984): 121
- [141] Zevnik, F. C., and R. L. Buchanan. "Generalized correlation of process investment." *Chemical Engineering Progress* 59, no. 2 (1963): 70-77.
- [142] Klumpar, I. V., R. F. Brown and J. W. Fromrne. "Rapid capital estimation based on process modules." *Process Economics International*, no. 1, (1988):5-10.
- [143] Ctplaton.com. (2019). Platon PG - AIR series: CT Platon. [online] Available at: <http://www.ctplaton.com/en/products/flow/plastic-tube-flowmeters/platon-pg---air-series.php> [Accessed 10 Jun. 2019].
- [144] Okon, Aniekan. "Combustion dynamics in a lean premixed combustor with swirl forcing and fuel conditions." PhD diss., Cardiff University, 2017.
- [145] Gardiner, William Cecil, and Alexander Burcat, eds. *Combustion chemistry*. New York: Springer-Verlag, 1984.
- [146] Ctplatoncom. (2019). Platon PG - AIR series: CT Platon. [online] Available at: <http://www.ctplaton.com/en/products/flow/plastic-tube-flowmeters/platon-pg---air-series.php> [Accessed 10 Jun. 2019].
- [147] Rtellason.com. (2019). [online] Available at: <http://rtellason.com/manuals/FarnellFg3FunctionGenerator.pdf> [Accessed 10 Jun. 2019].
- [148] 350, t. and analyzer (2019). testo 350 Portable Emission Analyzer | Emission | Parameters | Testo, Inc. [online] Testo.com. Available at: <https://www.testo.com/en-US/testo-350/p/0632-3510> [Accessed 10 Jun. 2019].
- [149] GmbH, L. (2019). LaVision - Manuals. [online] Lavision.de. Available at: <https://www.lavision.de/en/downloads/manuals/> [Accessed 10 Jun. 2019].

- [150] Runyon, Jon, Richard Marsh, Yura Alexander Sevcenco, Daniel Pugh, and Steven Morris. "Development and commissioning of a chemiluminescence imaging system for an optically-accessible high-pressure generic swirl burner." (2015): 1-6.
- [151] Kutne, P., I. Boxx, M. Stöhr, and W. Meier. "Experimental analysis of the combustion behaviour of low calorific syngas mixtures in a gas turbine model combustor." In Proceedings of the European Combustion Meeting, pp. 23-4. 2007.
- [152] Higgins, Bryan, M. Q. McQuay, François Lacas, Juan-Carlos Rolon, Nasser Darabiha, and Sébastien Candel. "Systematic measurements of OH chemiluminescence for fuel-lean, high-pressure, premixed, laminar flames." *Fuel* 80, no. 1 (2001): 67-74.
- [153] Mathworks.com. (2019). Abel Inversion Algorithm - File Exchange - MATLAB Central. [online] Available at <http://www.mathworks.com/matlabcentral/fileexchange/43639-abel-inversion-algorithm> [Accessed 10 Jun. 2019].
- [154] Bland, J. Martin, and Douglas G. Altman. "Statistics notes measurement error." *Bmj* 312, no. 7047 (1996): 1654.
- [155] Han, Zhiyi, and Simone Hochgreb. "The response of stratified swirling flames to acoustic forcing: Experiments and comparison to model." *Proceedings of the Combustion Institute* 35, no. 3 (2015): 3309-3315.
- [156] GmbH, L. (2019). LaVision. [online] [Lavision.de](https://www.lavision.de/en/). Available at: <https://www.lavision.de/en/> [Accessed 9 Oct. 2019].
- [157] Luque, J, Crosley, D. LIFBASE (version 2.1.1). SRI report No. MP 99-009. SRI International; 1999. Available from: <https://www.sri.com/engage/products-solutions/lifbase>
- [158] Runyon, J. O. N. "Gas turbine fuel flexibility: pressurized swirl flame stability, thermoacoustics, and emissions." PhD diss., Cardiff University, 2017.
- [159] Emadi, Majid, Douglas Karkow, Taleb Salameh, Ameet Gohil, and Albert Ratner. "Flame structure changes resulting from hydrogen-enrichment and pressurization for low-swirl premixed methane-air flames." *international journal of hydrogen energy* 37, no. 13 (2012): 10397-10404.
- [160] Kuo, Kenneth Kuan-yun, and Ragini Acharya. *Fundamentals of turbulent and multiphase combustion*. John Wiley & Sons, 2012.
- [161] O'Neill, Philippa L., David Nicolaidis, D. Honnery, and Julio Soria. "Autocorrelation functions and the determination of integral length with reference to experimental and numerical data." In 15th Australasian fluid mechanics conference, vol. 1, pp. 1-4. Sydney, NSW, Australia: Univ. of Sydney, 2004.
- [162] Kim, Tae Young, Young Hoo Kim, Yeong Jong Ahn, Sun Choi, and Oh Chae Kwon. "Combustion stability of inverse oxygen/hydrogen coaxial jet flames at high pressure." *Energy* 180 (2019): 121-132.
- [163] [Janaf.nist.gov](https://janaf.nist.gov/tables/O-029.html). (2019). [online] Available at: <https://janaf.nist.gov/tables/O-029.html> [Accessed 30 Jun. 2019].
- [164] Wojcik, Adam, Hugh Middleton, and Ioannis Damopoulos. "Ammonia as a fuel in solid oxide fuel cells." *Journal of Power Sources*, 118 (2003), pp. 342-348.
- [165] Großmann, Katharina, Peter Treiber, and Jürgen Karl. "Steam methane reforming at low S/C ratios for power-to-gas applications." *International Journal of Hydrogen Energy* 41, no. 40 (2016):

17784-17792.

- [166] Fawwaz Alrebei, Odi, Ali Al-Doboan, Philip Bowen, and Agustin Valera Medina. "CO₂-Argon-Steam Oxy-Fuel Production for (CARSOXY) Gas Turbines." *Energies* 12, no. 18 (2019): 3580.
- [167] Smallbusiness.chron.com. (2019). What Does Working Capital as a Percent of Sales Tell You?. [online] Available at: <https://smallbusiness.chron.com/working-capital-percent-sales-tell-you-71681.html> [Accessed 6 Jul. 2019].
- [168] Investopedia. (2019). General And Administrative Expense (G&A). [online] Available at: <https://www.investopedia.com/terms/g/general-and-administrative-expenses.asp> [Accessed 6 Jul. 2019].
- [169] Smallbusiness.chron.com. (2019). The Employee Labor Percentage. [online] Available at: <https://smallbusiness.chron.com/calculate-employee-labor-percentage-15980.html> [Accessed 6 Jul. 2019].
- [170] Worldcat.org. (2019). A dictionary of business and management (eBook, 2009) [WorldCat.org]. [online] Available at: <https://www.worldcat.org/title/dictionary-of-business-and-management/oclc/317550872> [Accessed 6 Jul. 2019].
- [171] Catalogue.pearsoned.co.uk. (2019). Pearson - Corporate Financial Management, 5/E - Glen Arnold. [online] Available at: <http://catalogue.pearsoned.co.uk/educator/product/Corporate-Financial-Management/9780273758839.page> [Accessed 6 Jul. 2019].
- [172] Investopedia. (2019). How Your Tax Rate Really Works. [online] Available at: <https://www.investopedia.com/terms/t/taxrate.asp> [Accessed 6 Jul. 2019].
- [173] Bragg, S. and Bragg, S. (2019). Economic life. [online] AccountingTools. Available at: <https://www.accountingtools.com/articles/2017/5/6/economic-life> [Accessed 6 Jul. 2019].
- [174] Db0nus869y26v.cloudfront.net. (2019). [online] Available at: https://db0nus869y26v.cloudfront.net/en/Cost_escalation [Accessed 6 Jul. 2019].
- [175] En.wikipedia.org. (2019). Modified internal rate of return. [online] Available at: <https://en.wikipedia.org/wiki/MIRR> [Accessed 6 Jul. 2019].
- [176] Iotafinance.com. (2019). annuity factor method (AFM) (Financial definition). [online] Available at: <https://www.iotafinance.com/en/Financial-Definition-annuity-factor-method-AFM.html> [Accessed 6 Jul. 2019].
- [177] Investopedia. (2019). Revenue. [online] Available at: <https://www.investopedia.com/terms/r/revenue.asp> [Accessed 6 Jul. 2019].
- [178] Collinsdictionary.com. (2019). Depreciation expense definition and meaning | Collins English Dictionary. [online] Available at: <https://www.collinsdictionary.com/us/dictionary/english/depreciation-expense> [Accessed 6 Jul. 2019].
- [179] To Toqan, M. A., J. M. Beer, P. Jansohn, N. Sun, A. Testa, A. Shihadeh, and J. D. Teare. "Low NO_x emission from radially stratified natural gas-air turbulent diffusion flames." In *Symposium (International) on Combustion*, vol. 24, no. 1, pp. 1391-1397. Elsevier, 1992.
- [180] Yu, Byeonghun, Sung-Min Kum, Chang-Eon Lee, and Seungro Lee. "An experimental study of heat transfer and pollutant emission characteristics at varying distances between the burner and the heat exchanger in a compact combustion system." *Energy* 42, no. 1 (2012): 350-357.

- [181] Ward, George D., and Charles E. Ward. "Insitu wet combustion process for recovery of heavy oils." U.S. Patent 4,691,773, issued September 8, 1987.
- [182] Visaton.de. (2019). WS 17 E - 8 Ohm | Visaton. [online] Available at: <http://www.visaton.de/en/products/woofers/ws-17-e-8-ohm> [Accessed 10 Jun. 2019].
- [183] Peters, N. "Laminar Flamelet Concepts in Turbulent Combustion, 21st." In International Symposium on Combustion, The Combustion Institute, Pittsburgh. 1986.
- [184] Borghi, Roland. "Turbulent combustion modelling." *Progress in energy and combustion science* 14, no. 4 (1988): 245-292.
- [185] Hebbar, G. S. (2014). NOx from diesel engine emission and control strategies-a review. *International Journal of Mechanical Engineering and Robotics Research*, 3(4), 471.
- [186] Evulet, A. T., ELKady, A. M., Branda, A. R., & Chinn, D. (2009). On the performance and operability of GE's dry low NOx combustors utilizing exhaust gas recirculation for postcombustion carbon capture. *Energy Procedia*, 1(1), 3809-3816.
- [187] AHowell, A. R., & Calvert, W. J. (1978). A new stage stacking technique for axial-flow compressor performance prediction.
- [188] Takizuka, T., Takada, S., Yan, X., Kosugiyama, S., Katanishi, S., & Kunitomi, K. (2004). R&D on the power conversion system for gas turbine high temperature reactors. *Nuclear Engineering and Design*, 233(1-3), 329-346.
- [189] Weisbrodt, I. A. (1996). Summary report on technical experiences from high-temperature helium turbomachinery testing in Germany (No. IAEA-TECDOC--899).
- [190] Nayagam, V., Haggard Jr, J. B., Colantonio, R. O., Marchese, A. J., Dryer, F. L., Zhang, B. L., & Williams, F. A. (1998). Microgravity n-heptane droplet combustion in oxygen-helium mixtures at atmospheric pressure. *AIAA journal*, 36(8), 1369-1378.
- [191] Al-Doboan, A. (2019). A novel blend, CARSOXY, as a working fluid for advanced gas turbine cycles (Doctoral dissertation, Cardiff Univeristy).
- [192] Çelikten, İ., Mutlu, E., & Solmaz, H. (2012). Variation of performance and emission characteristics of a diesel engine fueled with diesel, rapeseed oil and hazelnut oil methyl ester blends. *Renewable Energy*, 48, 122-126.
- [193] AKoc, A. B., & Abdullah, M. (2013). Performance and NOx emissions of a diesel engine fueled with biodiesel-diesel-water nanoemulsions. *Fuel Processing Technology*, 109, 70-77.
- [194] Bellows, B. D., Bobba, M. K., Forte, A., Seitzman, J. M., & Lieuwen, T. (2007). Flame transfer function saturation mechanisms in a swirl-stabilized combustor. *Proceedings of the combustion institute*, 31(2), 3181-3188.
- [195] Kim, D., Lee, J. G., Quay, B. D., Santavicca, D. A., Kim, K., & Srinivasan, S. (2010). Effect of flame structure on the flame transfer function in a premixed gas turbine combustor. *Journal of Engineering for Gas Turbines and Power*, 132(2).
- [196] Hirsch, C., Fanaca, D., Reddy, P., Polifke, W., & Sattelmayer, T. (2005, January). Influence of the swirler design on the flame transfer function of premixed flames. In *ASME Turbo Expo 2005: Power for Land, Sea, and Air* (pp. 151-160). American Society of Mechanical Engineers Digital Collection.
- [197] Wilson, T. L., Campbell, G. A., & Mutharasan, R. (2007). Viscosity and density values from

excitation level response of piezoelectric-excited cantilever sensors. *Sensors and Actuators A: Physical*, 138(1), 44-51.

- [198] <https://www.boconline.co.uk/en/index.html>
- [199] Beseler, K., Tyagi, A., & O'Connor, J. A. (2020). Development of a Diagnostic Damkohler Number for Interpreting Laser-Induced Fluorescence Data in Turbulent Flames. In *AIAA Scitech 2020 Forum* (p. 2278).
- [200] Chakraborty, N., Alwazzan, D., Klein, M., & Cant, R. S. (2019). On the validity of Damköhler's first hypothesis in turbulent Bunsen burner flames: A computational analysis. *Proceedings of the Combustion Institute*, 37(2), 2231-2239.
- [201] Li, J., Tang, A., Cai, T., & Zhou, C. (2020). Effect of dimethyl ether addition on flame stability of premixed methane/air in a micro-planar quartz combustor. *Chemical Engineering and Processing-Process Intensification*, 147, 107740.
- [202] Cai, T., Tang, A., Zhao, D., Zhou, C., & Huang, Q. (2020). Flame dynamics and stability of premixed methane/air in micro-planar quartz combustors. *Energy*, 193, 116767.
- [203] Liang, Z. H., Rongwong, W., Liu, H., Fu, K., Gao, H., Cao, F., ... & Nath, D. (2015). Recent progress and new developments in post-combustion carbon-capture technology with amine based solvents. *International Journal of Greenhouse Gas Control*, 40, 26-54.
- [204] Hadjipaschalis, I., Kourtis, G., & Poullikkas, A. (2009). Assessment of oxyfuel power generation technologies. *Renewable and Sustainable Energy Reviews*, 13(9), 2637-2644.

APPENDIX 3

Appendix 3.1 Cycle analyses MATLAB codes

This appendix provides MATLAB codes corresponding to the cycles which have been discussed previously for the parametric study. These codes are ready to run, where the default parameter to be estimated is set to be the cycle efficiency with respect to compressor pressure ratio and compressor inlet stagnation temperature. This can be adjusted by setting the "A_1(ii, II) =" term to be equal to any required parameter in the code.

Appendix 3.1.1 Simple Cycle

```

%% Simple cycle
clear all
VV=[3:1:4];
QQ=[287:1:288];
%source store

for ii=1:length(VV)
    for II=1:length(QQ)
        %% Input values
        poci=VV(ii)
        %compressor pressure_ratio
        toci=QQ(II)
        %compressor inlet temperature[k]
        poci=1.04
        %compressor inlet pressure[bar]
        toti=1100
        %turbine inlet temperature[k]
        nc=0.85
        %Isentropic efficiency_of_the_compressor
        nt=0.87
        %Isentropic efficiency_of_the_turbine
        nm=0.99
        %mechanical_efficiency
        f=0.0096
        %fuel_to_air_ratio
        vc=1.4
        %gamma_compression
        cpc=1.005
        %Cp_compression [kJ/kg K]
        vt=1.333
        %gamma_expansion

        cpt=1.148
        %Cp_expansion [kJ/kg K]
        deltapb_poco=0.02
        %combustion pressure losses
        deltapbc_poco=0.003 %cold-side pressure losses
        in heat exchanger(%)
        deltapbh=0.04
        %hot-side pressure losses
        in heat exchanger[bar]
        Patm=1.04
        %ambient pressure[bar]
        qnetp=43100
        %feul heat
        %%%compression stage%%
        %note:(compressor_outlet_temperature)[k]
        toco=((toci/nc)*((poco_poci)^((vc-1)/vc))-1)+toci;
        %note:(wtc=work required from the turbine to run the compressor per unit of mass)[kJ/kg]
        wtc=(cpc/nm)*(toco-toci);
        %note:(poco=compressor_outlet_pressure)[bar]
        poco=(poco_poci)*poci;
        %note:(poti=turbine_inlet_pressure)[bar]
        poti=poco*(1-(deltapb_poco));
        %note:(poto=turbine_outlet_pressure)[bar]
        poto=Patm;

        %note:(poti_poto=turbine_outlet_pressure)[bar]
        poti_poto=poti/poto;

        %note:(toto=turbine_outlet_temperature)[k]
        toto=toti-((toti*nt)*(1-(poto/poti)^((vt-1)/vt)));
        %note:wt=Turbine work per unit of mass[kJ/kg]
        wt=cpt*(toti-toto);
        %note:sfc=Specific fuel consumption[kJ/kW]
        sfc=(3600*f)/(wt-twc);
        %note:n=Cycle efficiency;
        n=3600/(sfc*qnetp);
        A_1(ii, II)=n;
    end
end
Qmat=ones(length(VV),1)*QQ;
Vmat=VV'*ones(1,length(QQ));
surfc(Vmat,Qmat,A_1)
xlabel('poco_poci') %VV ii
ylabel('Cycle efficiency') %QQ II
zlabel('toci')

%
AA(ii,iii)=Twstar;
% end
% end

%2 dimensional plot
figure
plot(VV,A_1(:,2))

```

Appendix 3.1.2 Heat exchanged gas turbine cycle

```

%%%%%%%% Heat
exchanged simple
cycle %%%%%%%%%%
clc
clear all
VV=[3:1:4];
QQ=[287:1:288];
%source store

for ii=1:length(VV)

    for
    II=1:length(QQ)

%% Input values
poco_poci=VV(ii)
%compressor_pressur
e_ratio
toci=QQ(II)
%compressor_inlet_p
ressure[bar]
poci=1.04
%compressor_inlet_t
emperatur[k]
toti=1100
%turbine_inlet_temp
erature[k]
nc=0.85
%Isentropic_efficie
ncy_of_the_compress
or
nt=0.87
%Isentropic_efficie
ncy_of_the_turbine
nm=0.99
%mechanical_efficie
ncy
f=0.0096
%fuel_to_air_ratio
vc=1.4
%gamma_compression
cpc=1.005
%Cp_compression[
kJ/kg K]
vt=1.333
%gamma_expansion
cpt=1.148
%Cp_expansion[
kJ/kg K]
deltapb_poco=0.02
%combustion
pressure losses
deltaphc_poco=0.03
%cold-side pressure
losses in heat
exchanger(%)
deltaphh=0.04
%hot-side pressure
losses in heat
exchanger[bar]
Patm=1.04
%ambient
pressure[bar]
qnetp=43100
%feul heat
%%%%%%%%compression
stage%%%%%%%%%
%note:(compressor_o
utlet_temperatur)[k
]
toco=((toci/nc)*(((
poco_poci)^((vc-
1)/vc))-1))+toci;
%note:(wtc=work
required from the
turbine to run the
compressor per unit
of
%mass)[kJ/kg]
wtc=(cpc/nm)*(toco-
toci);
%note:(poco=compres
sor_outlet_pressur
e)[bar]
poco=(poco_poci)*po
ci;
%note:(poti=turbine
_inlet_pressure)[ba
r]
poti=poco*(1-
(deltapb_poco)-
(deltaphc_poco));
%note:(poto=turbine
_outlet_pressure)[b
ar]
poto=Patm+deltaphh;
%note:(poti_poto=tu
rbine_outlet_pressu
re)[bar]
poti_poto=poti/poto
;
%note:(toto=turbine
_outlet_temperature
)[k]
toto=toti-
((toti*nt)*((1-
(poto/poti)^(vt-
1)/vt)))));

%note:wt=Turbine
work per unit of
mass[kj/kg]
wt=cpt*(toto-toti);
%note:sfc=Specific
fuel
consumption[kg/kW]
sfc=(3600*f)/(wt-
wtc);
%note:n=Cycle
efficiency;
n=3600/(sfc*qnetp);
A_1(ii,II)=toti-
toto;
        end
    end
    Qmat=ones(length(VV
),1)*QQ;
    Vmat=VV'*ones(1,len
gth(QQ));
    surfc(Vmat,Qmat,A_1
)
    xlabel('poco_poci')
    %VV ii
    ylabel('n')%QQ II
    zlabel('toto')

    % AA(ii,iii)=n;
    % end
    % end

%2 dimensional plot
figure
plot(VV,A_1(:,2))

```

Appendix 3.1.3 Simple cycle and free turbine arrangement code

```

##### Simple cycle&
free turbine
#####
clc
clear all
VV=[11:1:12];
QQ=[287:1:288];
%source store

for ii=1:length(VV)

    for
    II=1:length(QQ)

%% Input values
poco_poci=VV(ii)
%compressor_pressure_
ratio
toci=QQ(II)
%compressor_inlet_pre
ssure[bar]
poci=1.04
%compressor_inlet_tem
peratur[k]
toti=1350
%turbine_inlet_temper
ature[k]
nc=0.86
%Isentropic_efficienc
y_of_the_compressor
nt=0.89
%Isentropic_efficienc
y_of_the_turbine
nm=0.99
%mechanical_efficienc
y
nft=0.89
%free turbine
efficiency
f=0.0204
%fuel_to_air_ratio
vc=1.4
%gamma_compression
cpc=1.005
%Cp_compression[
kJ/kg K]
vt=1.333
%gamma_expansion
cpt=1.148
%Cp_expansion[ kJ/kg
K]
vft=1.333
%gamma_expansion_free
_turbine
cpft=1.148
%Cp_expansion_free_tu
rbine[ kJ/kg K]
deltapb_poco=0.06
%combustion pressure
losses
deltaphc_poco=0.003
%cold-side pressure
losses in heat
exchanger(%)
deltaphh=0.04
%hot-side pressure
losses in heat
exchanger[bar]
deltapexh=00
%exhust pressure
losses
Patm=1.04
%ambient
pressure[bar]
qnetp=43100
%feul heat
#####compression
stage#####
%note:(compressor_out
let_temperatur)[k]
toco=((toci/nc)*((po
co_poci)^( (vc-
1)/vc))-1))+toci;
%note:(wtc=work
required from the
turbine to run the
compressor per unit
of
%mass) [kJ/kg]
wtc=(cpc/nm)*(toco-
toci);
%note:(poco=compresso
r_outlet_pressure)[ba
r]
poco=(poco_poci)*poci
;
%note:(poti=turbine_i
nlet_pressure)[bar]
poti=poco*(1-
(deltapb_poco));
%note:(toto=turbine_o
utlet_temperatur)[k]
toto=toti-(wtc/cpt);
%note:(tofti=free_tur
bine_inlet_temperatur
)[k]
tofti=toto;
%note:(poti_poto=turb
ine_pressure_ratio)
poto_poti=(1-((toti-
toto)/(toti*nt)))^(vt
/(vt-1));
%note:(poto=turbine_o
utlet_pressure)[bar]
poto=poto_poti*poti;
%note:(pofti=freeturb
ine_intlet_pressure)[
bar]
pofti=poto;
%note:(pofto=freeturb
ine_outlet_pressure)[
bar]
pofto=Patm+deltapexh;
%note:(tofto=free_tur
bine_outlet_temperatu
r)[k]
tofto=tofti-
((tofti*nft)*(1-
(pofto/pofti)^( (vft-
1)/vft)));
%note:(wft=Specific
output work or free
turbine specific
work)[kJ/kg]
wft=cpft*(tofti-
tofto);
%note:(sfc=SSpecific
fuel
consumption[kg/kW]
sfc=3600*f/wft;
%note:n=Cycle
efficiency
n=3600/(sfc*qnetp);
A_1(ii,II)=n;
end
Qmat=ones(length(VV),
1)*QQ;
Vmat=VV'*ones(1, lengt
h(QQ));
surfc(Vmat,Qmat,A_1)
xlabel('poco_poci')
%VV ii
ylabel('toci')%QQ II
zlabel('sfs')

% AA(ii,iii)=n;
% end
% end

%2 dimensional plot
figure
plot(VV,A_1(:,2))

```

Appendix 3.1.4 Evaporation cycle code

```

%%%%%%%%%%%%%%%%%%%%%%%%%%%%%%%%%%%%%%%%%%%%%%%%%%%%%%%%%%%%%%%%%%%%%%%%
Evaporation cycle
%%%%%%%%%%%%%%%%%%%%%%%%%%%%%%%%%%%%%%%%%%%%%%%%%%%%%%%%%%%%%%%%%%%%%%%%
clc
clear all
VV=[3:1:4];
QQ=[287:1:288];
%source store

for
ii=1:length(VV)

    for
II=1:length(QQ)

%% Input values
poco_poci=VV(ii)
%compressor_pressure_ratio
toci=QQ(II)
%compressor_inlet_pressure[bar]
poci=1.04
%compressor_inlet_temperature[k]
toti=1100
%turbine_inlet_temperature[k]
nc=0.85
%Isentropic_efficiency_of_the_compressor
nt=0.87
%Isentropic_efficiency_of_the_turbine
nm=0.99
%mechanical_efficiency
f=0.0096
%fuel_to_air_ratio
vc=1.4
%gamma_compression
cpc=1.005
%Cp_compression[kJ/kg K]
vt=1.333
%gamma_expansion

cpt=1.148
%Cp_expansion[kJ/kg K]

deltapb_poco=0.02
%combustion
pressure_losses
deltaphc_poco=0.03
%cold-side
pressure_losses
in heat
exchanger(%)
deltaphh=0.04
%hot-side
pressure_losses
in heat
exchanger[bar]
deltapev_poco=0.03
%evaporator
pressure_losses
(%)
Patm=1.04
%ambient
pressure[bar]
qnetp=43100
%feul heat
%%%%%%%%%%%%%%%%%%%%%%%%%%%%%%%%%%%%%%%%%%%%%%%%%%%%%%%%%%%%%%%%%%%%%%%%
%note:(compressor_outlet_temperature)[k]
toco=((toci/nc)*((poco_poci)^((vc-1)/vc))-1)+toci;
%note:(wtc=work required from the turbine to run the compressor per unit of %mass) [kJ/kg]
wtc=(cpc/nm)*(toco-toci);
%note:(poco=compressor_outlet_pressure)[bar]
poco=(poco_poci)*poci;
%note:(poti=turbine_inlet_pressure)[bar]
poti=poco*(1-(deltapb_poco)-

(deltaphc_poco)-(deltapev_poco));
%note:(poto=turbine_outlet_pressure)[bar]
poto=Patm+deltaphh;
%note:(poti_poto=turbine_outlet_pressure)[bar]
poti_poto=poti/poto;
%note:(toto=turbine_outlet_temperature)[k]
toto=toti-((toti*nt)*((poto/poti)^((vt-1)/vt))-1));

wt=cpt*(toto-toti);
sfc=(3600*f)/(wt-wtc);
%
n=3600/(sfc*qnetp);
A_1(ii,II)=n;
    end
end
Qmat=ones(length(VV),1)*QQ;
Vmat=VV'*ones(1,length(QQ));
surfc(Vmat,Qmat,A_1)
xlabel('poco_poci') %VV ii
ylabel('n') %QQ II
zlabel('toto')

%
AA(ii,iii)=Twstar;
% end
% end

%2 dimensional
plot
figure
    plot(VV,
        A_1(:,2)

```

Appendix 3.1.5 humidified gas turbine cycle code

```

clc
clear all
VV=[3:1:4];
QQ=[287:1:288];
%source store

for ii=1:length(VV)

    for
        II=1:length(QQ)

            %% Input values
            poco_poci=VV(ii)
            %compressor_pressure_ratio
            toci=QQ(II)
            %compressor_inlet_pressure[bar]
            poci=1.04
            %compressor_inlet_temperature[k]
            toti=1100
            %turbine_inlet_temperature[k]
            nc=0.85
            %Isentropic_efficiency_of_the_compressor
            nt=0.87
            %Isentropic_efficiency_of_the_turbine
            nm=0.99
            %mechanical_efficiency
            f=0.0096
            %fuel_to_air_ratio
            vc_carsoxy=000
            %gamma_compression
            cpc_carsoxy=0000
            %Cp_compression[kJ/kg K]
            vt_carsoxy=0000
            %gamma_expansion
            cpt_carsoxy=0000
            %Cp_expansion[kJ/kg K]
            deltapb_poco=0.02
            %combustion pressure losses
            deltaphc1_poco=0.03
            %cold-side pressure losses of the after cooler(%)
            deltaphc2_poco=0.03
            %cold-side pressure losses
            recuperator(%)
            deltaphh2=0.04
            %hot-side pressure losses after
            recuperator(%)
            deltaphh3=0.04
            %pressure losses in economizer[bar]
            deltaphu=0.04
            %pressure losses due to the humidification
            deltapcond=0.04
            %pressure losses due to the condenser
            Patm=1.04
            %ambient pressure[bar]
            qnetp=43100
            %feul heat
            %compression stage
            %note:(compressor_outlet_temperature)[k]
            toco=((toc/nc)*(((poco_poci)^(vc_carsoxy-1)/vc_carsoxy))-1)+toci;
            %note:(wtc=work required from the turbine to run the compressor per unit of mass) [kJ/kg]
            wtc=(cpc_carsoxy/nm)*(toco-toci);
            %note:(poco=compressor_outlet_pressure) [bar]
            poco=(poco_poci)*poci;
            %note:(poti=turbine_inlet_pressure) [bar]
            poti=poco*(1-(deltapb_poco)-(deltaphc1_poco)-(deltaphc2_poco)-(deltaphu/poco));
            %note:(poto=turbine_outlet_pressure) [bar]
            poto=Patm+deltaphh2+deltaphh3+deltaphu;
            %note:(poti_poto=turbine_outlet_pressure) [bar]
            poti_poto=poti/poto;
            %note:(toto=turbine_outlet_temperature) [k]
            toto=toti-(((toti*nt)*(1-((poto/poti)^(vt_carsoxy-1)/vt_carsoxy)))));
            %note:wt=Turbine work per unit of mass[kJ/kg]
            wt=cpt_carsoxy*(toti-toto);
            %note:sfc=Specific fuel consumption[kg/kW]
            sfc=(3600*f)/(wt-wtc);
            %note:n=Cycle efficiency;
            n=3600/(sfc*qnetp);
            A_1(ii,II)=n;
        end
    end
    Qmat=ones(length(VV),1)*QQ;
    Vmat=VV'*ones(1,length(QQ));
    surfc(Vmat,Qmat,A_1)
    xlabel('poco_poci')
    %VV ii
    ylabel('n')%QQ II
    zlabel('toto')

    %
    AA(ii,iii)=Twstar;
    % end
    % end

    %2 dimensional plot figure
    plot(VV,A_1(:,2))

```

Appendix 3.2.1 Image procession (background correction, averaging and fluctuation)

This appendix provides the MATLAB code which performs background correction, averaging and plots the heat release fluctuation. The code is ready to run. It plots regional and integral fluctuations. The reader is instructed to follow the comments in the code.

```

%%% define
background, dataset
and timestep
bgrname =
'rawData_carsoxy_cy
l_1lpermmrthane_bac
kground';
dataset =
'rawData_carsoxy_cy
l_1p5lpermmrthane_1
60l_min_nonexited';
timestep = 1; %
time step in
seconds

%%% define region
in image
region = [0 10 60
45]; % coordinate
format [X1 Y1 X2
Y2] in defined unit
unit = 'phys'; %
'phys' specifies
coordinates in
physical units
%
'mesh' specifies
coordinates in mesh
units

%%% load background
and average
load(bgrname); %
load saved
background dataset
bgr = v; % assign
dataset to variable
bgr
bgrMean =
averf(bgr); %
average background
dataset
bgrCrop =
extractf(v, region,
unit); % extract
region of interest

bgrCropMean =
averf(bgrCrop); %
average background
of region
clear v;

%%% load dataset
load(dataset);
vCrop = extractf(v,
region, unit); %
extract region of
interest

%%% substract
background
vsubbgr = operf('-
',v,bgrMean); % of
whole image
vCropsubbgr =
operf('-
',vCrop,bgrCropMean
); % of region

%%% calculate mean
image
vsubmean =
averf(vsubbgr); %
of whole image
vCropsubmean =
averf(vCropsubbgr);
% of region

%%% calculate
OH*/OH integral and
plotting
% x values for plot

timescale =
(1:length(vsubbgr))
*timestep;

% integral of the
region image
totalSamples =
length(vsubbgr);

for i =
1:totalSamples % of
whole image
integralWI(i) =
sum(sum(vsubbgr(i).
w))/sum(sum(vsubmea
n.w));
end

for i =
1:totalSamples % of
region
integralCropWI(i) =
sum(sum(vCropsubbgr
(i).w))/sum(sum(vCr
opsubmean.w));
end

% plot whole image
figure;
averf(vsubbgr);
title('Whole Image
Subtracted
Background')

figure;
scatter(timescale,
integralWI);
title('Whole')
xlabel('Time')
ylabel('OH*/OH')
axis tight

% plot region image
figure;
averf(vCropsubbgr);
title('Region Image
Subtracted
Background')

figure;
scatter(timescale,
integralCropWI);
title('Region')
xlabel('Time')
ylabel('OH*/OH')
axis tigh

```

Appendix 3.2.2 Abel deconvolution code

This appendix provides the MATLAB code which specially resolves the captured chemiluminescence images of the flame.[150]

```

Image='rawData_85ga
in_300img_40LpermA
r_1LpermMethane_une
xited';
R=344/30.5325466990
471;
CentXPix=260;
WhichWay=1;
function [ImAbel] =
HalfAbel(Image, R,
CentXPix, WhichWay)
[i j] = size
(Image);
n = (j/2) + 1;
if WhichWay == 1
NewEdge = (2*(j-
CentXPix));
%Initialize output
image matrix
ImAbel = zeros(i,
NewEdge);
k = (NewEdge/2) -
1;
%For loop cycles
through each row of
the input image
for z = 1:i
%Extract single
image row
A = Image(z,
CentXPix:j);
%Convert image row
to double precision
A2 = im2double(A,
'indexed');
%Calls the Abel
inversion function
one row at a time
with an
%input of 5 cosinus
expansions in the
Fourier-series-like
%expansion
[f_rec , X] =
abel_inversion(A2,R
,5);
%Add the Abel
deconvoluted row to
the output matrix
ImAbel(z,
(NewEdge/2):NewEdge
) = f_rec(:,1);
%Rotate the Abel
deconvoluted row
about the central
axis
f_rec =
flipud(f_rec);
ImAbel(z, 1:k) =
f_rec(2:(NewEdge/2)
,1);
end
end
if WhichWay == 2
NewEdge =
(2*CentXPix);
ImAbel = zeros(i,
NewEdge);
k = (NewEdge/2) -
1;
%For loop cycles
through each row in
the input image
for z = 1:i
%Extract single
image row
A = Image(z,
1:(CentXPix+1));
A = fliplr(A);
%Convert image row
to double precision
A2 = im2double(A,
'indexed');
%Calls the Abel
inversion function
one row at a time
with an input
%of 5 cosinus
expansions in the
Fourier-series-like
expansion
[f_rec , X] =
abel_inversion(A2,R
,5);
%Add the Abel
deconvoluted row to
the output matrix
ImAbel(z,
(NewEdge/2):NewEdge
) = f_rec(:,1);
%Rotate the Abel
deconvoluted row
about the central
axis
f_rec =
flipud(f_rec);
ImAbel(z, 1:k) =
f_rec(2:(NewEdge/2)
,1);
end
end
end

```

Appendix 3.3 PLIF image processing and analyses codes

Appendix 3.3.2 PLIF Laser energy shot-to-shot correction

This MATLAB code corrects for laser energy shot-to-shot variation. The reader is advised to read the instruction inside code (marked as comments, %)

```
function LASER_ENERGY_CORRECTION2(NumImages)
    %Inset number of images below
    NumImages=;
    %%%%%%%%%%%%%%%%%%%%%%%%%%%%%%%%%%%%%%%%%
    %%%%%%%%%%%%%%%%%%%%%%%%%%%%%%%%%%%%%%%%%
    %
    [listOfFiles, folder] = uigetfile('*.tif', 'Select your image', 'MultiSelect', 'on');
    fullFileName = fullfile(folder, listOfFiles{1});
    [I, cmap] = imread(fullFileName);
    [columns, rows] = size(I);
    %BASELINE_double = double(BASELINE);
    image3d = zeros(columns, rows, NumImages);
    if NumImages ~= length(listOfFiles)
        msg = 'Error Occured - Image Number Mismatch';
        error(msg);
    else
        for k = 1 : length(listOfFiles)
            fullFileName = fullfile(folder, listOfFiles{k});
            I2 = imread(fullFileName);
            I2_double = double(I2);
            %I2_NO_BG = I2_double - BASELINE_double;
            image3d(:,:,k) = I2_double;
            end
            %Inset the location of the '.txt' file of the normalized laser shot to shot recordings inside (cd').
            %Please note that this file must contain the laser energy for each captured image after being normalized to the maximum recorded laser energy.
            cd '';
            %%%%%%%%%%%%%%%%%%%%%%%%%%%%%%%%%%%%%%%%%
            %%%%%%%%%%%%%%%%%%%%%%%%%%%%%%%%%%%%%%%%%
            %%%%%%%%%%%%%%%%%%%%%%%%%%%%%%%%%%%%%%%%%
            %Please insert the name of the '.txt' file (i.e. load the_normalized_laser_shot_to_shot_recordings.txt)
            load .txt;
            %Please insert the name of the '.txt' file (i.e. A=textread('the_normalized_laser_shot_to_shot_recordings.txt'));
            A=textread('');
            %Please specify where would you like to save the corrected image inside (Cd')
            cd '';
            for k=1:length(listOfFiles)
                filename=sprintf('image%d.tif',k);
                filename1=image3d(:,:,k)./A(k);
                saveasstiff(filename1,filename);
            end
            end
            load chirp;
            end
            sound(y, Fs);
        end
    end
end
```

Appendix 3.3.3 PLIF Laser sheet profile correction [150]

This appendix provides the MATLAB code which performs background correction, averaging and corrects for laser energy shot-to-shot variation. The reader is advised to read the instruction inside code (marked as comments, %).

```
function [PLIF_AVGout,
PLIF_cmap] =
PLIF_AVG_SHEETNORM(NumImages,
PLIF_BG,Sheet_correction_reagon)
%NumImages=500
%PLIF_BG=I=imread('OH_PLIF_BG_CARSXY_ALL.tif')
% Open dialog box to prompt for .TIF OH PLIF file selection
[listOfFiles, folder] =
uigetfile (*.tif',
'Select your image',
'MultiSelect', 'on');
fullFileName =
fullfile(folder,
listOfFiles{1});
[I cmap] =
imread(fullFileName);
[rows columns] =
size(I);
PLIF_AVGout_zero =
zeros(rows,columns);
PLIF_Sheet_Norm_zero =
zeros(rows,columns);
PLIF_BG_double =
im2double(PLIF_BG);
%Error check if the number of selected images is equal
NumImages
if NumImages ~=
length(listOfFiles)
msg = 'Error Occured - Image Number Mismatch';
error(msg);
else
for
j=1:length(listOfFiles)
fullFileName =
fullfile(folder,
listOfFiles{j});
% Read in first instantaneous OH PLIF image
I2 =
imread(fullFileName);
% Convert the image to double precision
I2_double =
im2double(I2);

% Apply 3x3 pixel median filter to reduce noise
I2_double_filt =
medfilt2(I2_double,
'symmetric');
% Correct the instaneous OH PLIF image for the input background
% image
I2_double_NoBG =
I2_double_filt-
PLIF_BG_double;

% Apply laser sheet intensity distribution correction
for i = 1:columns
% Find the maximum OH PLIF intensity value in each column
[ColMax Loc] =
max(I2_double_NoBG(:,i))
;
% Convert the column pixel location to "mm" distance
LocMM = Loc/11.27;
LocNorm = LocMM / (LocMM /35.15);
GaussInten = 1*exp(-
((LocNorm-35.15)/21)^2);
% Normalize the maximum OH PLIF intensity value
IntenNorm =
ColMax/GaussInten;
PLIF_Sheet_Norm_zero(:,i) =
I2_double_NoBG(:,i);
PLIF_Sheet_Norm_zero(Loc, i) = IntenNorm;
% Apply the Gaussian normalization in upstream direction from % the maximum OH PLIF intensity location
for l = 1:1
if (Loc - l) == 0
break
end
LocNormL = 35.15-((Loc-
(Loc-1))*(1/11.27));
GaussIntenL = 1*exp(-
((LocNormL-
35.15)/21)^2);

IntenNormL =
I2_double_NoBG((Loc-1),
i)/GaussIntenL;
PLIF_Sheet_Norm_zero((Loc-1), i) = IntenNormL;
end
% Apply the Gaussian normalization in the downstream % direction from the maximum OH PLIF intensity location
for k = 1:1
if (Loc + k) > 520
break
end
LocNormK = 40+((Loc+k)-
Loc)*(1/11.27));
GaussIntenK = 1.1*exp(-
((LocNormK-40)/9.1)^2);
IntenNormK =
I2_double_NoBG((Loc+k),
i)/GaussIntenK;
PLIF_Sheet_Norm_zero((Loc+k), i) = IntenNormK;
end
end
PLIF_AVGout_zero
=PLIF_AVGout_zero +
PLIF_Sheet_Norm_zero;
end
end
%Calculate the temporal average OH PLIF image
Sheet_correction_reagon_double =
im2double(Sheet_correction_reagon)
PLIF_AVGout1
=PLIF_AVGout_zero ./
NumImages;
PLIF_AVGout=imdivide(PLIF_AVGout1,Sheet_correction_reagon_double)
%imdivide(PLIF_AVGout_zero,Sheet_correction_reagon_double);
%Output the .TIF file colormap for easier image plotting
PLIF_cmap = cmap;
end
```

Appendix 3.3.4 PLIF flame properties [150]

This appendix provides a MATLAB code to calculate a number of flame properties (i.e. flame area, the centre of the highest intensity, brush thickness at the highest heat intensity) of the output image from the MATLAB code provided in Appendix 3.3.3. The reader is advised to read the instruction inside code (marked as comments, %).

```
function [FlameMax,
FlameSurf, FlameThk,
FlameArea, I_PLIF_MAX_LOCS,
LFT_EDGE_LOCS,
RHT_EDGE_LOCS, ROW_FLM_THK]
= PLIF_FLAME_MAX(PLIF_AVG,
CenterLinePixel, PixScale,
ProgVar)
%PLIF_AVG=imread('image19.t
if');
%CenterLinePixel=366%%in
pixels
%PixScale=11.26667 %%in
pixels/mm.
%ProgVar=0.5 %%in (0-0.5)
[rows columns] =
size(PLIF_AVG);
X = 1:CenterLinePixel;
X = X.';
% Select half of the
average OH PLIF image to
evaluate
PLIF_AVG_Half =
imcrop(PLIF_AVG, [0 0
CenterLinePixel rows]);
% Find the maximum OH PLIF
intensity value in the
selected half image
I_PLIF_MAX_Crop =
max(PLIF_AVG_Half(:));
FlameMax = zeros(rows,
CenterLinePixel);
FlameSurf = zeros(rows,
CenterLinePixel);
I_PLIF_MAX_LOCS =
zeros(rows,1);
LFT_EDGE_LOCS =
zeros(rows,1);
RHT_EDGE_LOCS =
zeros(rows,1);
ROW_FLM_THK =
zeros(rows,1);
% Calculate the pixel area
(mm^2) from the input pixel
scale (pix/mm)
PixelArea = (1/PixScale)^2;
for k = 1:rows
% Find the maximum OH PLIF
intensity value in each row
[I_PLIF_MAX I_PLIF_MAX_LOC]
= max(PLIF_AVG_Half(k,:));
% If the maximum value is
less than 50% of the
overall image
% maximum PLIF intensity,
move to the next row
if
I_PLIF_MAX/I_PLIF_MAX_Crop
< 0.5
continue
end
FlameMax(k, I_PLIF_MAX_LOC)
= 1;
I_PLIF_MAX_LOCS(k) =
((CenterLinePixel/PixScale)
-
(I_PLIF_MAX_LOC/PixScale));
% Extract the entire row
distribution of OH PLIF
intensity values
I_PLIF_ROW =
PLIF_AVG_Half(k,:);
I_PLIF_ROW = I_PLIF_ROW.';
% Fit a 9th order
polynomial to the row OH
PLIF intensity
% distribution
[P,~,MU] =
polyfit(X,I_PLIF_ROW, 9);
F = polyval(P,X,[],MU);
% Calculate the 1st
derivative of the row OH
PLIF intensity distribution
Fx = gradient(F);
% Extract OH PLIF intensity
values from the left edge
of the row
% to the maximum location
Fx_LR =
flipud(Fx(1:I_PLIF_MAX_LOC-
1));
% Error checking
FX_LR_EMPCHK =
isempty(Fx_LR);
if FX_LR_EMPCHK == 1 ||
numel(Fx_LR) < 3
continue
end
% Find the locations of the
peaks in the 1st derivative
% distribution from the
left edge to the maximum
location
[Fx_LR_PK, Fx_LR_LOC] =
findpeaks(Fx_LR);
% If no peaks are found,
take 2nd derivative and
find Locations closest to 0
if numel(Fx_LR_LOC)==0
Fx2 = gradient(Fx);
[P2,~,MU2] = polyfit(X,Fx2,
9);
F2 = polyval(P2,X,[],MU2);
Fx2_LR =
flipud(Fx2(1:I_PLIF_MAX_LOC
-1));
Fx_LR_LOC =
find(abs(Fx2_LR-
0))==min(abs(Fx2_LR-0)));
end
% Calculate the left edge
location
LFT_EDGE_LOC =
(I_PLIF_MAX_LOC -
ceil(2*ProgVar*Fx_LR_LOC(1)
));
if LFT_EDGE_LOC < 0
continue
end
% Convert the left edge
location to mm
LFT_EDGE_LOCS(k) =
((CenterLinePixel/PixScale)
- (LFT_EDGE_LOC/PixScale));
% Extract OH PLIF intensity
values from the maximum
location to
% the right edge of the row
Fx_RL =
Fx((I_PLIF_MAX_LOC+1):Cente
rLinePixel);
% Error checking
FX_RL_EMPCHK =
isempty(Fx_RL);
if FX_RL_EMPCHK == 1 ||
numel(Fx_RL) < 3
continue
end
% Find the locations of the
peaks in the 1st derivative
% distribution from the
maximum location to the
right edge
[Fx_RL_PK, Fx_RL_LOC] =
findpeaks(-Fx_RL);
% If no peaks are found,
take 2nd derivative and
find
% Location closest to 0
if numel(Fx_RL_LOC)==0
Fx3 = gradient(Fx);
[P3,~,MU3] = polyfit(X,Fx3,
9);
F3 = polyval(P3,X,[],MU3);
Fx3_RL =
Fx3((I_PLIF_MAX_LOC+1):Cent
erLinePixel);
Fx_RL_LOC =
find(abs(Fx3_RL-
0))==min(abs(Fx3_RL-0)));
end
% Calculate the right edge
location
RHT_EDGE_LOC =
(I_PLIF_MAX_LOC +
ceil(2*ProgVar*Fx_RL_LOC(1)
));
if RHT_EDGE_LOC >
CenterLinePixel
continue
end
% Convert the right edge
location to mm
RHT_EDGE_LOCS(k) =
((CenterLinePixel/PixScale)
- (RHT_EDGE_LOC/PixScale));
% Binarizing the flame
surface from left to right
in the row
FlameSurf(k,LFT_EDGE_LOC:RH
T_EDGE_LOC) = 1;
% Calculating the
individual row flame
thickness (mm)
ROW_FLM_THK(k) =
0.5*(LFT_EDGE_LOCS(k)-
RHT_EDGE_LOCS(k));
end
% Calculate the mean flame
thickness (mm) from the row
thicknesses
FlameThk =
mean(nonzeros(ROW_FLM_THK))
;
% Calculate the mean flame
area (mm^2) from the binary
flame surface
FlameArea =
(bwarea(FlameSurf))/PixelAr
ea;
end
```

APPENDIX 4

Appendix 4.1 Efficiency results with respect to variable compressor inlet temperatures and compressor pressure ratio.

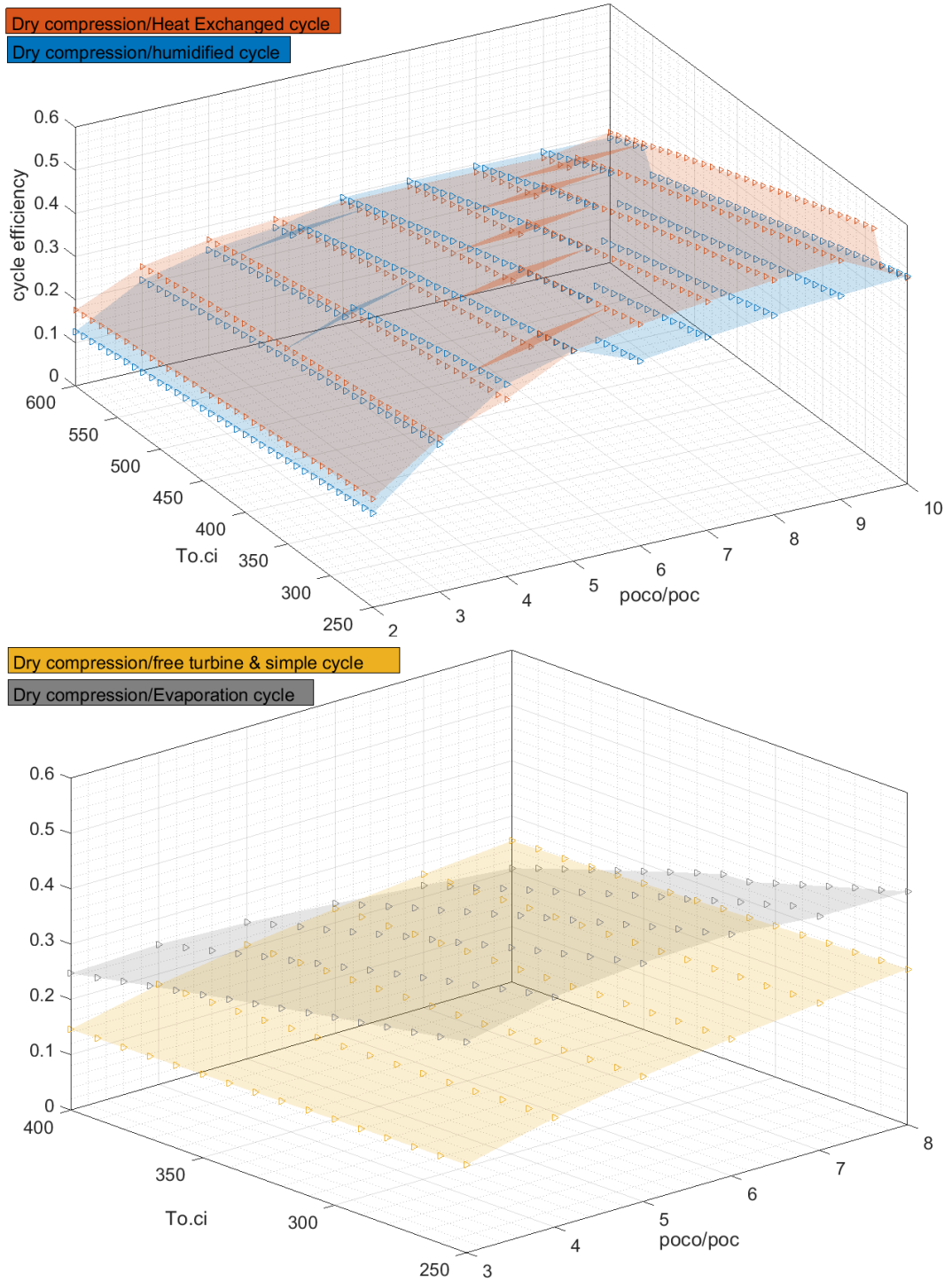


Figure AP4.1. Efficiency results for all cycles with dry compression.

Appendix 4.2 Efficiency results with respect to variable molar fractions of Argon, CO₂, and H₂O.

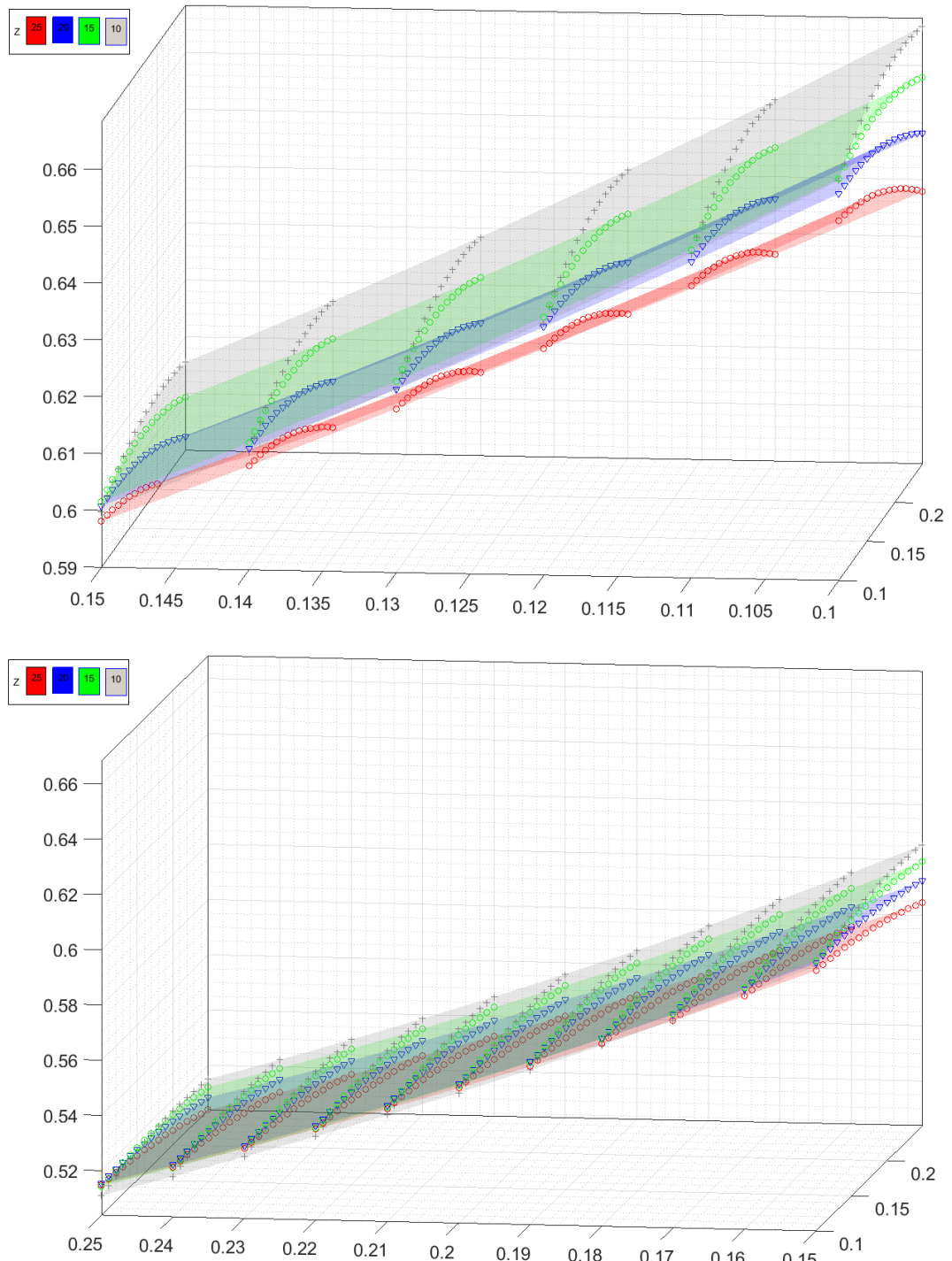


Figure AP 4.2. Efficiency results with respect to variable molar fractions of Argon, CO₂, and H₂O.

Appendix 4.3 Efficiency results for blend 58 and the new suggested blend

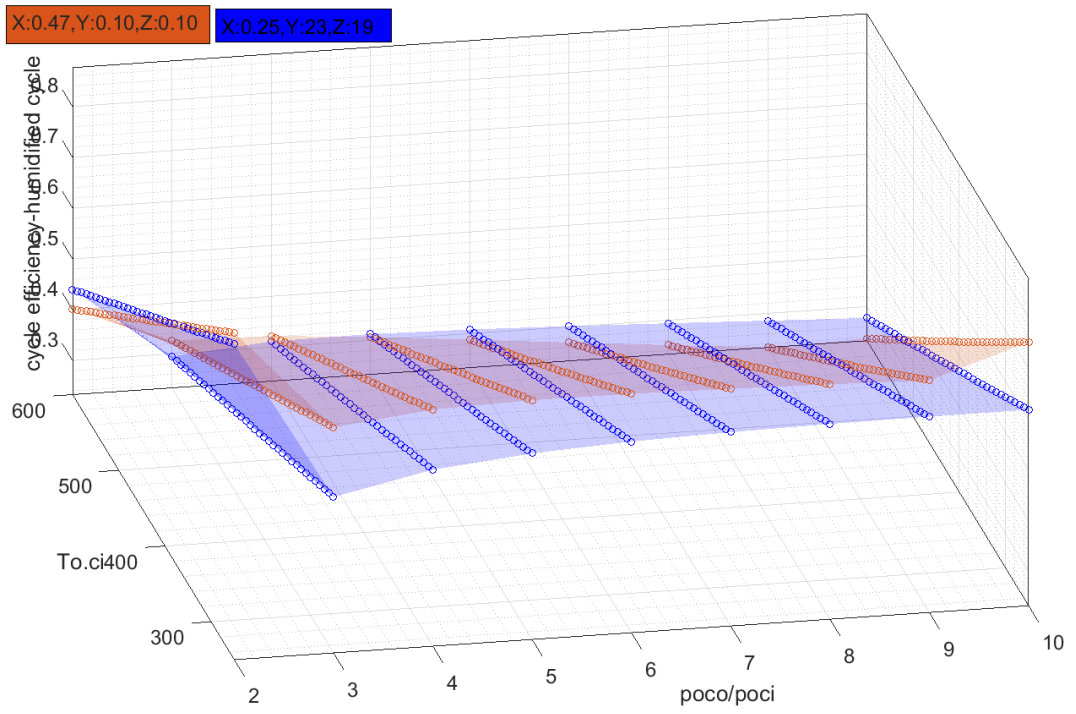


Figure AP 4.3. Efficiency results for blend 58 and the new suggested blend

Appendix 4.4 Efficiency results with respect to the turbine inlet temperature

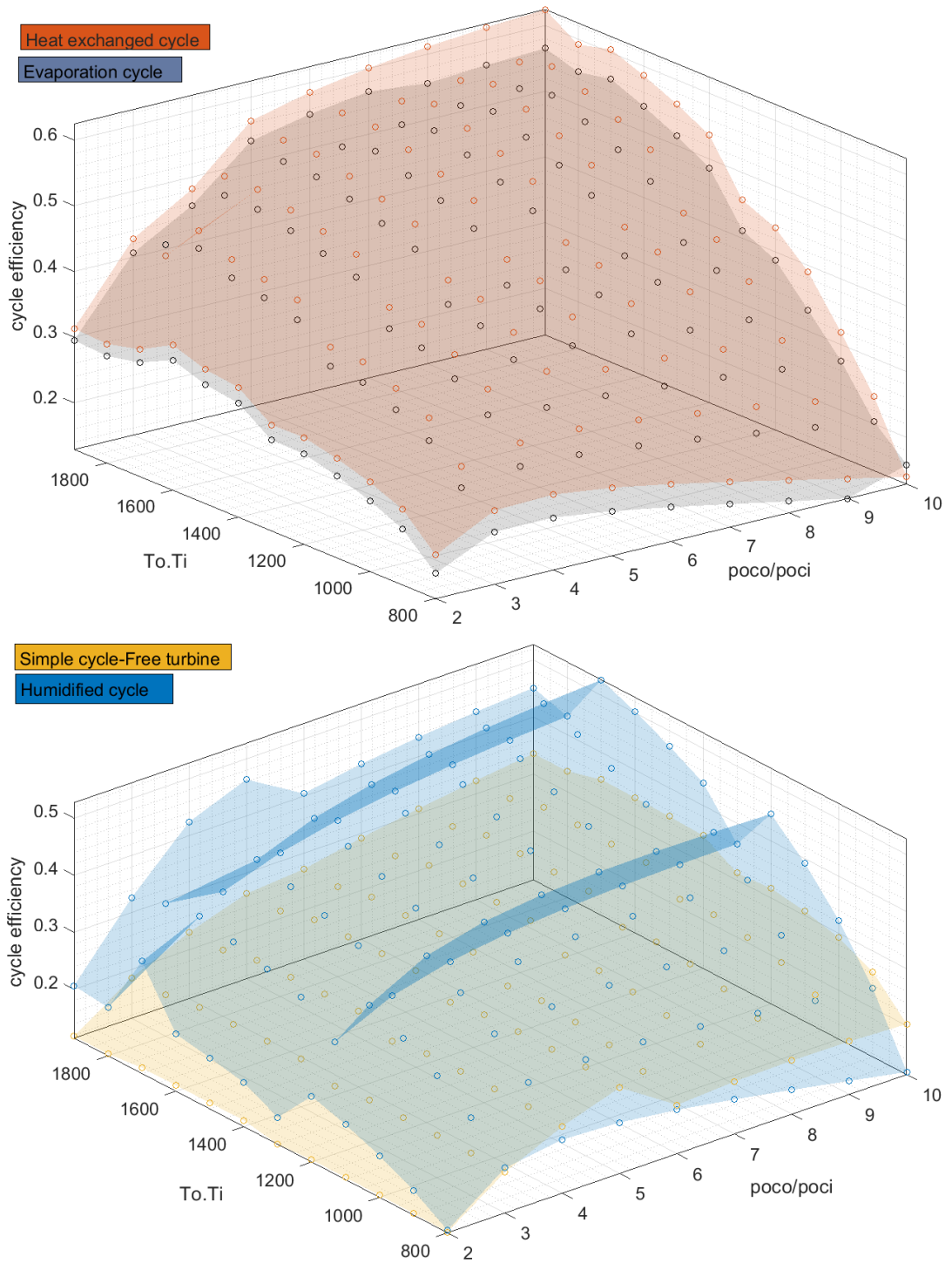


Figure AP4.4. Efficiency results for all cycles with dry compression

